



**Study of thermal performance of falling-  
film absorbers with and without film  
inversion**

**PAPIA SULTANA**  
**(B.Sc. in Mech. Eng., B.U.E.T)**

**DOCTORAL THESIS**

**DEPARTMENT OF MECHANICAL ENGINEERING**  
**NATIONAL UNIVERSITY OF SINGAPORE**  
**2006**

## **ACKNOWLEDGEMENT**

In the course of this project, much assistance and services have been received from various sources for which the author is indebted.

First of all the author would like to express her gratitude to her supervisor Professor N.E. Wijesundera, Department of Mechanical Engineering, National University of Singapore for his sincere guidance, inspiration and valuable suggestions during the course of study. The author also extended her thanks to her co-supervisors Associate Professor. J.C. Ho, Associate Professor Christopher Yap, Department of Mechanical Engineering, National University of Singapore for their constant support and inspiration.

The author is finally thankful to all the staff members in the Thermal Process and Energy Conversion laboratories.

## NOMENCLATURE

$A$	absorber area [ $m^2$ ]
$A(t)$	transient area of forming droplet [ $m^2$ ]
$a$	constant used in equilibrium temperature and LiBr-concentration relationship
$b$	constant used in equilibrium temperature and LiBr-concentration relationship [ $K^{-1}$ ]
$c_{pw}$	specific heat of water [ $kJkg^{-1}K^{-1}$ ]
$c_T$	specific heat capacity of solution [ $kJkg^{-1}K^{-1}$ ]
$c_w$	specific heat capacity of solution [ $kJkg^{-1}$ ]
$D$	mass diffusivity [ $m^2s^{-1}$ ]
$d$	tube diameter [ $m$ ]
$e$	internal energy [ $kJkg^{-1}$ ]
$Ga$	Galileo number
$g$	gravitational acceleration [ $ms^{-2}$ ]
$h_{water}$	convective heat transfer coefficient of coolant water [ $Wm^{-2}K^{-1}$ ]
$h_i$	heat transfer coefficient from solution bulk to the wall [ $Wm^{-2}K^{-1}$ ]
$h_o$	heat transfer coefficient from the interface to the solution bulk [ $Wm^{-2}K^{-1}$ ]
$h_v$	vapour-side heat transfer coefficient [ $kWm^{-2}K^{-1}$ ]
$h$	tube gap [ $m$ ]
$i_{ab}$	enthalpy of absorption [ $kJkg^{-1}$ ]
$i$	enthalpy [ $kJkg^{-1}$ ]
$i_{vs}$	difference between enthalpy of vapor and enthalpy of solution [ $kJkg^{-1}$ ]
$J$	mass flux ratio [%]
$k$	thermal conductivity [ $Wm^{-1}K^{-1}$ ]
$k_{ef}$	effective mass transfer coefficient [ $ms^{-1}$ ]
$k_m$	mass transfer coefficient [ $ms^{-1}$ ]
$\bar{k}_m$	average mass transfer coefficient of the absorber [ $ms^{-1}$ ]
$L$	tube length [ $m$ ]
$M_s$	mass flow rate of solution along one side of the tube [ $kg.m^{-1}s^{-1}$ ]
$M$	no of grid points along the flow direction
$\dot{m}_e$	rate of inflow to form drop [ $kg s^{-1}$ ]
$\dot{m}_o$	rate of outflow from form drop [ $kg s^{-1}$ ]
$\dot{m}_{eb}$	rate of inflow during bridging period [ $kg s^{-1}$ ]
$\dot{m}_v$	mass flux of water vapor [ $kg.m^{-2}s^{-1}$ ]
$m_v$	mass flux of water vapor [ $kg.m^{-2}s^{-1}$ ]
$\dot{m}_{vd}$	absorption rate of water vapor by droplet [ $kg.s^{-1}$ ]
$m_w$	mass flow rate of coolant [ $kg.s^{-1}$ ]
$m_{ws}$	absorption rate of water vapor along one side of the tube [ $kg.m^{-1}s^{-1}$ ]
$m_s$	mass flow rate of solution along one side of the tube [ $kg.m^{-1}s^{-1}$ ]
$m_{sd}$	mass of forming droplet [ $kg$ ]

---

$m_{sj}$	mass flow rate of jet/sheet [ $kg.s^{-1}$ ]
$m_l$	mass flow rate of LiBr along one side of the tube [ $kg.m^{-1}s^{-1}$ ]
$N$	no of grid points across the flow direction
$p$	pressure [ $Pa$ ]
$Q$	heat transfer rate per unit length of the tube [ $W.m^{-1}$ ]
$Re$	Reynolds number
$r_o$	outside radius of tube [ $m$ ]
$r_i$	inside radius of tube [ $m$ ]
$r_d$	radius of the forming droplet [ $m$ ]
$T$	temperature [ $^{\circ}C$ ]
$T_{wall}$	wall temperature [ $^{\circ}C$ ]
$T_w$	temperature of coolant [ $^{\circ}C$ ]
$T_{if}$	temperature of solution at the vapor-liquid interface [ $^{\circ}C$ ]
$t$	time of formation [s]
$U_{bw}$	overall heat transfer coefficient from the bulk solution to the coolant [ $Wm^{-2}K^{-1}$ ]
$\bar{U}_{bw}$	average heat transfer coefficient of the absorber [ $Wm^{-2}K^{-1}$ ]
$u$	velocity along the direction of flow [ $ms^{-1}$ ]
$V$	volume [ $m^3$ ]
$v$	cross flow velocity [ $ms^{-1}$ ]
$W$	mass concentration of LiBr [kg of LiBr/kg of solution]
$WR$	wetting ratio
$w_{if}$	Li-Br concentration at the vapor-liquid interface [kg of LiBr/kg of solution]
$w$	mass concentration of LiBr [kg of LiBr/kg of solution]
$x$	axis in flow direction [ $m$ ]
$y$	axis in cross flow direction [ $m$ ]
$z$	axis along the tube length [ $m$ ]

***Greek symbols***

$\alpha$	thermal diffusivity, [ $m^2s^{-1}$ ]
$\alpha_1, \alpha_2$	roots of the quadratic equation
$\beta$	spacing between neighboring droplets or jets [ $m$ ]
$\tau_b$	duration of bridging [s]
$\lambda$	departure site spacing [ $m$ ]
$\Gamma$	peripheral mass flow rate [ $kg.m^{-1}s^{-1}$ ]
$\delta$	film thickness [ $m$ ]
$\eta$	dimensionless y-axis
$\nu$	kinematic viscosity, [ $m^2s^{-1}$ ]
$\mu$	dynamic viscosity, [ $kg.m^{-1}s^{-1}$ ]
$\sigma$	surface tension [ $N.m^{-1}$ ]
$\xi$	dimensionless x-axis
$\rho$	density [ $kg.m^{-3}$ ]
$\theta$	angle radian
$\phi$	temperature driving potential [ $^{\circ}C$ ]

$\psi$	concentration driving potential [kg of LiBr/kg of solution]
$\varphi$	angular displacement [degree]
$\Delta V_b$	decrease in the drop volume [ $m^3$ ]
$\Delta m_{do}$	mass transferred during bridging period [kg]

***Subscripts***

<i>av</i>	average
<i>b</i>	break up
<i>co</i>	coolant outlet
<i>c</i>	coolant
<i>d</i>	droplet
<i>e</i>	entrance
<i>i</i>	inlet
<i>in</i>	inlet
<i>if</i>	interface
<i>0</i>	inlet
<i>o</i>	outlet/exit
<i>s</i>	solution
<i>si</i>	solution inlet
<i>sb</i>	solution bulk
<i>sf</i>	solution falling film
<i>so</i>	solution outlet
<i>bulk</i>	solution bulk
<i>v</i>	vapor
<i>vs</i>	solution-vapor
<i>w</i>	water
<i>wo</i>	coolant/water outlet
<i>wall</i>	wall
<i>n</i>	tube number
<i>f</i>	formation
max	maximum

## TABLE OF CONTENTS

<b>ACKNOWLEDGEMENT</b>		i
<b>NOMENCLATURE</b>		ii
<b>TABLE OF CONTENTS</b>		v
<b>LISTS OF FIGURES</b>		ix
<b>LISTS OF TABLES</b>		xix
<b>SUMMARY</b>		xx
<b>CHAPTER 1</b>	<b>INTRODUCTION</b>	1
1.1	Vapor absorption systems	2
1.2	Role of absorbers in vapour absorption system	4
1.3	General configurations of absorbers	5
1.4	Factors affecting the performances of conventional tubular absorbers	7
1.5	Performance improvements of tubular absorbers	8
1.6	Review of previous researches on tubular absorbers	9
1.7	Objectives of present research	11
1.8	Significance of present research	12
1.9	Scopes of present research	13
<b>CHAPTER 2</b>	<b>LITERATURE REVIEW</b>	16
2.1	Theoretical studies of absorption processes	17
2.2	Experimental investigations with conventional absorbers	25
2.3	Study of falling film hydrodynamics in horizontal tube banks	27
2.4	Study of existing droplet hydrodynamics model	31
2.5	Study of falling film absorption models in the inter-tube flow regime	33
2.6	Study of film-inverting falling film absorber	34
2.7	Summary	35
<b>CHAPTER 3</b>	<b>THEORETICAL STUDIES</b>	37
3.1	Numerical models of horizontal tubular absorbers	38
3.1.1	Detail round tube model and segmented plate model	39
3.1.2	Numerical simulation model of a single tube	40
3.1.3	Modeling of counter-flow coolant	43
3.1.4	Numerical model for a tube-bundle absorber	45
3.1.4.1	Solution method	45
3.1.4.2	Non-uniform mesh generation	45
3.1.4.3	Solution steps	46
3.1.4.4	Grid independence	51
3.1.4.5	Incomplete wetting of the tubes	52
3.1.5	Vertical flat plate model	52
3.1.6	Results: numerical model	54
3.1.7	Inter-tube flow and absorption	58
3.2	Simplified model of horizontal tubular absorbers	59

3.2.1	Simplified model for a single horizontal tube	59
3.2.2	Inter-tube absorption	65
3.2.2.1	Droplet formation model	66
3.2.2.2	Idealized droplet formation model	74
3.2.2.3	Steady-jet/sheet model	75
3.2.2.4	Transfer coefficients in the inter-tube flow regime	78
3.2.3	Simplified model for a horizontal- tube-bundle absorber	79
3.2.4	Approximate expressions for driving potentials	82
3.2.5	Results and discussion : modeling	83
3.2.5.1	Comparison of idealized droplet formation model	83
3.2.5.2	Comparison of numerical and simplified coupled models	87
3.3	Summary	99
<b>CHAPTER 4</b>	<b>EXPERIMENTAL PROGRAM</b>	<b>100</b>
4.1	Description of the set-up	100
4.1.1	Test section	103
4.1.2	Flow distributor	103
4.1.3	Test tubes	104
4.1.4	Flow circuit	104
4.1.5	Liquid pump	105
4.1.6	Working fluid	105
4.2	Alignment testing	105
4.3	Measuring Equipments	107
4.3.1	Flow meter	107
4.3.2	Video camera	107
4.3.3	Image grabbing software	107
4.3.4	Analyzing software	107
4.4	Instrumentation	108
4.5	Inter-tube flow hydrodynamics	108
4.5.1	Spacing between the droplets and jets	113
4.6	Analysis of experimental data	114
4.7	Summary	117
<b>CHAPTER 5</b>	<b>RESULTS AND DISCUSSION: INTER-TUBE FLOW</b>	<b>118</b>
5.1	Tube gap configuration at 15 mm	118
5.2	Tube gap configuration at 10 mm	123
5.2.1	Time variations of droplet size	132
5.2.2	Inter-tube flow hypothesis	132
5.2.3	Flow pattern changes over the tube gaps	134
5.3	Tube gap configuration at 6 mm	136
5.4	Summary	145
<b>CHAPTER 6</b>	<b>RESULTS AND DISCUSSION: INTER-TUBE ABSORPTION</b>	<b>146</b>
6.1	Comparison of the inter-tube absorption models applied to a single drop/jet	146
6.2	Simulation results for absorption performance	148
6.3	Summary	159

<b>CHAPTER 7</b>	<b>FILM INVERTING ABSORBERS</b>	160
7.1	Operating principles of film-inverting absorbers	160
7.2	The Coanda Effect	163
7.3	Film-inversion based on the Coanda Effect	165
7.3.1	Experimental investigations of the Coanda-Effect Based Film-Inverting Process	166
7.3.1.1	Experimental procedure	167
7.3.1.2	Experimental results: flow observations	167
7.3.1.3	Effect of solution flow rate	170
7.4	Coanda-Effect Based Film-Inverting Absorber(CEBFIA)-numerical model	170
7.4.1	Numerical results for SFT-CEBFIA	172
7.4.2	Performance improvement by the film-inverting absorber	181
7.5	Design considerations for film inverting absorbers	185
7.5.1	Working principle of Two-Film-Tube CEBFIA	189
7.5.2	Performance evaluation of Two-Film-Tube CEBFIA	191
7.5.2.1	Numerical simulation: Two-Film-Tube and Single - Film-Tube CEBFIA designs	195
7.5.3	Hydrodynamics of the TFT film-inverting absorber	200
7.5.3.1	Experimental results	202
7.5.4	Practical design aspects of TFT- CEBFIA	205
7.6	Summary	206
<b>CHAPTER 8</b>	<b>CONCLUSIONS AND RECOMMENDATIONS</b>	207
<b>REFERENCES</b>		213
<b>APPENDICES</b>		
<b>APPENDIX-A</b>	<b>NUMERICAL MODEL OF TUBULAR ABSORBERS</b>	221
A.1	Numerical solution of the governing equations for the round tube	221
A.2	Numerical solution of the governing equations for the flat plate	223
A.3	Discretization of governing equations	225
A.3.1	Non-uniform grid generation	225
A.3.1.1	Backward difference scheme	225
A.3.1.2	Central difference scheme	227
A.3.2	Discretization of energy equation	230
A.3.2.1	Near wall treatment	232
A.3.2.2	Near interface treatment	232
A.3.3	Discretization of species concentration equation	234
A.3.3.1	Near wall treatment	235
A.3.3.2	Near interface treatment	235
A.4	Sensitivity analysis of entering and leaving angle to a tube	237



<b>APPENDIX-B</b>	<b>UNCERTAINTY OF IMAGE ANALYSIS</b>	240
B.1	Manual edge detection process	240
B.2	Semi-automated edge detection process	241
B.3	Comparison of the two edge detection process	243
B.4	Image quality and manual edge detection process	245
<b>APPENDIX-C</b>	<b>SENSITIVITY ANALYSIS</b>	249
C.1	Sensitivity analysis with varying transfer coefficients	249
C.2	Sensitivity analysis with inlet temperature and concentration	253
<b>APPENDIX-D</b>	<b>CALIBRATION OF FLOW METER AND FABRICATION DETAILS</b>	257
D.1	Flow meter calibration	257
D.2	Detailed drawings of the test tubes	258
D.3	Detailed drawing of the distributor	259
<b>APPENDIX-E</b>	<b>INTER-TUBE FLOW HYPOTHESIS</b>	261
E.1	Mass continuity of the flow between the tubes	261

## LISTS OF FIGURES

<b>Number</b>	<b>Title</b>	<b>Page</b>
Figure 1.1	Vapor compression and vapor absorption cycles	2
Figure 1.2	Horizontal tubular absorber configuration	6
Figure 1.3	Continuous falling film absorber.	7
Figure 1.4	Film-inverting falling film absorber.	7
Figure 3.1	Different models of horizontal tubular absorber	38
Figure 3.2.(a)	Single tube falling film configuration (flat plate model)	39
Figure 3.2.(b)	Single tube falling film configuration (round tube model)	39
Figure 3.3	Actual horizontal tubular absorber	43
Figure 3.4	Schematic representation of coolant flow model.	43
Figure 3.5	Computational domain	45
Figure 3.6	Schematic diagram of film entering and leaving angle to a tube.	49
Figure 3.7	Solution flow diagram.	50
Figure 3.8	Bulk concentrations along the absorber length at different grid sizes	51
Figure 3.9	Schematic representation of coolant flow of a vertical plate absorber	53
Figure 3.10	Film thickness [m] variations along the length of the absorber; (a) detailed round tube model, (b) segmented plate model, (c) vertical plate model.	55
Figure 3.11	Absorbed mass flux [ $\text{kg}\cdot\text{m}^{-2}\cdot\text{s}^{-1}$ ] variations along the length of the absorber; (a) detailed round tube model, (b) segmented plate model, (c) vertical plate model.	56
Figure 3.12	Bulk solution temperature variations along the length of the absorber; (a) detailed round tube model, (b) segmented plate model, (c) vertical plate model.	57
Figure 3.13	Bulk solution concentration [%LiBr/100] along the length of the absorber; (a) detailed round tube model, (b) segmented plate model, (c) vertical plate model.	57
Figure 3.14	Continuous sheet flow between the tubes	58
Figure 3.15	Physical model of the falling-film over a tube.	60
Figure 3.16	Schematic diagram of tube-bundle absorber	60

Number	Title	Page
Figure 3.17(a)	Droplet profile during formation.	66
Figure 3.17(b)	Droplet profile during bridging.	66
Figure 3.17(c)	Steady jet profile.	66
Figure 3.18	Schematic diagram of the formation of a hemispherical droplet.	73
Figure 3.19	Physical model for inter-tube flow.	75
Figure 3.20	Comparison of droplet formation models. Graphs: (a) bulk temperature change by the present model; (b) bulk temperature change by the model of Siyoung and Garimella [88]; (c) interface temperature change by the present model; (d) interface temperature change by the model of Siyoung and Garimella [88]; Experimental conditions: Seventh tube, $\Gamma = 0.024 \text{ kgm}^{-1}\text{s}^{-1}$ , $WR=0.8$ ; as described in [88].	84
Figure 3.21	Comparison of droplet formation models. Graphs: (a) bulk and interface concentration change by the present model; (b) bulk and interface concentration change by the model of Siyoung and Garimella [88]; Experimental conditions: Seventh tube, $\Gamma = 0.024 \text{ kgm}^{-1}\text{s}^{-1}$ , $WR=0.8$ ; as described in [88].	85
Figure 3.22	Comparison of tube surface temperature. Graphs: (a) numerical model with inter-tube flow; (b) simplified model with inter-tube flow; (c) simplified model without inter-tube flow; (d) numerical model without inter tube flow; ( ) experiment of Nomoura et al. [75]; conditions: $\Gamma=0.058 \text{ kgm}^{-1}\text{s}^{-1}$ , $T_{si} = 54^{\circ}\text{C}$ , $w_{si}=0.62$ , $WR = 0.8$ .	86
Figure 3.23	Comparison of inter-tube solution temperature. Graphs: (a) numerical model with inter-tube flow; (b) simplified model with inter-tube flow; (c) tube surface temperature of simplified model with inter-tube flow;(d) continuous temperature plot of simplified model with inter tube flow; ( ) experiment of Nomoura et al. [75]; conditions: $\Gamma=0.058 \text{ kgm}^{-1}\text{s}^{-1}$ , $T_{si} = 54^{\circ}\text{C}$ , $w_{si}=0.62$ , $WR = 0.8$ .	86
Figure 3.24	Local and average overall heat transfer coefficient along the absorber; experimental conditions: $\Gamma=0.0595 \text{ kgm}^{-1}\text{s}^{-1}$ , $T_{si} = 39.8^{\circ}\text{C}$ , $w_{si}=0.604$ , $WR = 1.0$ [43].	88
Figure 3.25	Local and average mass transfer coefficient along the absorber; experimental conditions: $\Gamma=0.0595 \text{ kgm}^{-1}\text{s}^{-1}$ , $T_{si} = 39.8^{\circ}\text{C}$ , $w_{si}=0.604$ , $WR = 1.0$ [43].	89

Number	Title	Page
Figure 3.26	Comparison of tube-wise bulk temperature of solution. Graphs: (a) numerical model; (b) simplified model with tube-wise variable transfer coefficients; (c) simplified model with constant transfer coefficients; conditions: $\Gamma = 0.0595 \text{ kgm}^{-1} \text{ s}^{-1}$ , $T_{si} = 39.8^{\circ}\text{C}$ , $w_{si} = 0.604$ , $WR = 1.0$ [43].	91
Figure 3.27	Comparison of tube-wise bulk concentration of LiBr (%/100). Graphs: (a) numerical model; (b) simplified model with tube-wise variable transfer coefficient; (c) simplified model with constant transfer coefficient; conditions: $\Gamma = 0.0595 \text{ kgm}^{-1} \text{ s}^{-1}$ , $T_{si} = 39.8^{\circ}\text{C}$ , $w_{si} = 0.604$ , $WR = 1.0$ [43].	91
Figure 3.28	Comparison of tube-wise coolant average temperature. Graphs: (a) numerical model; (b) simplified model with tube-wise variable transfer coefficient; (c) simplified model with constant transfer coefficient; conditions: $\Gamma = 0.0595 \text{ kgm}^{-1} \text{ s}^{-1}$ , $T_{si} = 39.8^{\circ}\text{C}$ , $w_{si} = 0.604$ , $WR = 1.0$ [43].	92
Figure 3.29	Comparison of ‘extracted’ and ‘averaged’ overall heat transfer coefficients; experimental conditions of Islam [43].	92
Figure 3.30	Comparison of ‘extracted’ and ‘averaged’ effective mass transfer coefficients; experimental conditions of Islam [43].	93
Figure 3.31	Bulk concentration of LiBr changes over a tube. Graphs: (a) simplified model with constant film thickness; (b) simplified model with variable film thickness.	94
Figure 3.32	Bulk temperature changes over a tube. Graphs: (a) simplified model with constant film thickness; (b) simplified model with variable film thickness.	94
Figure 3.33	Comparison of the driving potential $\phi$ along the absorber. Graphs: (a) simplified model with exact roots; (b) simplified model with approximate roots; experimental conditions of Nomoura et al. [75].	95
Figure 3.34	Comparison of the driving potential $\psi$ along the absorber. Graphs: (a) simplified model with exact roots; (b) simplified model with approximate roots; experimental conditions of Nomoura et al. [75].	96

Number	Title	Page
Figure 3.35	Comparison of tube-wise averaged bulk temperature and tube surface temperature at the top of a tube by the numerical model without inter-tube absorption. Graphs: (a) variable wetting ratio from Nomoura et al. [75] ;(b) wetting ratio 0.8; (c) wetting ratio 1.0 ; (▲) tube surface temperature from the experiment of Nomoura et al. [75]; conditions: $\Gamma=0.058 \text{ kgm}^{-1}\text{s}^{-1}$ , $T_{si}=54^{\circ}\text{C}$ , $w_{si}=0.62$ .	97
Figure 3.36	Comparison of tube-wise averaged bulk temperature and tube surface temperature at the top of a tube by the simplified model without inter-tube absorption. Graphs: (a) variable wetting ratio from Nomoura et al. [75] ;(b) wetting ratio 0.8; (c) wetting ratio 1.0 ; (▲) tube surface temperature from the experiment of Nomoura et al. [75]; conditions: $\Gamma=0.058 \text{ kgm}^{-1}\text{s}^{-1}$ , $T_{si}=54^{\circ}\text{C}$ , $w_{si}=0.62$ .	98
Figure 4.1	Schematic diagram of experimental set-up	101
Figure 4.2	Photographs of the experimental set-up	101
Figure 4.3	Schematic diagram of the test section side view	102
Figure 4.4	Assembly of the guide bar, (b) Complete assembly of the structure, (c) Testing of vertical alignment of the tube array	102
Figure 4.5	Distance between two horizontal guide bars	104
Figure 4.6	Change in wetted length of the tubes as the flow progresses	112
Figure 4.7	Flow diagram of the experimental program.	115
Figure 4.8	Use of image analysis program	116
Figure 5.1	A typical droplet cycle [images are taken at solution flow rate $0.0079 \text{ kg.s}^{-1}$ ]	119
Figure 5.2	The volume and surface area changes during a droplet cycle [images are taken at solution flow rate $0.0079 \text{ kg.s}^{-1}$ ].	119
Figure 5.3	Sequential video images at solution flow rate $0.008 \text{ kg.s}^{-1}$ [Re: 17.6] for a tube gap of 15 mm	121
Figure 5.4	Sequential Sequential video images at solution flow rate $0.0145 \text{ kg.s}^{-1}$ [Re: 30.3] for a tube gap of 15 mm.	122
Figure 5.5	Sequential video images at flow rate $0.0079 \text{ kg.s}^{-1}$ [Re: 16.5] for a tube gap of 10 mm.	125

<b>Number</b>	<b>Title</b>	<b>Page</b>
Figure 5.6	Sequential video images at flow rate $0.0118 \text{ kg.s}^{-1}$ [Re: 24.7]; for a tube gap of 10 mm	126
Figure 5.7	Sequential video images at flow rate $0.0145 \text{ kg.s}^{-1}$ [Re: 28.85] for a tube gap of 10 mm.	127
Figure 5.8	Sequential video images at solution flow rate $0.022 \text{ kg.s}^{-1}$ [Re: 45.1] for a tube gap of 10 mm.	128
Figure 5.9	Transient volume and surface area variation at each of the 6 droplet sites [Re = 16; solution flow rate: $0.0079 \text{ kg.s}^{-1}$ ].	129
Figure 5.10	Transient volume and surface area variation at each of the 7 droplet sites [Re = 24.7; solution flow rate: $0.0118 \text{ kg.s}^{-1}$ ].	130
Figure 5.11	Transient volume and surface area variation at each of the 6 droplet sites [Re = 28.85; solution flow rate: $0.0145 \text{ kg.s}^{-1}$ ].	131
Figure 5.12	Sequential video images to show the droplet behaviors among several tube gaps.	135
Figure 5.13	Sequential video frames at flow rate $0.0079 \text{ kg.s}^{-1}$ ; tube gap 6mm	138
Figure 5.14	Transient volume and surface area variation at solution flow rate $0.0079 \text{ kg.s}^{-1}$ ; tube gap 6mm.	140
Figure 5.15	Sequential video images at solution flow rate $0.011 \text{ kg.s}^{-1}$ ; tube gap 6mm.	141
Figure 5.16	Transient volume and surface area at solution flow rate $0.011 \text{ kg.s}^{-1}$ ; tube gap 6mm.	142
Figure 5.17	Sequential video images at solution flow rate $0.0163 \text{ kg.s}^{-1}$ [Re: 34.02]; tube gap 6mm.	143
Figure 5.18	Transient volume and surface area at solution flow rate $0.0163 \text{ kg.s}^{-1}$ [Re: 34.02]; tube gap 6mm.	144
Figure 6.1	Experimental data of a droplet surface area profile with polynomial fit during formation at 6 mm tube gap situation.	147
Figure 6.2	Variation of drop area with time. Graphs: (a) tube gap = 6 mm, flow rate $\Gamma = 0.027 \text{ kg.m}^{-1}\text{s}^{-1}$ , (b) tube gap = 10 mm, flow rate $\Gamma = 0.02 \text{ kg.m}^{-1}\text{s}^{-1}$ .	151
Figure 6.3	Variation of drop volume with time. Graphs: (a) tube gap = 6 mm, flow rate $\Gamma = 0.027 \text{ kg.m}^{-1}\text{s}^{-1}$ , (b) tube gap = 10 mm, flow rate $\Gamma = 0.02 \text{ kg.m}^{-1}\text{s}^{-1}$ .	151

<b>Number</b>	<b>Title</b>	<b>Page</b>
Figure 6.4	Schematic description of inter-tube droplet flow regime; operating conditions are $w_{s,in} = 0.60$ , $T_{s,in} = 39.8^{\circ}c$ , $p = 1.388kpa$ , $L = 0.2m$ , $r_i = 0.011m$ .	152
Figure 6.5	Schematic description of inter-tube jet flow regime; operating conditions are $w_{s,in} = 0.60$ , $T_{s,in} = 39.8^{\circ}c$ , $p = 1.388kpa$ , $L = 0.2m$ , $r_i = 0.011m$ .	152
Figure 6.6	Mass flux ratio at varying flow rate and tube gap.	156
Figure 6.7	Sensitivity of mass flux ratio with higher mass transfer coeff. ; Tube gap: 10 mm.	158
Figure 7.1	Flow over the film-inverting round tube absorber.	162
Figure 7.2	Pressure variation perpendicular to streamlines.	163
Figure 7.3	Demonstration of Coanda Effect [17]	164
Figure 7.4	Coanda Effect based film inversion; by single film arrangement of the tubes.	165
Figure 7.5(a)	Left hand side view with light	168
Figure 7.5(b)	Right hand side view without light.	168
Figure 7.6	A closer view of the alternate flow surfaces.	168
Figure 7.7	Film flow at three different flow rates (a) $0.022 \text{ kg.s}^{-1}$ (b) $0.016 \text{ kg.s}^{-1}$ (c) $0.008 \text{ kg.s}^{-1}$	169
Figure 7.8	Temperature profile across the flow [ $\eta = y/\delta$ ] for the first tube in film-inverting absorber; operating conditions: set-1 in Table 7.2.	173
Figure 7.9	Concentration profile across the flow [ $\eta = y/\delta$ ] for the first tube in film-inverting absorber; operating conditions: set-1 in Table 7.2.	174
Figure 7.10	Concentration profile (% of LiBr/100) across the flow [ $\eta = y/\delta$ ] for tube 2 in film-inverting absorber; operating conditions: set-1 in Table 7.2.	175
Figure 7.11	Concentration profile (% of water/100) across the flow [ $\eta = y/\delta$ ] for tube 2 in film-inverting absorber, operating conditions: set-1 in Table 7.2.	176

<b>Number</b>	<b>Title</b>	<b>Page</b>
Figure 7.12	Temperature profile across the flow [ $\eta = y/\delta$ ] for tube 2 in film-inverting absorber, operating conditions: set-1 in Table 7.2.	177
Figure 7.13(a)	Variation of mass flux of water vapor along the direction of flow; (a) film-inverting absorber; (b) continuous falling film absorber, operating conditions: set-1 in Table 7.2.	178
Figure 7.13(b)	Variation of bulk and interface temperature along the direction of flow; (a) film-inverting absorber; (b) continuous falling film absorber [ $\xi = \theta/\pi$ ], operating conditions: set-1 in Table 7.2.	179
Figure 7.13(c)	Variation of bulk and interface concentration along the direction of flow; (a) film-inverting absorber; (b) continuous falling film absorber [ $\xi = \theta/\pi$ ], operating conditions: set-1 in Table 7.2.	179
Figure 7.14	Tube-wise variation of mass flux; (a) by the film inverting tubular absorber, (b) by the conventional absorber without film-inversion, operating conditions: set-2 in Table 7.2.	181
Figure 7.15	Variation of tube-wise averaged interface and bulk concentration (%LiBr/100); by the (a) film inverting tubular absorber, (b) conventional absorber without any film-inversion, operating conditions: set-1 in Table 7.2.	182
Figure 7.16	Variation of tube-wise averaged interface and bulk temperature; by the (a) film inverting tubular absorber, (b) conventional absorber without any film-inversion, operating conditions: set-1 in Table 7.2.	183
Figure 7.17	Tube-wise variation of coolant average temperature; by the (a) film inverting tubular absorber, (b) conventional absorber without any film-inversion, operating conditions: set-1 in Table 7.2.	183
Figure 7.18 (a)	Film-inverting design with guide vane [45]	186
Figure 7.18 (b)	Semi-circular film-inverting design [single column]	186
Figure 7.18 (c)	Semi-circular film-inverting design [multiple columns].	186
Figure 7.19	Two-Film-Tube [TFT] assembly of film-inverting absorber.	188
Figure 7.20 (a)	Tube arrangement for separation of the flow	188



<b>Number</b>	<b>Title</b>	<b>Page</b>
Figure 7.20 (b)	Tube arrangement for flow merging	188
Figure 7.21	Single-Film-Tube [SFT] assembly of film-inverting absorber.	190
Figure 7.22 (a)	Number of participating films in a TFT column of Figure 7.19	191
Figure 7.22 (b)	Number of participating films in a SFT column of Figure 7.21	191
Figure 7.22 (c)	Film entering and leaving angles for TFT assembly.	192
Figure 7.22 (d)	Film entering and leaving angles for SFT assembly.	192
Figure 7.23	Variation of (i) vapour mass flux [ $\text{kg}\cdot\text{m}^{-2}\cdot\text{s}^{-1}$ ] (ii) Bulk concentration [%LiBr/100] (iii) Bulk temperature in the first two tubes of TFT and SFT assembly shown in Figure 7.22(a) and 7.22(b); operating conditions: set 4 in Table 7.2; angular positions are given in Table 7.4 for TFT and configuration 1 in Table 7.5 for SFT.	196
Figure 7.24	Tube-wise variation of coolant temperature of TFT and SFT arrangements shown in Figure 7.22(a) and 7.22(b); operating conditions: set 4 in Table 7.2; angular positions are given in Table 7.4 for TFT and configuration 1 in Table 7.5 for SFT.	197
Figure 7.25	Photograph of the test set up with modified test section.	200
Figure 7.26	Images to explain mechanism of TFT film inversion.	201
Figure 7.27	Experimental verification of the TFT film-inverting concept	202
Figure 7.28	Final TFT configurations [flow rate: $0.0163 \text{ kg}\cdot\text{s}^{-1}$ ].	202
Figure 7.29	Final TFT configurations [flow rate: $0.008 \text{ kg}\cdot\text{s}^{-1}$ ].	204
Figure A.1	Transformation of co-ordinates.	221
Figure A.2	Taylor series representation for non-uniform grid; backward difference scheme.	226
Figure A.3	Taylor series representation for non-uniform grid; central difference scheme.	227
Figure A.4	Non-uniform grid along $\eta$ direction.	228
Figure A.5	Nodal distribution	230
Figure A.6	Control volume near the wall	232

<b>Number</b>	<b>Title</b>	<b>Page</b>
Figure A.7	Sensitivity of mass flux [ $kg.m^{-2}s^{-1}$ ] at different angular values: operating conditions of Islam [43].	237
Figure A.8	Sensitivity of bulk concentration [%LiBr/100] at different angular values: operating conditions of Islam [43].	238
Figure A.9	Sensitivity of bulk temperature [K] at different angular values: operating conditions of Islam [43].	238
Figure B.1	Manual edge detection process using Matrox inspector	241
Figure B.2	Comparison of the two edge detection processes for a sample jet at 6 mm tube gap situation.	242
Figure B.3	Comparison of the two edge detection processes for a sample jet at 10 mm tube gap situation.	242
Figure B.4	Sample images taken by video camera (400x300 pixels).	245
Figure B.5	Sample images taken by still camera (3008x2000 pixels)	245
Figure B.6	Application of manual edge detection on image taken by video camera [CANON MVX 35i].	246
Figure C.1	Sensitivity of mass flux ratio with varying mass transfer coeff. $k_m$ [tube gap: 10 mm]	250
Figure C.2	Sensitivity of mass flux ratio with varying mass transfer coeff. $k_m$ [tube gap: 6 mm]	251
Figure C.3	Sensitivity of mass flux ratio with varying heat transfer coeff. $h_o$ [tube gap;10 mm]	252
Figure C.4	Sensitivity of mass flux ratio with varying heat transfer coeff. $h_o$ [tube gap: 6 mm]	253
Figure C.5	Sensitivity of inter-tube mass flux with varying inlet concentration of LiBr solution [%LiBr/100] for a tube gap of 10 mm.	254
Figure C.6	Sensitivity of inter-tube mass flux with varying inlet temperature LiBr solution [ $^{\circ}C$ ] for a tube gap of 10 mm.	255
Figure D.1	Flow meter calibration chart for 54% wt. concentration of LiBr.	257
Figure D.2	Detailed drawings of the test tube [dimension unit: mm].	258

<b>Number</b>	<b>Title</b>	<b>Page</b>
Figure D.3	Detailed drawings of the distributor [dimension unit: mm].	259
Figure E.1	Typical droplet cycle; (a) development stage, (b) bridge form stage, (c) pull back stage	257

## LISTS OF TABLES

<b>Name</b>	<b>Title</b>	<b>Page</b>
Table 4.1	Operating conditions	106
Table 4.2	Working fluid properties	106
Table 4.3	Camera specifications	106
Table 4.4	Transition film Reynolds number for 54% wt concentration LiBr solution	109
Table 4.5	Experimental observations-1; Tube gap: 10mm; wetted length: 21 cm	110
Table 4.6	Experimental observations-2; Tube gap: 6mm; wetted length: 20 cm	111
Table 4.7	Drop/jet spacing calculated from video images; Tube gap: 10mm	113
Table 4.8	Drop/jet spacing calculated from video images; Tube gap: 6 mm	113
Table 6.1	Model comparisons; results of the seventh tube from [88]	147
Table 6.2	Mass transfer coefficient for inter-tube droplet flow	149
Table 6.3	Absorption rate/Tube gap: 10mm, wetted length: 21cm	154
Table 6.4	Absorption rate/Tube gap: 6mm, wetted length: 20cm	155
Table 7.1	Sensitivity of the entering and leaving angles	172
Table 7.2	Experimental operating conditions of Islam et al. [45]	172
Table 7.3	Absorption performance of tubular film-inverting absorbers	184
Table 7.4	TFT assembly of CEBFIA; angular arrangement of Figure 7.22 (c)	193
Table 7.5	SFT assembly of CEBFIA; angular arrangement of Figure 7.22 (d)	194
Table 7.6	Comparison absorption performances of TFT and SFT assembly	199
Table B.1	Error analysis of the edge detection processes.	244
Table B.2	Error analysis of different images.	247
Table E.1	Error estimation at flow rate $0.0079 \text{ kg.s}^{-1}$ ; tube gap 10 mm	263
Table E.2	Error estimation at flow rate $0.0118 \text{ kg.s}^{-1}$ ; tube gap 10 mm.	264
Table E.3	Error estimation at flow rate at $0.0145 \text{ kg.s}^{-1}$ ; tube gap 10 mm.	265

## **Summary**

The improvement in efficiency of absorption cooling machines requires a deeper understanding of the heat and mass transfer processes occurring between the liquid and vapor phases in the absorber. The main objective of the present study is to develop a realistic model of the horizontal bank of tubes absorber, which may be used in studies to improve the efficiency of absorption machines. In order to fulfill this objective, detailed mathematical models are developed and simulations are carried out for a tubular absorber in which simultaneous heat and mass transfer occurs to a falling-film. An attempt is made to take into account the detailed geometry of the bank of horizontal tubes. A numerical model is developed initially for the single tube and is later extended to simulate the bank of horizontal tubes in the practical absorber. The same modelling procedure is followed for the conventional flat plate model of the horizontal bank of tubes absorber. A detailed comparison between the predictions of the models is made. Some practical phenomena regarding the inter-tube flow and the partial wetting of the absorber tubes are considered to test the applicability of the model to practical designs. The simulation results of the present round tube absorber model with inter-tube flow are compared with well known experimental data from the literature [75]. The comparisons show reasonable agreement.

A simplified model is developed for the design analysis of horizontal tubular absorbers. The analytical procedure follows the model presented by Islam et al. [46] for vertical plate absorbers. However, considerable modifications are done to make the model applicable to a bank of horizontal tubes with the coolant flowing in a serpentine fashion in the opposite direction. The present model, which also includes a simplified analysis of inter-tube flow, is therefore more realistic when applied to counter-flow tubular absorbers. Moreover, the model can be used to extract overall heat and mass transfer coefficients from experimental data of horizontal tubular absorber.

Inter-tube absorption models are developed for three different modes of inter-tube flow which are droplet, jet and sheet flow mode. First, the inter-tube sheet flow absorption model is numerically developed introducing a continuous sheet between each tube junction. Later, semi-empirical heat and mass transfer models of the inter-tube droplet and steady jet/sheet flow modes are developed based on known transfer coefficients for inter-tube absorption. The models operate extracting the hydrodynamics data from the experiments. Hence, a detailed experimental program is undertaken in order to obtain inter-tube flow hydrodynamics data for a wide range of operating conditions. The experimental data are processed by a digital image analysis program. At first, the inter-tube flow events at various operating conditions are recorded with the video camera. The sequential video images are then analyzed with the image analysis program. The time-dependent droplet volume and surface area profiles are developed at varying flow rates which form the basis of the developed models to operate. This way, the absorption data obtained from the developed models provide more realistic absorption performances of a tubular absorber. The contribution of inter-tube absorption is thoroughly examined at several operating conditions. The contribution of inter-tube absorption into the total performance of the horizontal tubular absorber is found to be significant, though the results depend on the assumed heat and mass transfer coefficients in the developed models.

The film-inverting absorber model shows significant improvement of absorption performance. It is believed that the film-inverting absorber can resolve some of the issues regarding the inter-tube flow and partial wetting of the tubes. Islam et al. [45] developed a film-inverting tubular absorber which resulted in experimental performance improvements of 90-100 percents. However, they used guide fins between the tubes to affect the film inversion. In the present study, a new film-inverting tubular absorber is proposed using the Coanda Effect to achieve film-inversion. The film-inverting

mechanism is analyzed in detail with the help of the absorption model of the new film-inverting absorber. The experimental investigation of the Coanda-Effect Based film-inverting hydrodynamics is also performed to verify the practical feasibility of the new design. In order to increase the vapour absorption rate more, a Two-Film-Tube (TFT) film-inverting absorber design is proposed. The performance of the TFT film-inverting absorber is simulated numerically and compared with the Single-Film-Tube (SFT) film-inverting absorber. The TFT film-inverting absorber increased the absorption rate over the SFT design. The practical feasibility of the new design concept was verified by performing experimental investigations of the film-flow hydrodynamics of the TFT absorber. The experimental results demonstrate the feasibility of this novel design.

## **CHAPTER 1**

### **INTRODUCTION**

Absorbers of vapor absorption cooling systems are critical components of the system. The lower coefficient of performance (COP) of the vapor absorption system is invariably related to the poor performance of the absorber. The performance of the absorber is dependent on the available absorption surface area which in turn is dependent on the geometric configuration of the absorber. Among various configurations, falling- film type horizontal tubular absorber is most common because of its lower manufacturing cost and ease of installation. However, the performance of the horizontal tubular absorbers is affected by some practical issues related to the tubular configuration.

The major issue related to the tubular absorber performance is the partial wetting of the absorber tubes. In this absorber design a thin film of solution falls down over the horizontal tubes. As the flow progresses, the wetted surface of the horizontal tubes gradually decreases due to poor surface wettability of the solution over the tubes. This effect becomes so severe that in some cases absorber could suffer from 'drying out'. Due to the absorber drying out, less surface area participates in the absorption, which reduces absorption performance.

Another issue related to the absorber performance is the variation in inter-tube flow modes. The type of inter-tube flow depends on several controlling factors which are discussed in detail in a later chapter. Moreover, the different modes of inter-tube flow affects partial wetting of the tubes.

Prior to addressing the details of the above issues, it is useful to consider the role of the absorber in the vapor absorption cooling system. This will provide the background to identify the factors which affect the performance of the horizontal tubular absorbers and develop techniques for the performance improvement.



## 1.1 Vapour absorption systems

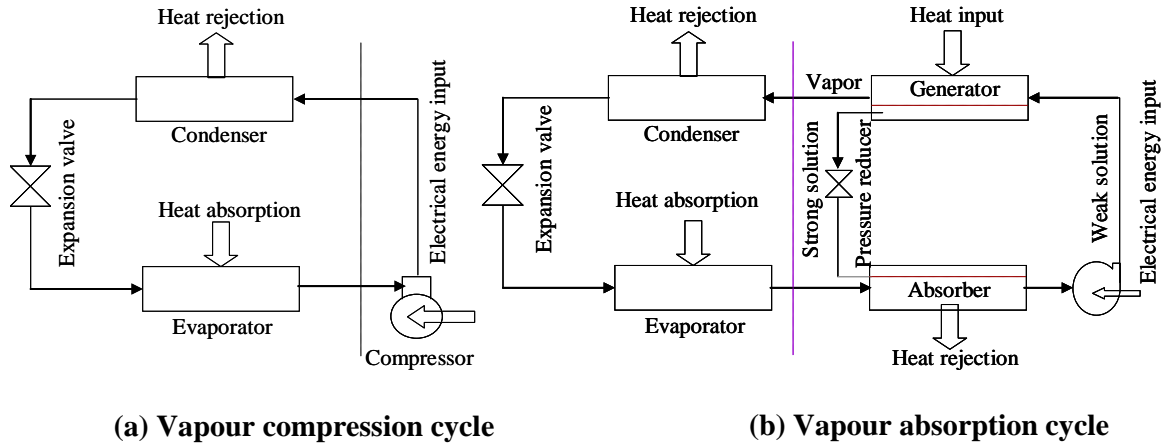


Figure 1.1 Vapour compression and vapor absorption cycles

The vapour absorption system is the viable alternative to the vapor compression refrigeration system because it has several advantages. Vapour absorption systems use working fluids that have no known adverse environmental effects like global warming and ozone depletion. Figure 1.1 (a) and (b) illustrate the working principles of both the vapour compression and vapour absorption refrigeration cycles respectively. A refrigeration cycle normally operates with the condenser, expansion valve and evaporator as shown in both figures. The low pressure refrigerant vapour from the evaporator is transformed into high pressure vapour and is delivered to the condenser. The vapour compression system uses a compressor for this task as shown schematically in Figure 1.1 (a). In the condenser, the vapour is condensed and the resulting heat is released to the ambient. The condensed refrigerant is finally expanded to the evaporator pressure through an expansion valve to continue the cycle.

However, in the vapour absorption system, the compressor is replaced by a combination of an absorber and a generator as shown schematically in Figure 1.1 (b). In this system, the low pressure vapour leaving the evaporator is first absorbed in an appropriate absorbing liquid in the absorber. The associated absorption process is the conversion of

vapour into liquid with rejection of heat. In the next step, the pressure of the liquid is elevated with a liquid pump and is delivered to the generator. Finally, in the generator, the vapour is driven off the liquid by the help of the heat from a high temperature source. The liquid solution returns to the absorber through a pressure reducer or throttle valve to maintain the pressure difference between the generator and absorber. The refrigerant on the other hand continues its passage through the rest of the cycle in a manner similar to that of a vapour compression system.

The main advantage of the vapour absorption system is that the absorption cycle is basically a heat operated cycle whereas the vapour compression cycle is a work operated cycle. For the work operated cycle, the pressure of the refrigerant is elevated by a compressor which requires work. The heat operated cycle on the other hand is mainly operated by the heat required to drive off the vapour from the generator. Though there is a requirement of some work in the absorption cycle to drive the pump, the amount of work is small compared with that needed in the vapour-compression cycle.

The heat required in the generator unit of vapour absorption system can be provided from various sources such as heat derived from solar collectors. Moreover, because of the rapidly rising cost of energy, low temperature level heat rejected to the atmosphere in chemical or process plants can be used to operate absorption system. Thus the vapour absorption system is an energy saving and environmental friendly device.

Lithium Bromide-water is widely used as an absorbent and refrigerant pair in vapour absorption systems due to their various advantageous properties. Lithium bromide is a solid salt crystal. In the presence of water vapour it absorbs the vapour and becomes a liquid solution. The boiling point of Lithium-Bromide is much higher than that of water which helps the refrigerant water vapour to boil off from the liquid as pure vapour. This is the major advantage of using Lithium Bromide-water solution in the vapour

absorption system because no absorbent can possibly be carried over to the other sections of the refrigeration cycle such as the evaporator.

## **1.2 Role of absorbers in vapour absorption system**

The absorber is usually the largest and the most expensive component of the absorption cooling system. It is a place where the low pressure refrigerant vapour or the absorbate is absorbed in an absorbent solution. In practical absorbers, a thin film of liquid solution composed of absorbent and absorbate flows down over the absorber surface. The film is in contact with stagnant vapour of absorbate at a constant pressure different from the equilibrium vapour pressure of the inlet solution. As a result of this difference, mass transfer of absorbate takes place at the liquid-vapour interface. The absorbed absorbate diffuses into the liquid film. The heat generated in the absorption process, that is the heat of absorption flows through the film to the external coolant. The purpose of the coolant is to sustain the absorption process by continually removing the heat released.

The performance of the vapour absorption system is greatly dependent on the rate of absorption of the refrigerant vapour into the absorbent liquid. Lower absorption rate can reduce the flow of refrigerant which in effect can reduce the overall system performance. So a lower coefficient of performance (COP) of the absorption refrigeration machines is mainly due to the lower performance of the absorber.

Another major feature of vapor absorption machines is the absorber being the most expensive part of the system mostly due to its size, weight and complexity of the absorption process. It is the size of the absorber which greatly affects the heat and mass transfer processes during the cycle operation. If the transport processes are improved, greater reduction in the absorber size can be achieved and hence a reduction of overall system cost. Therefore, much of recent work is focused on the performance improvement of the absorber by enhancing the transport processes.

Enhancement of the vapour absorption rate in the absorber can also be achieved through the increase of useful surface area of absorption. The higher the participating surface area of absorption, the higher is the vapor absorption rate without increasing the overall size of the absorber. The useful surface area of absorption is affected by the flow hydrodynamics involved in any design. Therefore, it is important to study the various configurations of the absorbers in order to understand how much useful surface area of absorption could be achieved by these designs.

### **1.3 General configurations of absorbers**

Falling film absorbers are widely used in most of the vapour absorption refrigeration machines because of their higher heat transfer coefficients and smaller need of liquid inventories than flooded absorbers. Among them horizontal tubular absorbers are the most popular because they offer advantages in dealing with liquid distribution, non-condensable gases and ease of installation as also described by Hu and Jacobi [39].

In this configuration, a thin film of absorbent solution leaving the distributor falls down over the horizontal bank of tubes which is surrounded by a pool of refrigerant vapour from the evaporator as shown in Figure 1.2. Absorption of the refrigerant vapour occurs as the solution falls over and between the tubes. During the absorption process, the heat of absorption is released at the vapour-liquid interface. If this heat is not removed, it will impede the absorption process. To remove the heat of absorption, cooling water is passed through the tubes in serpentine form.

The flow over horizontal tubular absorbers is divided into two distinct flow regimes, which are i) falling film flow regime and ii) inter-tube flow regime. The falling film flow regime is a thin-film flow over each tube under the action of gravity. After falling down the tube, the solution film enters into the inter-tube flow regime. The nature of flow of solution in the inter-tube regime is mainly dependent on solution mass flow rate. The flow in this regime may take various forms like droplet, jet and sheet flow [39].

Absorption process continues in this flow regime regardless of the mode of inter tube flow. The solution film enters into a new falling film regime right after leaving the inter-tube flow regime. Thus the falling film flow over the bank of horizontal tubes is composed of alternate falling film and inter-tube flow regimes.

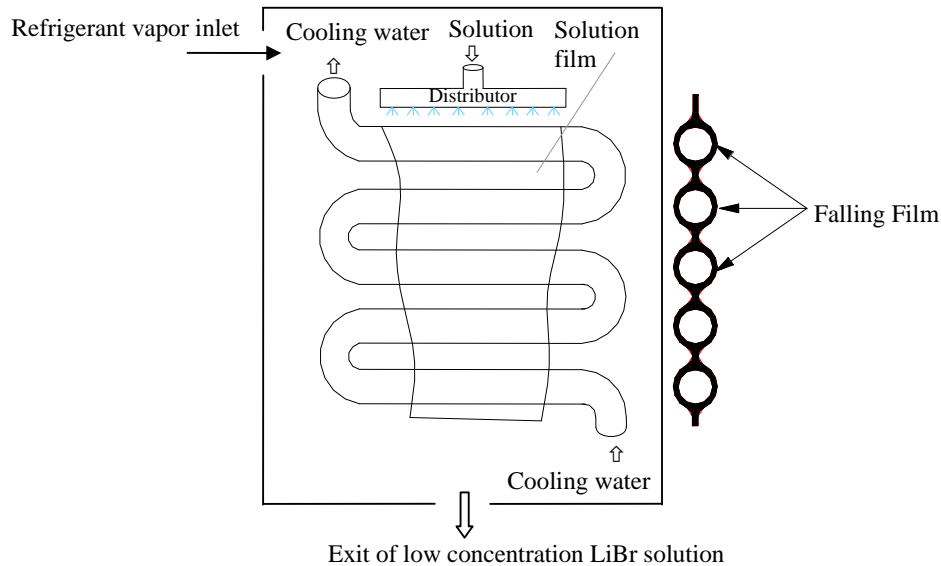


Figure 1.2 Horizontal tubular absorber configuration

If a bank of horizontal bare tubes is used in the absorber, the configuration is called a continuous falling film absorber for which the flow patterns are discussed above. The schematic representation of this conventional falling film absorber is shown in Figure 1.3. Recently, a film-inverting falling film absorber was introduced by Islam et al. [45] where the solution film is guided to flow in alternate directions by the use of guide vanes. The schematic representation of this film-inverting falling film absorber is shown in Figure 1.4. The flow pattern of the film-inverting absorber is different than that of continuous falling film absorber mainly due to the absence of so called inter-tube flow regime. The performance of the film-inverting falling film absorbers is discussed later in Chapter 7.

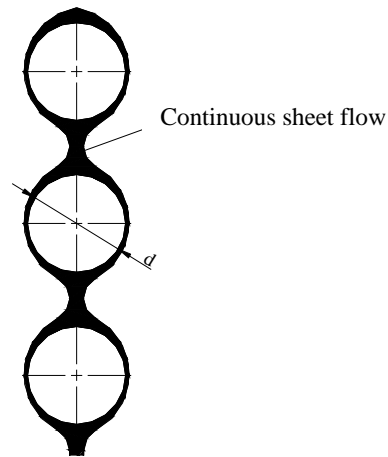


Figure 1.3 Continuous falling film absorber.

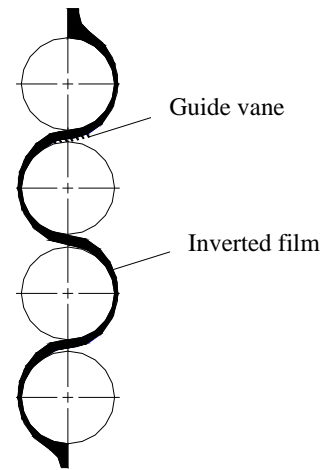


Figure 1.4 Film-inverting falling film absorber.

#### 1.4 Factors affecting the performances of conventional tubular absorbers

The performance of conventional horizontal tubular absorber is greatly controlled by several factors which are described in the following paragraphs.

- Distribution of solution in the absorber

The uniform distribution of solution film over the absorber tubes must provide as large surface area as possible for exposure to the absorbate vapour so to enhance the rate of vapour absorption. Due to complex surface phenomena and flow instabilities, a uniform distribution of solution film over the tubes is difficult to maintain. As a result, the wetted surface of the absorber tubes gradually decreases as the flow progresses downwards. In some cases more than 50 percents of the tubular surface may not participate in the absorption process [75]. The absorber will perform poorly under these ‘dry-out’ conditions.

- Flow pattern

The flow pattern especially in the inter-tube flow regime may increase the exposed surface area of absorption depending on the several flow modes. In most industrial absorbers the solution flow rate is usually maintained such that droplet flow exists in

each inter-tube flow regime for which the exposed area of absorption may be high as stated by Kirby and Perez-Blanco [59]. The details of the inter-tube flow and absorption phenomena are discussed in Chapter 5 and 6.

- Transport processes in the film

When the non-adiabatic absorption process occurs in a falling film at the liquid-vapour interface, the temperature of the film rises. If this heat is not transferred rapidly across the film towards the external coolant, the vapour absorption process may be ceased. On the other hand, lower diffusion coefficient of water in the absorbent solution causes the vapour to remain closed to the interface which could retard the vapour absorption process. Eventually the interface becomes saturated because of which the rate of vapour absorption decreases significantly as the film flows down. Therefore the enhancement of vapour absorption process becomes necessary.

- Subcooling

Subcooling characterizes the lack of equilibrium between the solution film and the vapour at the absorber exit. It is a measure of difference between the solution saturation temperature and the actual solution temperature at the absorber exit. It offers a good opportunity for improved absorber performance.

## 1.5 Performance improvements of tubular absorbers

The performance of the conventional tubular absorbers decreases significantly specially in the later part of the absorber mainly for the reasons described above. To improve the performance of the conventional tubular absorber three types of modifications can be done as described by Islam et al. [45]. The first type of modification is the use of modified surface absorber. The surface structures like the fins or protrusions are added to the external surface of the absorber to facilitate the formation of a stable liquid film over a maximum section of the falling film with more uniform distribution of liquid.

The second modification is achieved through the use of surface active agents to the absorbent liquid to enhance the vapour absorption process. By adding surface acting chemical agents, turbulence at the surface of the falling film is induced which in turn improves the rate of absorption.

The third type of modification is based on the fluid flow characteristics of the falling film and the thermodynamic aspects of the absorption process. The enhancement of rate of absorption of vapour can be achieved by using film-inverting concept as reported by Islam et al. [45]. The concept of film-inversion is to achieve repeated inversion of the surface of the falling-film so that vapour absorption process is enhanced at the liquid-vapour interface. During film inversion, alternate surface inversion causes the relatively colder surface to come in contact with vapour tube after tube. As a result, this regenerated surface provides better absorption performance. This phenomenon can increase the absorption rate greatly especially in the later part of the absorber.

### **1.6 Review of previous research on tubular absorbers**

The flow structure in a conventional horizontal-tube absorber consists of both falling film and inter-tube flow regimes which have been discussed in section 1.3. In order to make satisfactory prediction of the absorber performance, both the film flow regimes should be taken into consideration during the modeling of horizontal tubular absorbers. A literature review presented in chapter 2 reveals that most of the previous researchers have focused on the falling film regime of the tubular absorbers because of their simplified view of the tubular configuration. The actual configuration of the horizontal tubular absorbers have been simplified with an equivalent vertical flat plate absorber where the solution film falls down the face of one side of the plate with cooling water flowing on the other side of the plate in counter-current direction. This equivalent flat plate absorber model is unable to incorporate the inter-tube absorption phenomena.



The inter-tube flow issues are not only common to the horizontal tubular absorbers, but also are equally important to any heat exchangers with horizontal bank of tubes configuration. Researchers have performed detailed fluid flow studies to characterize inter-tube flow in general because of its importance in a number of applications. However, very few researchers have incorporated the inter-tube flow issues in the absorption model. A few attempts have been made for the incorporation of inter-tube droplet flow and absorption, but with simplified views on the flow hydrodynamics and tubular design [59, 88]. Very recently, Killion and Garimella [53] developed a method to obtain droplet hydrodynamics data using high speed video photography. Their experimental arrangement provided large spaces between the tubes which may not apply in the case of practical absorber configuration. Moreover, the hydrodynamics data were not used for the prediction of absorption rate in the inter-tube flow regime.

The lack of experimental data on the actual contribution of the inter-tube flow and absorption into the overall absorber performance suggests that a realistic and complete tubular absorber model needs to be developed so that better prediction can be achieved. Hence the inter-tube absorption models have to be developed based on the various flow modes. Furthermore, in the falling film regime, the tubular absorber model should consider the actual curvature effect of each tube avoiding any design simplification. A model incorporating these features would better represent the performance of practical absorbers.

The performance improvement of the horizontal tubular absorber is a major consideration of this current research. Among the various performance improvement techniques, film inversion mechanism has been proved to be very effective. Islam et al. [45] found that film-inversion leads to 90 % to 100 % improvement in the absorption rate. However, there is need to consider practical and cost-effective optimum design of the film-inverting tubular absorber for commercial operation. Hence the current research

is focused on the development of an absorber model and the performance improvement analysis of the horizontal tubular absorber by taking into consideration the features stated in this section.

### **1.7 Objectives of present research**

The main objective of the present research was to study the thermal performance of horizontal tubular absorbers with and without film inversion with a view to improve their absorption effectiveness. In order to fulfill this objective, following detailed tasks were undertaken.

1. Mathematical models of horizontal tubular absorbers with and without film inversion were developed. In order to develop a more realistic absorber model, both the falling film regime and the inter-tube flow regime are incorporated into the absorption model when no film-inversion is considered. The falling film absorption model takes into consideration the curvature effect of the tubes. The inter-tube absorption model is developed such that it incorporates the possible modes of inter-tube flow such as droplet, jet and sheet flows. The film-inverting absorber model is developed based on the alternate surface inversion of the falling film.
2. An experimental study of inter-tube flow hydrodynamics was performed. The absorption models for different inter-tube flow modes require information regarding the flow mode hydrodynamics. To fulfill this requirement, actual experiments on the inter-tube flow hydrodynamics are conducted. Later, data extracted from the experiments are incorporated to the corresponding absorption models.
3. A comparison of performances of horizontal tubular absorbers with and without incorporation of inter-tube flow was performed. In order to estimate reliably the performance improvement, the inter-tube absorption is compared to the total absorption in both falling film and inter-tube flow regimes.

4. A simplified model of the horizontal tubular absorber was developed. In order to reduce the computational effort needed for a detailed numerical model stated in 1, an analytical model is developed taking into consideration the curvature effect of the round tubes and the counter-flow coolant. This analytical model can be used as a design tool of the horizontal tubular absorber specially for the extraction of the overall transfer coefficients of the absorber. Similar to the detailed numerical model, simplified model also incorporates the absorption into the inter-tube flow regime.
5. Design proposal of a Coanda-effect based film-inverting absorber was introduced. Several alternative designs are proposed to make use of maximum possible surface area of absorption in the film-inverting configuration. Hydrodynamics tests are carried out to test the practical feasibility of the designs.
6. Comparison of the predictions of horizontal tubular absorber model with and without film inversion was carried out.

### **1.8 Significance of present research**

The numerical model of the horizontal tubular absorbers of this study takes into consideration curvature effect of the tubes. This work is a direct extension of similar work on single tube absorber by Chowdhury et al. [19]. Incorporation of the curvature effect of the tubes actually provides the opportunity to take into consideration inter-tube flow issues. Thus the aim of developing a more realistic absorber model is realized.

In the experiments conducted on horizontal tubular absorbers, inter-tube flow issues are inseparable. Due to the lack of experimental data, the actual contribution of the inter-tube absorption can be predicted from the developed absorber model for wide range of operating conditions. There is need to estimate the impact of the absorption in the inter-tube flow on the overall performance of the absorber. The simulation data will be helpful in understanding and quantifying the contribution of the inter-tube flow to the overall absorption process, a feature previously considered to be not very significant.

The simplified model of the tubular absorber is developed as a design tool for the extraction of overall heat and mass transfer coefficients of the absorber. Previously, a similar approach was used for the development of a simplified model of the vertical plate absorber by Islam et al. [46]. Their study did not consider the tube bundle absorber for which the film flow characteristics are different. In the present study, the simplified model is developed for the horizontal tube bundle absorber with regard to curvature effects of the tubes, serpentine flow of coolant and inter-tube absorption. The extraction of transfer coefficients from the simplified model is obtained for sets of operating conditions of Islam [43] and compared with the values obtained from the detailed numerical model. A satisfactory comparison was obtained which justified the simplified model as a design tool in further applications.

The film-inverting absorber has been found to improve the performance of horizontal tubular absorber. In the current research, the proposed design configuration of the film inverting absorber will contribute to the design and manufacture of tube-bundle absorber with improved performance. The hydrodynamics test results would lead to practical design models which do not require guide vanes or fins for inverting the LiBr solution film.

## **1.8 Scope of present research**

This study is essentially focused on the development of mathematical models of horizontal tubular absorbers. The simulation results obtained from the developed models will be compared with relevant experimental data from published studies. The experimental studies of different falling film flow modes and the newly proposed film-inverting tube bundle absorber were conducted under purely hydrodynamic conditions. These experimental studies did not consider absorption. It is believed that the effect of absorption of water vapour into the LiBr-H<sub>2</sub>O solution would not have a significant

effect on the liquid flow behavior of the inter-tube flow or the design of the tube bundle configuration.

In chapter 2, a literature survey is performed in order to study both previous and contemporary researches on falling film tubular absorbers. The purpose is to identify the gaps in the current state-of-the-art which provide a focus for the present work.

In chapter 3, a detailed numerical model is developed taking into consideration actual horizontal tubular absorber configuration. Practical issues regarding the inter-tube flow and absorption are discussed and incorporated into the model. A simplified heat and mass transfer model is developed which provides a simplified design tool for the performance evaluation of the tubular absorber.

In order to study the various inter-tube flow hydrodynamics, an experimental program was undertaken and discussed in chapter 4. The test set-up design and fabrication details are presented together with the data analysis program. The different inter-tube flow patterns are verified with the similar experimental results obtained by the previous researchers. This way the results obtained from the present experiments form the basis of data analysis program. A digital image analysis program used to study the sequential video images is presented.

In chapter 5, both the qualitative and quantitative results are presented for different inter-tube flow hydrodynamics for a wide range of operating conditions. The inter-tube flow behaviour is studied from the sequential video images. Later, the transient characteristic profiles of inter-tube flow modes are presented and analyzed. The findings form the basis of predicting the absorption performances of inter-tube flow regime.

In chapter 6, absorption models are developed for inter-tube droplet and jet or sheet flow mode. The developed models are used to predict the inter-tube absorption rate at various

operating conditions. The simulated absorption performance of the inter-tube flow regime is presented and discussed.

In chapter 7, new design proposals are made for the film-inverting tubular absorbers based upon Coanda Effect of fluid flow. The numerical absorption model is developed for the new film inverting design and is used for the analysis of detailed film-inverting mechanism. The Coanda-Effect Based Film-Inverting Absorber, CEBFIA, is assembled in multiple columns to form the basis of Two-Film-Tube film-inverting absorber. The performance evaluation of the proposed Two-Film-Tube film-inverting absorber is numerically performed. The experimental investigations of the film-inverting hydrodynamics of both proposed designs are performed using the same experimental set-up described in chapter 4. The main conclusions of the study are presented in chapter 8, together with the recommendations for future work on absorbers.

## **CHAPTER 2**

### **LITERATURE REVIEW**

The absorber of an absorption refrigeration system is widely acknowledged as the most critical part of the system both in terms of cycle performance and system cost as stated by Killion and Garimella [48]. As the heat transfer area of an absorber is about 40% of the total heat transfer area in an absorption machine [65], the manufacturing cost of the machine would drop significantly, if the heat transfer area of the absorber is decreased by enhancing heat and mass transfer in the absorber. Clear understanding of the heat and mass transfer processes in the absorber therefore becomes important to achieve this goal. In this chapter, a review of the published literature that is directly related to the absorption process is presented. In order to develop a complete model of a horizontal tube-bundle absorber, it is important to understand the behavior of a falling liquid film over the tube bank. There are several unresolved issues regarding the inter-tube flow such as different modes of flow between the tubes and the associated effect of incomplete wetting of the tube surfaces. To understand the above phenomena, the reported literature on falling film hydrodynamics is reviewed. Few researchers have attempted to incorporate the inter-tube flow and absorption into the study of horizontal tubular absorbers. To develop a complete and realistic tubular absorber model, incorporation of inter-tube flow modes with associated absorption is vital. Hence the previous attempts on the study of inter-tube flow hydrodynamics and absorption are closely analyzed. As a result, this review is divided into several sections including theoretical studies of absorption processes, experimental investigations, the investigations of falling film hydrodynamics over the horizontal tube banks and the studies of existing inter-tube absorption models. Attention has also been given to the absorption heat pumps, which utilize water as the refrigerant and lithium-bromide as the absorbent.

Among the various performance improvement techniques of horizontal tubular absorbers, the film-inversion technique was found very effective as stated by Islam et al. [45]. One of the main objectives of the current research is to investigate the film-inverting falling film absorber performance. Therefore, in the last section of this chapter, descriptions are presented on the previous studies of film-inverting falling film absorbers.

### **2.1 Theoretical studies of absorption processes**

In recent years, researchers have made significant efforts to mathematically model the coupled heat and mass transfer phenomena that occur during falling film absorption. They used simplifying assumptions about governing equations for momentum, energy and mass conservation, boundary conditions, numerical and analytical solution methods. Experimental validations of their models were also provided. It is found that most reported work in the literature has focused on the simplified situations of absorption in laminar vertical films of lithium bromide-water. Few papers have considered the important situations of wavy films, turbulent films and films on horizontal tubes. Most of the previous numerical studies have also assumed a simplified geometry of the absorber in order to simulate the overall heat and mass transfer phenomena as well as the local phenomenon. Most of them represented the usual geometry of an absorption unit with bank of horizontal tubes by a vertical flat plate with the solution film flowing down the face of the plate. Very few researchers have considered individual tubes in order to simulate the absorption process by using numerical formulation with a grid fitted to the film shape over the tube.

Nakoryakov and Grigor'eva [73] modeled the absorption process in a smooth laminar film falling down an isothermal, impermeable vertical wall. Their modeling approach considered numerous assumptions many of which are still applicable in current research



attempts. They neglected the variation of film thickness because the change in solution flow rate due to absorption of vapour was likely to be low. Fourier separation of variable technique was used for the solution of the governing equations because the estimation of the solutions required to handle a large number of eigenvalues. Temperature and concentration distributions throughout the vertical falling film were determined. One of the interesting finding was that the mathematical solution depended not only on the boundary conditions like solution inlet concentration and temperature, wall temperature and the equilibrium constants, but also on the dimensionless parameters including the Lewis, Prandtl and Reynolds numbers.

Grossman [32] studied simultaneous heat and mass transfer process in a vertical falling film under laminar flow conditions. Both the adiabatic and isothermal wall conditions were taken into consideration. Most of the simplifying assumptions of Nakoryakov and Grigor'eva [73] were recognized in this study except for the assumptions of fully developed Nusselt velocity profile, and the isothermal wall case in which the solution temperature at the inlet was equal to the wall temperature. Two methods of solution were undertaken in order to solve the energy and diffusion equations simultaneously. The first method used was the same analytical approach of Nakoryakov and Grigor'eva extending for both adiabatic and isothermal wall cases. The second method was a numerical approach based on finite difference method. In both the cases, the author reported on the difficulty of applying the solution techniques near the absorber inlet. A similarity solution was therefore proposed to be used near the inlet region whereas either the analytical or the numerical solution was recommended to be used elsewhere in the film sufficiently away from the inlet. The results were plotted for various parameters like interface, bulk and wall temperatures and concentrations at several locations both along the film and across the film directions. Results were also plotted showing the

variations of interface to bulk solution heat and mass transfer coefficients and the bulk solution to wall heat transfer coefficient.

Andberg and Vliet [2] developed an absorption model for a vertical flat plate falling film absorber with constant temperature wall. The numerical model of the laminar film flow considered inter-diffusion term in the energy equation. Fully developed Nusselt's velocity profile together with variable film thickness, mass flow rate and change in velocity due to absorption of vapour were included in their model. A co-ordinate transformation was undertaken to incorporate the change in the flow field due to variable film thickness. A finite difference method of solution was used. Results were obtained for the variations of interface and bulk temperatures and concentrations, heat and mass fluxes and mass flow rate of solution. Comparisons were made with some experimental data available in the literature and good agreement was found except in the region of absorber inlet.

Andberg and Vliet [3] derived design guidelines of falling film absorbers. The detailed simulation results were obtained using their previous model Andberg and Vliet [2] under various operating conditions typical for commercial absorbers. They arrived at the common conclusion that as the solution approaches equilibrium condition, absorption process greatly slows down. A connection between absorber length and preferred concentration change was developed for variations of several independent variables like solution mass flow rate, inlet concentration, inlet temperature, absorber pressure and wall temperature. It was found that among the other variables, the mass flow rate of solution showed the most significant impact on required absorber length for a preferred percentage of absorption.

Andberg and Vliet [4] developed a simplified model for the absorption of water vapour into a laminar liquid film flowing over cooled horizontal tubes. The energy and species

transport equations were solved by employing a finite difference solution scheme for temperatures and a similarity solution for concentrations assuming a known concentration profile. The concentration profile was derived from a power-law estimate of the error function at the liquid-vapour interface. The results obtained from this simplified model and those obtained from a detailed model were compared for the input of known inlet conditions. Comparison showed agreement of the outlet concentration and temperature. Finally, the results obtained from the model were compared with commercially available absorber performance data. The actual and predicted outlet conditions of the horizontal tubular absorber showed satisfactory agreement.

Wekken and Wassenaar [97] presented a physical model of simultaneous heat and mass transfer in a laminar falling film over a cooled wall. Their formulation was based on similar assumptions made by Grossman [32] including fully developed velocity profile and constant film thickness. But the major contribution of their newly developed model was to incorporate the cross-flow coolant in the absorber model instead of assuming an adiabatic or isothermal wall. The results were obtained by employing a finite difference method of solution and data were presented for the variation of Nusselt number and Sherwood number with Fourier number for several values of the dimensionless parameters.

Habib and Wood [34] developed a numerical model for two-phase absorption in a laminar falling film along a vertical wall. In addition to the typical assumptions such as constant film thickness and isothermal wall conditions, the heat and mass transfer in the vapour phase was incorporated to the model. Moreover, the model considered the pressure gradients along the absorber and interfacial shear between the liquid-vapour phases. The results were obtained for the change of absorption rate along the absorber length for several input parameters like inlet film concentration, absorber pressure and

wall temperature. The maximum absorption rate was found to be located immediately after the absorber inlet and decayed exponentially thereafter.

Neima [74] studied non-isothermal vapour absorption into falling film in order to explicate and assess the effect of absorbate concentration level. He developed an integral formulation of the continuity, diffusion and energy equations for the analysis of combined heat and mass transfer process in a falling film under both adiabatic and isothermal wall conditions. It was found that the lateral convective term at the interface was essential to account for the case of physical system with finite absorbate concentration level. The addition of convective term resulted in enhanced transfer rates.

Yang and Wood [100] developed a numerical model for the absorption process on a smooth liquid falling film. This work was an extension of similar work performed by Grossman [32] for a case where the inlet solution temperature was different from the isothermal wall temperature. Using both LiCl-H<sub>2</sub>O and LiBr-H<sub>2</sub>O as the working fluids, an empirical thermodynamic equilibrium relationship among temperature, concentration and pressure was used in their formulation. The results were obtained for the similar cases of Andberg and Vliet [2] and good agreements were found.

Ibrahim and Vinnicombe [41] developed a hybrid method of solution which combined an analytical solution with the finite difference method for the analysis of the performance of falling film absorbers. The analytical solution was used near the entry region to obtain the concentration and temperature profiles as starting values for the finite difference method at a sufficient distance away from the entry region. The analytical solution was also used near the liquid-vapour interface to evaluate the boundary conditions along the whole length of the absorber. Theoretical performance data were obtained and compared with those of earlier works. Their model was found to be accurate and consistent with practical absorbers.

Conlisk [20] analyzed the falling film absorption using boundary layer techniques. The assumptions were essentially similar to those of Grossman [32] except for the film thickness. The film thickness was allowed to vary due to the absorption of vapour. The transverse velocity component was neglected in the energy equation but was incorporated to the species conservation equation. The solution of the governing equations was performed by using Laplace Transformation technique. The simulation results were presented for the variation of different parameters e.g. wall temperature, solution flow rate and tube length.

Chowdhury et al. [19] developed a numerical model for the simultaneous heat and mass transfer process during absorption of vapour into laminar liquid film flowing over cooled horizontal tubes. The single tube model was developed for the constant temperature of the tube wall. The change in solution flow rate and film thickness due to the absorption of vapour was incorporated to the model for which Nusselt's condensation theory was implemented. The longitudinal velocity and the transverse velocity were determined from the Nusselt's fully developed velocity profile and continuity equation respectively. The co-ordinate transformations were performed with necessary step to incorporate the change in film thickness with angular position. Due to the steeper gradient of concentration and temperature profile, uniform fine meshes were used near the interface region. The finite difference method of solution was used for the simultaneous solution of energy and species conservation equations. The simulation results were obtained to show the contour profiles of temperature and concentration over the entire flow field. Results were also plotted for the variation of mass and heat fluxes, bulk temperature and concentration, interface temperature and concentration along the dimensionless distance of the tube. Parametric studies were undertaken to show the optimum solution flow rate that maximized the vapour absorption rate.

Tsai and Perez-Blanco [93] studied the limits of mass transfer enhancement for vertical falling film absorption. In order to ascertain the transfer coefficients of a fully mixed film, mathematical formulation was developed relating the transfer coefficient to the exposure time of a transient film. The relation established that the increase of transfer coefficients was achieved with the increase of mixing frequency and subsequent decrease of exposure time.

Min and Choi [68] solved the Navier-Stokes equations in order to investigate the absorption process on a horizontal tube. Their main objective was to develop a model taking into consideration the surface tension effects especially near the upper and lower stagnation points during the film flow over a horizontal tube. The momentum, temperature and concentration equations were solved using SIMPLER algorithm. The free surface location was achieved through the use of MAC method. Detailed simulation results of the flow field, temperature and concentration fields were presented for various solution flow rates with and without the effects of surface tension. Regions of recirculation near both upper and lower stagnation points were detected when the surface tension effects had been considered. Heat and mass transfer data were also presented in terms of Sherwood number and Nusselt number variations along the angular displacement of the tube with and without the effects of surface tension. Surface tension effects caused sharp drop off absorption rate in the near entrance region because of the thick layer of the film. Absorption rate recovered well after that when the film thinned down again. The change in absorption rate without the effects of surface tension on the other hand showed a steady decrease and leveled off at certain angular distance. Absorption rate with effect of surface tension was found 4% higher than that of without any surface tension effect.

Killion and Garimella [48] provided a comprehensive review of the considerable efforts made by the previous researchers for the development of coupled heat and mass transfer model of falling-film absorption. Their review was not focused on the experimental works or the effects of additives and non-absorbable gases in falling film absorption. The objective was to emphasize the key areas of future interests which were summarized as film and vapour hydrodynamics, the potential interaction of the heat and mass transfer process on film hydrodynamics, surface wetting, heat transfer in vapour phase and common simplifications of governing equations. They also pointed out the importance of experimental validation of the developed models with assessment of local absorption phenomena along with the overall performance predictions.

Siyoun and Garimella [88] studied falling film and droplet mode heat and mass transfer in a horizontal tube absorber. The effect of incomplete wetting was introduced by the wetting ratio of the tubes. They developed mathematical models for the falling film flow regime as well as the droplet formation and fall flow regime. Simulation results for temperature, concentration variations and heat and mass transfer rates were presented and compared with similar experimental data from the literature. The effects of wetting ratio and solution flow rate on cooling capacity were discussed in detail.

Islam et al. [46] developed simplified models for coupled heat and mass transfer in falling-film absorbers. The main objective was to develop a coupled model which could be used as a design tool of falling film absorbers. The initially developed non-linear coupled model was simplified to the linearized coupled model by making simplifying assumptions. The developed model was intended to extract the heat and mass transfer coefficients from experimental data. The data were obtained from their experiments and also from those of Miller [65] for this purpose. The results were obtained for the variation of Nusselt number and effective Sherwood number, which included the overall

heat transfer coefficient and effective mass transfer coefficient respectively, with film Reynolds number using the linearized coupled model.

Farhanieh and Babadi [16] developed a finite difference method of solution for the vapour-absorption into liquid films flowing over the tube bundle of an absorber. They employed boundary layer assumptions for the transport of mass, momentum and energy similar to those made by Chowdhury et al. [19] for film flow over single horizontal tube. During extension of the numerical model of single tube for tube bundle, they assumed the absorber tube bundle to be a single-pass coolant stream. As a result, the tube surface temperature remained unchanged for all the tubes in a column. The mass transfer within the inter-tube region was ignored. Parametric studies were performed in order to examine the effects of solution flow rate, absorber pressure and tube radius on the overall heat and mass transfer for a single tube and tube bundle absorber.

## **2.2 Experimental investigations with conventional absorbers**

Cosenza and Vliet [22] experimentally investigated the falling film absorption for smooth horizontal tubular surfaces. A correlation was developed for the absorption heat transfer in terms of the film Nusselt number as a function of film Reynolds number from the experimental data. The experimental results were compared with those obtained from their previous falling film absorption model and good agreement was found. Estimation of the effects of tube diameter and use of additives on absorption process were also accomplished.

Nomura et al. [75] observed the internal heat transfer and absorption phenomena of a falling film absorber of a bank of tubes configuration. An experimental set-up was fabricated for the measurement of film temperatures on the tube surfaces and also in the inter-tube region. Observing the upstream tube surface temperatures which were lower than the inter-tube film temperatures, they suggested that a significant amount of vapour



might have been absorbed in the inter-tube region. Photographic evidence was provided to show the film flow characteristics over the bank of horizontal tubes. It was observed that the wetted surface area of the tubes gradually decreased as the film traveled downwards. As a result, the local wetting ratio sometimes could become less than 0.5.

Matsuda et al. [62] experimentally investigated absorber and generator performances in an absorption-refrigeration machine. The effects of Lithium-Bromide concentration and vapour pressure on the performance of a vertical falling film absorber were assessed. Both the heat and mass transfer coefficients were found to increase with the increase of vapour-pressure. An increase of concentration caused a reduction or negligible changes of the transfer coefficients. The reason for this behavior was believed to be the increase of film thickness due to the increase of viscosity of highly concentrated solution.

Hoffman et al. [37] experimentally investigated the detailed mechanisms of heat and mass transfer in a falling film tubular absorber. The test set-up consisted of 24 horizontal tubes was operated under vacuum in a glass cylinder. Heat transfer coefficients were determined for sets of operating conditions including variations of solution flow rate, concentration, temperature and vapour pressure. Heat transfer coefficient was correlated to surface tension and viscosity of solution. No correlation of the heat and mass transfer coefficients was reported.

Wassenaar [96] predicted and measured the effect of flow rate and tube spacing on horizontal tube absorber performance. A model was developed for absorption in a cooled falling film. This model considered the flow domain in the inter-tube region. The inter-tube flow was incorporated to the absorber model by assuming that the flow causes complete mixing of the liquid in this region. The film flow along each side of a tube was simplified to that along the side of an equivalent vertical flat plate with a length of half of the tube perimeter. Thus the model was consisted of a series of segmented cooled

vertical plates. The experimental results were obtained for a range of tube spacing and compared to the model predictions. The model predictions using experimental wetted fraction of absorber tubes were in satisfactory agreement with the experimental data. The wetted fraction of the tubes was attributed to the change in surface tension gradient.

Deng and Ma [24] experimentally investigated the characteristics for a falling film tubular absorber. The experimental results showed much greater increase in the mass transfer coefficient than the heat transfer coefficient as the solution flow rate increases. An expression for the heat transfer coefficient was developed which incorporated the effect of solution inlet concentration.

Miller and Keyhani [67] experimentally investigated the mechanisms of heat and mass transfer processes in a falling film. An experimental vertical tube absorber was fabricated for the measurement of the temperature profile along the length of the absorber using thermo-graphic phosphors. Experimental data were used for the validation of the developed correlations of coupled heat and mass transfer processes.

### **2.3 Study of falling film hydrodynamics in horizontal tube banks for inter-tube and falling-film flow regimes**

Sideman et al. [91] studied the transport characteristics of films flowing over horizontal smooth tubes. An experimental set-up was fabricated to investigate the film flow characteristics and the inter-tube flow modes. Inter-tube flow modes were identified in the form of films/drops/jets based on liquid flow rate and tube spacing. The effects of flow characteristics and changes of inter-tube flow modes were examined for the variation of local, spatial and time average transfer coefficients. The mode of liquid feeding also showed influence on the transfer rate. Theoretical models were also developed taking into consideration the continuous film flow and falling drop case between the tubes. The falling drop case was simplified to the falling of an orderly sheet

along the tube with the same average flow rate. The simulation results showed good agreement with the experimental data for both smooth film flow and dripping between the tubes.

Ganic and Roppo [28] experimentally observed the sub-cooled film flowing over an electrically heated cylinder. Their observation revealed two major inter-tube flow regimes; droplet flow regime at lower flow rate and column or jet flow regime at higher flow rate. They identified tube spacing to be a factor for the flow mode transition. It was predicted that the liquid columns gradually transformed to the continuous sheet between the tubes at very high flow rate.

Rogers [83] studied laminar falling film flow on horizontal tubes. An analytical approach was employed to study the film flow behavior specially the interruption of falling films. The laminar film flow over the tube was divided into a developing and a developed region. Integral method was used for the solution of the equations of motion and energy in both regions. Heat transfer characteristics of the falling film were also studied.

Kutateladze et al. [61] studied the film condensation of stationary vapour on horizontal tube banks. The effect of condensate flow rate on heat transfer was investigated. They recommended a modified Archimedes number for the flow mode transitions based on the capillary constant.

Kocamustafaogullari and Chen [51] studied the flow along a vertical tube bank of horizontal evaporators. The tube-to-tube evaporating film heat transfer coefficients were analyzed. A hydrodynamic model was developed to incorporate a thin liquid sheet falling between the tubes. The flow was approximated as a uniform velocity impinging jet on the top of a tube. Stagnation point boundary layer theory was used to determine

the velocity profile near the impinging point. Simulation data were obtained for the local variation of average heat transfer coefficient for a tube in the bank under various operating conditions such as variable flow rate, saturation temperature, tube spacing. Gradual decrease of heat transfer coefficient from the topmost tube was noticed until a fully developed region was achieved.

Rogers and Goindi [84] experimentally investigated the laminar falling film characteristics on a large diameter horizontal tube. A test rig was fabricated for the measurement of local heat transfer coefficients from the steam heated tube to the thin films of water. For the prediction of local heat transfer coefficients, the theoretical model developed by Rogers [83] was used and good agreement between the measured and predicted values of the transfer coefficient was found.

Armbruster and Mitrovic [6] studied falling film flow patterns over smooth horizontal tubes. A model was developed for the inter-tube flow mode transitions based on Reynolds number and Galileo number which were related by an empirical constant. The identifiable three modes of inter-tube flow were; droplet, jet and sheet flow modes. The jet flow mode was also divided into two categories which were staggered jet at higher pressure of the stagnation point, and in-line jet at lower pressure of the stagnation point. They concluded that mode transition occurred entirely because of liquid flow rate and mode transition hysteresis occurred entirely for the event of transition from jet to sheet mode.

Armbruster and Mitrovic [7] studied the heat transfer characteristics in falling film on a horizontal smooth tube. An experimental program was undertaken to perform experiments under the variations of a wide range of parameters. The flow patterns showed three modes of inter-tube flow; droplet/jet/sheet with the varying solution flow rates. Observations were also made on the film breakdown which was mainly controlled

by the changes of flow modes, heat transfer and thermo-physical properties of liquid. The temperature distributions in axial and circumferential direction of the test tube were measured and these were found to be affected by the change in flow mode.

Hu and Jacobi [39] experimentally observed the inter-tube film flow characteristics and mode transitions. The inter-tube flow modes were classified into six different categories; a) droplets, b) droplets-jets, c) in-line jets, d) staggered jets, e) jet-sheet and f) sheet. The parameters which actually controlled the inter-tube flow mode transition were thoroughly investigated. In their case, mode transition hysteresis was present for all flow mode transitions and correlations were provided for the mode transition Reynolds number and modified Galileo number with and without the effect of hysteresis. Finally, a simplified flow regime map was provided for all the possible flow mode transitions.

Hu and Jacobi [40] measured the departure-site spacing or the spacing between droplet or jet generation sites falling between horizontal tubes. For a wide range of operating conditions, measurements of the departure site spacing were accomplished. The departure-site spacing varied due to the variation of solution flow rate and showed a decrease with the increase of flow rate specially for the liquids with higher Galileo number. Moreover, the departure site spacing did not show any dependence on the change of tube spacing. Based on the important observations, improved correlations were developed for the departure-site spacing and the other parameters like Reynolds number, Galileo number and tube size. They also presented visual observations of jet shape for a range of tube spacing and suggested further work to be done in this regard.

Killion and Garimella [52] studied the flow of liquid films and inter-tube droplets in a horizontal tube bank. The main purpose was to observe detailed droplet flow hydrodynamics in the absence of actual absorption using water as the working fluid. Sufficient spacing was allowed between the tubes in a column for better visualization.

The high-speed digital video photography was used to capture the formation of a droplet underneath a tube from its development, shape transitions sequences throughout the development until its detachment from the base. The detached part of the droplet was then observed to collide on the surface of the next tube below with allied waves and film disturbances. Recommendations were made to observe the similar phenomena coupled with absorption because the droplet evolution process might affect absorption performance.

Frances and Ojer [27] reproduced empirical relationships for a plane surface taking into account of the inter-tube hydrodynamics belonging to the droplets or droplets-jets/jets. From those relationships, a non-dimensional peripheral flow rate was found. A critical value of the peripheral flow rate below which incomplete wetting occurred was then calculated depending on the contact angle. Based upon their visual observation, the steady wetted fraction after film rupture was estimated. For the wetting model of a whole tube bundle, wetting fraction adjustments as well as a peripheral mass flow rate adjustment were made.

#### **2.4 Study of existing droplet hydrodynamics model**

In the preceding section, a review of theoretical and experimental studies on falling-film flows in a single absorber tube and in a tube bundle was presented. These studies were concerned mainly on characteristics of falling films, and less so on droplet characteristics. Published studies on droplet characteristics are presented here.

Yung et al. [105] studied vapor-liquid interaction and entrainment in falling film evaporators. Thin film Taylor wavelength formula was used to determine the spacing between droplet and column generation sites along the horizontal tube. The primary and secondary droplet sizes were determined from a standard correlation derived from the observation of droplet flow hydrodynamics such as drop detachment and break up.

Criteria were established for the commencement of column formation. The deflection of droplets and columns due to vapor cross-flow was incorporated in a mathematical expression.

Yoshinori et al. [104] developed a model in order to estimate the diameter of drops and bubbles formed in a flow normal to the nozzle axis. During the formation of drops and bubbles in flowing liquids, the acting force balance was used in this formulation. The drops and bubbles were allowed to form in two stages, viz. the expansion and detachment stages. The model predictions were tested with existing experimental data and good agreement was found.

Pallas and Harrison [77] developed an automated drop shape apparatus for the determination of interfacial tension. An exclusive computer-based image acquisition system was developed which eliminated manual analysis. The various types of droplets like pendant, emergent, sessile or captive drops were generated employing the mechanical high-pressure cell and plumbing system. The measurement technique was based upon the principle of reading the profile of a drop of one fluid poised in a second fluid to obtain the tension between the two fluids. High speed image analysis procedure was developed coupled with the statistical reduction of errors.

Del Rio and Neumann [23] developed axisymmetric drop shape analysis (ADSA) techniques for the determination of interfacial properties from the profiles of pendant and sessile drops. By establishing a numerical fit between the actual and predicted shape of a drop, computation of interfacial properties was accomplished. For the prediction of the drop shape, a mathematical model was developed based on Laplace equation of capillarity. The method was also capable of computing volume and surface area of the axisymmetric drops.

Killion and Garimella [53] developed a method to determine the shape of pendant droplets in falling film tubular absorbers. They used a digital image analysis program in order to obtain the exact shape of the developing droplet. By using spline fits to the transient droplet profiles and assuming droplet profiles to be axisymmetric, the transient volume and surface area of the developing droplet were calculated. They allowed sufficient space between the tubes so that the droplets could grow completely and detached to form tiny spherical droplets during falling.

### **2.5 Study of falling film absorption models in the inter-tube flow regime**

Morioka et al. [47] analyzed the steam absorption by a sub-cooled droplet of aqueous solution of LiBr by placing it into a stream of steam at low pressure. The absorption of steam by the droplet was numerically examined. The shape of the droplet was assumed to be a sphere with negligible deformation in spherical shape. It was found that the distributions of temperature and concentration in a droplet were significantly influenced by the circulatory motion due to the contact with the steam flow. The absorption rate was found to be increased by about several tens of a percent compared with that for the stagnant droplet.

Kirby and Perez Blanco [59] presented a design model for horizontal tubular absorbers incorporating three distinct flow regimes, viz. the falling-film, droplet formation and fall flow regimes. In each flow regime, mass and energy balances for absorber elements were undertaken in a 2-D model of the absorption process. The droplet was assumed to be consisted of a repeated series of spherical shells or layers. The droplet formation model considered the fresh surface assumption in order to determine the interface conditions during the formation period. Thus, the interface temperature of the drop during the formation period remained unchanged with the temperature of the fresh solution. The model well predicted the absorber performance. They furthermore



recommended that the role of droplets might be crucial for improved absorber performance.

Siyong and Garimella [88] developed a model for droplet formation and fall during absorption similar to the models developed by Kirby and Perez Blanco [59]. In their case, a hemispherical droplet during formation stage was allowed to grow until its volume reaches half of the volume of a falling spherical droplet. The free fall droplet size was calculated using the correlation developed by Yung et al. [105]. Absorption performances of both the falling film regime and the droplet formation and fall flow regime were calculated at various operating conditions of Nomoura et al. [75]. The contribution of vapour absorption during droplet formation was found significant especially at higher flow rate.

## **2.6 Study of film-inverting falling film absorber**

In this section, a review of research studies on film inversion of falling film absorbers is presented. Islam et al. [45] developed a novel absorber that contributed to the improvement of performance of a falling-film absorber by enhancing the rate of absorption of vapor. The enhancement of vapor absorption was achieved by inverting the liquid film flowing down the cooled absorber surface in alternate directions. The film-inverting absorber performances were investigated both experimentally and numerically. A conventional horizontal tube absorber was modified to change the continuous film into a repeatedly inverting film by inserting guide vanes at each tube junction in a vertical array. The measured performances of the film-inverting absorber were compared with those of conventional tubular absorber resulting in 100 percent performance improvement due to film-inversion. The numerical simulation results of a film-inverting vertical-plate absorber also showed equally high performance improvement.

Goel and Goswami [30] presented a new design of a compact falling film absorber. They studied several enhancement techniques to improve the absorber performance, but found a method more effective than others which utilized the vertical space between the nearby coolant tubes. Thus, their main concern was to form a falling film between adjacent tubes to increase the liquid-vapour interfacial area. Since the intermediate falling film in continuous sheet flow mode requires a higher solution flow rate, they proposed for an alternative solution to be applicable for lower flow rates, wrapping a mesh/fabric between the left and right sides of two adjacent tubes. Their proposal also considered selection of the mesh material with good wetting characteristics. The new design concept was numerically investigated. The proposed design was found to be more compact and efficient than the falling film absorber where absorption in the vertical spacing was not taken into account. An absorber size reduction of about 25 percent was reported for the operating conditions considered.

## **2.7 Summary**

In this chapter, review of the research studies on falling film tubular absorbers was presented. Both the theoretical studies and the experimental studies of the falling film absorbers were reviewed. The review of the theoretical studies aimed to highlight the modeling approaches taken by previous researchers and to present governing equations, boundary conditions, assumptions and the solution methods used. The reported studies on the flow characteristics of falling film over horizontal tube banks were taken into consideration especially for the inter-tube flow. This review helped to categorize the distinct modes of inter-tube flow and the influential parameters for the mode changes. The hydrodynamic models developed for inter-tube droplet flow mode were included in this review to serve the purpose of developing a complete absorber model. The smaller number of studies which incorporated the inter-tube absorption to the tubular absorber model was also analyzed. Finally a review was conducted on the performance

improvement of the horizontal tubular absorbers using the film-inverting concept. This study helped to understand the mechanism of film-inversion which might overcome various unresolved issues created by the conventional tubular absorbers.

## **CHAPTER 3**

### **THEORETICAL STUDIES**

Among the different absorber configurations used in absorption cooling machines, the most common design is the absorber with a bundle of horizontal tubes. The vapour absorbing solution is sprayed at the top from a distributor and cooling water flows through the tubes in countercurrent fashion. The solution flows over the tubes in the form of a falling film and drips from one tube to the next as sheets, jets or drops. The wetted surface of the absorber tubes is found to decrease progressively as the solution flows down to the bottom. Even when the partial tube wetting and inter-tube flow patterns are ignored, the modeling of the horizontal tubular absorber as a heat and mass exchanger is complex because the flow over the tube surface may not be in the form of a smooth circumferential film. Despite these physical complexities, there have been a number of papers published on the modeling of horizontal tubular absorbers.

It was observed from the theoretical studies of horizontal tubular absorbers discussed in section 2.1 that most of the previous modeling attempts assumed a simplified geometry of the horizontal tubular absorber instead of the actual bank of tubes configuration. In this section, however, a detailed numerical model of the horizontal tubular absorber is developed taking into account of the tubular effect of individual tubes. The single round tube model of Chowdhury et al. [19] is extended for the bank of horizontal tubes with counter-flow coolant through the absorber tubes. The numerical models are also developed for the equivalent vertical flat plate absorber and the segmented flat plate absorber which were previously considered as the simplified geometry of tubular absorbers. Model predictions are compared later to discuss the effect of making such geometrical simplifications. A simplified design model for horizontal tubular absorbers with a counter-flowing coolant is developed next. The simplified model was previously

developed by Islam et al. [46] for the vertical plate absorber. Necessary modifications are made to their model to incorporate the actual tubular configuration of the absorber. The detailed numerical model, discussed in the following section, is used as the base line to obtain the relevant heat and mass transfer coefficients. The predictions of the models are compared with available experimental data

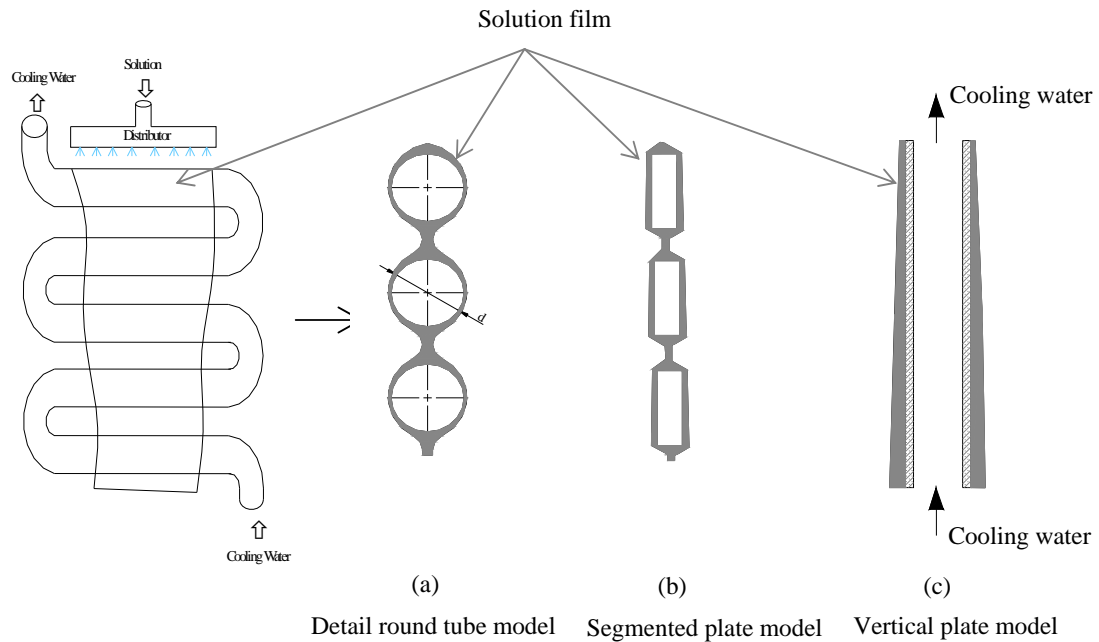


Figure 3.1 Different models of horizontal tubular absorber

### 3.1 Numerical models of horizontal tubular absorbers

The development of a detailed numerical model for a round tube absorber is, in general, tedious. It is therefore more convenient to simulate the round tube absorber with cooled vertical plate segments as was done by Islam et al. [44, 46] and Wassenaar [96]. The effect of approximating the geometry is investigated numerically by performing computations with three geometrical models which included (i) a series of round tubes which is the geometry of the real absorber (ii) a series of vertical plate segments where 2 parallel segments represented each tube with coolant flow between the segments and (iii) two parallel continuous vertical plates with a coolant passage between them where

the total area of the plates is equal to the circumferential area of the tubes. The schematic diagrams of the three geometrical models of the tubular absorbers are shown in Figure 3.1. Among the three geometrical models, the numerical model of the detailed round tube and the segmented plate model are nearly similar and hence discussed together. The vertical plate model is briefly described later.

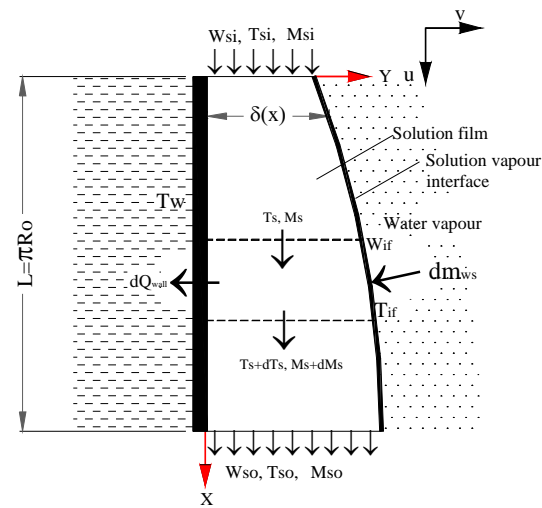


Figure 3.2 (a) Single tube falling film configuration (Flat plate model)

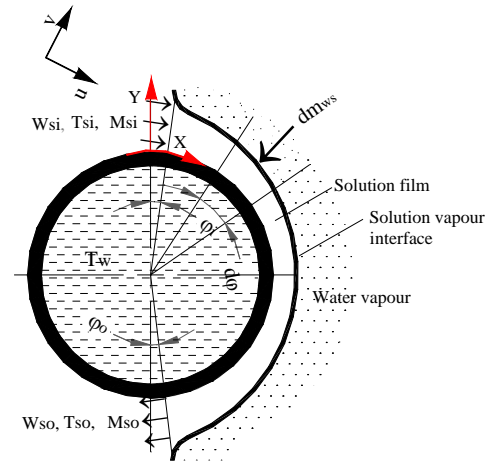


Figure 3.2 (b) Single tube falling film (Round tube model)

### 3.1.1 Detailed round tube model and segmented plate model

Both the detailed round tube model and segmented plate model consider each absorber tube individually. A single isolated tube is considered first. In this, the film flow is initiated by the absorbent solution, which is introduced onto the top-most tube as droplets or a sheet from the distributor as shown in Figure 3.1. This single tube model is solved numerically with a similar approach taken by Chowdhury et al. [19]. The computations are performed per unit length of each tube as demonstrated in Figure 3.2. The falling film configurations are slightly different for the round tube and the segmented plate models. The major differences are shown in Figure 3.2 (a)-(b). The round tube falling film configuration shows thicker film near the entrance and exit region of the tube because of the asymptotic nature of the film thickness variation with

angular position. However in the case of the flat plate falling film configuration, the film thickness is not dependent on its angular position. It varies solely due to the change in solution flow rate due to vapour absorption. The same coolant flow model is used for both round tube and segmented flat plate models in order to extend the single tube model for whole bank of absorber tubes as discussed in section 3.1.3.

### 3.1.2 Numerical simulation model of a single tube

A single isolated tube is considered in which the film flow is initiated by the absorbent solution, which is introduced onto the top-most tube from the solution distributor. In this section the main equations of a numerical simulation model for the falling film over a round tube are presented. The analysis is first carried out for a single horizontal tube and later extended to a series of horizontal tube which constitutes the tube-bundle absorber.

The following assumptions are made in developing the physical model;

- (i) all thermo-physical properties of solution are assumed constant
- (ii) heat transfer from the vapor is neglected
- (iii) the solution film flow is laminar and non-wavy
- (iv) the velocity distribution and the thickness variation of the film is assumed to be similar to those obtained in Nusselt model for condensation and
- (v) there is no chemical reaction.

Subject to the above assumptions, the governing mass and energy conservation equations for two-dimensional incompressible, steady and laminar film flow are written for an elemental control volume as follows.

Conservation of mass gives:

$$\frac{\partial u}{\partial x} + \frac{\partial v}{\partial y} = 0 \quad (3.1)$$

Conservation of energy gives:

$$\frac{\partial(uT)}{\partial x} + \frac{\partial(vT)}{\partial y} = \alpha \frac{\partial}{\partial y} \left( \frac{\partial T}{\partial y} \right) \quad (3.2)$$

The species conservation equation for the absorbent is:

$$\frac{\partial(uw)}{\partial x} + \frac{\partial(vw)}{\partial y} = D \frac{\partial}{\partial y} \left( \frac{\partial w}{\partial y} \right) \quad (3.3)$$

The applicable boundary conditions are listed below.

At entry to the tube the temperature and concentration of the solution are uniform

$$\left. \begin{array}{l} x = x_i \\ 0 \leq y \leq \delta \end{array} \right\} \quad T = T_{si}, \quad w = w_{si} \quad (3.4)$$

The temperature of the wall at a section of the tube is uniform and the wall is impermeable.

$$\left. \begin{array}{l} x_i \leq x \leq x_o \\ y = 0 \end{array} \right\} \quad T = T_{wall}, \quad \frac{\partial w}{\partial y} = 0 \quad (3.5)$$

The rate of vapour absorption at the interface of the film is equal to the radial diffusion rate

$$\left. \begin{array}{l} x_i \leq x \leq x_o \\ y = \delta \end{array} \right\} \quad \dot{m}_v = - \frac{\rho D}{w_{if}} \frac{\partial w}{\partial y} \Big|_{\delta} \quad (3.6)$$

The rate of absorption enthalpy release at the interface is equal to the heat conduction rate

$$k_s \left[ \frac{\partial T}{\partial y} \right]_{y=\delta} = i_{ab} \dot{m}_v \quad (3.7)$$

The interface equilibrium condition can be expressed as

$$T_{if} = f(p, w_{if}) \quad (3.8)$$

The heat transfer coefficient from the bulk solution to the tube wall is obtained from the expression:

$$h_i = \frac{k_s}{T_{sb} - T_{wall}} \left[ \frac{\partial T}{\partial y} \right]_{y=0} \quad (3.9)$$



The heat transfer coefficient from the interface to the bulk solution is given by:

$$h_o = \frac{k_s}{T_{if} - T_{sb}} \left[ \frac{\partial T}{\partial y} \right]_{y=\delta} \quad (3.10)$$

The mass transfer coefficient from the interface to the bulk solution is given by:

$$k_m = \frac{\rho D}{(w_{sb} - w_{if})(1 - w_{if})} \left[ \frac{\partial w}{\partial y} \right]_{y=\delta} \quad (3.11)$$

The film thickness and the velocity distribution across the film are taken as those obtained in the Nusselt analysis of laminar condensation over a round horizontal tube [72].

Hence, film thickness is given by

$$\delta = \left[ \frac{3\nu\Gamma}{\rho g \sin \theta} \right]^{\frac{1}{3}} \quad (3.12)$$

and velocity along the flow is written as:

$$u = \frac{g \sin \theta}{2\nu} \left[ 2\delta y - y^2 \right] \quad (3.13)$$

The governing equations, Eqs.(3.1)-(3.3) subject to the boundary Eqs. (3.4)-(3.8) are solved numerically using the control volume approach. The solution domain is transformed from the circular shape to a rectangular form as was done by Chowdhury et al. [19] for the case of round tube model. In the interest of brevity, these transformations and additional details of the numerical solution procedure are summarized in Appendix A.1 and A.3. Moreover, the transformation of the governing equations and the boundary conditions for the segmented flat plate model are presented in Appendix A.2

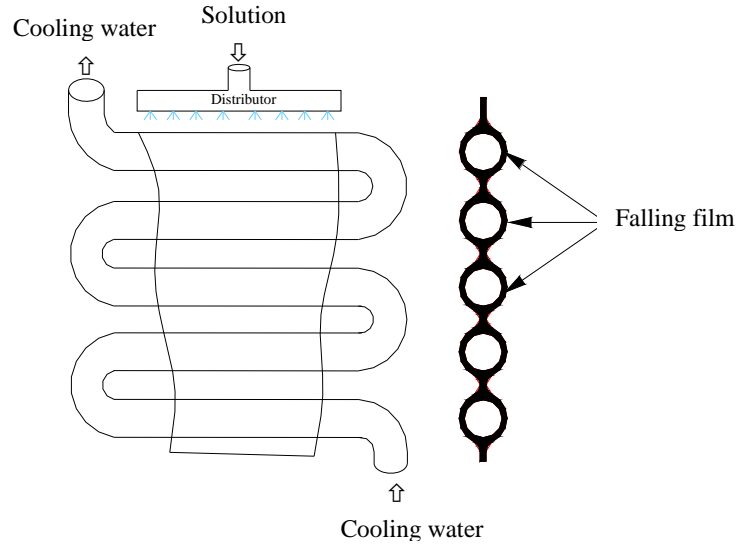


Figure 3.3 Actual horizontal tubular absorber.

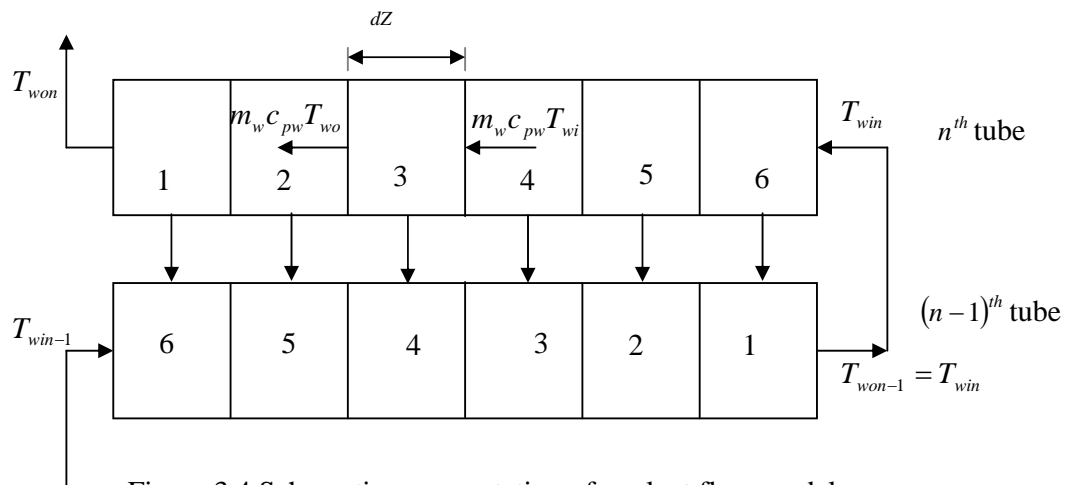


Figure 3.4 Schematic representation of coolant flow model.

### 3.1.3 Modeling of counter-flow coolant

The horizontal tubes are arranged in a vertical plane with cooling water flowing in a serpentine path as shown in Figure 3.3. For the overall system modeling of the counter-flow absorber, the following assumptions are made.

- (i) Each absorber tube is divided into equal number of segments.
- (ii) The wall temperature is assumed to be constant of each segment.
- (iii) The falling film is uniformly distributed along each segment.
- (iv) The edges of the tube bank are perfectly insulated.

The schematic diagram of the segmented tube is exhibited in Figure 3.4. For each differential tube segment, the following energy balance equations can be written;

$$Qdz = m_w c_{pw} (T_{wo} - T_{wi}) \quad (3.14)$$

$$\text{Where } Q = \left[ \sum_{\theta_i}^{\theta_o} k_s r_o \left[ \frac{\partial T}{\partial y} \right]_{y=0} d\theta \right] \quad (3.15)$$

$$Qdz = h_{water} 2\pi r_o (T_{wall} - T_{wav}) \quad (3.16)$$

$$\text{Where } T_{wav} = \frac{T_{wi} + T_{wo}}{2} \quad (3.17)$$

By rearranging the above equations, the following expressions are developed,

$$T_{wall} = T_{wav} + \frac{Qdz}{2\pi r_o h_{water}} \quad (3.18)$$

$$T_{wi} = T_{wo} - \frac{Qdz}{m_w c_{pw}} \quad (3.19)$$

Eqs. (3.14)-(3.19) together with Eqs. (3.1)-(3.13) are iteratively solved for segments 1 to 6 of a particular tube 'n' as demonstrated in Figure 3.4. After getting converged results for the particular tube, the solution film enters to the next tube below in such way that the liquid film leaving segment 1 of n<sup>th</sup> tube enters to the segment 6 of (n-1)<sup>th</sup> tube with the same temperature and concentration profiles leaving the previous segment directly up. Similarly, the solution film leaving the segment 2 of n<sup>th</sup> tube enters to the segment 5 of (n-1)<sup>th</sup> tube with same temperature and concentration profiles during leaving the previous segment. This procedure continues until the entire tube length is covered. Thus except the topmost tube of the horizontal tube bank, the inlet conditions of the solution film differ segment –wise. The detailed solution procedure is discussed in the following section.

### 3.1.4 Numerical model for a tube-bundle absorber

The extension of the single-tube numerical model to a series of horizontal tubes follows the procedures outlined below.

#### 3.1.4.1 Solution method

The governing equations are discretized using the finite difference method and solved numerically using a 2<sup>nd</sup> order scheme. Due to the presence of strong convection along the flow direction, three-point backward difference scheme is used in this direction. Central difference scheme is used along the cross flow direction. The discretized forms of the governing equations are given in Appendix A.3.

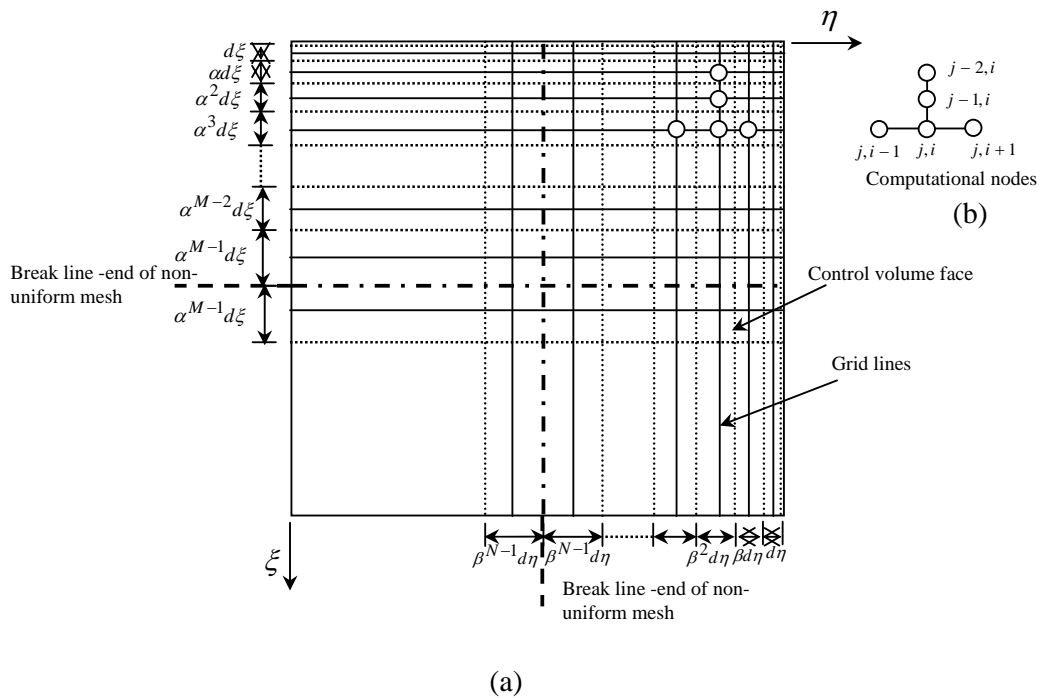


Figure 3.5 Computational domain

#### 3.1.4.2 Non-uniform mesh generation

Non-uniform meshes are used near entrance and interface regions. Interface conditions are derived based on the concentration and temperature gradient at the interface. The steep gradient at the interface requires a fine mesh at this boundary as suggested by

Chowdhury et al. [19]. Because of strong convection present along the flow, a fine mesh is also used at the entrance boundary as suggested by Ibrahim and Vinnicombe [41].

To save computational time, instead of using a uniform fine mesh, a gradually increasing non-uniform fine mesh is introduced. The non-uniform mesh spacing used in this study follows a geometric progression in both directions of flow as shown in Figure 3.5. Intermediate boundaries are specified until where the mesh size spacing follows a geometric progression as illustrated with the break lines in Figure 3.5. In the regions after the intermediate boundaries, the mesh sizes match with the last mesh size from the geometric progression series before the boundaries. The reason of not using fine mesh in the entire computational field is simple. The concentration and temperature gradients gradually decrease away from the interface region as well as the entrance region. Therefore, fine meshes beyond some distance from the boundary regions do not increase the accuracy of computations while increasing the computational time. Sensitivity of the results is tested before setting the position of the intermediate boundaries. More descriptions are given in Appendix A.3.1.

### 3.1.4.3 Solution steps

#### Single tube

The computation begins with the tube segments of Figure 3.4. The thin film flow over the tube cross-section is assumed to be uniformly distributed in each segment. The computational domain is therefore the solution film over the tube cross-section as shown in Figure A.1. At the beginning of the computations, the system design parameters and the fluid properties are specified. Due to the asymptotic nature of the film thickness variation with angular position expressed in Figure 3.2(b), the computation starts and stops at sufficient distance away from the inlet and the outlet of the flow domain. Hence the initial angular position  $\theta_i$  and the corresponding value for  $\xi_i$  are determined following a sensitivity analysis presented in Appendix A.4. Likewise, the final or the

outlet angular position  $\theta_o$  and the corresponding value of  $\xi_o$  are determined. Once the inlet and the outlet boundaries are fixed, computation is started. As the computation begins, all the nodes on the tube wall along  $\eta = 0$  of Figure 3.5 are entered with a guessed value of constant wall temperature. Subsequently, the entrance nodes along  $\xi = 0$  are established on the basis of input parameters such as mass flow rate, inlet temperature and concentration of the solution. Once the entrance conditions are known, the calculation cycle starts for film thickness, velocity components, temperature and concentration on the nodes at a section adjacent to the entrance nodes.

As demonstrated in Figure 3.5(b), at a particular row  $j$  along the  $\xi$  direction, use of the 2<sup>nd</sup> order backward difference scheme requires information from two corresponding back rows. Hence the entrance conditions for the temperature, concentration are extended at two corresponding back rows i.e. at  $(j-1)$  and  $(j-2)$  th. Operation begins with the determination of the film thickness,  $\delta$  using Eq. (3.12). Afterward velocity  $u$  and  $v$  at all the nodes on the  $(j-1)$ ,  $(j-2)$  and  $j$ -th rows are calculated by Eq. (3.13) and Eq. (3.1) respectively. An approximate mass flux  $\dot{m}_v$  is assumed. With this assumption all the matrix coefficients of the Tri-diagonal matrix (TDM) for concentration are determined as expressed in Appendix A.3.3. A TDM solver is needed to get the concentration at every inner node along  $\eta$  direction. Concentrations on the surface nodes are determined from the boundary conditions.

Once the interface concentration is known, Eq. (3.8) provides the interface temperature followed by the determination of all the coefficients of the temperature matrix expressed in Appendix A.3.2. With the same TDM solver, temperature at every inner node is calculated. Boundary temperatures are known already. When the temperature and the concentration at all nodes of the  $j$ -th row are known, the mass flux of vapor,  $\dot{m}_v$  is calculated from Eq. (3.7). The difference between the assumed mass flux and the calculated mass flux is checked. If the difference is greater than a pre-determined small

value, the cycle is repeated. When the convergence for a particular row,  $j$  is reached, the sequence of operations described above proceeds to the next row ( $j+1$ ) with the increase of  $\xi$  by an incremental value  $kd\xi$ . The value of  $k$  depends on types of mesh used described in Appendix A.3.1. When uniform meshes are used along the direction of  $\xi$ , the value of  $k$  is 1 otherwise for non-uniform meshes, value of  $k$  is not equal to 1. The calculations stop at  $\xi = \xi_o$  for a particular tube.

The amount of net heat transfer to the coolant flowing through the particular tube segment is calculated using Eq. (3.15). With this calculated total heat transfer to the coolant and the guessed coolant outlet temperature, Eq. (3.18) calculates a new wall temperature. When the difference between the assumed wall temperature and the calculated wall temperature is less than a prescribed accuracy value, the calculations are ended for the tube segment. After obtaining the converged solution for  $T_{wall}$ , Eq. (3.19) provides the coolant inlet temperature of the tube segment. The calculated  $T_{wi}$  is considered the outlet coolant temperature,  $T_{wo}$  for the next tube segment. The entire computational sequence is repeated until the last tube segment is reached. The coolant entering temperature to the last segment is assigned as the coolant entering temperature to the present and the outlet temperature for the next tube as shown in Figure 3.4.

### **Solution of the bank of tubes**

Figure 3.4 explains that every tube is divided into an equal number of segments. LiBr solution after leaving a segment of a tube enters the segment of next tube just underneath with the same distribution patterns of temperature, concentration during its leaving the previous computational domain. It is assumed that the solution enters the present tube at the same angle during its leaving the previous tube as demonstrated in Figure 3.6.

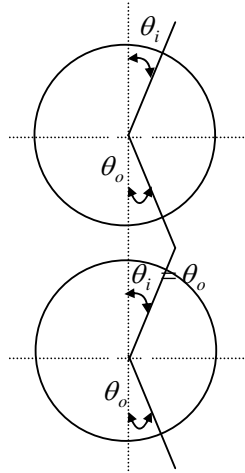


Figure 3.6 Schematic diagram of film entering and leaving angle to a tube.

Therefore, for the next consecutive tubes both the film entering and the leaving angles to a tube become equal to each other. The choices of entering and leaving angles to a tube are made after a thorough sensitivity analysis presented in Appendix A.4. As the computation continues for the tube bank, with the known coolant outlet temperature, computation begins with the assumption of a constant wall temperature in the present tube segment. The solution procedures for the single tube model are repeated. The tube-by-tube solution procedure is used until the last tube is considered. The coolant inlet temperature computed for the last tube is then compared with the experimentally known value. If the difference between the computed and the experimental values is greater than a predetermined small value, the whole calculation procedure is repeated with a new value assumed for the coolant outlet temperature. The use of under-relaxation parameters speeds up convergence of the solutions. A simplified block diagram of the entire solution procedure is represented in Figure 3.7 for further clarification. It is important to specify that the computational sequences for the tube segments are skipped in the diagram just for simplicity.



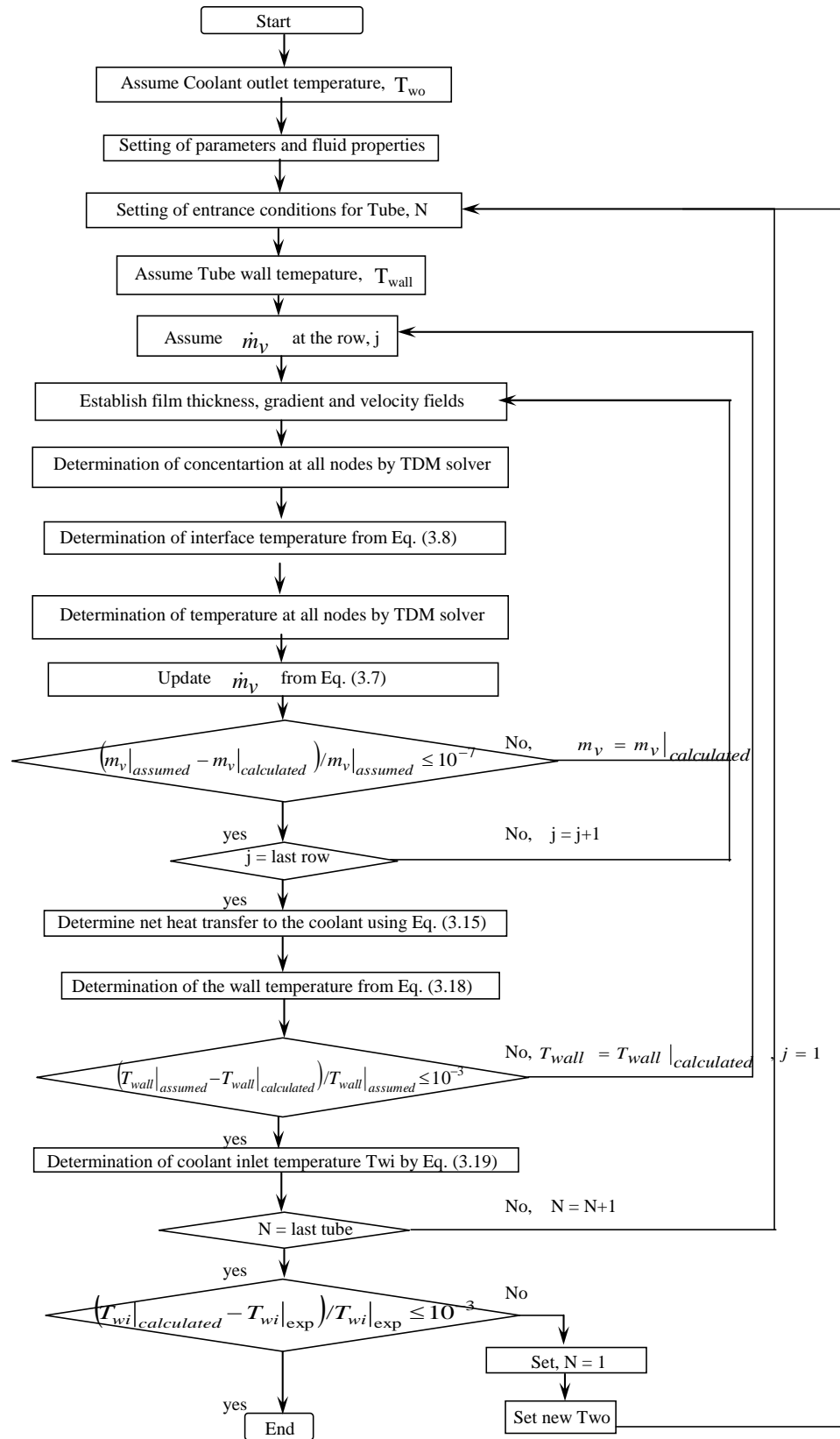


Figure 3.7 Solution flow diagram.

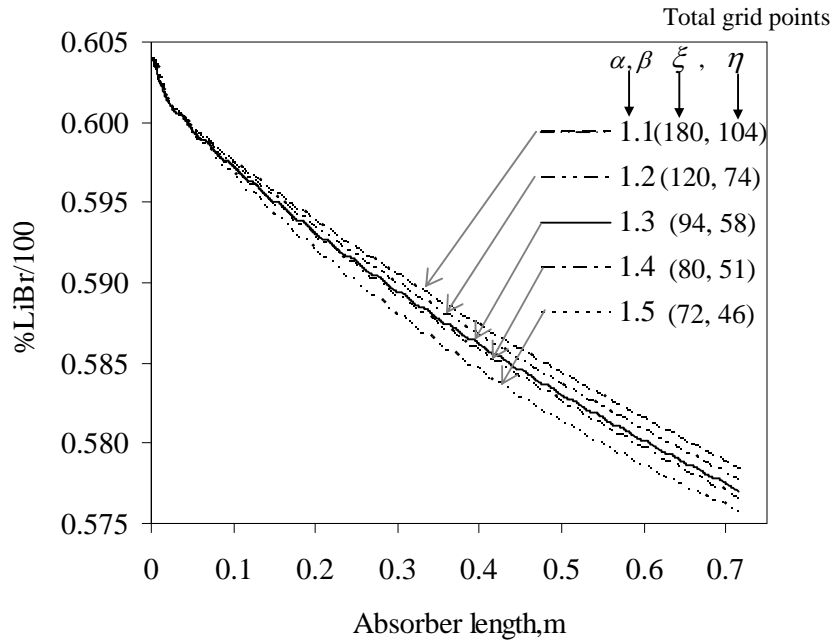


Figure 3.8 Bulk concentration along the absorber length at different grid sizes

#### 3.1.4.4 Grid independence

As already demonstrated in Figure 3.5, the grid sizes in the non-uniform region gradually increases following a geometric progression rule along  $\xi - \eta$  directions. Selecting different values of geometric series constants  $\alpha, \beta$  along  $\xi, \eta$  directions respectively, a great deal of grid size variations can be achieved. In this study however, the  $\alpha, \beta$  selections are kept equal. The grid size variations in both non-uniform and uniform regions along  $\xi - \eta$  are therefore achieved by maneuvering the number of grid points in each region and the total non-uniform grid length along  $\xi, \eta$  for different choices of  $\alpha, \beta$ . The values of  $\alpha, \beta$  are chosen in this study from 1.1 to 1.5 with increment of 0.1 at each level. It is to be noted that  $\alpha = \beta = 1$  generates uniform grids along  $\xi - \eta$  fields. Grid independence is tested for the single tube model before extending it to the column of tubes. Grid independence is also tested for overall performance of the horizontal tubular absorber for which sample results are presented in Figure 3.8.

### 3.1.4.5 Incomplete wetting of the tubes

A major issue related to the tubular absorber performance is the partial wetting of the absorber tubes as the solution flows across the tubes under gravity. Due to partial wetting less surface area of the falling film participates in vapour absorption. In order to investigate the effect of partial wetting on the performance, this effect is incorporated in the modeling. The absorber models described in sections 3.1.2-3.1.3 and later in section 3.2 are modified to include variable wetting ratios for the different tubes in a manner similar to that of Frances and Ojer [27].

Due to partial wetting there is a progressive decrease in the effective length of the tubes which is computed by multiplying the actual tube length by the local wetting ratio.

If the wetting ratio changes from one tube to the next, the mass flow rate per unit length is given by:

$$m_{s,n} = m_{s,n-1} \frac{WR_{n-1}}{WR_n} + \frac{N_d \dot{m}_{vd}}{WR_n L} \quad (3.20)$$

where the second term on RHS represents the mass of vapour absorbed in the inter-tube flow and  $N_d$  is the number of droplet/jet generating locations underneath the tube to be described in chapter 5 and chapter 6.

### 3.1.5 Vertical flat plate model

An equivalent vertical plate model of a horizontal tubular absorber is also considered in the present study. As shown in Figure 3.1, in the vertical plate model, a film of solution forms on the face of the plate and cooling water flows on the other side of the plate in a counter-current direction. The effective length of the vertical plate is determined from the following relation:

$$L_p = N\pi r_o + (N-1)h; \quad (3.21)$$

Where N is total number of tubes with length L and h is the gap between tubes.

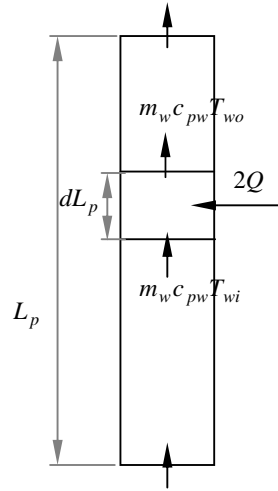


Figure 3.9 Schematic representation of coolant flow of a vertical plate absorber

Since the coolant flows on the other side of the plate, the wall temperature varies along the entire length of the absorber. Hence, the coolant flow model is developed based on variable wall temperature. The schematic representation of counter-flow coolant is exhibited in Figure 3.9. The governing equations Eqs. (3.1) - (3.3) are still used though the boundary conditions are revised as stated below.

At entry to the plate the temperature and concentration of the solution are uniform

$$\left. \begin{array}{l} x = x_i \\ 0 \leq y \leq \delta \end{array} \right\} \quad T = T_{si}, \quad w = w_{si} \quad (3.22)$$

The wall is impermeable.

$$\left. \begin{array}{l} x_i \leq x \leq x_o \\ y = 0 \end{array} \right\} \quad \frac{\partial w}{\partial y} = 0 \quad (3.23)$$

The rate of vapour absorption at the interface of the film is equal to the radial diffusion rate

$$\left. \begin{array}{l} x_i \leq x \leq x_o \\ y = \delta \end{array} \right\} \quad \dot{m}_v = -\frac{\rho D}{w_{if}} \frac{\partial w}{\partial y} \Big|_{\delta} \quad (3.24)$$

Film thickness is defined as

$$\delta = \left[ \frac{3\mathcal{M}}{\rho g} \right]^{\frac{1}{3}} \quad (3.25)$$

and velocity along the flow is written as:

$$u = \frac{g}{2\nu} [2\delta y - y^2] \quad (3.26)$$

On the coolant side, following energy balance equations are written;

$$2QL = m_w c_{pw} (T_{wo} - T_{wi}) \quad (3.27)$$

$$\text{where } Q = k_s d L_p \left. \frac{\partial T}{\partial y} \right|_{y=0} \quad (3.28)$$

$$QL = h_{water} L d L_p (T_{wall} - T_{wav}) \quad (3.29)$$

$$\text{where } T_{wav} = \frac{T_{wi} + T_{wo}}{2} \quad (3.30)$$

The governing equations Eqs. (3.1)-(3.3), (3.25)-(3.26), together with the boundary conditions Eqs. (3.22)-(3.24) are solved simultaneously with Eqs. (3.27)- (3.30). The solution procedure described for detailed round tube absorber is also applicable for vertical plate absorber with some minor changes.

### 3.1.6 Results : numerical model

The results obtained from three geometrical models of horizontal tubular absorbers are summarized below. For the sake of comparison, none of the models incorporate inter-tube absorption. The operating conditions are taken from the experiments of Islam [43]. Under the same operating conditions, film thickness, absorbed mass flux, bulk temperature and concentration of LiBr, variations along the length of the absorber are shown in Figures 3.10-3.13. The length of the absorber is the same for the three models, which is calculated from  $L_p = (\pi_0 \times 24 + 23 \times 0.006)$  on one side for total 24 tubes with 6 mm tube-to-tube distance [43].

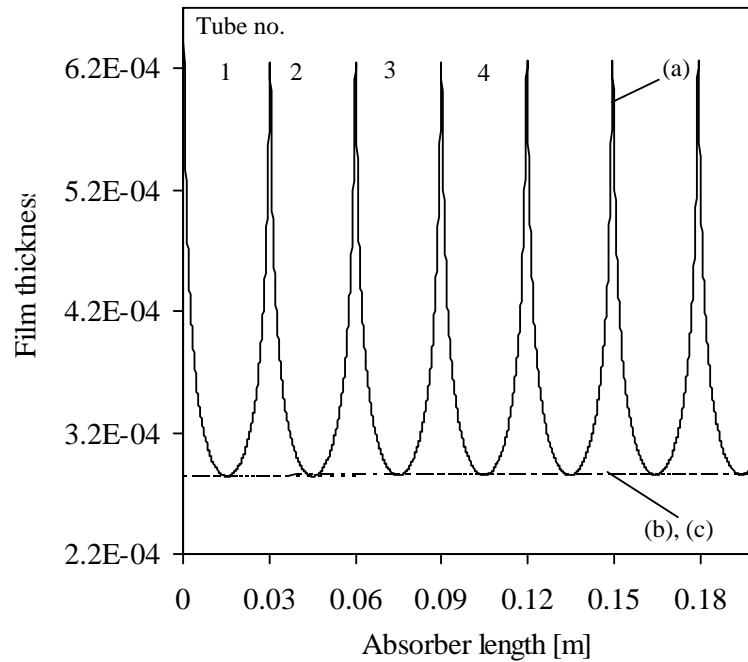


Figure 3.10 Film thickness [m] variations along the length of the absorber; (a) detailed round tube model, (b) segmented plate model, (c) vertical plate model.

The variation of the absorbed mass flux predicted by the three geometrical models are shown in Figure 3.11. The solution enters the first tube with a high degree of sub-cooling. Here the solution film enters the absorber with a temperature ( $39.8^{\circ}C$ ) much lower than the equilibrium temperature ( $53.25^{\circ}C$ ) at the inlet condition ( $w_{in} = 0.604$ ). This results in a high mass absorption rate in the first tube. The mass flux after the first tube shows oscillatory changes due to the variation of the film thickness with angular position as predicted by the detailed round tube model. The tube-wise variation of film thickness is clearly visible in Figure 3.10 by the different models. Following the asymptotic variations of film thickness over the round tubes, at the entrance and exit of a tube where the film is thicker, the absorption rate is lower while it is a maximum near the middle of the tube. But the other two flat plate models show continuous decrease of the mass flux along the entire length of the absorber. Among the two plate models, the continuous

plate model shows higher mass flux even though the film thickness is same for both which is expressed in Figure 3.10.

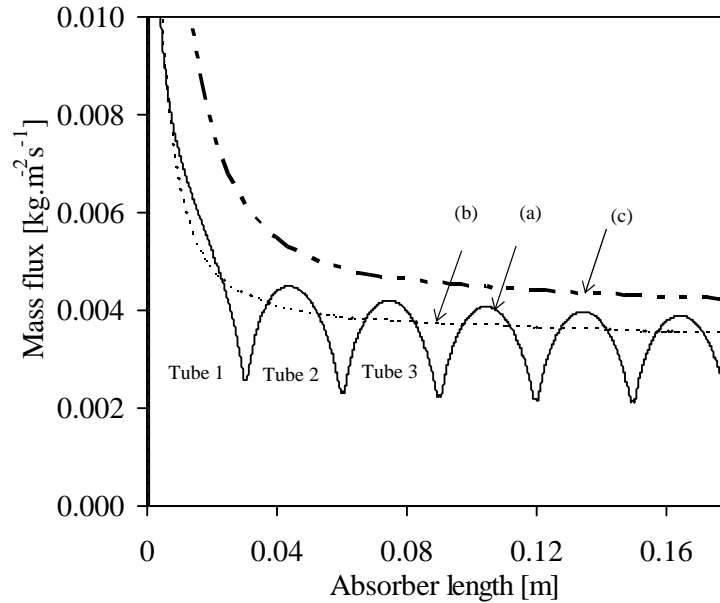


Figure 3.11 Absorbed mass flux [ $\text{kg}\cdot\text{m}^{-2}\cdot\text{s}^{-1}$ ] variations along the length of the absorber; (a) detailed round tube model, (b) segmented plate model, (c) vertical plate model.

The difference between the predictions of the two plate models is due mainly to the differences in the coolant temperature variation for the two models. For the segmented-plate model, each segment represents a single tube across which the coolant temperature is constant whereas for the vertical plate model, the coolant temperature varies continuously from inlet to outlet, as in a vertical tube absorber. The continuous cooling of the vertical plate leads to higher mass absorption rate.

The variation of the solution bulk temperature predicted by the three geometrical models are shown in Figure 3.12. The solution bulk temperature rises rapidly across the first tube as seen in the figure and decrease gently thereafter. The predictions of the round tube model and the segmented plate model agree closely. The vertical plate model predicts a higher solution temperature due to the larger mass absorption rate.

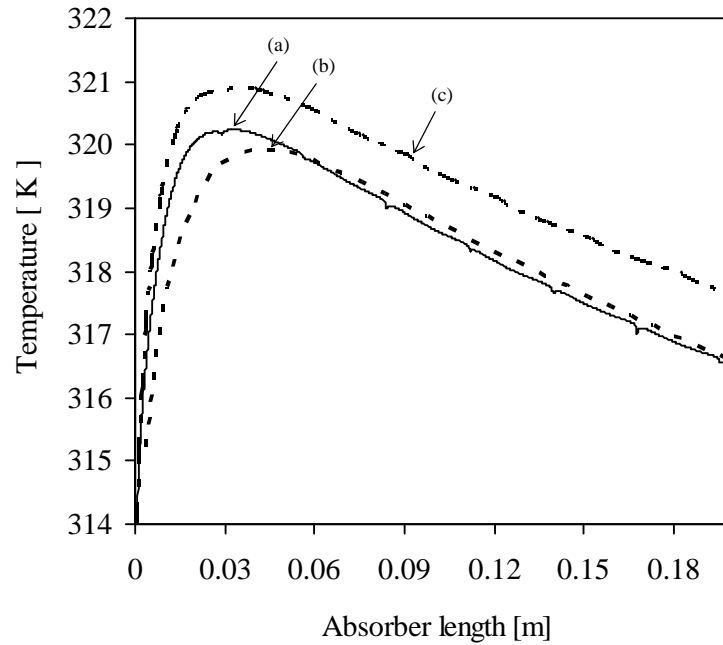


Figure 3.12 Bulk solution temperature variations along the length of the absorber; (a) detailed round tube model, (b) segmented plate model, (c) vertical plate model.

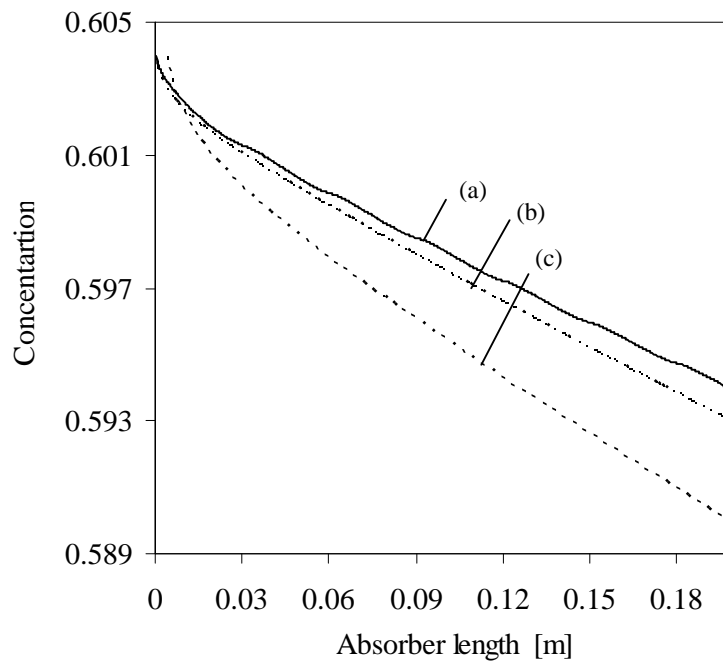


Figure 3.13 Bulk solution concentration [%LiBr/100] along the length of the absorber; (a) detailed round tube model, (b) segmented plate model, (c) vertical plate model.

In Figure 3.13, the variation of bulk concentration of LiBr solution is plotted along the length of the absorber. Comparing the three model results, vertical plate model exhibits much lower drop in bulk concentration followed by segmented flat plate model and the



detailed round tube model. The concentration drop is directly proportional to the mass flux of absorbed vapour which explains the concentration change by the three models.

### 3.1.7 Inter-tube flow and absorption

When the thin film of solution leaves a tube, it enters to the inter-tube flow regime. Inter-tube flow may take several forms like droplet or jet or sheet depending on solution mass flow rate as described by Hu and Jacobi [39]. In a later chapter, details of the experimental and theoretical studies on different inter-tube flow modes are presented. Among the three possible modes of inter-tube flow, inter tube sheet flow is taken into consideration here because of the possible implementation of numerical solution explained in Figure 3.14.

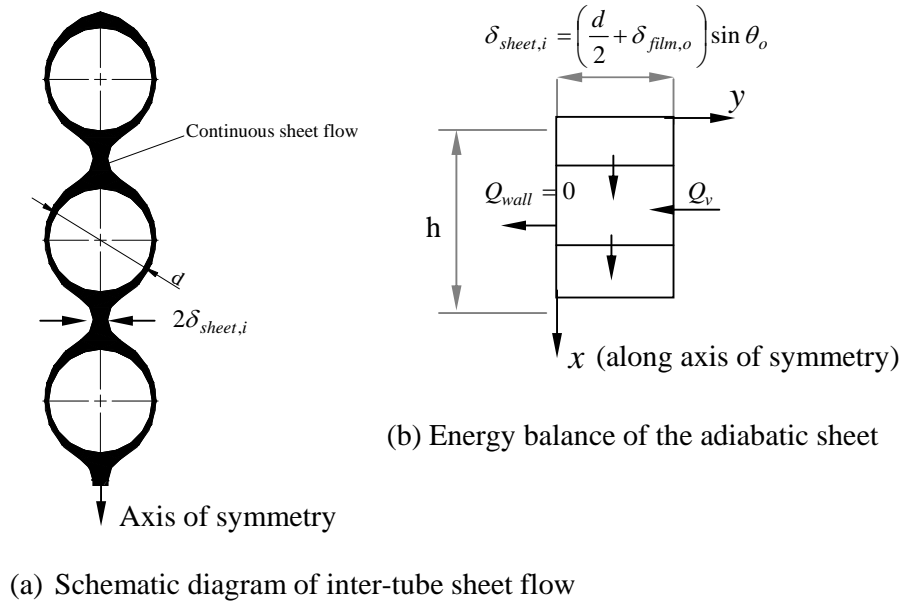


Figure 3.14 Continuous sheet flow between the tubes

The numerical model of inter-tube sheet flow necessitates using an adiabatic flat plate formulation in between the tubes as demonstrated in Figure 3.14 (a) and (b). The governing equations in section 3.1.5 are used with a modified wall side boundary

condition. Instead of using a variable wall temperature, an adiabatic wall is defined on the boundary [ $Q_{wall} = 0$ ].

The necessary changes are made in the discretization of the governing equations. The numerical solution procedure remains the same as that discussed in section 3.1.4.3. Row-wise computation begins with an assumption of mass flux  $\dot{m}_v$  at  $x = 0$  of Figure 3.14 (b). After getting a converged solution for the mass flux of vapor at each row, the calculation stops at the near entrance of the next consecutive tube at  $x = h$ , where  $h$  is the gap between two tubes as shown in Figure 3.14 (b).

### 3.2 Simplified model of horizontal tubular absorbers

The detailed numerical simulation model developed in the forgoing section incorporates most of the important physical processes in a tubular absorber. Nevertheless it may not be suitable for routine design application and for the analysis of experimental data. For use in the latter situations, it is desirable to develop a simplified model similar to the models used in heat exchanger analysis. Such a model is presented in the following section. The simplified design model is developed for horizontal tubular absorbers with a counter-flowing coolant. The detailed numerical model described above is used as the base line to obtain the relevant heat and mass transfer coefficients. The predictions of the models are compared with available experimental data.

#### 3.2.1 Simplified model for a single horizontal tube

In this section a simplified model is developed for the design analysis of horizontal tubular absorber. The analytical procedure follows the model presented by Islam et al. [46] for vertical plate absorbers. However, considerable modifications are done to make the model applicable to a bank of horizontal tubes with the coolant flowing in a serpentine fashion in the opposite direction. The present model, which also includes a simplified analysis of inter-tube flow, is therefore more realistic when applied to

counter-flow tubular absorbers. Moreover, the model can be used to extract overall heat and mass transfer coefficients from experimental data of horizontal tubular absorber.

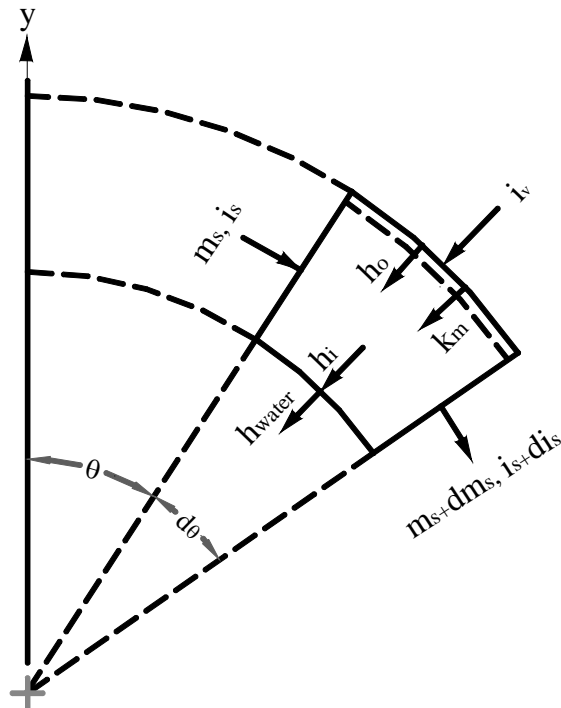


Fig. 3.15 Physical model of the falling-film over a tube.

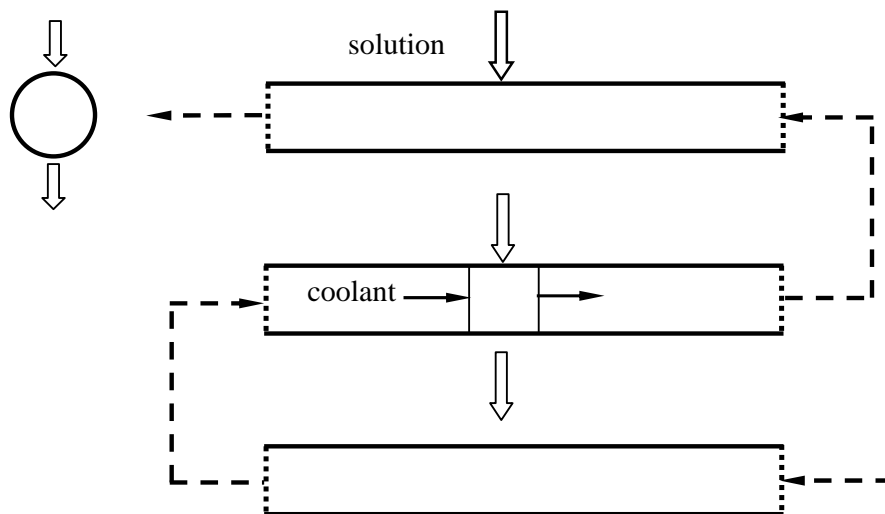


Fig. 3.16 Schematic diagram of tube-bundle absorber.

The governing equations are written for a control volume at a section in a single horizontal tube as shown in Figures 3.15 and 3.16. The heat and mass transfer from the

interface to the bulk solution and the heat transfer from the bulk solution to the coolant are represented in terms of the respective heat and mass transfer coefficients.

Mass balance for the control volume in Figure 3.15 gives

$$m_s + dm_s = m_s + (r_o + \delta)m_{ws} d\theta \quad (3.2.1)$$

where  $m_{ws}$  is the rate of absorption of water vapour per unit length at the interface,  $\delta$  is the local film thickness and  $r_o$  is the outer radius of the tube.

The energy conservation equation of the control volume is

$$m_s i_s + i_v m_{ws} (r_o + \delta) d\theta = (m_s + dm_s)(i_s + di_s) + U_{bw}(T_s - T_w)r_o d\theta \quad (3.2.2)$$

where  $U_{bw}$  is the overall heat transfer coefficient from the bulk solution to the coolant.

The cooling water temperature  $T_w$  at the section is assumed uniform and independent of the angular position  $\theta$ .

From Eqs. (3.2.1) and (3.2.2)

$$i_{vs} \frac{dm_s}{d\theta} = m_s \frac{di_s}{d\theta} + r_o U_{bw} (T_s - T_w) \quad (3.2.3)$$

where  $i_{vs} = i_v - i_s$

Enthalpy of the solution is expressed as a function of temperature and concentration

$$i_s = f(T_s, w_s) \quad (3.2.4)$$

Differentiating Eq. (3.2.4)

$$\frac{di_s}{d\theta} = c_w \frac{dw_s}{d\theta} + c_T \frac{dT_s}{d\theta} \quad (3.2.5)$$

The coefficients  $c_w$  and  $c_T$  which are essentially specific heat capacities that are assumed constant over the narrow range of temperatures and mass fractions encountered in real absorbers. Also, the solution mass flow rate is assumed constant in coefficient of Eq. (3.2.3).

Subject to the above assumptions, the energy Eq. (3.2.3) for the solution film can be written as,

$$m_s c_T \frac{dT_s}{d\theta} + m_s c_w \frac{dw_s}{d\theta} = i_{vs} \frac{dm_s}{d\theta} - r_o U_{bw} (T_s - T_w) \quad (3.2.6)$$

The overall heat transfer coefficient from solution bulk to the coolant is given by

$$\frac{1}{U_{bw}} = \frac{1}{h_{water}} + \frac{1}{h_i} + \frac{\delta_{wall}}{k_{wall}} \quad (3.2.7)$$

The mass transfer rate equation can be written as:

$$dm_s = \rho_s k_m (w_s - w_{if})(r_o + \delta)d\theta \quad (3.2.8)$$

The interface boundary condition is obtained by applying the energy equation to an infinitesimal control volume surrounding the interface. This gives:

$$k_m \rho_s (w_s - w_{if}) i_{ab} r_o d\theta = h_o (T_{if} - T_s) r_o d\theta \quad (3.2.9)$$

where  $i_{ab}$  is the enthalpy of absorption.

Assuming the interface equilibrium condition to be linear

$$w_{if} = a + bT_{if} \quad (3.2.10)$$

where a and b are functions of the absorber pressure

From Eqs. (3.2.9) and (3.2.10) it follows that

$$w_{if} = \frac{\lambda(a + bT_s) + bw_s}{(\lambda + b)} \quad \text{where} \quad \lambda = \frac{h_o}{i_{ab} k_m \rho_s} \quad (3.2.11)$$

Substituting in Eq. (3.2.8) for  $w_{if}$

$$\frac{dm_s}{d\theta} = (r_o + \delta) \rho_s k_{ef} [w_s - (a + bT_s)] \quad (3.2.12)$$

where the effective mass transfer coefficient is defined as:

$$\frac{1}{k_{ef}} = \frac{1}{k_m} + \frac{i_{ab} b \rho_s}{h_o} \quad (3.2.13)$$

Since the mass flow rate of absorbent is constant

$$m_s = \frac{m_l}{w_s} \quad (3.2.14)$$

Differentiating Eq. (3.2.14)

$$\frac{dm_s}{d\theta} = - \left[ \frac{m_l}{\bar{w}_s^2} \right] \frac{dw_s}{d\theta} \quad (3.2.15)$$

The RHS of the above expression is made linear by approximating the variable term  $w_s^2$  with the average value  $\bar{w}_s^2$ . The validity of assumption has been discussed in [46].

From Eqs. (3.2.12) and (3.2.15)

$$\frac{dw_s}{d\theta} = - \frac{\bar{w}_s^2}{m_l} (r_o + \delta) \rho_s k_{ef} [w_s - (a + bT_s)] \quad (3.2.16)$$

Substituting in Eq. (3.2.6) from Eq. (3.2.16) the following form of the energy equation is obtained.

$$\frac{dT_s}{d\theta} = (r_o + \delta) k_{ef} \rho_s \left[ \frac{i_{vs}}{m_s c_T} + \frac{c_w \bar{w}_s^2}{c_T m_l} \right] [w_s - (a + bT_s)] - \frac{r_o U_{bw}}{m_s c_T} (T_s - T_w) \quad (3.2.17)$$

Eqs. (3.2.16) and (3.2.17) can be expressed in terms of two new variables, as was done in [46]. These variables are essentially driving potentials for heat transfer and mass transfer respectively and they may be expressed as:

$$\phi = T_s - T_w \quad \text{and} \quad \psi = w_s - (a + bT_s) \quad (3.2.18)$$

For the present analysis with a round tube the water temperature  $T_w$  is assumed to be independent of  $\theta$ .

The Eqs. (3.2.16) and (3.2.17) when expressed in terms of the new variables take the forms:

$$\frac{d\phi}{d\theta} = (r_o + \delta) k_{ef} \rho_s \left[ \frac{i_{vs}}{m_s c_T} + \frac{c_w \bar{w}_s^2}{c_T m_l} \right] \psi - \frac{r_o U_{bw}}{m_s c_T} \phi \quad (3.2.19)$$

$$\frac{d\psi}{d\theta} = -(r_o + \delta) k_{ef} \rho_s \left[ \frac{bi_{vs}}{m_s c_T} + \frac{bc_w \bar{w}_s^2}{c_T m_l} + \frac{\bar{w}_s^2}{m_l} \right] \psi + \frac{r_o b U_{bw}}{m_s c_T} \phi \quad (3.2.20)$$

Eqs. (3.2.19) and (3.2.20) are nonlinear due to a significant variation of the film thickness with the angular position  $\theta$ . However, if the solutions of the equations are sought at angular distances away from the inlet and the outlet positions, 0 and  $\pi$ , the

above equations may be made linear by assuming an average film thickness. Moreover, the effective mass transfer coefficient  $k_{ef}$  may be averaged to include the film thickness variation. The effect of these assumptions on the predictions of the model is investigated numerically later in the chapter. By assuming the coefficients of the coupled Eqs. (3.2.19) and (3.2.20) to be constant an analytical solution can be obtained. For this purpose these equations are expressed in the form:

$$\frac{d\phi}{d\theta} = g_1\psi - g_2\phi \quad (3.2.21)$$

$$\frac{d\psi}{d\theta} = -g_4\psi + g_3\phi \quad (3.2.22)$$

where

$$g_1 = (r_o + \delta)k_{ef}\rho_s \left[ \frac{i_{vs}}{m_s c_T} + \frac{c_w \bar{w}_s^2}{c_T m_l} \right], \quad g_2 = \frac{r_o U_{bw}}{m_s c_T} \quad (3.2.23)$$

$$g_4 = (r_o + \delta)k_{ef}\rho_s \left[ \frac{bi_{vs}}{m_s c_T} + \frac{bc_w \bar{w}_s^2}{c_T m_l} + \frac{\bar{w}_s^2}{m_l} \right], \quad g_3 = \frac{r_o b U_{bw}}{m_s c_T} \quad (3.2.24)$$

The solutions for Eqs. (3.2.21) and (3.2.22) are obtained using the Laplace transform technique and the final form can be expressed as follows:

$$\phi(\theta) = a_1 \exp(\alpha_1 \theta) + a_2 \exp(\alpha_2 \theta) \quad (3.2.25)$$

$$\psi(\theta) = b_1 \exp(\alpha_1 \theta) + b_2 \exp(\alpha_2 \theta) \quad (3.2.26)$$

where the roots of the characteristic equation are:

$$\alpha_1, \alpha_2 = -0.5(g_2 + g_4) \pm 0.5[(g_2 + g_4)^2 - 4(g_2 g_4 - g_1 g_3)]^{0.5} \quad (3.2.27)$$

The coefficients of the solutions are given by:

$$a_1 = \frac{\phi_0(\alpha_1 + g_4) + \psi_0 g_1}{\alpha_1 - \alpha_2} \quad (3.2.28)$$

$$a_2 = \frac{\phi_0(\alpha_2 + g_4) + \psi_0 g_1}{\alpha_2 - \alpha_1} \quad (3.2.29)$$

$$b_1 = \frac{\psi_0(\alpha_1 + g_2) + \phi_0 g_3}{\alpha_1 - \alpha_2} \quad (3.2.30)$$

$$b_2 = \frac{\psi_0(\alpha_2 + g_2) + \phi_0 g_3}{\alpha_2 - \alpha_1} \quad (3.2.31)$$

where  $\phi_0$  and  $\psi_0$  are the values at the inlet angular position  $\theta_{in}$ .

The above model can be applied to each section of the various horizontal tubes of the absorber. The application of the model to obtain the overall performance of the tube-bundle absorber is considered in a later section.

### 3.2.2 Inter-tube absorption

The solution flow between consecutive tubes of a tube-bundle absorber is a complex, often transient, process that could involve drop flow, jet flow or sheet flow. In the drop flow mode, drops originate at sites located on the underside of a tube. Depending on the inter-tube spacing and the liquid flow rate, a developing drop could touch the surface of the tube below. When this happens, the drop forms a narrow neck at which point it breaks up and part of the liquid is pulled back towards the point of origin while the rest of the liquid is transferred to the tube below. If the inter-tube spacing is sufficiently large, the drop will develop fully and break up at a narrow neck with the separated liquid taking a spherical shape and falling under gravity as a drop to land on the tube below. The details of these drop generation and break-up processes are reported in chapter 5 of present study.

In this section, simplified coupled heat and mass transfer models for the absorption of vapour during drop formation and steady jet flow are developed. Several assumptions, similar to those described in section 3.2.1 are made in the development of the present simplified model.



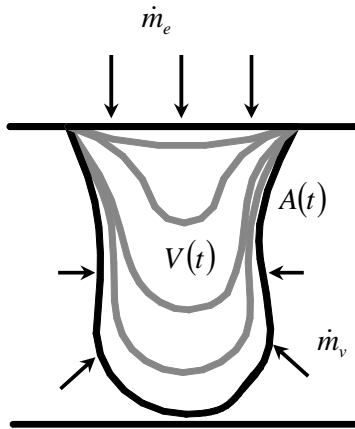


Figure 3.17(a) Droplet profile during formation.

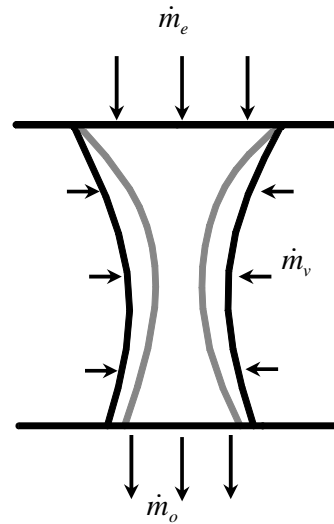


Figure 3.17(b) Droplet profile during bridging.

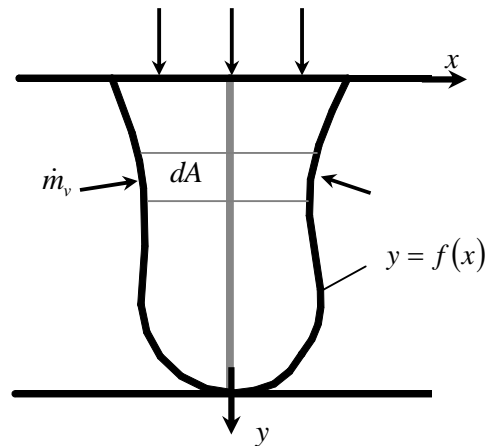


Figure 3.17(c) Steady jet profile.

### 3.2.2.1 Droplet formation model

The formation of a droplet under a tube is likened to the filling of a flexible vessel with solution entering through the opening at the top of the vessel as illustrated schematically in Figure 3.17(a). As time progresses, the drop expands in volume and eventually touches the tube below as seen in Figure 3.17(b) when fluid begins to flow out through an outlet port in the control volume representing the drop. This phase is usually called

the bridge formation stage. The present drop formation model is developed to include the physical processes shown in both Figures 3.17(a) and 3.17(b). Since the control volume in Figure 3.17(b), with an entry and exit port, is more general, the governing conservation equations of mass, species and energy are derived for this configuration of the control volume. For the processes in Figure 3.17(a), the exit port closed.

Vapour is absorbed at the outer surface of the drop whose shape changes with time as illustrated in Figure 3.17(a). The state of the contents of the drop is defined by a mean temperature and concentration which change with time. The drop formation model is developed in terms of the time dependent droplet volume  $V(t)$  and surface area  $A(t)$ , where vapour absorption occurs. In the present study, the variation of the volume and surface area of the droplet is obtained from experimental data as described in section 5.2-5.3 for different tube gaps and fluid flow rates. In a recent paper, Killion and Garimella [53] also presented such data on the variation of drop volume and surface area.

The heat and mass transfer rates from the outer surface of the droplet to the bulk liquid are expressed in terms of an overall heat transfer coefficient  $h_o$  and a mass transfer coefficient  $k_m$ . The heat transfer from the liquid-vapour interface to the bulk vapour is represented by the heat transfer coefficient  $h_v$ . This heat loss, in general, is estimated to be small [88]. However, the present formulation allows the formal inclusion of the vapour-side heat transfer with little additional effort.

The overall mass balance for the drop gives:

$$\frac{dm_{sd}}{dt} = \dot{m}_{vd} + \dot{m}_e - \dot{m}_o \quad (3.2.32)$$

where LHS is the rate of increase of mass while the RHS is the sum of the vapour absorption rate and the net mass flow rate into the control volume.  $m_{sd}$  is the mass of

the forming drop and  $\dot{m}_o$  is the rate of outflow of liquid when the bridge is formed. It should be noted that,  $\dot{m}_o = 0$  for the drop development stage shown in Figure 3.17(a).

Mass balance of LiBr in the drop can be expressed as:

$$\frac{d(m_{sd}w_s)}{dt} = \dot{m}_e w_e - \dot{m}_o w_s \quad (3.2.33)$$

where  $w_s$  is the average concentration of LiBr in the drop. The concentration of the liquid leaving through the bridge is assumed to be the same as that of the bulk liquid.

Energy conservation gives:

$$\frac{d(m_{sd}e_s)}{dt} = \dot{m}_{vd}i_v + \dot{m}_e i_e - \dot{m}_o i_s - A(t)h_v(T_{if} - T_v) \quad (3.2.34)$$

where the RHS is the sum of the enthalpy of absorbed vapour, the net enthalpy flow into the control volume and the vapour-side heat transfer while the LHS is the rate of increase of the internal energy of the drop. The enthalpy of the leaving liquid and the bulk liquid are assumed equal. Heat transfer from the forming drop to the coolant tube is neglected.

The vapour absorption rate can be expressed by a mass transfer rate equation:

$$\dot{m}_{vd} = A(t)k_m \rho_s (w_s - w_{if}) \quad (3.2.35)$$

where  $A(t)$  is the exposed area of the drop which varies with time and  $w_{if}$  is the concentration at the interface.

Energy balance at the vapour-liquid interface of the drop gives:

$$A(t)k_m \rho_s (w_s - w_{if})i_{ab} = A(t)h_o(T_{if} - T_s) + A(t)h_v(T_{if} - T_v) \quad (3.2.36)$$

where  $i_{ab}$  is the enthalpy of absorption,  $T_{if}$  is the temperature at the interface and  $T_v$  is the temperature of the vapour.

The internal energy of the solution is assumed to vary linearly with temperature and concentration. Therefore

$$e_s = c_t T_s + c_w w_s + c_o \quad (3.2.37)$$

$$e_e = c_t T_e + c_w w_e + c_o \quad (3.2.38)$$

where  $e_e, c_t, c_w, c_o$  are constants.

Differentiating Eq. (3.2.37)

$$\frac{de_s}{dt} = c_w \frac{dw_s}{dt} + c_t \frac{dT_s}{dt} \quad (3.2.39)$$

The equilibrium relation at the interface is expressed in the linear form given by

$$w_{if} = a + bT_{if} \quad (3.2.40)$$

Substituting for  $w_{if}$  in Eq. (3.2.36) from Eq. (3.2.40), the following expression is obtained for  $T_{if}$ ,

$$T_{if} = \frac{k_m \rho_s i_{ab} (w_s - a) + h_o T_s + h_v T_v}{h_o + h_v + k_m \rho_s b i_{ab}} \quad (3.2.41)$$

Eliminating  $w_{if}$  between Eqs. (3.2.35) and (3.2.40), the vapour mass flow can be written as:

$$\dot{m}_{vd} = A(t) k_m \rho_s [w_s - (a + bT_{if})] \quad (3.2.42)$$

Substituting for  $T_{if}$  in Eq. (3.2.42) from Eq. (3.2.41), the vapour absorption rate can be expressed as:

$$\dot{m}_{vd} = A(t) k_{ef} \rho_s [(w_s - a - bT_s) + \left(\frac{h_v}{h_o}\right)(w_s - a - bT_v)] \quad (3.2.43)$$

where the effective mass transfer coefficient is defined as:

$$\frac{1}{k_{ef}} = \frac{1}{k_m} \left( \frac{h_v}{h_o} + 1 \right) + \frac{i_{ab} b \rho_s}{h_o} \quad (3.2.44)$$

From Eqs. (3.2.32) and (3.2.33)

$$m_{sd} \frac{dw_s}{dt} = -\dot{m}_{vd} w_s + \dot{m}_e (w_e - w_s) \quad (3.2.45)$$

From Eq. (3.2.32) and (3.2.34)

$$m_{sd} \frac{de_s}{dt} = \dot{m}_{vd}(i_v - e_s) + \dot{m}_e(i_s - e_s) - \dot{m}_o(i_s - e_s) - A(t)h_v(T_{if} - T_v) \quad (3.2.46)$$

In Eq. (3.2.46) the enthalpies of liquid  $i_e$  and  $i_s$  are approximately equal to the corresponding internal energies  $e_e$  and  $e_s$  respectively, which can be expressed in terms of the temperature and concentration using the linear relations (3.2.37) and (3.2.38). The LHS of Eq. (3.2.46) is expressed in terms of temperature and concentration using with Eq. (3.2.39). These manipulations result in the following equation:

$$\begin{aligned} m_{sd}c_w \frac{dw_s}{dt} + m_{sd}c_t \frac{dT_s}{dt} \\ = \dot{m}_{vd}(i_v - e_s) + \dot{m}_e c_t (T_e - T_s) + \dot{m}_e c_w (w_e - w_s) - A(t)h_v (T_{if} - T_v) \end{aligned} \quad (3.2.47)$$

Eliminating  $(dw_s / dt)$  between Eqs. (3.2.45) and (3.2.47),

$$m_{sd}c_t \frac{dT_s}{dt} = \dot{m}_{vd}(i_v - e_s + c_w w_s) + \dot{m}_e c_t (T_s - T_e) - A(t)h_v (T_{if} - T_v) \quad (3.2.48)$$

Substituting for  $\dot{m}_{vd}$  from Eq. (3.2.43) in Eq. (3.2.45), the following equation is obtained.

$$\frac{dw_s}{dt} = -\frac{k_{ef} \rho_s A(t) w_s}{m_{sd}} \left[ (w_s - a - bT_s) + \left( \frac{h_v}{h_o} \right) (w_s - a - bT_v) \right] + \left( \frac{\dot{m}_e}{m_{sd}} \right) (w_e - w_s) \quad (3.2.49)$$

Substituting for  $\dot{m}_{vd}$  from Eq. (3.2.43) and for  $T_{if}$  from Eq. (3.2.42) in Eq. (3.2.47) the following equation is obtained.

$$\begin{aligned} \frac{dT_s}{dt} = \frac{k_{ef} \rho_s A(t)}{m_{sd}c_t} [g_5 (w_s - a - bT_s) + g_6 \left( \frac{h_v}{h_o} \right) (w_s - a - bT_v)] \\ + \left( \frac{\dot{m}_e}{m_{sd}} \right) (T_s - T_e) - \left( \frac{A(t)h_v k_{ef}}{m_{sd}c_t k_m} \right) (T_s - T_v) \end{aligned} \quad (3.2.50)$$

where the coefficients are given by :

$$g_5 = i_v - e_s + c_w w_s \quad \text{and} \quad g_6 = i_v - e_s + c_w w_s - i_{ab} \quad (3.2.51)$$

The simultaneous solution of Eqs. (3.2.49) and (3.2.50) gives the variation of the concentration and temperature of the drop with time allowing for vapour –side heat transfer.

When the vapour-side heat transfer is neglected ( $h_v = 0$ ) and the mass of the drop is expressed by,  $m_{sd} = \rho_s V(t)$ , Eqs. (3.2.49) and (3.2.50) become:

$$\frac{dw_s}{dt} = -\frac{k_{ef} A(t) w_s}{V(t)} [w_s - (a + bT_s)] + \left( \frac{\dot{m}_e}{\rho_s V(t)} \right) (w_e - w_s) \quad (3.2.52)$$

and

$$\frac{dT_s}{dt} = \frac{k_{ef} A(t)}{V(t) c_t} (i_{vs} + c_w w_s) [w_s - (a + bT_s)] + \left( \frac{\dot{m}_e}{\rho_s V(t)} \right) (T_e - T_s) \quad (3.2.53)$$

where  $i_{vs} = (i_v - e_s)$ , which is assumed constant at the average value.

As a further simplification, Eqs. (3.2.52) and (3.2.53) can be reduced to a single equation by defining new variable given by :

$$\phi_s = [w_s - (a + bT_s)] \quad (3.2.54)$$

Differentiating Eq. (3.2.54) and substituting for  $(dw_s / dt)$  and  $(dT_s / dt)$  from Eqs.

(3.2.52) and (3.2.53) respectively, the combined Eq. (3.2.55) is obtained.

$$\frac{d\phi_s}{dt} = -\left( \frac{\beta_d A(t)}{V(t)} \right) \phi_s + \left( \frac{\dot{m}_e}{\rho_s V(t)} \right) (\phi_e - \phi_s) \quad (3.2.55)$$

where:

$$\beta_d = k_{ef} \left[ w_s + \frac{bc_w w_s}{c_t} + \frac{bi_{vs}}{c_t} \right] \quad (3.2.56)$$

It is seen that  $\phi_s$  is the departure of the bulk concentration of the drop from the equilibrium concentration at the corresponding bulk temperature. The corresponding value for the entering solution is  $\phi_e$ .

If the time variation of the drop area  $A(t)$  and drop volume  $V(t)$ , are known experimentally, Eq. (3.2.55) can be solved directly to obtain the variation of  $\phi_s(t)$  provided the liquid inflow rate can be estimated. Since the change in the volume of the drop resulting from the absorption of vapour is very small, it would be reasonable to assume that  $\dot{m}_e \approx \rho_s (dV(t)/dt)$ , for the drop development shown in Figure 3.17(a). The term  $(dV/dt)$  can be obtained from the slope of the volume versus time curve as shown in chapter 5 and 6.

It is interesting to note that the governing Eqs. (3.2.49) and (3.2.50) with vapour-side heat loss and Eqs.(3.2.52) and (3.2.53) without it are applicable to both the drop development stage shown in Figure 3.17(a) and the bridge formation stage shown in Figure 3.17(b). Although these equations do not involve the outflow rate,  $\dot{m}_o$  explicitly, the difference between the two situations is implicit in variation of  $A(t)$  and  $V(t)$  with time. For the bridge formation stage, an assumption has to be made about the liquid inflow rate to the control volume during the period. In the absence of any other information, it is reasonable to assume the liquid inflow rate remains constant at the value just before the formation of the liquid bridge.

The liquid outflow rate from the control volume during the bridging phase is given by:

$$\dot{m}_o \approx \dot{m}_{eb} - \rho_s \frac{dV(t)}{dt} \quad (3.2.57)$$

The total liquid mass transferred to the tube below during bridging is:

$$\Delta m_{do} = \dot{m}_{eb} \tau_b + \rho_s \Delta V_b \quad (3.2.58)$$

where  $\tau_b$  is the duration of liquid bridging and  $\Delta V_b$  is the decrease in the drop volume during this period.

The quantities involved in Eqs. (3.2.57) and (3.2.58) can be obtained from time variation of  $V(t)$ .

After the variation of  $\phi_s(t)$  is computed by solving Eq. (3.2.55), the resulting values are substituted in Eqs. (3.2.52) and (3.2.53) to solve for  $w_s$  and  $T_s$  respectively. The solution procedure is carried out continuously from the start of the drop formation to the break up of the liquid bridge using a fourth- order Runge-Kutta solution scheme. When the vapour-side heat transfer is included in the analysis, Eqs. (3.2.49) and (3.2.50) are solved using a similar numerical scheme. The variation of  $A(t)$  and  $V(t)$ , obtained from the video image analysis, is supplied as input data. The other input parameters are stated below.

- The thermo-physical property data required as input are: density, viscosity, specific heat, thermal conductivity, thermal and mass diffusivity of the LiBr solution.
- The initial conditions required are: mass, temperature, concentration of solution at the beginning of drop formation. The initial mass is assigned zero of the forming droplet. Initial temperature and concentration are assigned with the known values leaving the last falling film regime.

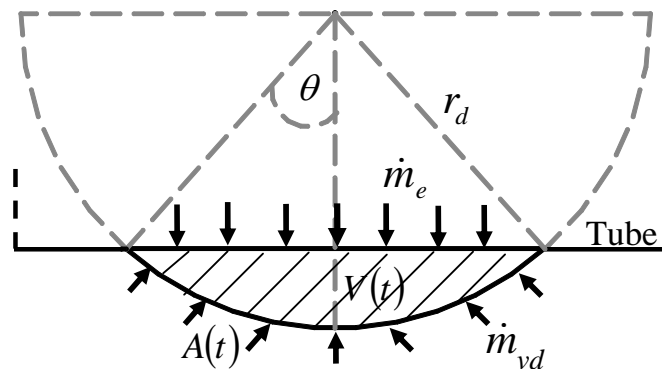


Figure 3.18 Schematic diagram of the formation of a hemispherical droplet.



### 3.2.2.2 Idealized droplet formation model

The droplet formation model stated above in section 3.2.2.1 can be applied for any known shape of the flexible vessel. In the present idealized model of the forming droplet, the shape is taken as a cap of a sphere as shown schematically in Figure 3.18. As time proceeds the angle  $\theta(t)$  of the cap increases from zero to  $\pi/2$ . The area and volume of the cap at any instant is obtained from the geometry of the spherical cap as:

$$A(t) = 2\pi r_d^2 [1 - \cos \theta] \quad (3.2.59)$$

and

$$V(t) = \pi r_d^3 [2 - 3\cos \theta + \cos^3 \theta]/3 \quad (3.2.60)$$

The equations developed in section 3.2.2.1 are applicable to the idealized droplet formation model in this section except the following assumptions.

Assuming that the rate of inflow of solution from top,  $\dot{m}_e$  to form the idealized drop is constant the mass balance for LiBr gives:

$$m_{sd} w_s = \dot{m}_e w_e t \quad (3.2.61)$$

The mass inflow rate  $\dot{m}_e$  is determined in a manner similar to that stated in section 3.2.5.1.

The solution of Eqs. (3.2.52) and (3.2.53) require as input the thermo-physical properties of the solution which are obtained from property tables. The mass transfer coefficient  $k_m$  is calculated using the correlation in Siyoung and Garimella [88] for this idealized droplet formation case. The convective heat transfer coefficient  $h_o$  during drop formation is determined from the heat and mass transfer analogy stated in section 3.2.2.4 where the exponent 'n' is taken as 0.33. The solution of Eqs. (3.2.52) and (3.2.53) involves an iterative procedure due to the non-linear form of the equations. As the drop develops, an increment in the time  $t$  and the angle  $\theta$  are assumed. The values of  $A(t)$ ,

$V(t)$ ,  $m_{sd}$ ,  $w_s$  and  $T_s$  are computed using Eqs. (3.2.59), (3.2.60), (3.2.61), (3.2.52) and (3.2.53) respectively. Iteration for the final value of  $\theta$  at a particular time  $t$  is carried out until the relation  $m_{sd} = V(t)\rho_s$  is satisfied. Thereafter the value of  $\theta$  is increased incrementally and the procedure is repeated until the value of  $\theta$  reaches  $\pi/2$ . At this stage the drop has attained a hemispherical shape and is assumed to be dislodged from the tube.

### 3.2.2.3 Steady-jet / sheet model

For the jet and sheet flow modes, the simplified model developed in section 3.2.1 could be applied with suitable modifications. The main equations of the model are outlined below. Figure 3.17(c) shows a jet profile and Figure 3.19 shows a sheet-flow strip between two tubes. The vapour is absorbed at outer exposed surface of the jet/sheet-flow strip which is assumed to have a fixed shaped. The flow is assumed steady but all the other assumptions made in the simplified model developed in section 3.2.1 are applied to the inter-tube flow situation. As in the case of drop formation, the liquid is not cooled during inter-tube jet/sheet flow and therefore the absorption process is adiabatic.

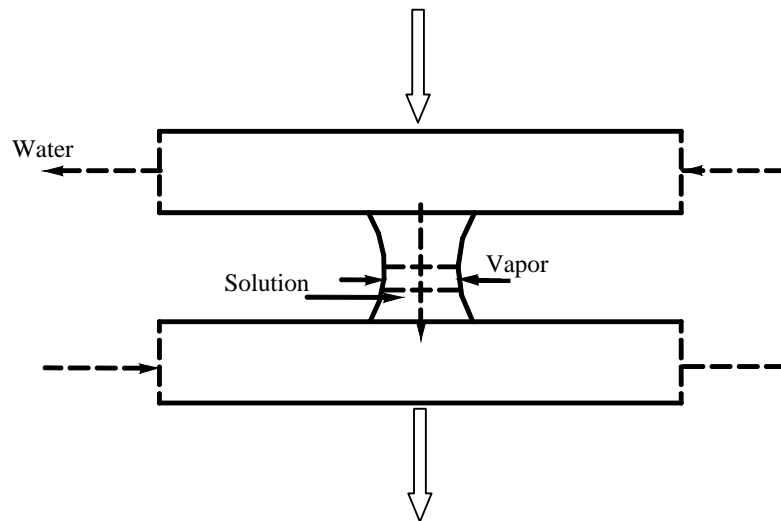


Figure 3.19 physical model for inter-tube flow.

The governing equation for the bulk solution concentration and bulk solution temperature are obtained by applying conservation equations of energy and mass to the small control volume shown in Figure 3.17(c) or 3.19. In this formulation, the heat transfer from the liquid-vapour interface to the bulk vapour is assumed to be zero. This gives:

$$d(m_{sj}i_s) = i_v dm_{sj} \quad (3.2.62)$$

The above equation can be expanded in a manner similar to equations (3.2.1) to (3.2.6) to yield the following equation:

$$i_{vs} dm_{sj} = m_{sj} c_T dT_s + m_{sj} c_w dw_s \quad (3.2.63)$$

where  $i_{vs} = i_v - i_s$

The mass transfer rate equation from the interface to the bulk of the solution may be expressed as:

$$dm_{sj} = \rho_s k_m (w_s - w_{if}) dA \quad (3.2.64)$$

where  $dA$  is the exposed area of the small control volume shown in Figure 3.17(c) or Figure 3.19.

Assume that the interface energy balance, given by Eq. (3.2.9), and the linear equilibrium condition expressed by Eq. (3.2.10) apply to the interface. Carrying out the manipulation leading Eq. (3.2.11), the mass flux may be expressed in following form:

$$dm_{sj} = \rho_s k_{ef} [w_s - (a + bT_s)] dA \quad (3.2.65)$$

Since the mass of LiBr is constant

$$m_{sj} = \frac{m_l}{w_s} \quad (3.2.66)$$

Differentiating Eq. (3.2.66) and linearizing the resulting expression in a manner similar to Eq. (3.2.15), the following expression is obtained:

$$dm_{sj} = \left[ \frac{-m_l}{w_s^2} \right] dw_s \quad (3.2.67)$$

Substitution of Eq. (3.2.67) into Eq. (3.2.65) gives:

$$\frac{dw_s}{dA} = -\frac{\bar{w}_s^2}{m_l} \rho_s k_{ef} [w_s - (a + bT_s)] \quad (3.2.68)$$

By substituting Eq. (3.2.65) and (3.2.68) into Eq. (3.2.63), the equation for the solution temperature may be written as:

$$\frac{dT_s}{dA} = k_{ef} \rho_s \left[ \frac{i_{vs}}{m_{sj} c_T} + \frac{c_w \bar{w}_s^2}{c_T m_l} \right] [w_s - (a + bT_s)] \quad (3.2.69)$$

Substituting the new driving potential,  $\psi = w_s - (a + bT_s)$ , the above equations are reduced to a single equation given by

$$\frac{d\psi}{dA} = -k_{ef} \rho_s \left[ \frac{bi_{vs}}{m_{sj} c_T} + \frac{bc_w \bar{w}_s^2}{c_T m_l} + \frac{\bar{w}_s^2}{m_l} \right] \psi \quad (3.2.70)$$

The solution of Eq. (3.2.70) gives exit value of the driving potential of the inter-tube flow as:

$$\psi_o = \psi_{in} e^{-g_5 A} \quad (3.2.71)$$

where

$$g_5 = k_{ef} \rho_s \left[ \frac{bi_{vs}}{m_{sj} c_T} + \frac{bc_w \bar{w}_s^2}{c_T m_l} + \frac{\bar{w}_s^2}{m_l} \right] \quad (3.2.72)$$

The solution concentration and temperature are obtained by direct substitution in Eqs. (3.2.68) and (3.2.69) as:

$$w_{so} = w_{si} - \frac{g_6}{g_5} (1 - e^{-g_5 A}) \quad (3.2.73)$$

$$T_{so} = T_{si} + \frac{g_7}{g_5} (1 - e^{-g_5 A}) \quad (3.2.74)$$

$$g_6 = \frac{\bar{w}_s^2}{m_l} \rho_s k_{ef} \quad \text{and} \quad g_7 = k_{ef} \rho_s \left[ \frac{i_{vs}}{m_{sj} c_T} + \frac{c_w \bar{w}_s^2}{c_T m_l} \right] \quad (3.2.75)$$

In Eq. (3.2.75),  $k_{ef}$  is the effective mass transfer coefficient which has to be suitably evaluated by using Eq. (3.2.44) with vapour side heat transfer coefficient  $h_v = 0$  and  $m_{sj}$  is the mass flow rate through the jet.

The profile of the steady jet is fitted with a polynomial as in the case of the evolving drops. The shape of the jet is taken as the solid of revolution obtained by rotating the jet profile curve about the axis of symmetry. The external area of the jet, shown in Figure 3.17(c), is given by

$$A = \int 2\pi x(1 + y'^2)^{1/2} dx \quad (3.2.76)$$

where  $y = f(x)$  is the polynomial curve of the profile and  $y' = dy/dx$ .

The bulk mean concentration and temperature of the jet/sheet at each section of  $A$  is obtained directly from Eq. (3.2.73) and Eq. (3.2.74) respectively. The initial values of these quantities  $w_{si}, T_{si}$  and the mass flow rate  $m_{sj}$  are known from the leaving conditions of the falling film from which the jet/sheet originates.

#### 3.2.2.4 Transfer coefficients in the inter-tube flow regime

The measured data for the mass transfer coefficient  $k_m$  for drop formation or jet/sheet flow are not available at the present time. Siyoung and Garimella [88] have used a correlation for mass transfer coefficient during drop formation which was developed by Skelland and Minhas [89] for drop formation in liquid-liquid extraction. In view of these uncertainties with regard to  $k_m$ , its value for drop formation or jet/sheet flow is taken to be the same as that for falling film. In the falling film regime, the mass transfer coefficient is determined from the detailed numerical model described in section 3.1. However, a detailed sensitivity study was carried out for which results are documented in Appendix C and also discussed in section 6.2. The heat transfer coefficient during inter-tube flow is determined from following heat and mass transfer analogy:

$$h_o = k_m (k_s / D_{ab}) (D_{ab} / \alpha)^n \quad (3.2.77)$$

where  $D_{ab}$  is the mass diffusivity of LiBr solution.

Unfortunately, no reported data on a suitable value for the exponent 'n' could be found in the literature. Therefore the effect of the value of the exponent on the predicted absorption rate was explored by a sensitivity study also described in Appendix C.

### 3.2.3 Simplified model for a horizontal- tube-bundle absorber

A schematic diagram of a horizontal tube-bundle absorber is shown in Figure 3.16. The analysis in section 3.2.1 for a single tube is now applied to the  $n^{\text{th}}$  tube of a series of N tubes. In the present analysis, the temperature and concentration of the solution entering a horizontal tube from top and leaving at the bottom are assumed to be spatially uniform. Although the analysis takes into consideration the variation of the cooling water temperature in a tube, for the purpose of estimating the heat transfer from the solution film to the water, the latter is assumed to be the average water temperature in the tube.

Application of the energy equation to the cooling water gives:

$$m_w c_{pw} \frac{dT_{wn}}{dz} = 2 \int_{\theta_i}^{\theta_o} r_o (T_{sn} - \bar{T}_{wn}) U_{bw} d\theta = 2 \int_{\theta_i}^{\theta_o} r_o \phi U_{bw} d\theta \quad (3.2.78)$$

The average water temperature for the  $n^{\text{th}}$  tube is  $\bar{T}_{wn}$ .

Substituting from equation (3.2.25) for  $\phi$  and rearranging

$$m_w c_{pw} \frac{dT_{wn}}{dz} = 2 \int_{\theta_i}^{\theta_o} r_o U_{bw} [a_1 \exp(\alpha_1 \theta) + a_2 \exp(\alpha_2 \theta)] d\theta \quad (3.2.79)$$

In Eq. (3.2.79) the quantities that vary from tube to tube are the inlet values of  $\phi_0$  and  $\psi_0$  that occur in the coefficients  $a_1$  and  $a_2$  as seen from Eqs. (3.2.28) and (3.2.29). The expressions for these coefficients are first substituted in Eq. (3.2.79) and the integration is carried out over  $\theta$  from entry to exit of the solution flow. The water temperature rise in a tube is then obtained by integrating the resulting expression over the tube length  $z$

from inlet to outlet. These manipulations result in the following expression for the inlet and outlet water temperatures of the  $n^{th}$  tube:

$$T_{won} - T_{win} = G\phi_{in} + H\psi_{in} \quad (3.2.80)$$

where  $\phi_{in}$  and  $\psi_{in}$  are values of the driving potentials at entry to the  $n^{th}$  tube. Once evaluated, the coefficients G and H, given below, have the same value for all the tubes.

$$G = \left( \frac{2r_o LU_{bw}}{m_w c_{pw}} \right) \left[ \frac{(\alpha_1 + g_4)[\exp(\alpha_1 \theta_o) - \exp(\alpha_1 \theta_i)]}{\alpha_1(\alpha_1 - \alpha_2)} + \frac{(\alpha_2 + g_4)[\exp(\alpha_2 \theta_o) - \exp(\alpha_2 \theta_i)]}{\alpha_2(\alpha_2 - \alpha_1)} \right] \quad (3.2.81)$$

$$H = \left( \frac{2r_o LU_{bw}}{m_w c_{pw}} \right) \left[ \frac{g_1[\exp(\alpha_1 \theta_o) - \exp(\alpha_1 \theta_i)]}{\alpha_1(\alpha_1 - \alpha_2)} + \frac{g_2[\exp(\alpha_2 \theta_o) - \exp(\alpha_2 \theta_i)]}{\alpha_2(\alpha_2 - \alpha_1)} \right] \quad (3.2.82)$$

$$\text{Now } \phi_{in} = \bar{T}_{sin} - \bar{T}_{wn} = \bar{T}_{sin} - 0.5(T_{win} + T_{won}) \quad (3.2.83)$$

Substituting in Eq. (3.2.80) the expression for  $\phi_{in}$  from Eq. (3.2.83) the relation between the inlet and outlet water temperatures is obtained in terms of quantities that are all known at the inlet to the  $n^{th}$  tube.

$$(G + 2)T_{won} + (G - 2)T_{win} = 2G\bar{T}_{sin} + 2H[\bar{w}_{sin} - (a + b\bar{T}_{sin})] \quad (3.2.84)$$

The outlet values of the potential  $\phi_{on}$  and  $\psi_{on}$  for the  $n^{th}$  tube are obtained by direct substitution in Eqs. (3.2.25) and (3.2.26) respectively. The outlet solution temperature from the  $n^{th}$  tube is given by the expression

$$\bar{T}_{son} = 0.5(T_{win} + T_{won}) + \phi_{on} \quad (3.2.85)$$

If inter-tube absorption is neglected, the average temperature and concentration of the solution leaving one tube is equal to the corresponding average quantities of the solution entering the tube below. This is also true for cooling water leaving one tube and entering the next. Therefore;

$$\bar{T}_{si(n+1)} = \bar{T}_{son}, \quad \bar{w}_{si(n+1)} = \bar{w}_{son}, \quad \psi_{i(n+1)} = \psi_{on} \quad \text{and} \quad T_{wo(n+1)} = T_{win} \quad (3.2.86)$$

It is seen from Eq. (3.2.83) that the heat transfer potential  $\phi$  for the solution at exit of a tube is not equal to the value at entry to the next tube because the average water temperature changes from one tube to the next.

When inter-tube vapour absorption, in the form of absorption into drops/jets or sheets between the two tubes, is included in the analysis, the concentration and temperature of the solution entering the tube below are obtained using Eqs. (3.2.52) and (3.2.53) or Eqs. (3.2.73) and (3.2.74) respectively.

The computational steps for the application of the above simplified model are summarized below. The basic input design data are used to calculate the coefficients  $g_1$  to  $g_4$ , the roots  $\alpha_1$ ,  $\alpha_2$  and finally the coefficients H and G. These quantities apply to all the absorber tubes. For a counter flow design, the inlet water temperature is usually known only at the inlet to the last (N) tube. Therefore the outlet water temperature from the first tube is guessed to be later corrected in an iterative manner. Eq. (3.2.84) is used to calculate the inlet water temperature to the first tube and the average water temperature in the tube. Since the values of the potentials  $\phi_m$  and  $\psi_m$  are known at the inlet to the tube, the corresponding values at exit are computed by direct application of Eqs. (3.2.25) and (3.2.26). Eqs. (3.2.85) and (3.2.86) give all the quantities needed to apply the above steps to the next tube when inter-tube absorption is neglected. When inter-tube absorption into drops/jets or sheets is included, Eqs. (3.2.52) and (3.2.53) or Eqs. (3.2.73) and (3.2.74) are used to compute the entry conditions to the next tube. Finally, the inlet water temperature of the last tube N, computed in the above manner, is compared with the actual water inlet temperature and the iteration is terminated when convergence is achieved.



### 3.2.4 Approximate expressions for driving potentials

Computations carried out using the experimental data from Islam [43] for a horizontal tubular absorber and from Miller [65] for a vertical tube absorber revealed that for practical situations one of the roots given by expression (3.2.27) is much larger than the other root [46]. It is therefore possible to derive approximate closed-form expressions for the roots of Eq. (3.2.27) which in turn may be used to obtain closed-form expressions for the temperature and concentration distributions across the absorber. The main expressions are outlined below.

Eliminating the potential  $\psi$  between the differential Eqs. (3.2.21) and (3.2.22) the following second order equation is obtained for the potential  $\phi$ .

$$\frac{d^2\phi}{d\theta^2} + (g_4 + g_2)\frac{d\phi}{d\theta} + (g_2g_4 - g_1g_3)\phi = 0 \quad (3.2.87)$$

Exact solution of Eq. (3.2.87), which is given by Eq. (3.2.25), shows that for practical ranges of operation of absorbers [43], the third term of the equation is much smaller than the other two terms for small values of  $\theta$ . Therefore neglecting the third term and integrating the resulting equation the following asymptotic form is obtained for small values of  $\theta$ .

$$\frac{d\phi}{d\theta} + (g_2 + g_4)\phi = c_1 \quad (3.2.88)$$

where  $c_1$  is a constant.

For large values of  $\theta$ , the first term in equation (3.2.87) is found to be much smaller than the other two terms. Neglecting the first term the asymptotic form of the equation is obtained as:

$$\frac{d\phi}{d\theta} + \left[ \frac{g_2g_4 - g_1g_3}{g_2 + g_4} \right] \phi = 0 \quad (3.2.89)$$

Eqs. (3.2.88) and (3.2.89) are similar to the governing equation for the fluid temperature difference of a counter-flow heat exchanger [25] with the exponents given by:

$$\alpha_{1a} = -(g_2 + g_4) \quad \text{and} \quad \alpha_{2a} = -\frac{(g_2 g_4 - g_1 g_3)}{(g_2 + g_4)} \quad (3.2.90)$$

Substituting from expressions (3.2.23) and (3.2.24), the exponents may be written in terms of the basic system parameters as:

$$\alpha_{1a} = -\frac{r_o U_{bw}}{m_s c_T} - f_c \left[ \frac{(r_o + \delta) \rho_s k_{ef}}{m_s} \right] \quad (3.2.91)$$

and

$$\frac{1}{\alpha_{2a}} = -\frac{1}{(r_o + \delta) \bar{w}_s} \left[ \frac{m_s}{\rho_s k_{ef}} \right] - \left[ \frac{r_o \bar{w}_s}{f_c} \right] \left[ \frac{m_s c_T}{U_{bw}} \right] \quad (3.2.92)$$

$$\text{where the parameter } f_c = b \left( \frac{i_{vs}}{c_T} + \frac{\bar{w}_s c_w}{c_T} \right) + \bar{w}_s \quad (3.2.93)$$

It is interesting to note that the exponent  $\alpha_{1a}$  is equal to the weighted sum of the number of transfer units for heat transfer,  $\left[ \frac{r_o U_{bw}}{m_s c_T} \right]$  and mass transfer,  $\left[ \frac{(r_o + \delta) \rho_s k_{ef}}{m_s} \right]$ . The exponent  $\alpha_{2a}$  is the reciprocal of the weighted sum of the reciprocals of the above transfer units. The parameter  $f_c$  is the sum of a dimensionless effective heat capacity and the mean concentration of the solution. The initial variation of the heat and mass transfer potentials given by Eqs. (3.2.25) and (3.2.26) is determined by the numerically larger exponent  $\alpha_{1a}$  while the variation at larger distances from the entrance of the absorber is dominated by the numerically smaller exponent  $\alpha_{2a}$ . The validity of the approximate expressions and their variations are explored numerically later in the chapter.

### 3.2.5 Results and discussion: modeling

#### 3.2.5.1 Comparison of idealized droplet formation model

The predictions of the drop formation model presented in section 3.2.2.2 can be compared with those of the corresponding model available in Siyoung and Garimella

[88] for the same experimental conditions. In their case, a hemispherical droplet during formation stage was allowed to grow until its volume reaches half of the volume of a falling spherical droplet. Similar to Kirby and Perez-Blanco [59], the interface condition of droplet at each instant of time was assumed such that interface temperature of the drop remained equal to the temperature of fresh solution. The time of formation of the droplet was calculated from the known final mass of the hemispherical droplet and the incoming solution flow rate,  $\dot{m}_e = 2m_s\beta$ . Here  $\beta$  is the droplet site spacing and  $m_s$  is the flow rate of solution along one side of the tube. The distance between the two neighboring droplets,  $\beta$  was calculated from Eq. (4.4). The details of their droplet model are described in [88]. The governing equations of the model were solved with 4<sup>th</sup> order RK method of solution.

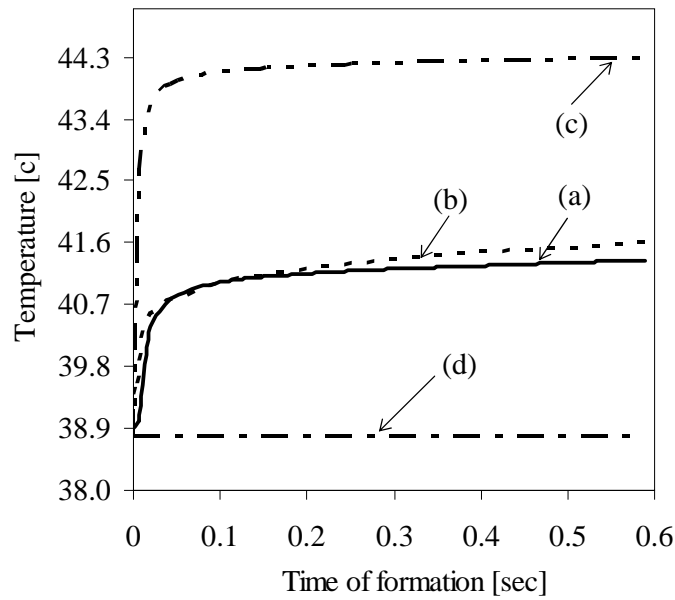


Fig. 3.20 Comparison of droplet formation models. Graphs: (a) (—) bulk temperature change by the present model; (b) (---) bulk temperature change by the model of Siyong and Garimella [88]; (c) (-·-·) interface temperature change by the present model; (d) (····) interface temperature change by the model of Siyong and Garimella [88]; Experimental conditions: Seventh tube,  $\Gamma = 0.024 \text{ kgm}^{-1}\text{s}^{-1}$ ,  $\text{WR}=0.8$ ; as described in [88].

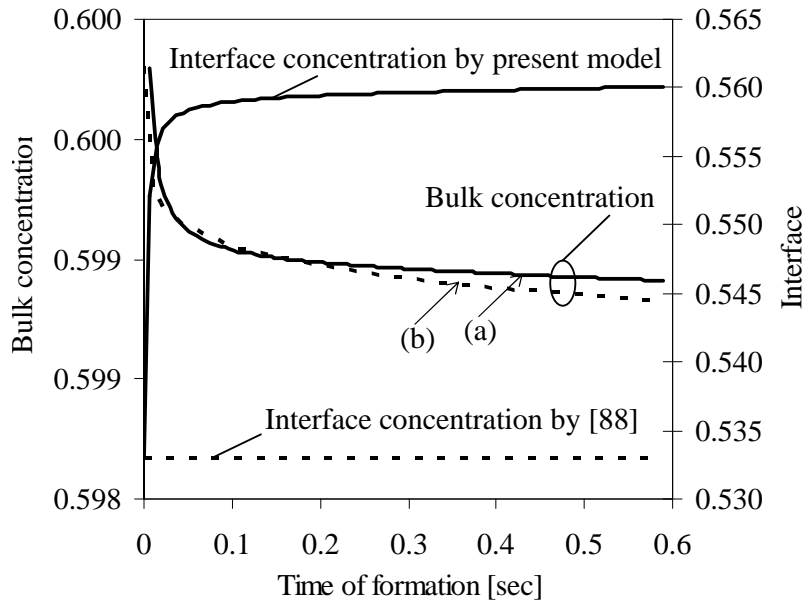


Fig. 3.21 Comparison of droplet formation models. Graphs: (a) (—) bulk and interface concentration change by the present model; (b) (---) bulk and interface concentration change by the model of Siyoung and Garimella [88]; Experimental conditions: Seventh tube,  $\Gamma = 0.024 \text{ kgm}^{-1}\text{s}^{-1}$ ,  $\text{WR}=0.8$ ; as described in [88].

The results for the temperature and concentration variations with time during the formation of the drop for a given set of conditions in [88] are shown in Figures 3.20-3.21. The results of Siyoung and Garimella [88] are included for comparison. There is reasonably good agreement between the predictions of the two models. As expected, the bulk temperature increases rapidly with time while the LiBr concentration decreases due to vapour absorption by the drop.

The comparison of the interface temperature and concentration variation is also plotted in Figures 3.20 and 3.21 respectively. Both the interface temperature and concentration are over predicted by the present model compared to the constant interface temperature and concentration predicted by Siyoung and Garimella [88]. Because of the difference in the interface conditions of the two models, present model exhibits slightly different bulk conditions as well.

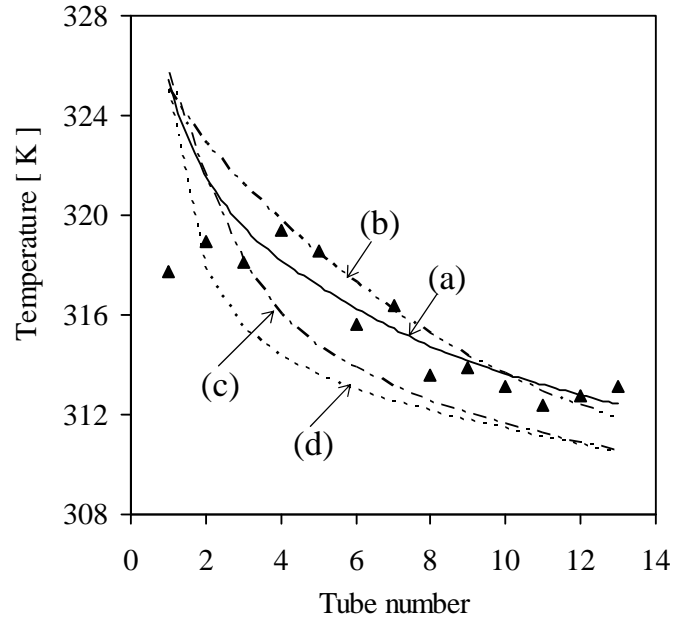


Fig. 3.22 Comparison of tube surface temperature. Graphs: (a) (—) numerical model with inter-tube flow; (b) (---) simplified model with inter-tube flow; (c) (-·-) simplified model without inter-tube flow; (d) (···) numerical model without inter tube flow; (▲) experiment of Nomoura et al. [75]; conditions:  $\Gamma = 0.058 \text{ kgm}^{-1} \text{ s}^{-1}$ ,  $T_{si} = 54^{\circ}\text{C}$ ,  $w_{si} = 0.62$ ,  $WR = 0.8$ .

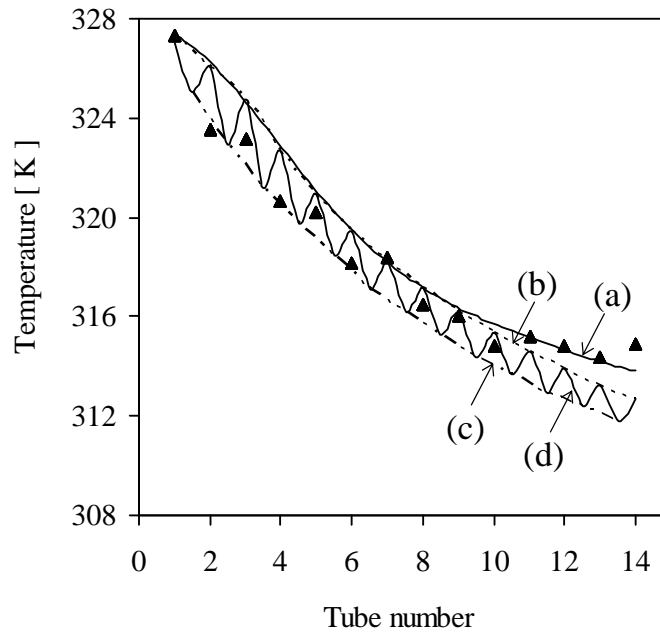


Fig. 3.23 Comparison of inter-tube solution temperature. Graphs: (a) (—) numerical model with inter-tube flow; (b) (---) simplified model with inter-tube flow; (c) (-·-) tube surface temperature of simplified model with inter-tube flow; (d) (···) continuous temperature plot of simplified model with inter tube flow; (▲) experiment of Nomoura et al. [75]; conditions:  $\Gamma = 0.058 \text{ kgm}^{-1} \text{ s}^{-1}$ ,  $T_{si} = 54^{\circ}\text{C}$ ,  $w_{si} = 0.62$ ,  $WR = 0.8$ .

Figures 3.22 and 3.23 show the predictions of the numerical model and the simplified-coupled model of the tube surface temperature and the inter-tube solution temperature for a set of experimental conditions in Nomura et al. [75] where there was droplet flow between the tubes. For comparison, computations are done both with and without idealized drop flow between the tubes as stated in section 3.2.2.2. In the simplified model, the same transfer coefficients were used for both the film-flow over the tubes as well as droplet flow between tubes. These coefficients were obtained using Eqs. (3.9), (3.10) and (3.11) of the numerical model as described in section 3.1.2. A constant tube wetting ratio of 0.8 was assumed in both models as was done by Siyoung and Garimella [88]. It is seen from the Figures 3.22 and 3.23 that the predictions of the models including idealized inter-tube droplet-flow are closer to the experimental data. The solution temperature variation predicted by the numerical model is the closest to the measurements.

A comparison of inter-tube solution temperatures predicted by the two models is shown in Figure 3.23. Here again, the models including idealized inter-tube drop flow gives better prediction of the experimental data. When the tube surface temperatures and the inter-tube solution temperatures of successive tubes, predicted by the simplified model, are joined, the ‘saw tooth’ temperature profile shown in Figure 3.23 is obtained. This is because the solution temperature rises in the inter-tube region due to the adiabatic absorption of the vapour as is also seen in Figure 3.20. The numerical model predicts a similar behaviour in the temperature variation.

### **3.2.5.2 Comparison of numerical model and simplified coupled model**

#### ***Effect of heat and mass transfer coefficients***

The predictions of the numerical model and the simplified-coupled model were compared with published experimental data available in the literature. The simplified model requires as input the heat transfer coefficients,  $h_i$ ,  $h_o$  and the mass transfer

coefficient  $k_m$  which are obtained from the results of the numerical simulation. The temperature and concentration fields are first obtained by solving the energy and species concentration Eqs. (3.2) and (3.3) using the finite difference method. Subsequently, the local values of  $h_i$ ,  $h_o$  and  $k_m$  are computed using Eqs. (3.9)- (3.11) and the overall transfer coefficients,  $U_{bw}$ ,  $k_{ef}$  are obtained by substitution in Eqs. (3.2.7) and (3.2.13). The average values of the transfer coefficients for entire tube bundle absorber, which are termed ‘averaged’ values, are then determined by computing the numerical average of the corresponding tube-wise values.

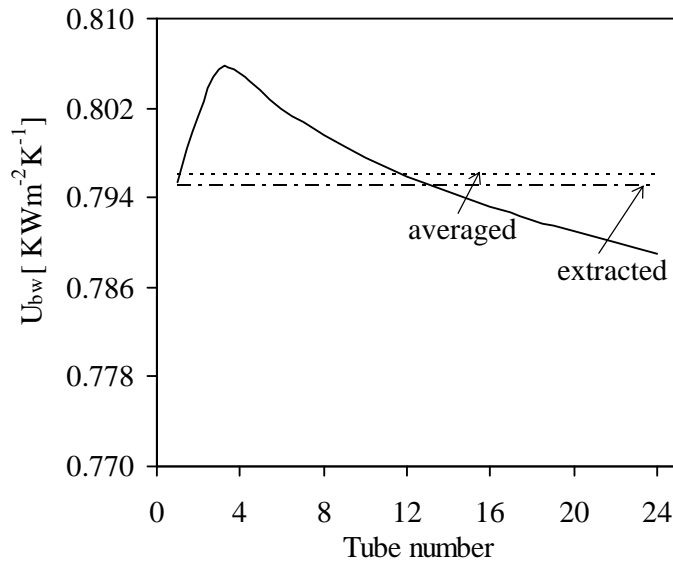


Fig. 3.24 Local and average overall heat transfer coefficient along the absorber; experimental conditions:  $\Gamma = 0.0595 \text{ kgm}^{-1}\text{s}^{-1}$ ,  $T_{si} = 39.8^{\circ}\text{C}$ ,  $w_{si} = 0.604$ ,  $WR = 1.0$  [43].

The simplified model can also be used to ‘extract’ the overall heat and mass transfer coefficients for a tube bundle absorber from measured experimental data. For each test run, the values of the driving potentials  $\phi$  and  $\psi$  at the inlet and outlet of the absorber are computed by substituting the measured values of the solution temperature and concentration and the coolant temperature in Eq. (3.2.18). When these inlet and outlet potentials are substituted in Eqs. (3.2.25) and (3.2.26) the only unknowns in the resulting

equations are  $U_{bw}$  and  $k_{ef}$  which can be obtained by direct solution of the two simultaneous equations. The values of the transfer coefficients thus obtained are termed ‘extracted’ values.

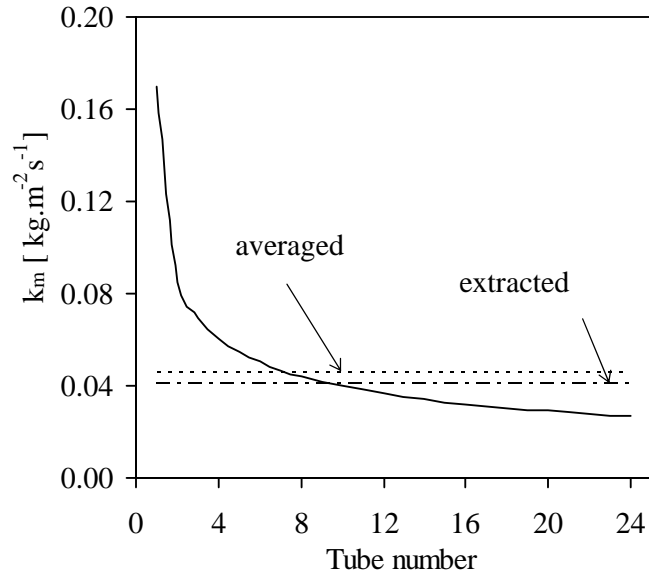


Fig. 3.25 Local and average mass transfer coefficient along the absorber; experimental conditions:  $\Gamma = 0.0595 \text{ kgm}^{-1} \text{ s}^{-1}$ ,  $T_{si} = 39.8^\circ\text{C}$ ,  $w_{si} = 0.604$ ,  $WR = 1.0$  [43].

Figures 3.24-3.25 show the variation of the local transfer coefficients together with the ‘extracted’ transfer coefficients obtained from the experimental data of Islam [43] and ‘averaged’ transfer coefficients from the numerical model for the same experimental conditions. The curves indicate that there is significant variation in the local transfer coefficients  $U_{bw}$  and  $k_m$  across the tubes of the absorber. The numerical simulation indicates that for low inlet solution temperatures, as in the case of the experimental data from Islam [43],  $U_{bw}$  increases over the first three tubes and then decrease steadily. The value of  $k_m$  on the other hand decreases continuously from the first to the last tube. In contrast, when the inlet solution temperature is high, as in the case of the experiments of Nomoura et al. [75], both local transfer coefficients  $U_{bw}$  and  $k_m$  were found to decrease continuously across the tubes.



When the solution enters the absorber with a temperature much lower than the corresponding equilibrium temperature, as is the case of Islam [43], equilibrium at the vapor-liquid interface is established almost instantaneously thus providing large driving potential for absorption. As a result, the vapor absorption rate is very high near the entrance of the absorber. On the other hand, if the driving potential at the entrance is low, as in the case of the data of Nomoura et al. [75], the initial sharp rise of the vapor absorption rate is not observed and the local transfer coefficients decrease continuously across the tubes. There is reasonable agreement between the ‘extracted’ and ‘averaged’ values of the transfer coefficients as seen in Figures 3.24 and 3.25 for the same experimental conditions [43].

For the application of the simplified model it is necessary to input the transfer coefficients,  $k_{ef}$  and  $U_{bw}$ . Since the simplified model is developed in a tube-wise-modular manner in section 3.2.3, it is possible to include the tube-wise variation of the above transfer coefficients shown in Figures 3.24 and 3.25. Alternatively, the ‘averaged’ transfer coefficients indicated in the above figures, may be used following the practice in traditional heat exchanger design.

The effect of the above two choices on the predicted solution bulk temperature, concentration and the coolant temperature are shown in Figures 3.26, 3.27 and 3.28 respectively. The predictions of the numerical model and the simplified model agree well when the tube-wise variable transfer coefficients are used in the simplified model.

When the ‘averaged’ or constant transfer coefficients are used, the initial fluctuation in the solution temperature is damped due to the averaging of the transfer coefficients but the outlet solution temperature is predicted within about one degree. The predicted outlet concentration approaches the numerically obtained value towards the exit of the absorber when variable transfer coefficients are used. There is however, a significant deviation in the outlet concentration when ‘averaged’ transfer coefficients are used. As

seen in Figure 3.28 the predicted coolant temperature variation across the tubes is much less sensitive to the use of variable or ‘averaged’ transfer coefficients.

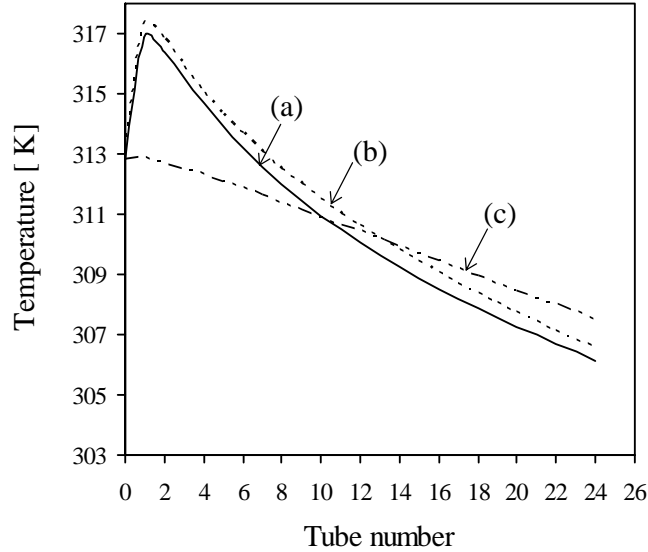


Fig. 3.26 Comparison of tube-wise bulk temperature of solution. Graphs: (a) (—) numerical model; (b) (---) simplified model with tube-wise variable transfer coefficients; (c) (-·-·-) simplified model with constant transfer coefficients; conditions:  $\Gamma = 0.0595 \text{ kgm}^{-1} \text{ s}^{-1}$ ,  $T_{si} = 39.8^{\circ}\text{C}$ ,  $w_{si} = 0.604$ ,  $WR = 1.0$  [43].

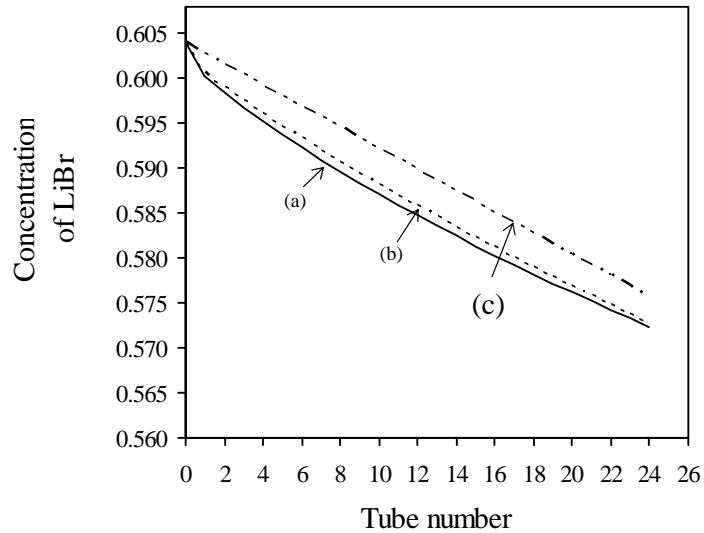


Fig. 3.27 Comparison of tube-wise bulk concentration of LiBr (%/100). Graphs: (a) (—) numerical model; (b) (---) simplified model with tube-wise variable transfer coefficient; (c) (-·-·-) simplified model with constant transfer coefficient; conditions:  $\Gamma = 0.0595 \text{ kgm}^{-1} \text{ s}^{-1}$ ,  $T_{si} = 39.8^{\circ}\text{C}$ ,  $w_{si} = 0.604$ ,  $WR = 1.0$  [43].

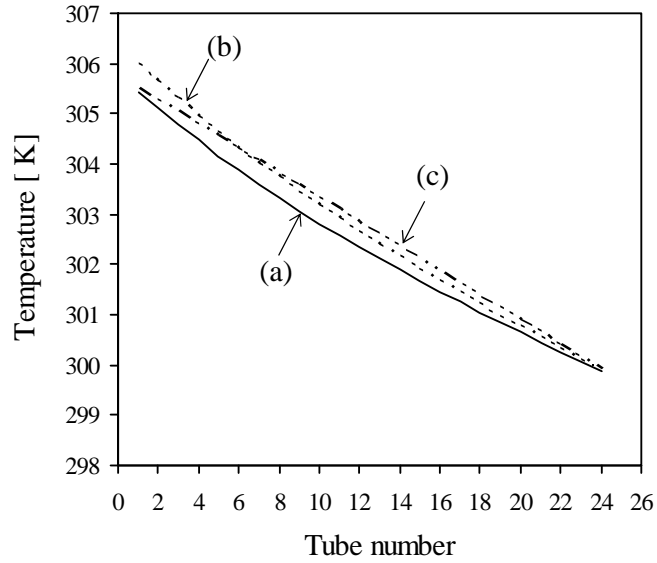


Fig. 3.28 Comparison of tube-wise coolant average temperature. Graphs: (a) (—) numerical model; (b) (---) simplified model with tube-wise variable transfer coefficient; (c) (-·-) simplified model with constant transfer coefficient; conditions:  $\Gamma = 0.0595 \text{ kgm}^{-1}\text{s}^{-1}$ ,  $T_{si} = 39.8^\circ\text{C}$ ,  $w_{si} = 0.604$ ,  $WR = 1.0$  [43].

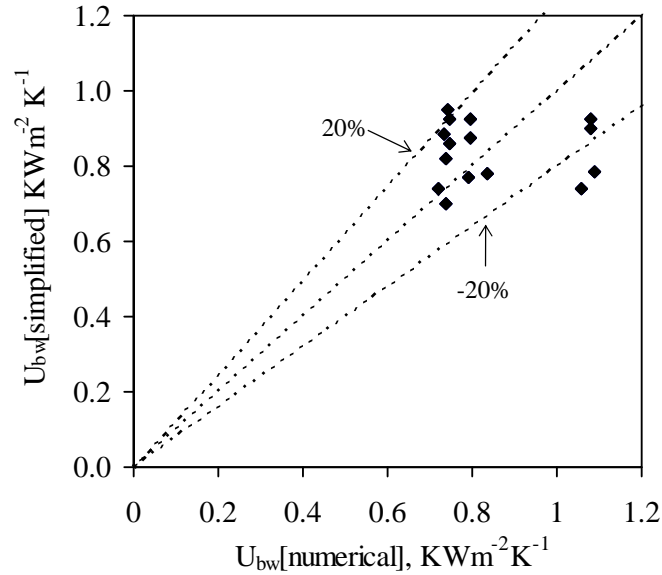


Fig. 3.29 Comparison of 'extracted' and 'averaged' overall heat transfer coefficients; experimental conditions of Islam [43].

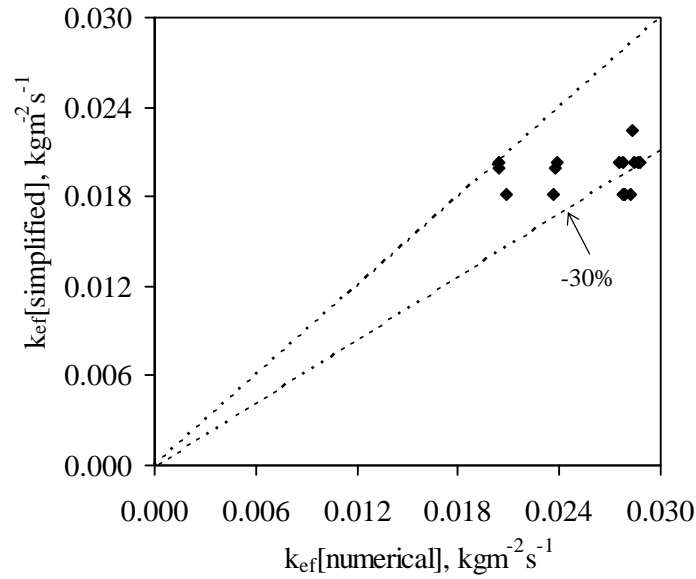


Fig. 3.30 Comparison of ‘extracted’ and ‘averaged’ effective mass transfer coefficients; experimental conditions of Islam [43].

One of the important applications of the simplified model is to extract the heat and mass transfer coefficients from experimental data for subsequent use in the design of absorbers. When the inlet and outlet values of the solution temperature, solution concentration and coolant temperature for an experimental test run are known, the inlet and outlet values of the driving potentials  $\phi$  and  $\psi$  can be calculated by substituting in Eq. (3.2.18). These values are then substituted in Eqs. (3.2.25) and (3.2.26) which are solved simultaneously to obtain the two transfer coefficients  $U_{bw}$  and  $k_{ef}$ . As these equations are non-linear, an iterative procedure has to be adopted for their solution.

The above procedure to extract  $U_{bw}$  and  $k_{ef}$  was applied to the experimental data of Islam [43], who tested an absorber with 24 horizontal tubes under a series of test conditions. The Reynolds number for the solution flow for all the test conditions were in the laminar flow regime. The average values of the transfer coefficients for the same test data were calculated using the numerical model which is applicable to laminar falling films. A comparison of the extracted and numerically computed transfer coefficients for

15 test runs is shown in Figures 3.29 and 3.30. For most of the data points the values of  $U_{bw}$  agree within about 20 percent while the average values of  $k_{ef}$  predicted by the numerical model are about 30 percent higher than the extracted values.

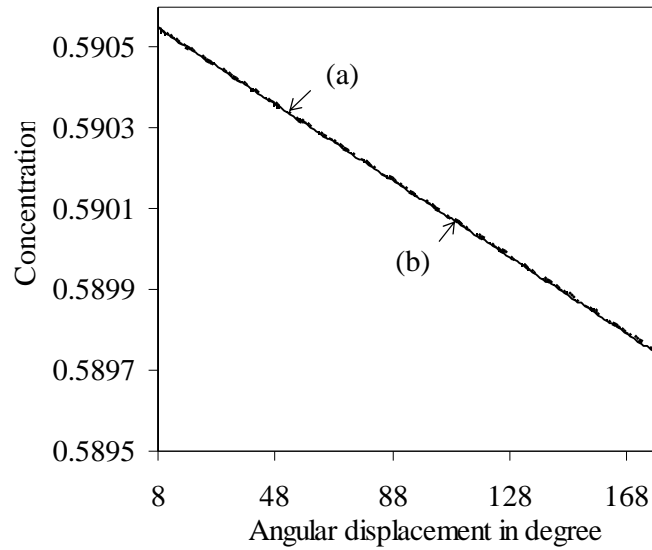


Fig. 3.31 Bulk concentration of LiBr changes over a tube. Graphs: (a) (—) simplified model with constant film thickness; (b) (---) simplified model with variable film thickness.

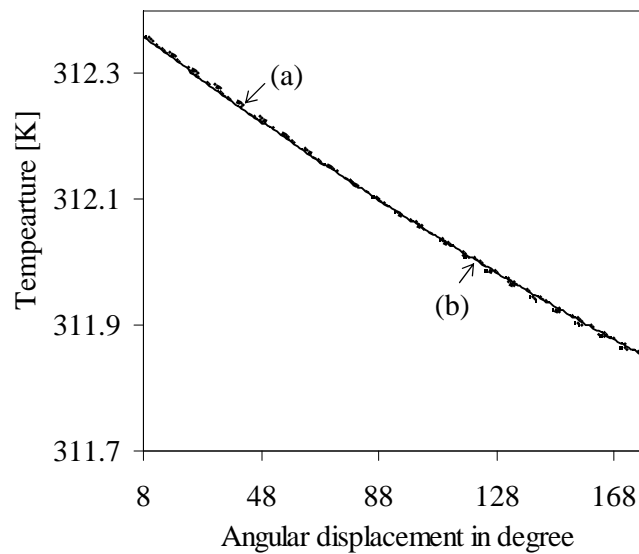


Fig. 3.32 Bulk temperature changes over a tube. Graphs: (a) (—) simplified model with constant film thickness; (b) (---) simplified model with variable film thickness.

### *Effect of liquid film thickness variation*

As was mentioned in section 3.2.1, the variation of the film thickness with angular position makes the governing equations Eq. (3.2.19) and (3.2.20) of the simplified model for a round tube non-linear. These equations were linearized by assuming an average film thickness, which lead to the analytical solutions given by Eq. (3.2.25) and (3.2.26). The effect of this assumption was investigated numerically solving the non-linear equations Eq. (3.2.19) and (3.2.20) using the Runge-Kutta method of solution. The variations of the predicted bulk solution concentration and temperature with angular position are shown in Figure 3.31 and 3.32 respectively. The differences in the predicted changes in concentration and temperature at the bottom of the tube by the non-linear and the linear forms of the simplified model are less than 0.1 percent.

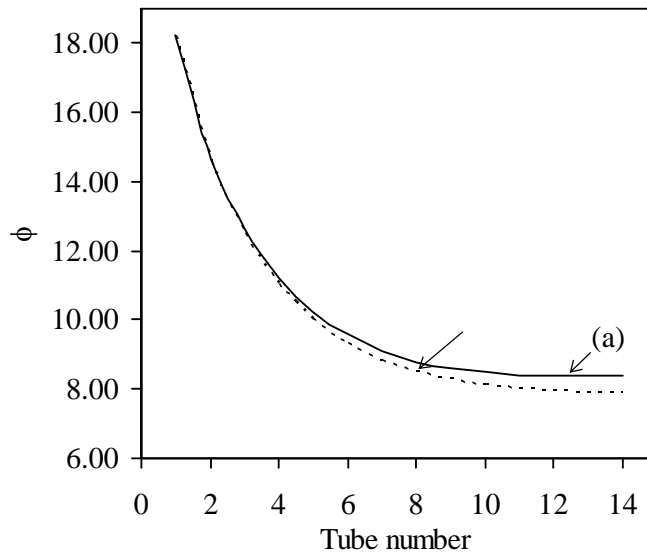


Fig. 3.33 Comparison of the driving potential  $\phi$  along the absorber. Graphs: (a) (—) simplified model with exact roots; (b) (---) simplified model with approximate roots; experimental conditions of Nomoura et al. [75].

### *Effect of approximate exponents*

The exponents  $\alpha_1$  and  $\alpha_2$  that occur in the development of the simplified model were approximated by more convenient expressions given by Eqs. (3.2.91) and (3.2.92). This

approximation was possible because for all experimental conditions considered in the present study, one of the roots of the characteristic equation Eq. (3.2.27) was much larger than the other root, typical values for a round tube absorber being -0.18 and -0.0026. The variation of the driving potentials  $\phi$  and  $\psi$ , predicted by using the approximate expressions is shown in Figures 3.33 and 3.34 respectively. There is good agreement between the exact and approximate distributions. The initial steep slope in the variations of  $\phi$  and  $\psi$  near the entrance of the absorber is governed by the larger exponent given by Eq. (3.2.91) whose contribution diminishes rapidly. The variation of the driving potentials thereafter is controlled by the smaller exponent given by Eq. (3.2.92).

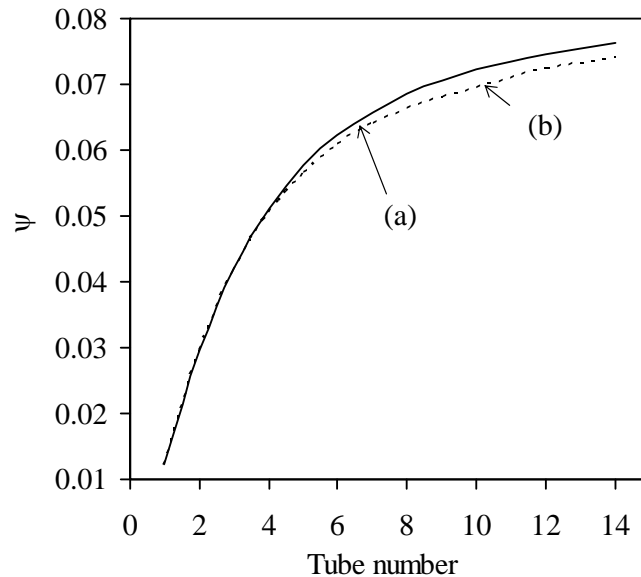


Fig. 3.34 Comparison of the driving potential  $\psi$  along the absorber. Graphs:(a) (—) simplified model with exact roots; (b) (---) simplified model with approximate roots; experimental conditions of Nomoura et al. [75].

### *Effect of wetting ratio*

The simulation results obtained from both simplified and numerical models using different wetting ratios of the tubes are presented in Figures 3.35-3.36. The contribution of inter-tube flow was not included in the simulations. The predictions using constant wetting ratios of 1.0, 0.8 were compared with those obtained with an experimentally-

determined variable wetting ratio [75]. Variable wetting ratios for successive absorber tubes can be conveniently included in the simulation because of the tube-wise modular nature of the model presented in section 3.2.3.

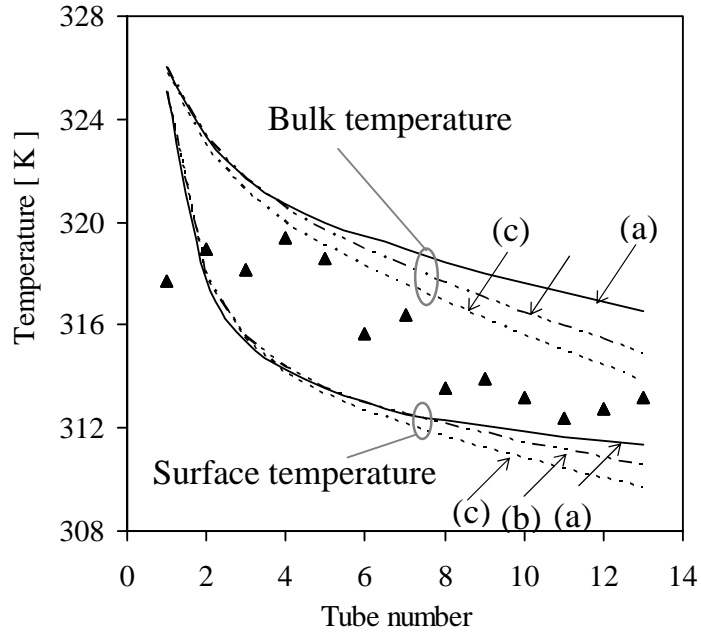


Fig. 3.35 Comparison of tube-wise averaged bulk temperature and tube surface temperature at the top of a tube by the numerical model without inter-tube absorption. Graphs: (a) (—) variable wetting ratio from Nomoura et al. [75]; (b) (---) wetting ratio 0.8; (c) (- -) wetting ratio 1.0; (▲) tube surface temperature from the experiment of Nomoura et al. [75]; conditions:  $\Gamma = 0.058 \text{ kgm}^{-1} \text{ s}^{-1}$ ,  $T_{si} = 54^\circ\text{C}$ ,  $w_{si} = 0.62$ .

The results from the numerical model and the simplified model shown in Figure 3.35 and 3.36 indicate that the predicted drop in the tube-wise averaged bulk solution temperature and the tube surface temperature at the top of a tube increases with the wetting ratio. This is to be expected because a lower wetting ratio results in a shorter effective length of the absorber tube and a thicker liquid film for the same total flow rate of liquid. These result in a diminished area for vapour absorption and a larger resistance to heat flow across the film. The numerical model predicts a larger effect of the wetting ratio on the temperature distribution compared to the simplified model. This is



presumably due to the averaging effect that results from the use of transfer coefficients in the simplified model which, however, are obtained from the numerical simulation.

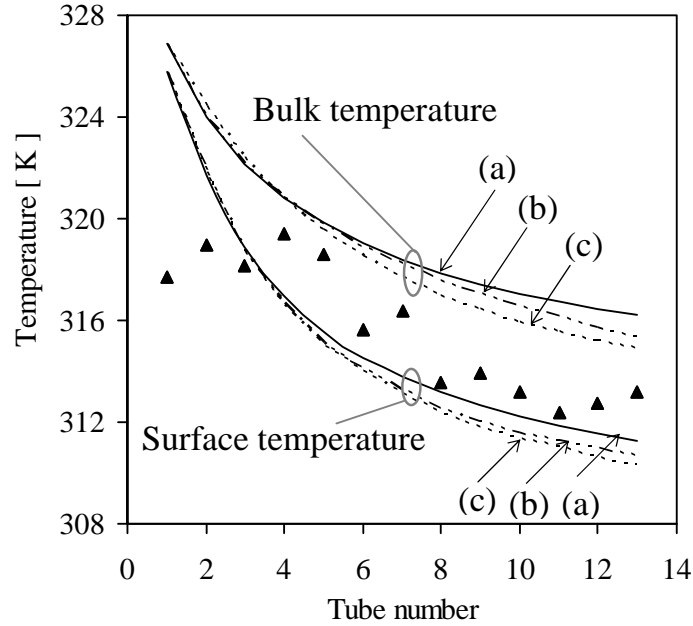


Fig. 3.36 Comparison of tube-wise averaged bulk temperature and tube surface temperature at the top of a tube by the simplified model without inter-tube absorption. Graphs: (a) (—) variable wetting ratio from Nomoura et al. [75]; (b) (-·-·-) wetting ratio 0.8; (c) (- - -) wetting ratio 1.0; (▲) tube surface temperature from the experiment of Nomoura et al. [75]; conditions:  $\Gamma = 0.058 \text{ kgm}^{-1} \text{ s}^{-1}$ ,  $T_{si} = 54^\circ \text{C}$ ,  $w_{si} = 0.62$ .

The effect of the wetting ratio is less pronounced in the first few tubes of the absorber where the wetting ratio is about 70 to 80 percent [75]. However, in the rest of the absorber the effect of wetting ratio is very significant because of its large decrease. The experimental results of Nomoura et al. [75] for the tube surface temperature measured at the top of each tube are also plotted in Figures 3.35 and 3.36. For both models, the simulation results with a variable wetting ratio are closer to the experimental data.

### 3.3 Summary

The development of a detailed numerical model of horizontal tubular absorber, incorporating the curvature effects of the absorber tubes, was presented in this chapter. The single round tube model was developed first which was later extended for the bank of absorber tubes with serpentine coolant flow through the tubes. Models were also developed for the simplified geometry of horizontal tubular absorber such as segmented flat plate and vertical plate absorber. Model comparisons were made. Later, a simplified coupled heat and mass transfer model of the horizontal tubular absorber was presented which also incorporated the tubular effects of absorber tubes with serpentine flow of coolant and inter-tube absorption. The transfer coefficients required as an input to the simplified coupled model were determined from the previously developed detailed numerical model. The simulation data were obtained from both detailed numerical model and simplified coupled model under known operating conditions of the tubular absorbers taken from prominent literatures. The predictions of the simplified coupled model agreed well with the results obtained from detailed numerical model especially when tube-wise variable transfer coefficients were used. Furthermore, the usefulness of the simplified coupled model as a design tool was demonstrated by extracting the transfer coefficients for heat and mass transfer of horizontal tubular absorber for sets of actual operating conditions. The experimental results for a horizontal tube-bundle absorber of Nomoura et al. [75] were used to compare with results predicted by the models developed in this study. Good agreement was found especially when idealized inter-tube drop flow was incorporated to the models. Partial wetting of the absorber tubes by the solution showed marked effect on the predictions of the models.

## **CHAPTER 4**

### **EXPERIMENTAL STUDIES**

Experimental investigations were undertaken to obtain the hydrodynamic data of various inter-tube flow modes. The range of the experiments covers the inter-tube flow studies at various flow rates and tube spacing using water and aqueous solution of Lithium Bromide as the working fluid. The test set-up was designed and fabricated in a manner that would allow the testing of different tubular configurations of the absorber. Provision was made in the design to permit flow visualization from all available positions. The experimental program including the design and construction of the test set-up, the instrumentation and the measurement is presented in this chapter. The data analysis methodology for the extraction of hydrodynamic data is also presented. Since the main purpose of the experimental arrangement is to obtain data on inter-tube flow hydrodynamics, no provisions were made for heat and mass transfer studies.

#### **4.1 Description of the test rig**

A schematic diagram and a photograph of the experimental test-rig are shown in Figure 4.1 and 4.2, respectively. The main components of the experimental test-rig are the test section, solution pump, flow meter, flow control valve and reservoir. The test section consists of 6 rows of horizontal tubes assembled in a single column. The liquid is distributed onto the topmost tube from a distributor so that a thin film of solution flows down along both sides of the test tubes. In between two consecutive tubes, the inter-tube flow pattern is varied depending on the solution flow rate. After leaving the test section and passing through an intermediate collector the solution is stored in a reservoir. The solution is pumped out from the reservoir using a positive displacement pump. The pump adds the sufficient pressure to the liquid so that it can reach the flow distributor in

the test section to complete the cycle. A flow control valve and a volume flow meter helps to maintain the desired solution flow rate.

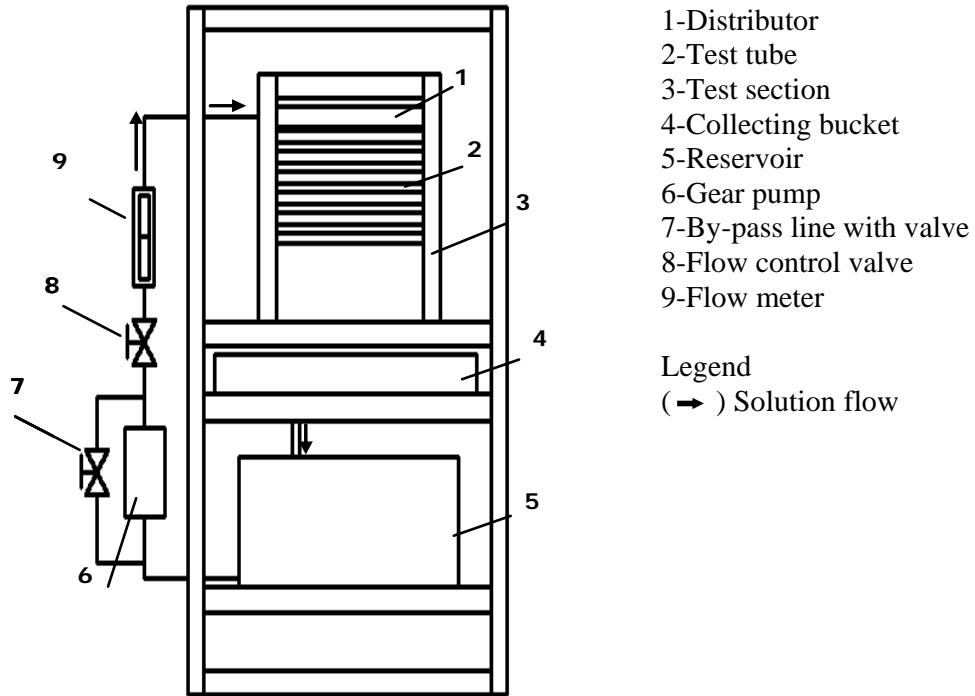


Figure 4.1 Schematic diagram of experimental set-up.

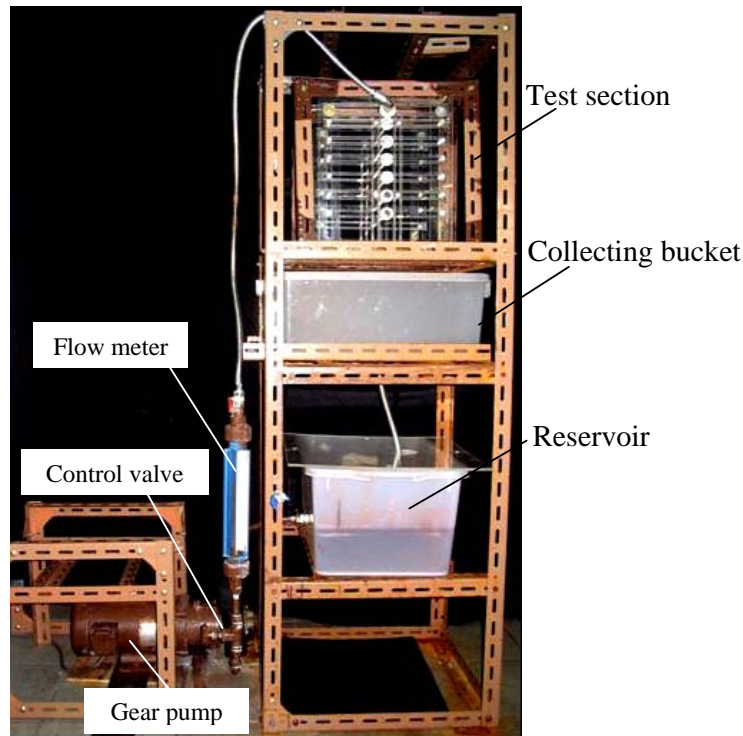


Figure 4.2 Photograph of the experimental set-up.

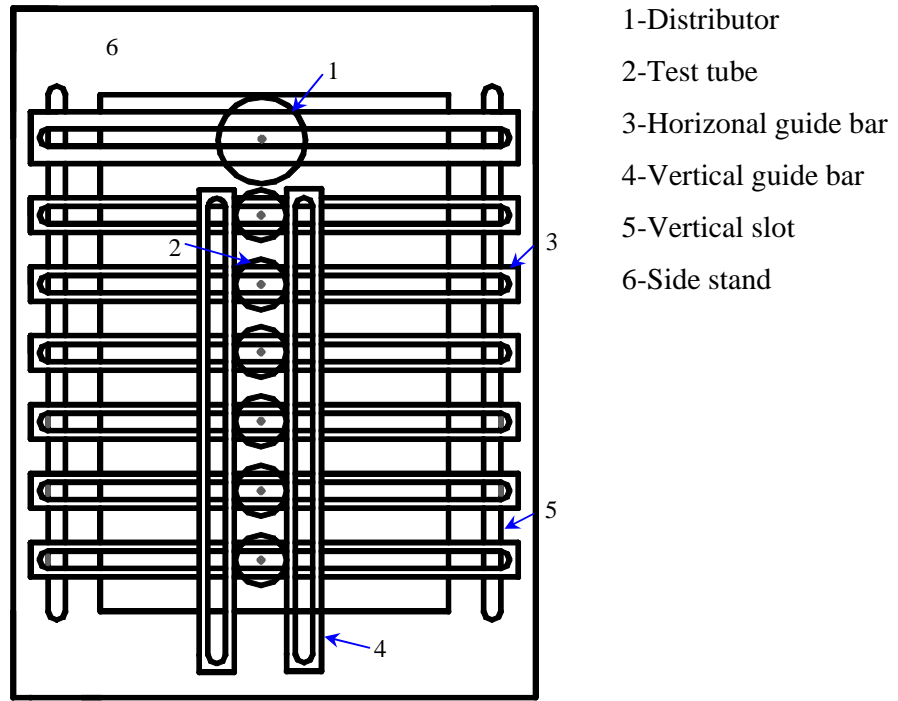


Figure 4.3 Schematic diagram of the test section side view.

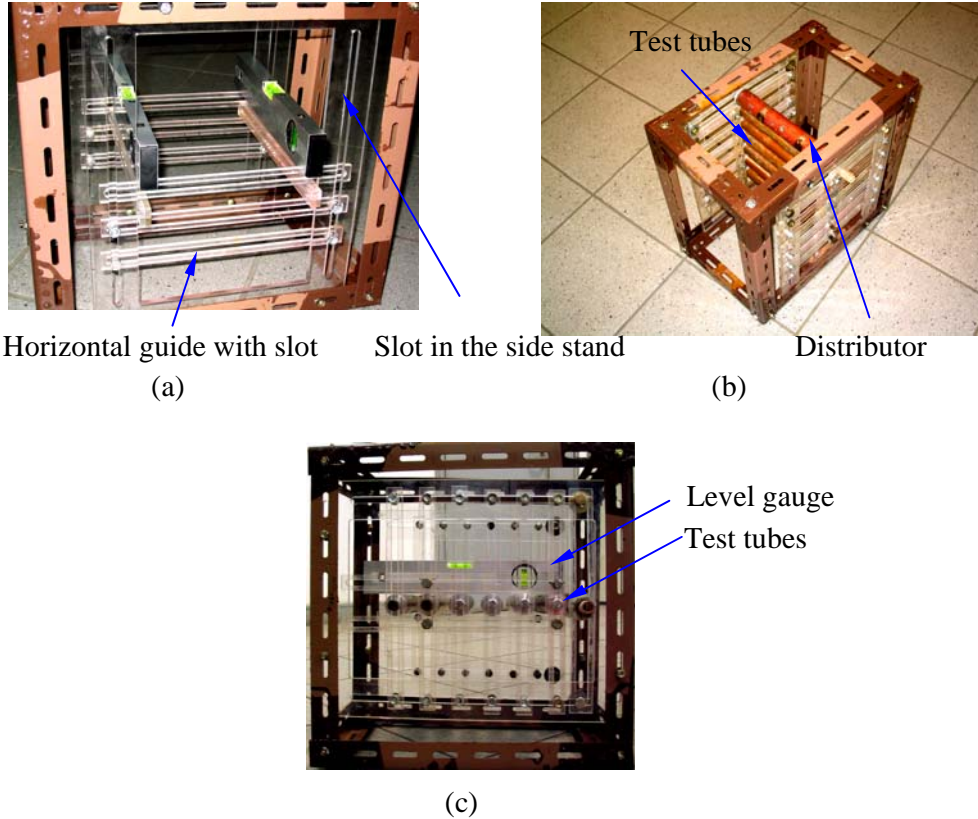


Figure 4.4(a) Assembly of the guide bar, (b) Complete assembly of the structure, (c) Testing of vertical alignment of the tube array.

### 4.1.1 Test section

The main objective of this experiment was to study the inter-tube flow hydrodynamics at different tube gaps and solution flow rates. The range of tube gap is specified in Table 4.1. To accommodate the variable tube gap, the test section was designed to provide both the horizontal and vertical movement of the test tubes. Moreover, for the ease of flow visualization, viewing windows were provided in the front and the sides of the test section.

The components of the test section are shown schematically in Figure 4.3. The figure represents a side view of the test tube assembly. The main components are: (i) side stands (ii) horizontal guide bars (iii) vertical guide bars (iv) test tubes and (v) flow distributor. The side stands and the guide bars are made of Perspex as shown in Figure 4.4. The vertical slots in the side stands help to support the horizontal guide bars to carry the test tubes from both sides. The distance between the horizontal guides is determined based on the required gap between two consecutive tubes as explained in Figure 4.5. The purpose of the long slot in each horizontal guide bar is to allow the test tubes to be fixed with screws in the gap. All the horizontal guide bars are identical except for the bars carrying the liquid distributor. The slot in the two uppermost horizontal guide bars is of a different size depending on the size of the inner tube of the distributor as shown Figure 4.3.

### 4.1.2 Flow distributor

In order to design a suitable flow distributor, various arrangements used by previous researchers were considered. After testing several proposals, the design of Killion and Garimella [52] was chosen with minor changes to ensure uniform distribution of liquid. The present flow distributor consists of two concentric annular tubes with equally spaced holes drilled in a single row in each tube. The holes of the inner tubes are positioned

upward while those of the outer tube are positioned downward. The annular space between the tubes, number of holes and the distance between two consecutive holes were determined by trial and error. The detailed drawing of the distributor is given in Appendix D.

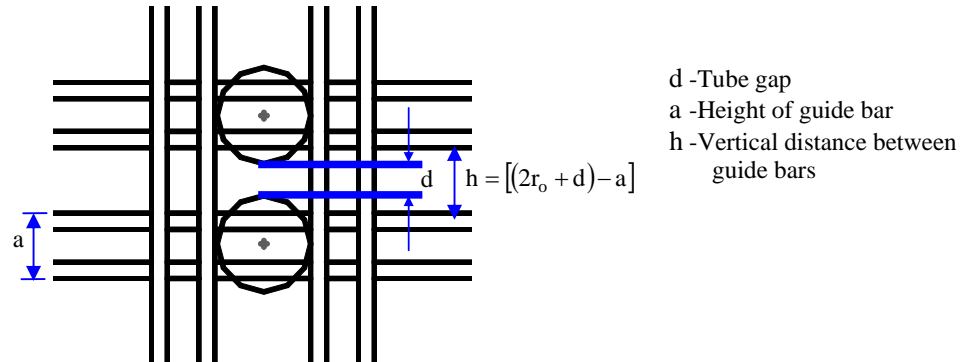


Figure 4.5 Distance between two horizontal guide bars.

#### 4.1.3 Test tubes

Six horizontal copper tubes of outer diameter 22 mm and length 240 mm are used in the present experimental investigation. The test tubes are supported from both sides in the tube bank as described in the previous section. From each side, flat aluminum bars with a threaded center hole is pressed into the hollow copper tube so that the tube can be fixed with the horizontal guide bars using screws. Detailed drawings of the test tubes are provided in Appendix-D. The test tubes were sufficiently rigid when they were fixed from both sides and also it was easy to maintain the horizontal alignment.

#### 4.1.4 Flow circuit

The solution flow circuit is shown schematically in Figure 4.1. The solution is pumped from the storage reservoir to the distributor at the top of the test section through a flow meter and a control valve. The solution flowing over the six horizontal tubes is collected

at the bottom of the test section and then transferred to the storage reservoir by gravity, thus completing the cycle.

#### **4.1.5 Liquid pump**

The type of liquid pump used in the present experiment is a magnetic gear pump which is suitable for pumping aqueous Lithium-bromide to be used as the working fluid. The capacity of the pump is  $0.36 \text{ m}^3/\text{h}$  with a maximum differential pressure of 16.63 kPa. The pump works with a by-pass connection including a control valve as shown in Figures 4.1-4.2.

#### **4.1.6 Working fluid**

Both the aqueous lithium bromide of 54 percent concentration by weight and water are used as working fluids in the present experiment. However, all the experimental data were recorded using aqueous lithium bromide as the working fluid. Water was used mainly for exploratory tests to ensure the proper functioning of the experimental system. The thermo-physical properties of aqueous lithium bromide of 54 percent concentration are obtained from the property charts available in published data sources [9]. The thermo-physical properties of LiBr solution are given in Table 4.2.

#### **4.2 Alignment testing**

For the gravity driven flow, it is essential to have all the test tubes in a vertical plane. The alignment of the horizontal guide bars was tested with level gauges during assembly. After fixing the side stands to the walls of the test section, the vertical distance between two horizontal guide bars was calculated to obtain the desired tube spacing. The distance between the two horizontal bars was calculated from the simple relation as shown in Figure 4.5. For  $N$  tubes ( $N=6$  in this study),  $2N$  bars were needed. At each step, 2 guide bars were fixed with the stand using screws after ensuring the perfect horizontality with the level gauges as shown in Figure 4.4(a). Since the bars were



sufficiently long, two gauges were needed simultaneously. When both the gauge indicated horizontal alignment, the screws were tightened. This procedure was repeated until all the bars were correctly aligned. The test tubes were then fixed with screws to the slots of the guide bars. To ensure the vertical alignment of the tubes, all the tubes in a column must be on the same vertical plane. For this purpose, the use of the vertical bars, similar to the horizontal guide bars from both sides of the tubes became very effective as shown in Figure 4.3. The orientation of the vertical bars was tested with the tri-squares. Finally, the test section was positioned in such way that the level gauge could be used to check the horizontal level of the vertical plane of the tube array as demonstrated in Figure 4.4(c). Both the horizontal and the vertical alignments of the tubes were tested before the experiment and often during running the experiments if necessary.

**Table 4.1 Operating conditions**

Tube size	D = 22mm L = 24cm
Tube spacing	6,10,15 mm
Working fluid	Water, Aqueous LiBr (54% wt concentration)
Flow rate	0.42 to 1.65 Lpm
Operating pressure in the test section	Atmospheric pressure
Operating temperature of solution	20-22 °C

**Table 4.2 Working fluid properties**

$\rho$ $kg.m^{-3}$	$\sigma$ $N.m^{-1}$	$\mu$ $kg.m^{-2}s^{-1}$	$Ga = \frac{\rho\sigma^3}{g\mu^4}$	$Ga^{1/4}$
1600	9.1E-02	4.8E-03	2.31E+08	123

**Table 4.3 Camera specification**

Video camera	Model number	Resolution	Frame speed
	CANON MVX35i	2.0Mpixels	30 ms

### **4.3 Measuring Equipment**

The following sections contain description of the measuring equipment used in the present experimental study.

#### **4.3.1 Flow meter**

A rotameter was used to measure the volume flow rate of both water and aqueous solution of LiBr as the working fluid. The measuring range of the rotameter is 0.4 to 4.5 Lpm. The liquid flow rate was controlled by a globe valve installed upstream of the flow meter as shown in Figures 4.1 and 4.2. For the two working fluids, the flow meter was calibrated separately measuring the liquid mass flow in specific time period. The calibration charts are provided in Appendix D.

#### **4.3.2 Video camera**

To capture the various inter-tube flow patterns at different operating conditions, a Digital Video Camera was used. The type of camera is CANON MVX35i with the frame speed of 30 per second. The specifications are listed in Table 4.3. The camera can be operated from different viewing angles including the frontal views of the tube array as well as the side views. For improved visualization, colored side screen and illuminating lights were used during video recording of the events.

#### **4.3.3 Image grabbing software**

Video Frame Capture software was used to obtain the frame-by-frame images. This software is operated within the frame speed limit of the video camera used.

#### **4.3.4 Analyzing software**

The image analysis software, MATROX INSPECTOR was used to perform the measurement of droplet and jet profiles from the sequential video images. The profiles of the droplets and jets were determined employing a manual edge detection process which is described in section 4.6.

#### 4.4 Instrumentation

Before starting a test run of the experiments, the tubes were thoroughly cleaned with sand paper. This ensures better wetting of the tubes. During any operating condition, the test tubes were arranged with the required tube spacing. The liquid was introduced onto the topmost tube from the distributor with a sufficiently high flow rate to ensure proper wetting of the tubes. The flow rate was controlled by the valve and measured with the flow meter. After ensuring proper wetting of the tubes, the flow rate was gradually decreased and set at the desired value. The change of inter-tube flow modes was observed and verified to the flow regime map available in the literature [39]. After the flow became steady with the desired flow mode at a particular flow rate, video recording of inter-tube events was carried out from different viewing positions.

#### 4.5 Inter-tube flow hydrodynamics

The experimental set-up described above was used to obtain the inter-tube flow hydrodynamics data. Previously similar experiments performed by Hu and Jacobi [39] helped them to develop a simplified flow regime map for the inter-tube flow modes. Neglecting the effect of hysteresis, the correlations developed by them [39] for the different flow modes transitions are;

$$\begin{array}{l} \text{Droplet/droplet-jet} \\ \text{Or} \\ \text{Droplet-jet/droplet} \end{array} \quad \text{Re} = 0.074Ga^{0.302} \quad (4.1)$$

$$\begin{array}{l} \text{Droplet-jet/jet} \\ \text{Or} \\ \text{Jet/droplet-jet} \end{array} \quad \text{Re} = 0.096Ga^{0.301} \quad (4.2)$$

$$\begin{array}{l} \text{Jet/jet-sheet} \\ \text{Or} \\ \text{Jet-sheet/jet} \end{array} \quad \text{Re} = 1.414Ga^{0.233} \quad (4.3)$$

The aim of the current experiments, however, is not entirely to find out the mode transition flow rates. The above relations are used as a guide to achieve the flow mode transitions with changes in the solution flow rate. For this purpose, before taking experimental data, the inter-tube flow modes are verified with the flow regime map given by Hu and Jacobi [39]. For the current working fluid, the transition Re is calculated first based on the developed correlations stated above whose values are given in Table 4.4. For example, when the flow Reynolds number is less than 24.83, the desired flow mode is the droplet mode. For Re number greater than 24.83 but less than 36.86, the desired mode is the mixed flow or the droplet-jet flow mode. When the Re number is greater than 36.86 but lower than 125.6, a jet flow mode is expected. For Re number greater than 125.6, the flow mode is changed to jet-sheet mode. However for practical tubular absorbers, Re greater than 125.6 may not be desirable since the waves and turbulence in the falling film flow may be created at higher flow rate.






**Table 4.4 Transition film Reynolds number for 54% wt concentration LiBr solution**

Transitions	Re
Droplet/droplet-jet	24.83
Droplet-jet/jet	36.86
Jet/jet-sheet	125.65





The observations of flow modes at different solution flow rates are summarized in Table 4.5-4.6. Observations were made based on the flow pattern in the gap between the 2<sup>nd</sup> and 3<sup>rd</sup> tubes. The authors, Hu and Jacobi [39] concluded that the tube diameter and the spacing between the tubes were not significant in the flow mode transitions. Hence the developed correlations pertained only to the Re and Ga of the working fluid. Based on their discussion, the same correlations are used to compare the flow modes at different tube spacing studied in the current experiment. The results given in Tables 4.5 and 4.6

indicate that the observed flow patterns are more or less similar to the theoretical flow patterns at various flow rates and tube spacing configurations.

**Table 4.5 Experimental observations-1; Tube gap: 10mm; wetted length: 21cm**

Flow rate $kg.s^{-1}$	$\Gamma$ $kg.m^{-1}s^{-1}$	Re	Status	Theoretical regime	Actual observation
0.0227	0.0542	45.19	$36.86 < Re < 125.6$	Jets	Jets 
0.0191	0.0457	38.08	$36.86 < Re < 125.6$	Jets	Droplet/jets 
0.0145	0.0346	28.85	$24.83 < Re < 36.86$	Droplet/jets	Droplet/jets 
0.0118	0.0282	23.52	$Re < 24.83$	Droplets	Droplets 
0.0079	0.0188	15.71	$Re < 24.83$	Droplets	Droplets 

**Table 4.6 Experimental observations-2; Tube gap: 6mm; wetted length: 20 cm**

Flow rate $kg.s^{-1}$	$\Gamma$ $kg.m^{-1}.s^{-1}$	Re	Status	Theoretical regime	Actual observation
0.0227	0.0569	47.44	$36.86 < Re < 125.6$	Jets	Jets 
0.0213	0.0533	44.46	$36.86 < Re < 125.6$	Jets	Jets 
0.0188	0.0471	39.24	$36.86 < Re < 125.6$	Jets	Droplet/jets 
0.0163	0.0408	34.02	$24.83 < Re < 36.86$	Droplets/jets	Droplets/jets 
0.0129	0.0323	26.93	$24.83 < Re < 36.86$	Droplets/jets	Droplets/jets 
0.0109	0.0274	22.83	$Re < 24.83$	Droplets	Droplets 
0.0077	0.0193	16.12	$Re < 24.83$	Droplets	Droplets 

The above observations may not produce similar results if a gap between the lower tubes e.g. gap between the 3<sup>rd</sup> and 4<sup>th</sup> or 4<sup>th</sup> and 5<sup>th</sup> is selected. It has been observed throughout

the experiment that, the topmost tube shows most uniform distribution of flow which is the nearest to the flow distributor as shown in Figure 4.6 (a) and (b). That is why the flow pattern between the 1<sup>st</sup> and 2<sup>nd</sup> tubes will not be representative of the average flow pattern. The current observations were mostly based on the 2<sup>nd</sup> and the 3<sup>rd</sup> tube gap. The gap between the other lower tubes may also not exhibit average flow pattern because of the following reasons. The deviations of the flow modes at several tube gaps under the same configuration could occur due to the gradual decrease of wetted surface as the flow progresses downwards as also demonstrated by Nomoura et al. [75]. Decrease of wetted surface increases the flow rate per unit length of the tube. Eventually the flow Re will increase and possibly exhibit slightly different flow regimes in the subsequent tube gaps.

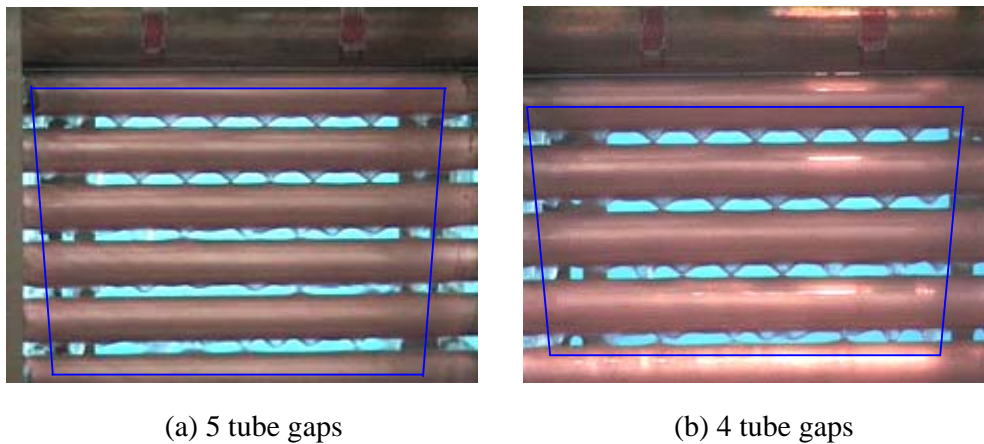


Figure 4.6 Change in wetted length of the tubes as the flow progresses.

However, from present observations, the change in wetted length of the tubes did not vary so much as shown in Figure 4.6 (a) and (b). Based on that, the flow pattern at the lowermost tube gaps may not deviate much from the theoretical flow pattern at a particular flow rate situation. This is probably due to the proper distribution of liquid over the tubes. Nevertheless use of more tubes in the same column could help to show the decrease in wetted length more clearly, similar to the observations of Nomoura et al. [75]. The present experiment was restricted to using six tubes mostly.

**Table 4.7 Drop/jet spacing calculated from video images; Tube gap: 10mm**

Flow rate [ $kg.s^{-1}$ ]	Tube length in each image [ $m$ ]	No of droplet stations	Spacing between drops/jets $\lambda$ [m]
0.0145	0.120	6	0.02
0.0118	0.147	7	0.021
0.0079	0.142	6	0.0236

**Table 4.8 Drop/jet spacing calculated from video images; Tube gap: 6 mm**

Flow rate [ $kg.s^{-1}$ ]	Tube length in each image [ $m$ ]	No of droplet stations	Spacing between drops/jets $\lambda$ [m]
0.0147	0.134	6	0.022
0.0109	0.139	6	0.023
0.0077	0.138	5	0.0236

#### 4.5.1 Spacing between the droplets and jets

In their work on the measurement of departure site spacing of the droplet and jet along a tube, Hu and Jacobi [40] proposed a correlation believed to be an improved version by taking into consideration the tube spacing and flow rate effects which were absent in previous correlations developed by others. The correlation is stated below:

$$\lambda = \frac{0.836A - 0.863 \text{Re} / Ga^{1/4}}{\left\{ 1 + \left( \frac{0.836A - 0.863 \text{Re} / Ga^{1/4}}{0.75A - 85 / Ga^{1/4}} \right)^2 \right\}^{1/2}} \quad \text{where} \quad A = \frac{2\pi\sqrt{3}}{\sqrt{1 + \frac{2}{(d/\sqrt{\sigma/\rho g})^2}}} \quad (4.4)$$



Similar measurements were performed from the video images of present experimental conditions which are tabulated in Tables 4.7 and 4.8 for two tube gap situations. At first the number of droplet or jet generating locations was counted over a series of sequential video images. The number of generating locations remains more or less constant over a certain period of time. Afterward the tube length of each image was measured and divided by the number of generating locations. The result was the possible measurement of the spacing between two consecutive droplets or jets. Instead of using the above mentioned correlation Eq. (4.4), the data given in Tables 4.7 and 4.8 is used in the inter-tube absorption models stated in chapter 6.

#### **4.6 Analysis of experimental data**

In this section, the data analysis methodology is discussed for the measurement of transient volume and surface area of the droplets. The transient volume and surface area of each droplet from the sequential video images were measured with the help of the image analysis program described here. The present image analysis program is based upon the manual edge detection process. As suggested by Killion and Garimella [53], detection of droplet edges relying on human eyes to regenerate the droplet profiles from the video images is a simple technique of edge detection. However the accuracy of such manual edge detection process greatly depends on image quality for which more discussions are available in Appendix B. The procedure is described below.

At each operating condition, the video recording of the inter-tube flow patterns were accomplished with a digital video camera. The sequential video images were obtained at the frame speed of 30 per second with the help of an image grabbing software. In order to determine the shape of the droplets from the video images, co-ordinate points on the droplet profile were selected with the help of image analysis software. These co-ordinates were used to obtain the best-fit polynomial for the droplet profile. Due to the often irregular shape of the droplet, an approximate polynomial profile was found to be

satisfactory. Choosing an axis of symmetry preferably at the centre of the droplet, the axi-symmetric droplet volume and surface area were calculated as discussed in section 3.2.2.3. A program written in COMPAQ VISUAL FORTRAN is used where the best polynomial fit was found out for the respective profile of the droplet, so as the volume and surface area. The procedure was repeated for each of the droplet generating locations within the same time period. The complete experimental program in conjunction with the output of data analysis program is schematically expressed in Figure 4.7.

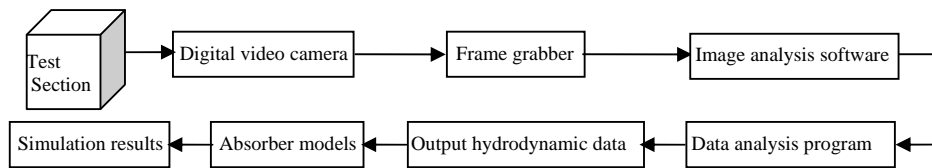


Figure 4.7 Flow diagram of the experimental program.

The development of the transient volume and surface area profiles at each of the droplet generating locations were based on several assumptions mainly due to the flow randomness involved. These are;

- The number of droplet generating sites remains constant during a particular time period.
- The shift of the centre of the droplet is relatively small.

The above assumptions were based upon the experimental observation data presented in the next chapter. During extraction of the hydrodynamic data from the images, focus was given on each consistent droplet generating site. Visually observing a set of sequential video images, the number of consistent droplet generating sites was determined. Droplets which originated in between two distinct droplet sites but did not

go through the entire droplet cycle were not included in the total number of distinct droplet sites.

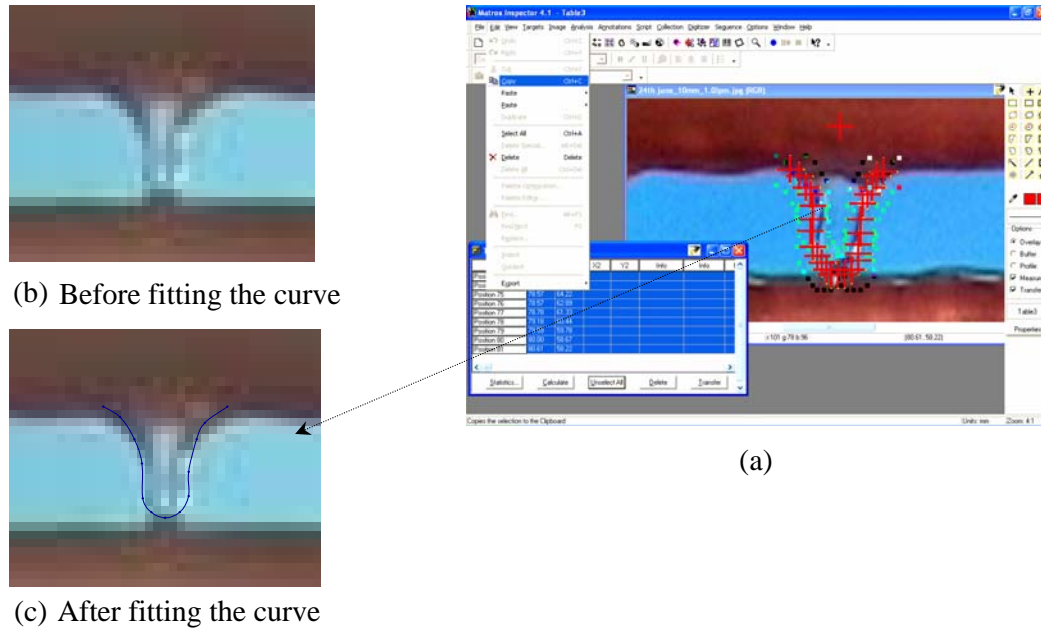


Figure 4.8 Use of image analysis program.

In Figure 4.8, the use of the image analysis program Matrox Inspector is pictorially documented. Samples images are used as examples to show the measurement from one of the several frames in fixed time period. The manual edge detection process for a particular droplet is explained in Figure 4.8(a) by clicking the edges of the droplet profile. The generated profile is then superimposed to the original image as shown in Figure 4.8(c). The best fitted superimposed profile to the original profile is found reasonable comparing the Figures 4.8(b) and 4.8(c). The uncertainty involved during manual edge detection process is discussed in details in appendix B. In Appendix B, a comparison was made between the manual edge detection and a semi-automated edge detection process in terms of accuracy. It was found that the accuracy of manual edge detection process greatly improved for higher resolution image.

**4.7 Summary**

The detailed experimental program for the study of inter-tube flow hydrodynamics was described in this chapter. The design and fabrication details of the test set-up were highlighted and discussed. The inter-tube flow patterns captured on the video camera were compared to the theoretical flow patterns at various operating conditions. The data analysis methodology for the quantitative measurements from the digital video images was provided. The manual edge detection image analysis program was described. Both the qualitative and quantitative experimental data will be discussed in the next chapter based on the image analysis program described here.

## **CHAPTER 5**

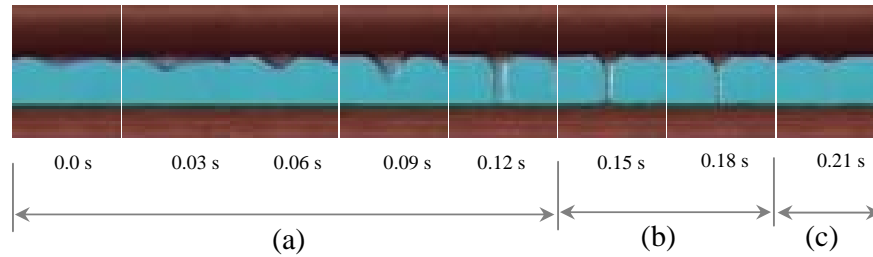
### **RESULTS AND DISCUSSION: INTER-TUBE FLOW**

The results obtained from the experimental investigation of inter-tube flow hydrodynamics are presented in this chapter. For three different tube-gap-configurations, video recordings of the inter-tube flow phenomena were accomplished at various solution flow rates. The tube gaps were 6, 10 and 15 mm while the flow rate varied from 0.42 to 1.65 Lpm for each of the tube-gap-configurations. The experimental results obtained for 15 mm tube-gap-configuration are described qualitatively while the experimental results obtained for 6 mm and 10 mm tube-gap-configurations are discussed in detail both qualitatively and quantitatively. In most of the practical tubular absorbers, the gap between the tubes is about 6 mm [24, 37, 44, 75]. Hence the inter-tube flow hydrodynamics data were obtained for this design configuration of the tubular absorber. Besides this, tube gaps of 10 mm and 15 mm were selected to observe the effect of varying tube gap on the inter-tube flow behaviour and to achieve better flow visualization.

#### **5.1 Tube-gap-configuration at 15 mm**

The following discussion is based on the sequential video images obtained at 15 mm tube gap configuration. At lower flow rates, the inter-tube flow generally takes the form of droplet flow which has been discussed in section 4.5. Under this circumstance, droplets are repeatedly generated from several locations along the tube. The frame-by-frame video images help to illustrate the evolution of droplet cycles and the stages involved in each cycle. Before considering the details of how these droplets are distributed at several locations, a few close-up images of a typical droplet growth are presented in Figure 5.1. Each droplet cycle consists of three distinct stages as indicated

in the figure. During the development stage, the mass of the droplet starts increasing until the droplet touches the tube surface below.



- a) Development stage [0-0.12 sec]
- b) Bridge formation stage [0.12-0.18 sec]
- c) Pull back stage after break up [0.18-0.21 sec]

Figure 5.1 A typical droplet cycle [images are taken at solution flow rate  $0.0079 \text{ kg}\cdot\text{s}^{-1}$ ]

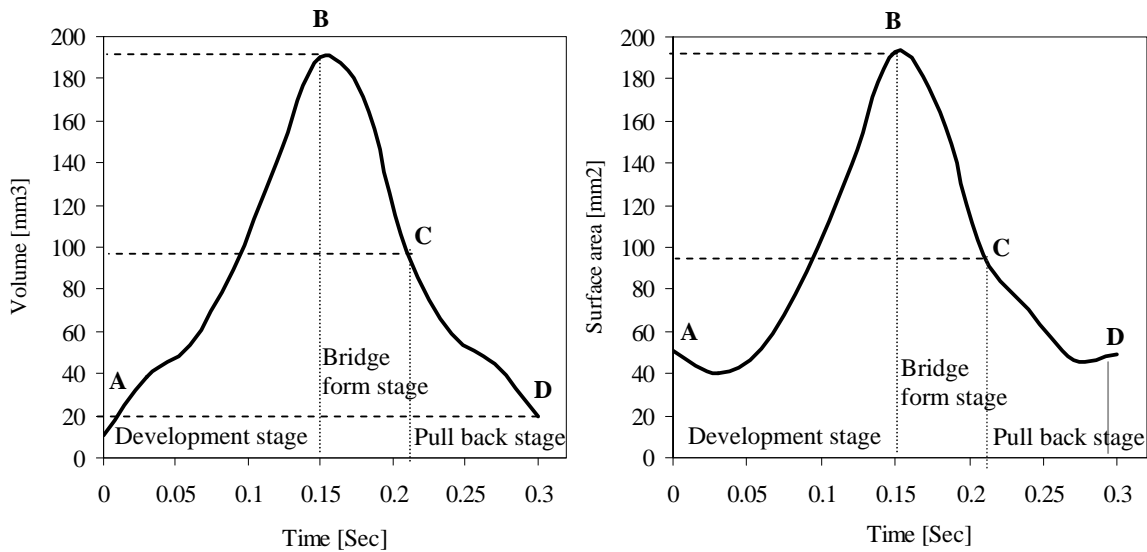


Figure 5.2 The volume and surface area changes during a droplet cycle [images are taken at solution flow rate  $0.0079 \text{ kg}\cdot\text{s}^{-1}$ ].

The volume and surface area of the droplet during this stage start increasing because of the gradual decrease of surface tension force. If the spacing between the tubes is large, the droplet keeps increasing in size until it detaches from its base. When the spacing between the tubes is small the droplet touches the tube surface below at the end of the development stage and forms a liquid bridge which allows the accumulated liquid mass

to flow through. During this bridge formation stage, the droplet starts to regain the surface tension force. Because of the increasing surface tension force, the liquid bridge is stretched downwards and eventually breaks up. After the break up, surface tension force quickly builds up in the remainder of the droplet and starts to pull back some of the liquid. The cycle ends as the pull back is completed followed by the beginning of the next droplet cycle. The part of the droplet which leaves the particular generating location during break up is considered as separate phenomena and hence is not included to the present analysis.

The changes of volume and surface area of the droplet during cycle of evolution are presented in Figure 5.2. These profiles are generated by applying the image analysis program, described in section 4.6 of chapter 4, to the sequential images of Figure 5.1. A typical droplet formation cycle starts at a point such as A at the left of Figure 5.2. As the drop grows in size its surface area and volume increase until it reached a point B where it touches the tube below forming a liquid bridge between the two tubes. At point C the bridge snaps at the narrow neck pulling the upper part of the bridge towards the top tube thus completing the droplet cycle at point D. The interesting observation is that the volume or the surface area never becomes zero at the two ends of the cycle with the indication of presence of residual droplet at the specific location.

In Figure 5.3, sequential video images are presented at a solution flow rate of  $0.0079 \text{ kg.s}^{-1}$ . The images are depicted for the gap between the second and the third tube which was considered to be the representative of the average flow pattern as discussed in section 4.5. The Roman numbers indicated at the top of the figure demarcate the number of droplet generating locations. At this flow rate, the theoretical flow regime is a droplet flow regime according to the transition Reynolds number given in Table 4.4. Furthermore, the sequential images indicate that within 0-0.72 seconds, none of the droplet generating locations exhibit jet flow mode. Instead, droplets repeatedly undergo

the evolution stages at all the locations. The bridge formation stage of any cycle does not stay longer to indicate jet flow mode. Thus this flow mode is exclusively a droplet flow mode.

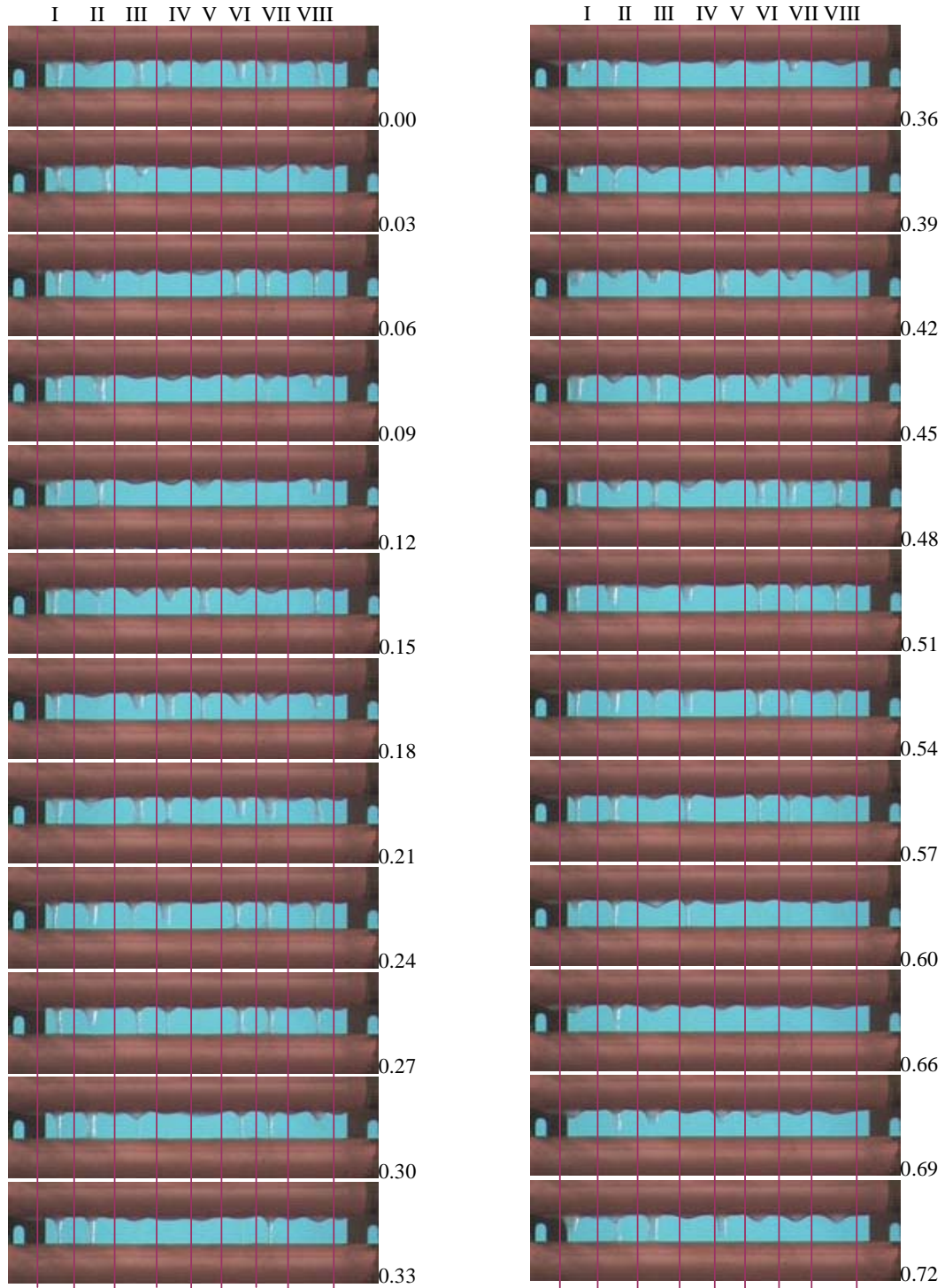


Figure 5.3 Sequential video images at solution flow rate  $0.008 \text{ kg}\cdot\text{s}^{-1}$  [Re: 17.6] for a tube gap of 15 mm.



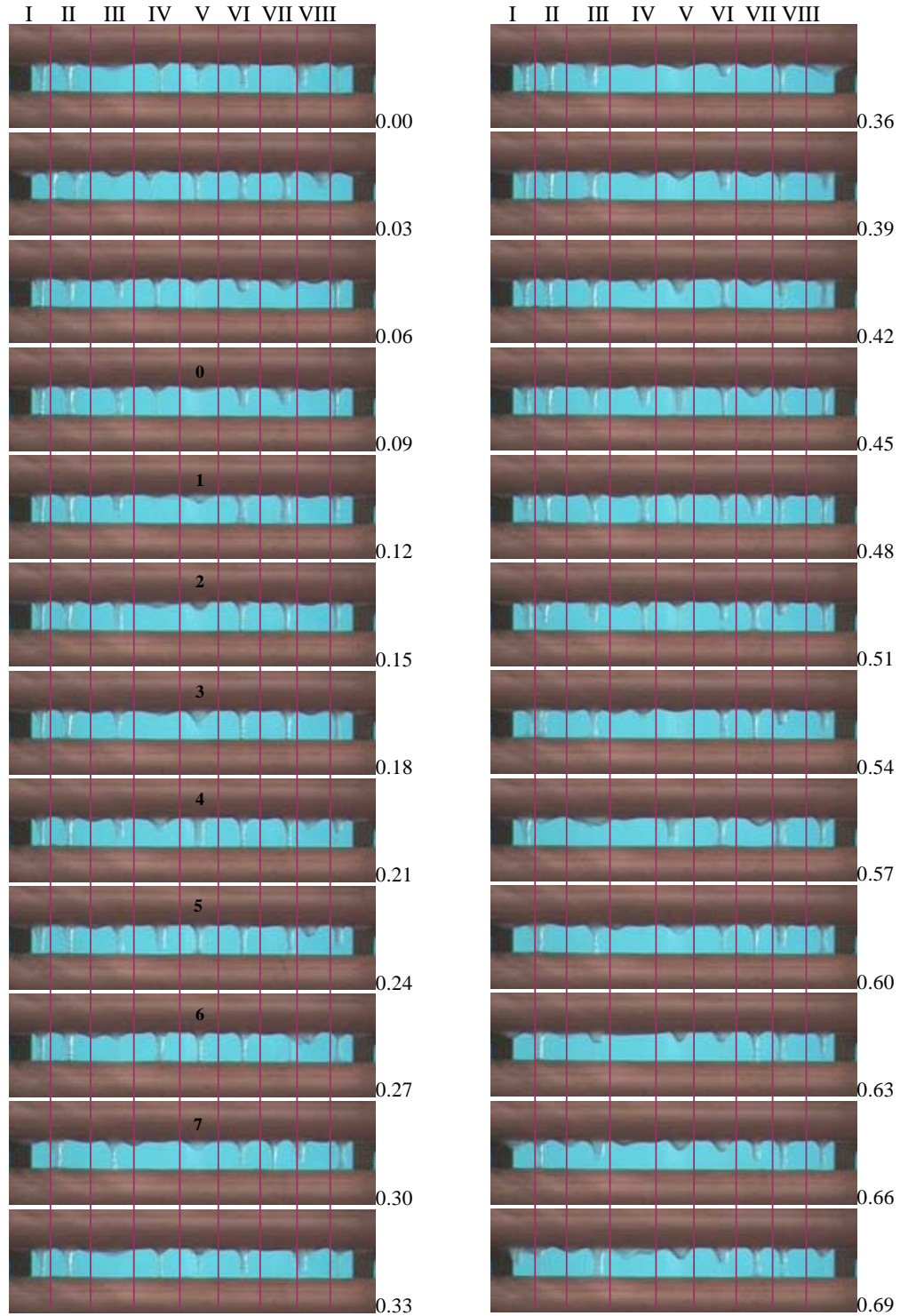


Figure 5.4 Sequential video images at solution flow rate  $0.0145 \text{ kg.s}^{-1}$  [Re: 30.3] for a tube gap of 15 mm.

In Figure 5.4, the sequential video images are shown for a slightly higher flow rate for the same tube gap. Under this condition, the flow regime is identifiable as a mixed flow

or droplet-jet flow regime as indicated in Table 4.4. The images shown in this figure also suggest the mixed flow behaviour. For instance, at droplet generating location II, the liquid bridge exists for 0-0.48 seconds out of the total period of 0.69 seconds. The presence of liquid bridge for such a long period of time indicates that the flow mode is about to change to the jet flow mode at this location. Moreover, within a droplet cycle, the duration of bridge formation stage becomes more longer as shown at droplet location V, from 0.09 to 0.3 seconds. All these imply that with further increase of flow rate, the flow mode will change to the steady droplet mode or jet flow mode.

## 5.2 Tube-gap-configuration at 10mm

The experimental results for inter-tube flow hydrodynamics are presented in this section for a tube spacing of 10 mm. Figure 5.5 shows a series of video images that depict the droplet-flow regime between the second and the third tubes at 10 mm tube spacing. Vertical lines are drawn to demarcate the droplet sites I to VI at the bottom of the second tube. The time-evolution of a typical drop at site III is indicated in the video images by the numbers 0 to 7. The drop development phase continues from time 0.03 sec until 0.12 sec. At this point the drop comes into contact with the bottom tube thus forming a bridge between the tubes. This liquid bridge exists for a brief time before it forms a narrow neck and breaks to pull back some of the liquid to the bottom of the top tube. At 0.18 sec, the breakup and pull back of the liquid bridge is almost complete. The break up stage is so short-lived that it could not be captured with frame speed limit of the present camera. After a brief interval of time, a new drop generation cycle is observed to start at the same site III. Figure 5.5 also shows that as time progresses, the number of droplet sites remains nearly the same except for a small random horizontal shift of the point of generation of the drop. Sometimes a droplet was observed to originate in between two distinct droplets but it did not go through the entire droplet cycle described above. Such droplets, marked with an 'x' in Figure 5.5, are not included in the total number of

distinct droplets. For instance, at site I, the drop seen between 0.21-0.42 is excluded in the analysis.

Figure 5.6 shows the sequential video images at a slightly higher flow rate of  $0.0118 \text{ kg.s}^{-1}$ . As the flow rate increases, it is noticeable from the images that spacing between two consecutive droplet sites becomes narrower as seen from the spacing between the vertical demarcating lines drawn in the figure. Furthermore, for a droplet cycle to be completed, slightly longer time is spent; 9 frames at present flow rate whereas 7 frames at previous flow rate at nearly same location, site-III. Comparing the time spent for different stages within a droplet cycle, it is seen that the bridge form stage exists slightly longer than previous flow rate. It suggests that with the increase of flow rate the droplet development stage becomes quicker whereas the bridge form stage becomes longer.

Figure 5.7 shows the sequential video images at a much higher flow rate of  $0.0145 \text{ kg.s}^{-1}$ . At this flow rate, the droplet flow randomness increases significantly. The droplet generating sites are not found uniformly spaced along the tube as in Figure 5.5. The shift of the droplet generating sites is seen clearly in the images, specially the position of site II. This can be attributed to the increase of randomness in droplet behavior with the increase of flow rate. Similar observations were made by Wassenar [96], who found considerable randomness in the position of the drop generation sites and the time interval between consecutive drops in their experiments. When the flow rate is increased to  $0.022 \text{ kg.s}^{-1}$ , steady liquid jets are formed between the two tubes as depicted in Figure 5.8. Although there are slight random variations in the shape of jets at the various sites, the position of the sites themselves appear to remain almost stationary.

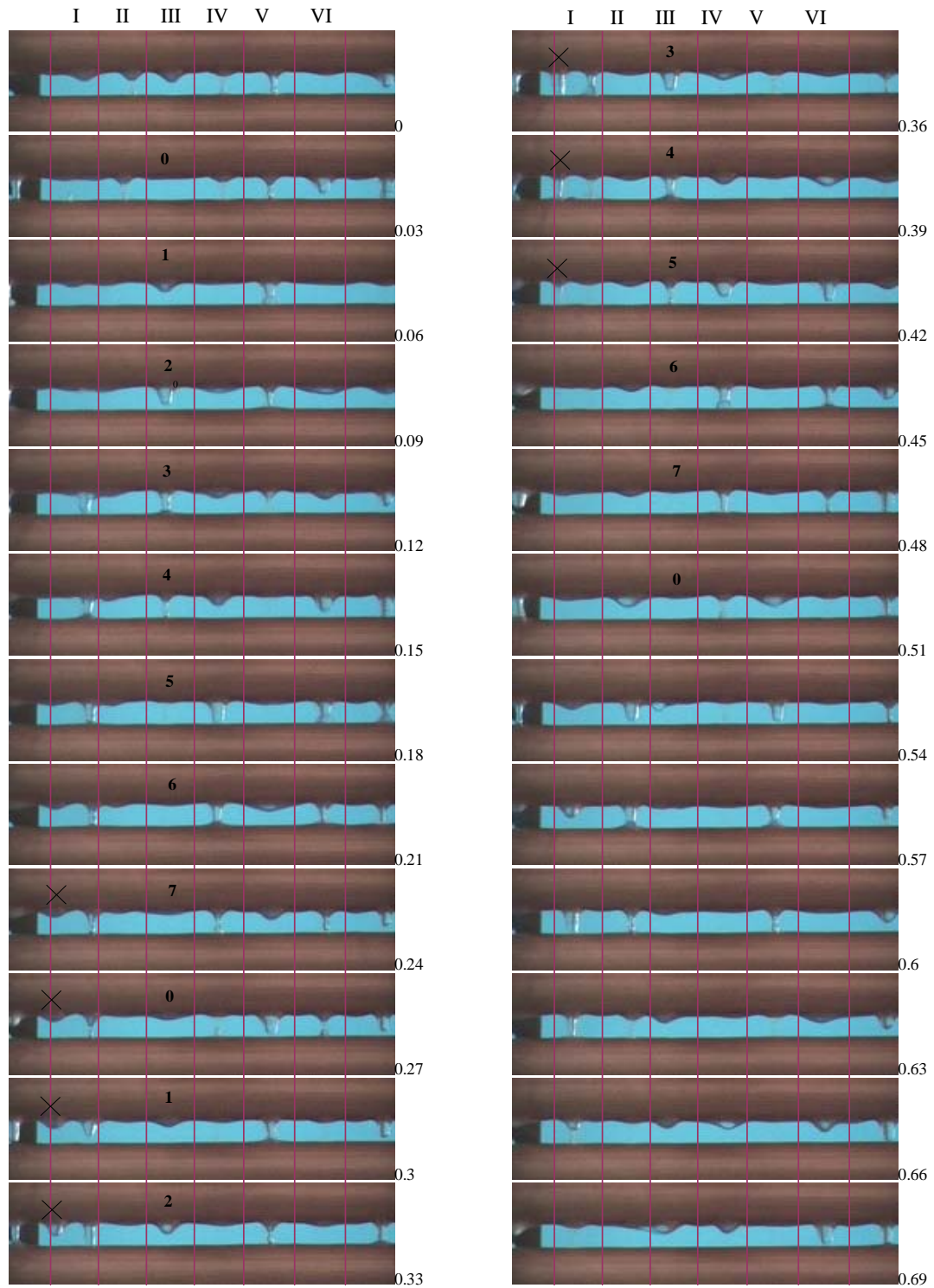


Figure 5.5 Sequential video images at flow rate  $0.0079 \text{ kg.s}^{-1}$  [Re: 16.5] for a tube gap of 10 mm.

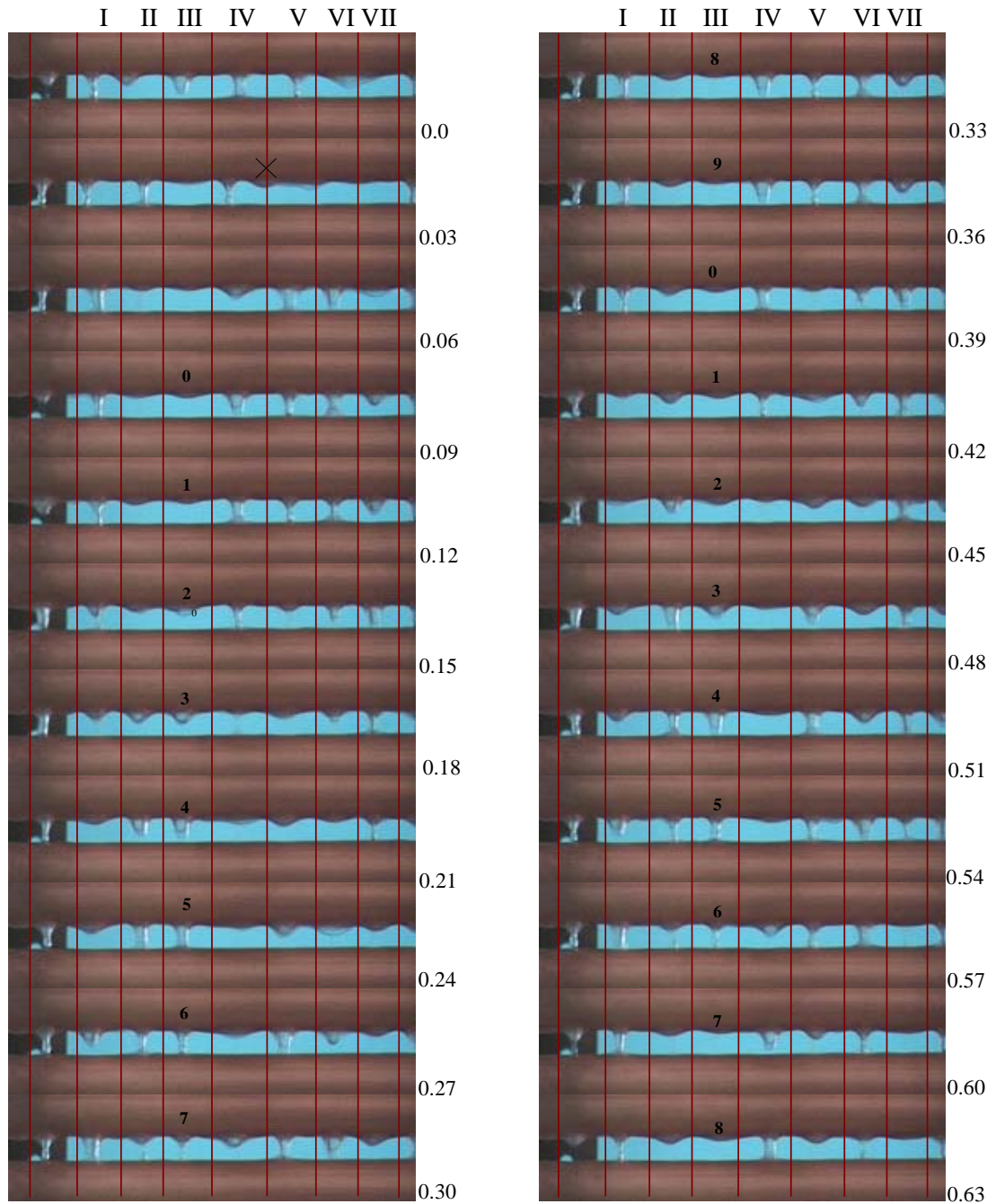


Figure 5.6 Sequential video images at flow rate  $0.0118 \text{ kg}\cdot\text{s}^{-1}$  [ $\text{Re}: 24.7$ ]; for a tube gap of 10 mm

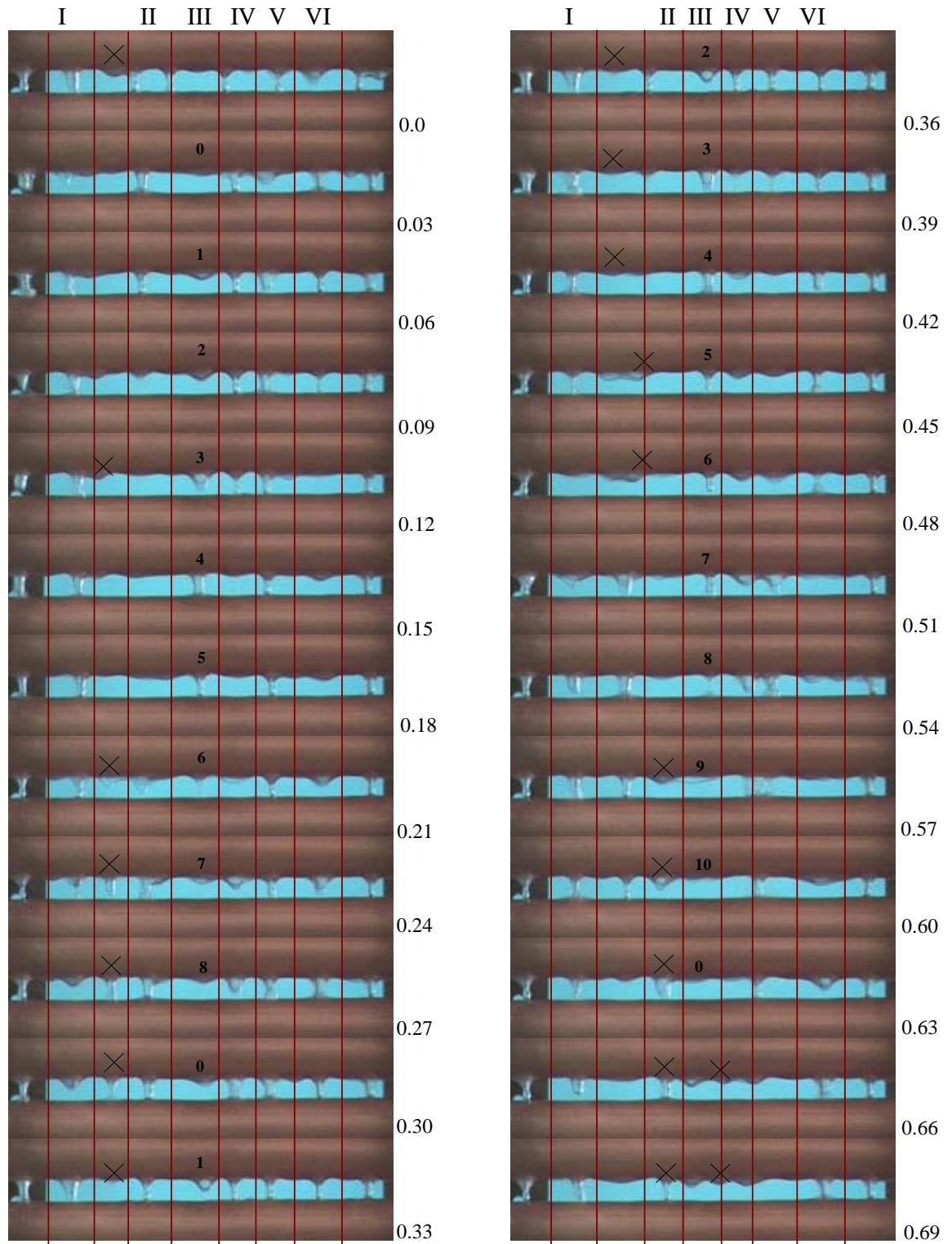


Figure 5.7 Sequential video images at flow rate  $0.0145 \text{ kg}\cdot\text{s}^{-1}$  [Re: 28.85] for a tube gap of 10 mm.

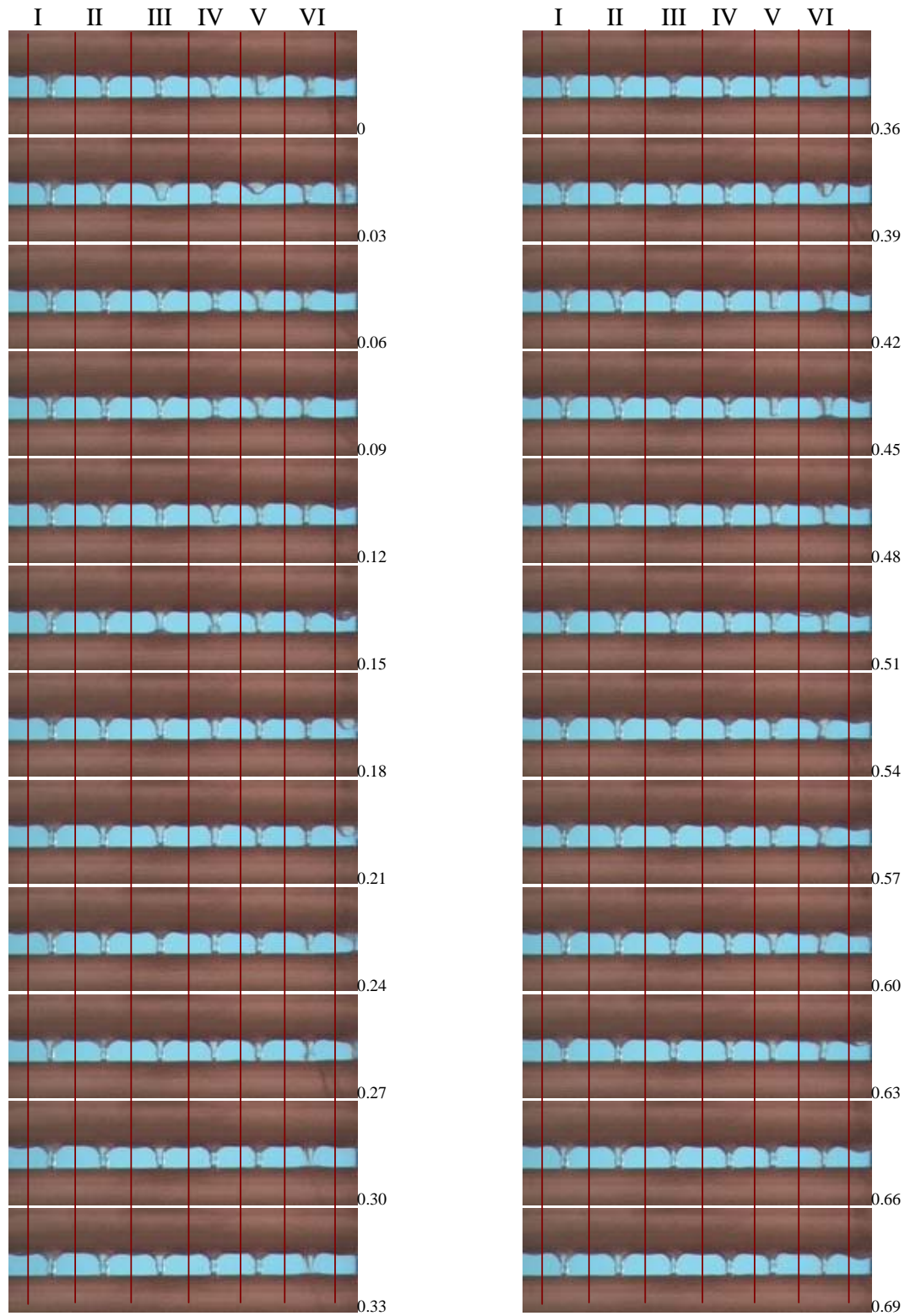


Figure 5.8 Sequential video images at solution flow rate  $0.022 \text{ kg}\cdot\text{s}^{-1}$  [Re: 45.1] for a tube gap of 10 mm.

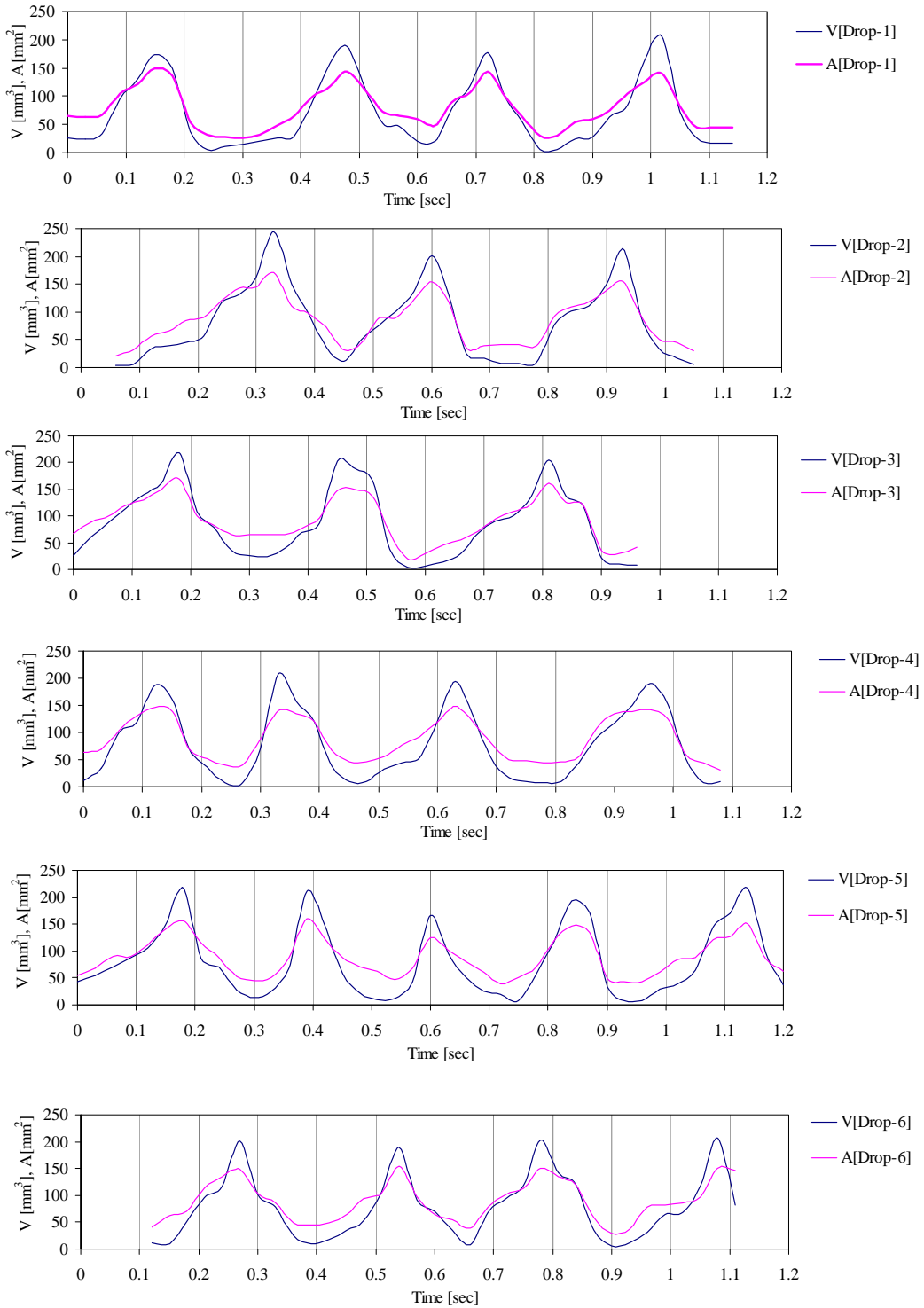


Figure 5.9 Transient volume and surface area variation at each of the 6 droplet sites [Re = 16; solution flow rate:  $0.0079 \text{ kg}\cdot\text{s}^{-1}$ ].



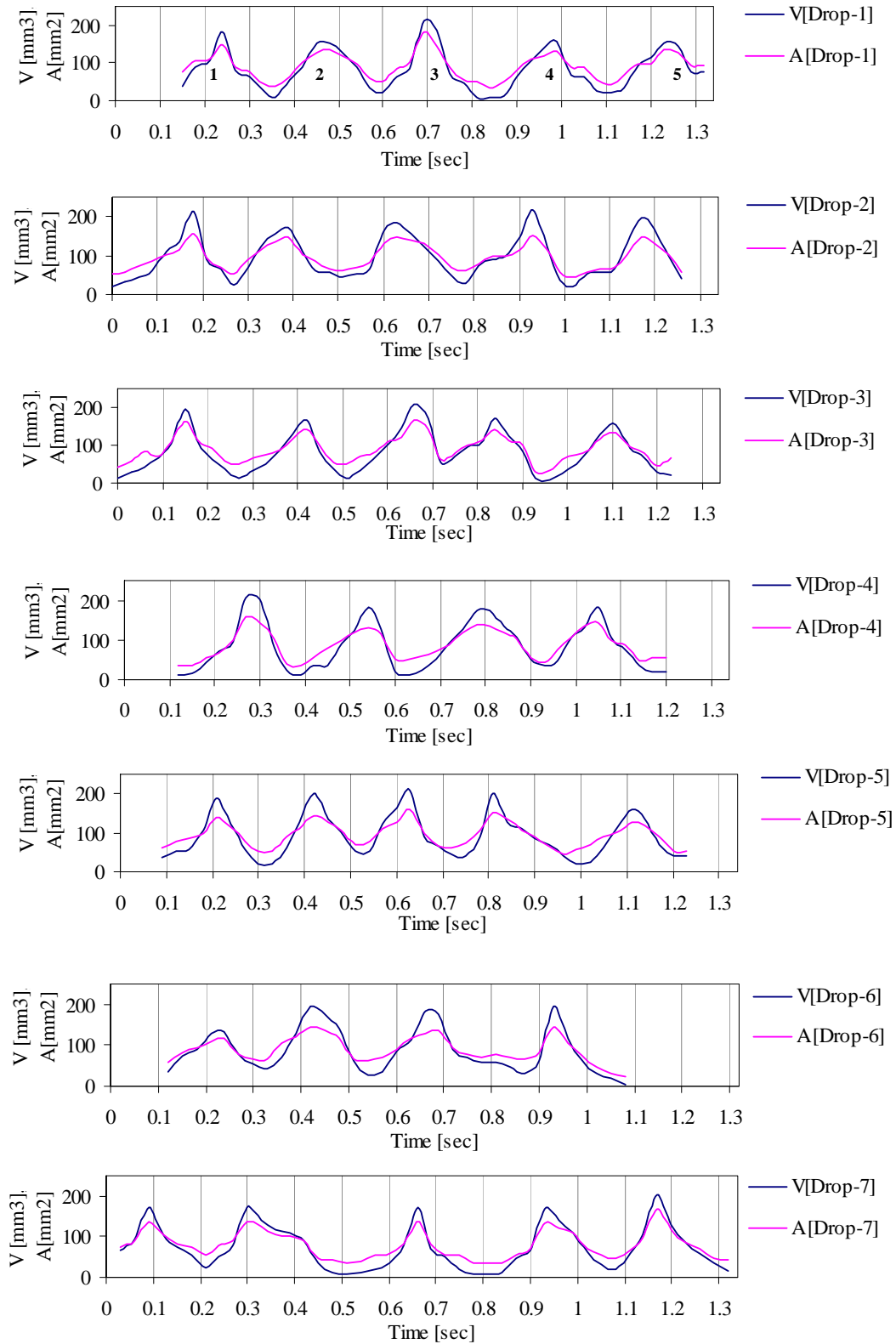


Figure 5.10 Transient volume and surface area variation at each of the 7 droplet sites  
[  $Re = 24.7$  ; solution flow rate:  $0.0118 \text{ kg}\cdot\text{s}^{-1}$  ].

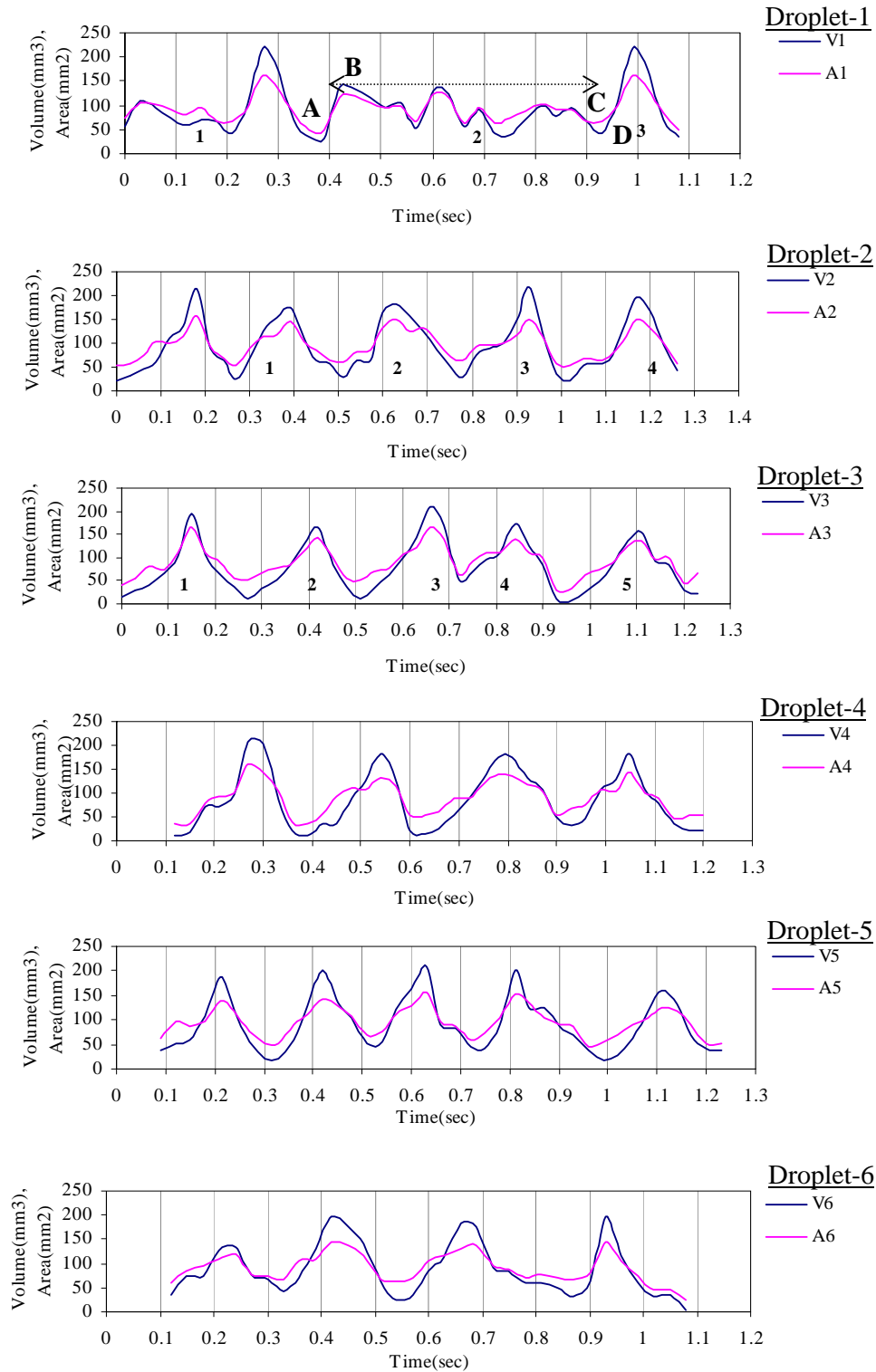


Figure 5.11 Transient volume and surface area variation at each of the 6 droplet sites  
 $[Re = 28.85; \text{solution flow rate: } 0.0145 \text{ kg}\cdot\text{s}^{-1}]$ .

### 5.2.1 Time variations of droplet size

The transient volume and surface area computation for each droplet evolution cycle originating at several generating locations of a tube has been accomplished. The methodology for the computation of the volume and surface area from the video images was described in section 4.6. The time dependent volume and surface area thus obtained are plotted separately for each droplet. Figure 5.9 shows the transient variation of the volume and surface area for the 6 droplets over a total period of about 1.2 s, where data are extracted from the video images shown in Figure 5.5. For cycles shown in Figure 5.9, the period for each cycle varies from about 0.25 s to 0.3 s. As expected from the video images, the droplet cycles originating at the same site as well as those across the 6 sites show random variations of the volumes and areas of the drops.

Figure 5.10 shows the transient volume and surface area curves at flow rate  $0.0118 \text{ kg.s}^{-1}$  over a total period of about 1.3 s. With the increase of flow rate, at most of the generating sites, the droplet cycles are repeated before the surface area or the volume could decrease to a minimum value at the end of a cycle.

Figure 5.11 shows the transient volume and surface area curves at a flow rate of  $0.0145 \text{ kg.s}^{-1}$ . At this flow rate the flow pattern approaches the droplet-jet mode. The droplet cycles at various sites are not as clearly identifiable as in Figure 5.9. The time interval from the formation of the bridge to the break up of the neck is in general longer as marked by B and C at the top of Figure 5.11. The random nature in the variation of the area and volume of the drops is more pronounced at this higher flow rate.

### 5.2.2 Inter-tube flow hypothesis

The following hypothesis is developed based on the observations of the study of inter-tube flow hydrodynamics described in the preceding sections. It was stated in section 5.1 that a droplet undergoes three stages in each cycle. The development of a droplet is initiated by the local flow rate defined as the filling rate  $\dot{m}_e$ . During the development

period, the liquid does not flow through the droplet, instead liquid is accumulated showing the increase of mass of the droplet. Based on this developing droplet behavior, following equation can be written;

$$\dot{m}_e = \frac{\rho V_{\max}}{t_f} \quad (5.1)$$

where  $V_{\max}$  is the droplet volume at the end of development stage and  $t_f$  is the time required for the development of the droplet or the time of formation of the droplet.

During the bridge formation stage, the liquid starts flowing through the droplet to the tube below. However, the liquid flow rate at this stage is not known. If an assumption is made for the flow rate of bridge formation stage to remain unchanged at  $\dot{m}_e$ , the amount of liquid flows through in  $t_b$  period of time is

$$m_{f1} = \dot{m}_e t_b \quad (5.2)$$

where  $t_b$  is the duration of bridge formation stage.

The break up phenomena causes certain mass of liquid to be transferred which is calculated as:

$$m_{f2} = (V_{\max} - V_b)\rho \quad (5.3)$$

where  $V_b$  is the volume of the droplet right after break up.

Therefore the actual amount that flows through the droplet in each cycle can be estimated as the summation of the above two equations Eqs. (5.2) and (5.3). However, if total summation is taken for each droplet cycle at each location within  $\tau$  sec of time, a new mass flow rate is estimated as presented in Appendix E. The estimated mass flow rate is then compared to the actual mass flow rate of liquid and percent difference is found out. The percent difference between the two mass flow rates indicates the percent error in making assumption for the mass flow rate to remain same during the development and the bridge formation stages of a droplet cycle. The percent error varies

from 27-37 percents. It is to be realized that the percent error is generated not only because of making a flow rate assumption but also because of the measurement difficulties of  $V_{\max}$ ,  $V_b$  from the video images. Because of the frame speed limit of the video camera used in the present study, the exact break up moment could not be captured in most of the droplet cycles. As a result, a time lag appeared and accurate measurement of volume  $V_b$ , right after break up, was difficult. More discussions are available in Appendix E. The implementation of this inter-tube flow hypothesis is useful in the formulation of droplet flow absorption model to be discussed in the next chapter.

### 5.2.3 Flow pattern changes over the tube gaps

In the preceding sections, the inter-tube flow patterns were studied for the gap between the second and the third tubes. The absorption model is therefore able to compute the average absorption in a particular tube gap which will be discussed in the next chapter. In order to apply the inter-tube absorption models for the bank of horizontal tubes, the flow pattern in a tube gap must be considered independent of any other variable except the flow rate. In other words, once a configuration is chosen i.e. the vertical distance between the tubes, flow pattern or the inter-tube flow regime is only controlled by the flow rate. The reason for making this assumption is described in details below.

The inter-tube flow behaviour is associated with flow randomness which includes non-uniform spatial distribution of the droplets along the tube; repeatable droplet evolution cycles even though the temporal distribution of these cycles is non-uniform. All these phenomena have been studied before focusing mainly a tube gap on particular. In addition to the above mentioned flow behavior, the spatial distribution of the droplets at different tube gaps is also non-uniform. It is very unlikely that the droplet sites become in-line over the tubes. Most of the droplet sites at different tube gaps are not along the same vertical plane.

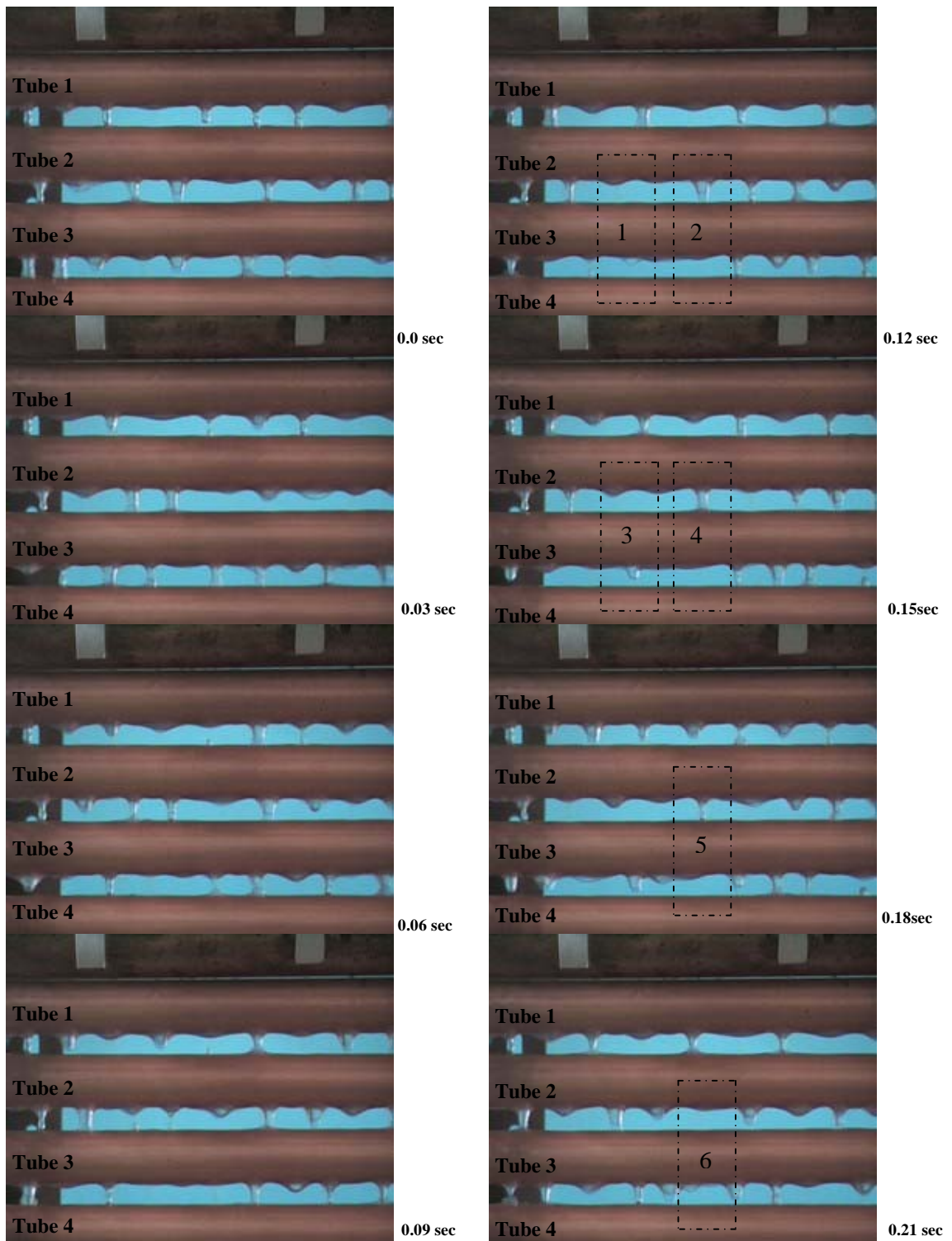


Figure 5.12 Sequential video images to show the droplet behaviors among several tube gaps.

More interestingly, a droplet may begin formation at any location or site without any direct vertical feed as shown in regions 1, 3 indicated by rectangles in Figure 5.12. Also

the liquid bridge which actually causes the flow between the tubes may not be able to initiate any droplet formation directly underneath as shown in regions 2, 4, 5 and 6 indicated by rectangles in Figure 5.12. All these indicate that the transient droplet volume and surface area curves at any tube gap may not be the representative curves for the droplets at other tube gaps.

Thus the generated transient droplet characteristic profiles cannot be generalized. For a bank of tubes absorber, it is therefore necessary to produce the transient profiles at all possible tube gaps which requires a considerable volume of image analysis effort. Although not identical to the droplet behavior discussed above for the gap between the second and the third tube, the general behavior in the rest of the tube gaps usually exhibit similar trends. In order to estimate the overall effect of the entire tube bank it is therefore assumed that the transient volume and surface area data obtained above for the gap between the second and the third tube could be used. It is speculated that this approach will still make a considerable estimate of the overall vapour absorption in the inter-tube flow region for the entire multi-tube absorber.

### **5.3 Tube-gap-configuration at 6mm**

Figures 5.13-5.18 present the video images and the corresponding transient volume and surface area profiles of the droplets for a tube spacing of 6mm. Most conventional falling film tubular absorbers comprise bank of tubes in a vertical array with about 6 mm tube to tube spacing. For this practical configuration, inter-tube flow hydrodynamic data were obtained at various solution flow rates. Similar to the previous tube spacing configurations, sequential video images of the flow regimes between the second and the third tube are presented. The video images shown in Figures 5.13, 5.15 and 5.17 reveal that the shape of the droplets is much different from the shape of the droplets formed at 10 mm tube spacing. Wider and nearly parabolic shaped droplets are formed underneath the tubes as less vertical space is available. Hu and Jacobi [40] also presented the change

of the shape of the jets with decrease in vertical spacing of the inter-tube flow regime. However their experimental study [39] revealed that the mode transition remains almost independent on vertical tube spacing.

Figure 5.13 shows sequential video images of the inter-tube droplet flow regime at flow rate  $0.0077 \text{ kg.s}^{-1}$ . The droplets are distributed at several generating sites along the tube length though the distribution is not uniform. The width of droplet generating sites III-V is narrower than the width of the droplet generating sites I and II as seen from the spacing between the vertical demarcating lines drawn in the figures. The droplet generating sequence from site-I is somewhat ambiguous and prominent droplet phases are not clearly visible. Most of the droplets originating at this site are in the bridge formation mode or steady droplet mode within the specified time period. However, the rest of the droplet generating sites produce repeated droplet cycles which are to be expected at the current flow rate.

In Figure 5.14, the transient droplet volume and surface area profiles are presented at the same flow rate. The droplet site I or droplet -1 exhibited inconsistent behaviour at the current flow rate showing extended droplet cycle with longer bridge formation period as marked by B and C in the top of the figure. The presence of droplet cycles with a longer bridge formation stage at one or two droplet generating sites even at a low flow rate could be an indication that the time distribution between the stages of a droplet cycle is influenced by the limitation of space. Since the flow is not uniformly distributed along the tube, not all the droplet generating locations show this behaviour. This may be why for the present flow rate the other droplet generating sites exhibit consistent behaviour with short droplet cycles at regular intervals except the droplet generating site-I. However, the transient profiles of droplet site II or droplet-2 and III or droplet-3 indicate that volume and surface area of the diminishing droplet does not always attain a minimum level or near zero level at the end of a cycle.



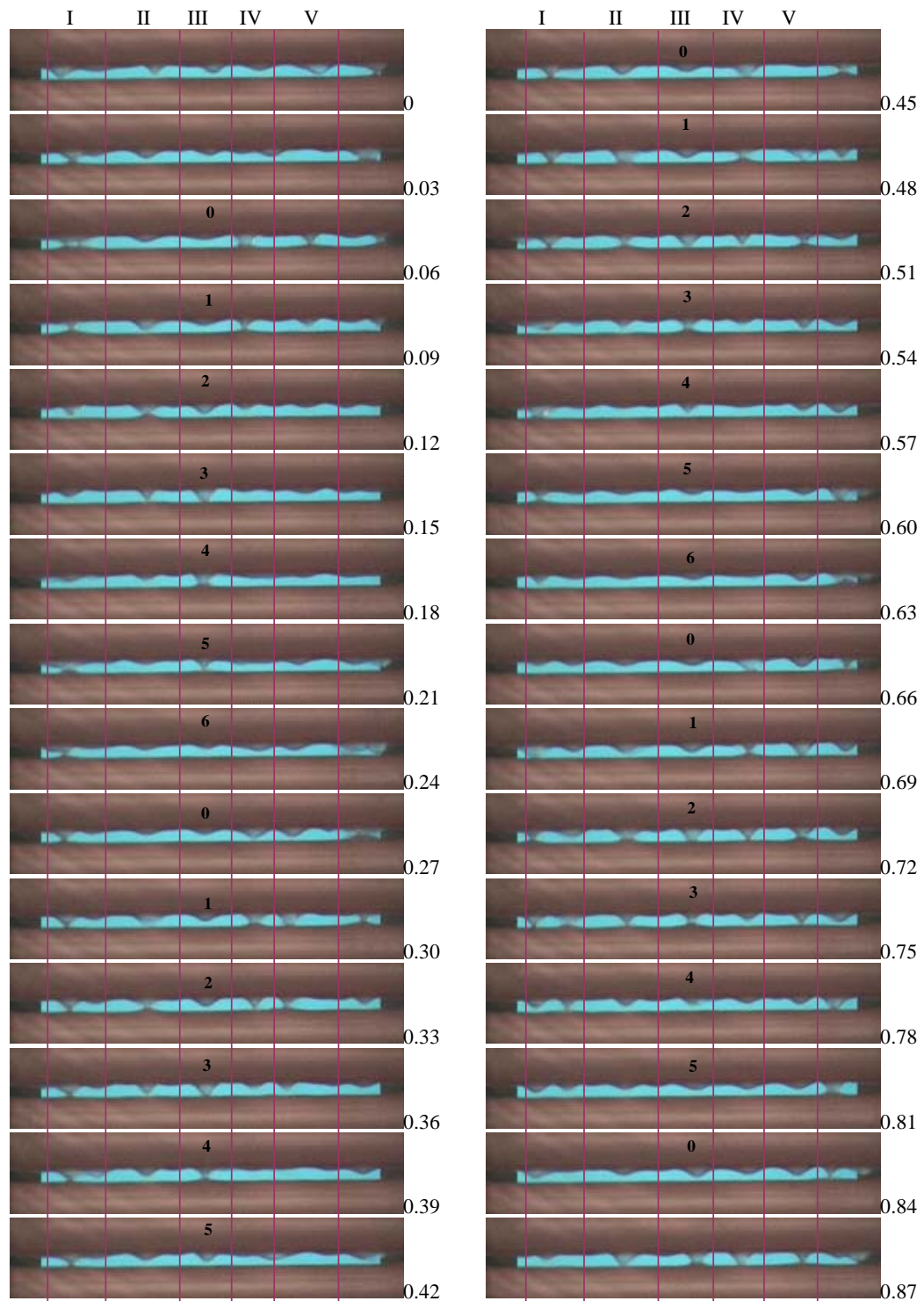


Figure 5.13 Sequential video frames at flow rate  $0.0079\text{kg}\cdot\text{s}^{-1}$ ; tube gap 6mm.

This behaviour of the droplet cycle at site II and III can also be verified with the video images shown in Figure 5.13. As shown in Figure 5.13, a new droplet cycle is initiated from the same location of III, before the pull back stage could be completed.

In Figure 5.15, the sequential video images are presented at a slightly increased flow rate of  $0.011 \text{ kg.s}^{-1}$ . As the flow rate increases, the exhibition of distinct droplet cycles by the different droplet generating locations or sites becomes unclear as depicted in the figure. The number of droplet generation sites increases slightly with the increase of flow rate. The durations of different droplet cycles originating at the same location are found uneven. For instance, at droplet generating site-III, the evolutions of the droplets are shown by the numbers 0-6 between 0.06-0.24 s and 0-12 between 0.27-0.63 s. The droplet cycle from 0.27-0.63 s at this present location indicates that the duration of the bridge formation stage of this cycle is longer starting from 0.45-0.54 s before the necking starts at 0.57 s. The next cycle from the same location becomes normal again continuing from 0.66-0.87 s marked by 0-7 in the figure. Another interesting behaviour of the droplets formed at 6 mm tube gap is that the change of shape of the droplets during necking of the liquid bridge and break up are different from those of the droplets formed at 10 mm tube gap.

The time-dependent volume and surface area profiles at the flow rate of  $0.011 \text{ kg.s}^{-1}$  for the several droplet generating sites are plotted in Figure 5.16. Since most of the sites generate droplets with slightly longer bridge formation stage, most of the droplet cycles are somewhat elongated after reaching the peak. The droplet generating site-VI or droplet-6 shows longest droplet cycle from 0.1 to 0.5 s because of the existence of the nearly steady droplet at this location.

More results are given in Figures 5.17-5.18 at a higher flow rate of  $0.016 \text{ kg.s}^{-1}$ . Both the sequential video images of Figure 5.17 and the corresponding transient characteristics profiles of Figure 5.18 show the droplet behaviour at several locations which are mostly

dominated by the bridge formation stage, especially at site I and VI marked by B and C at the top and bottom of Figure 5.18. At this flow rate of  $0.011 \text{ kg.s}^{-1}$ , the flow mode is recognized as droplet-jet flow mode as was mentioned in Table 4.6. Therefore, the existence of droplets with longer bridge form stage at one or two locations is anticipated at this condition.

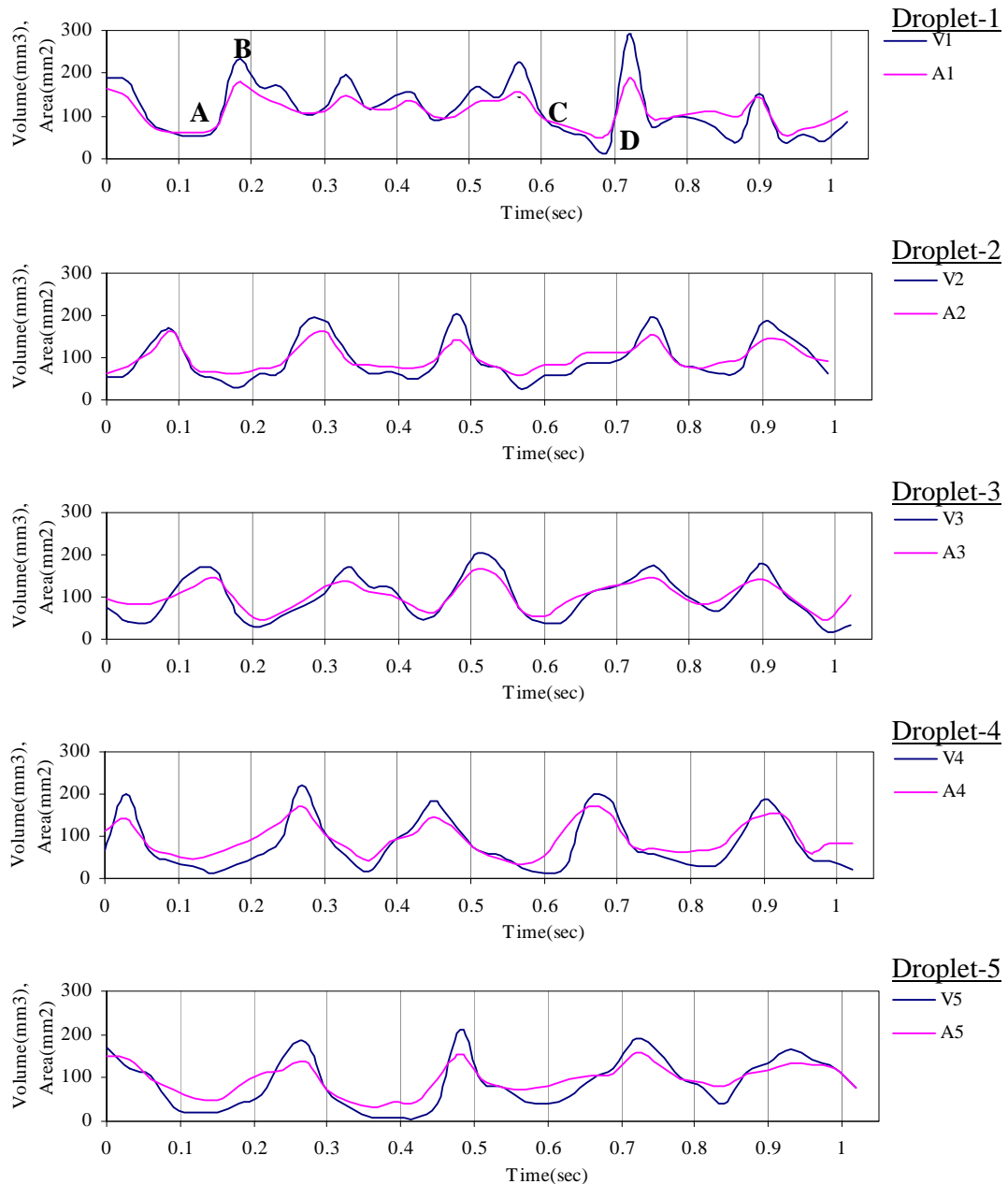


Figure 5.14 Transient volume and surface area variation at solution flow rate  $0.0079 \text{ kg.s}^{-1}$ : tube gap 6mm.

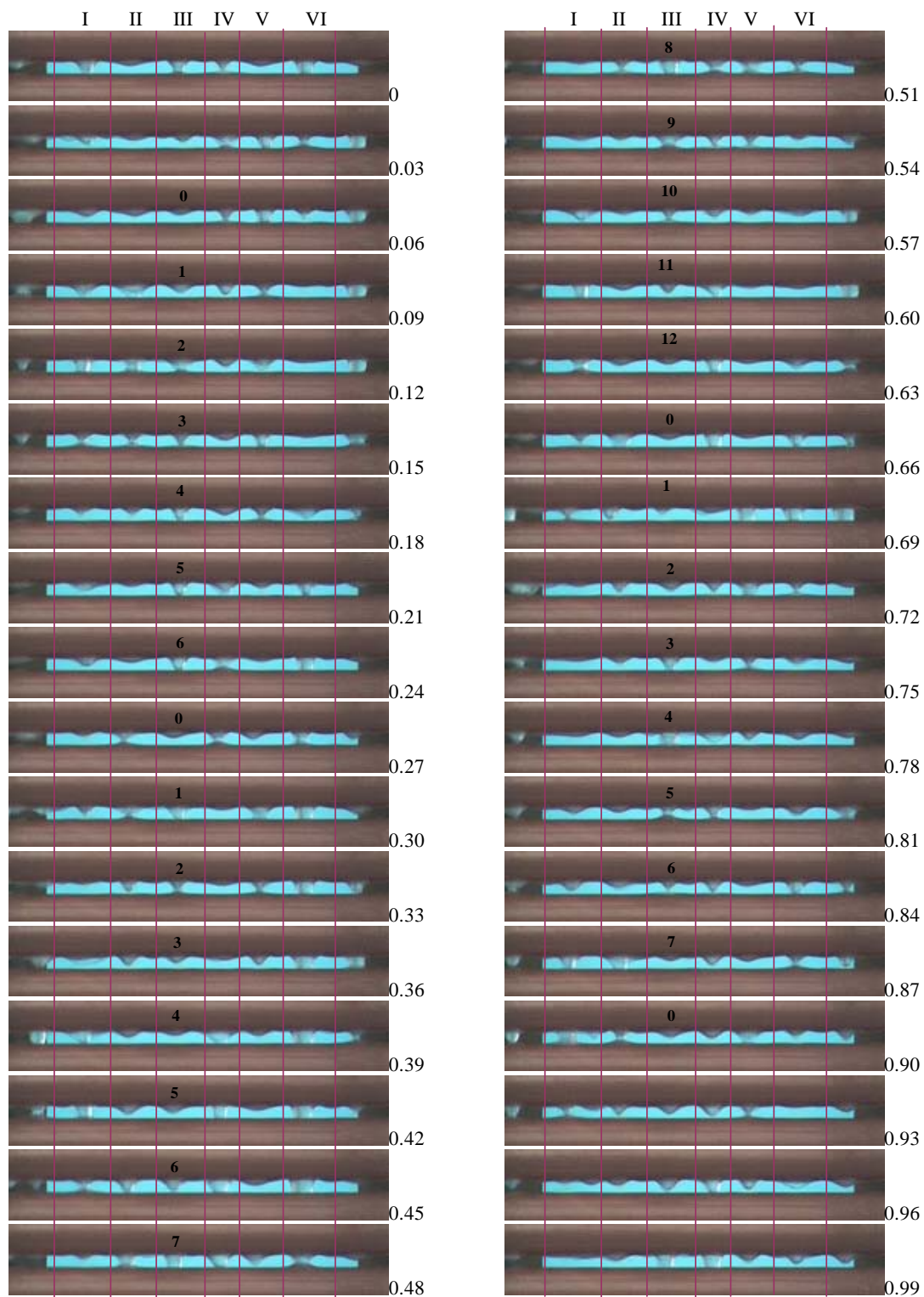


Figure 5.15 Sequential video images at solution flow rate  $0.011 \text{ kg.s}^{-1}$ ; tube gap 6mm.

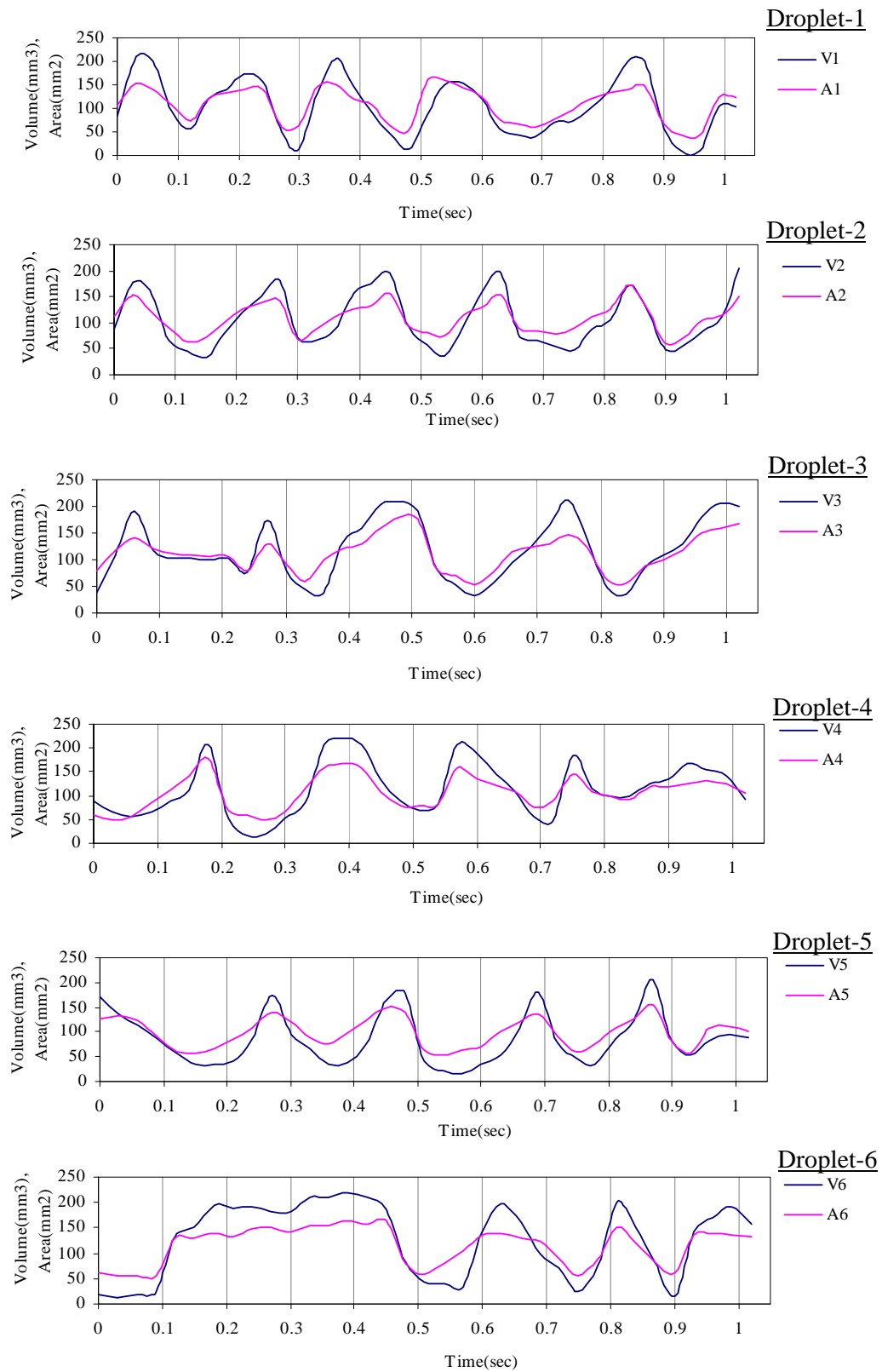


Figure 5.16 Transient volume and surface area at solution flow rate  $0.011 \text{ kg}\cdot\text{s}^{-1}$ ; tube gap 6mm.

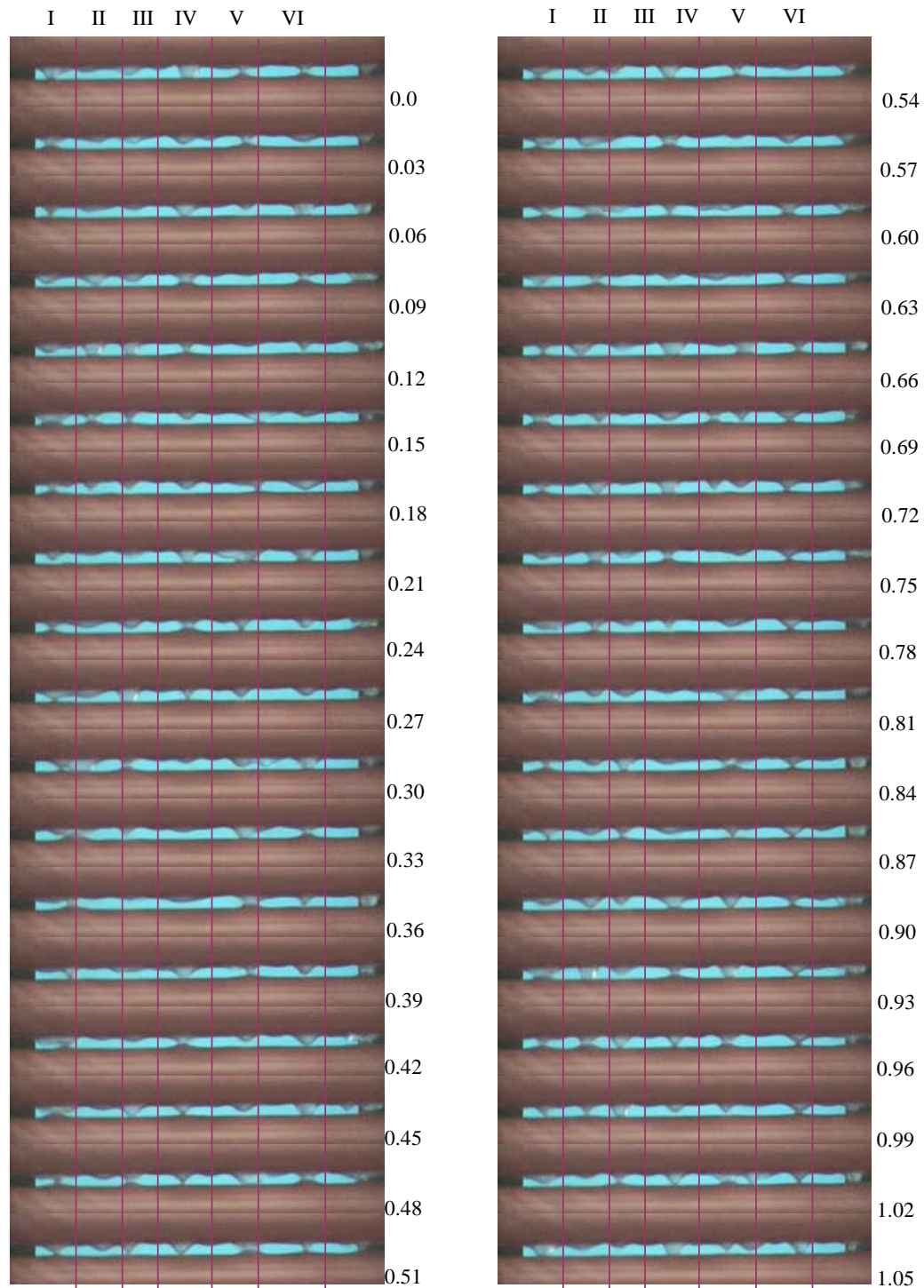


Figure 5.17 Sequential video images at solution flow rate  $0.0163 \text{ kg}\cdot\text{s}^{-1}$  [Re: 34.02]; tube gap 6mm.

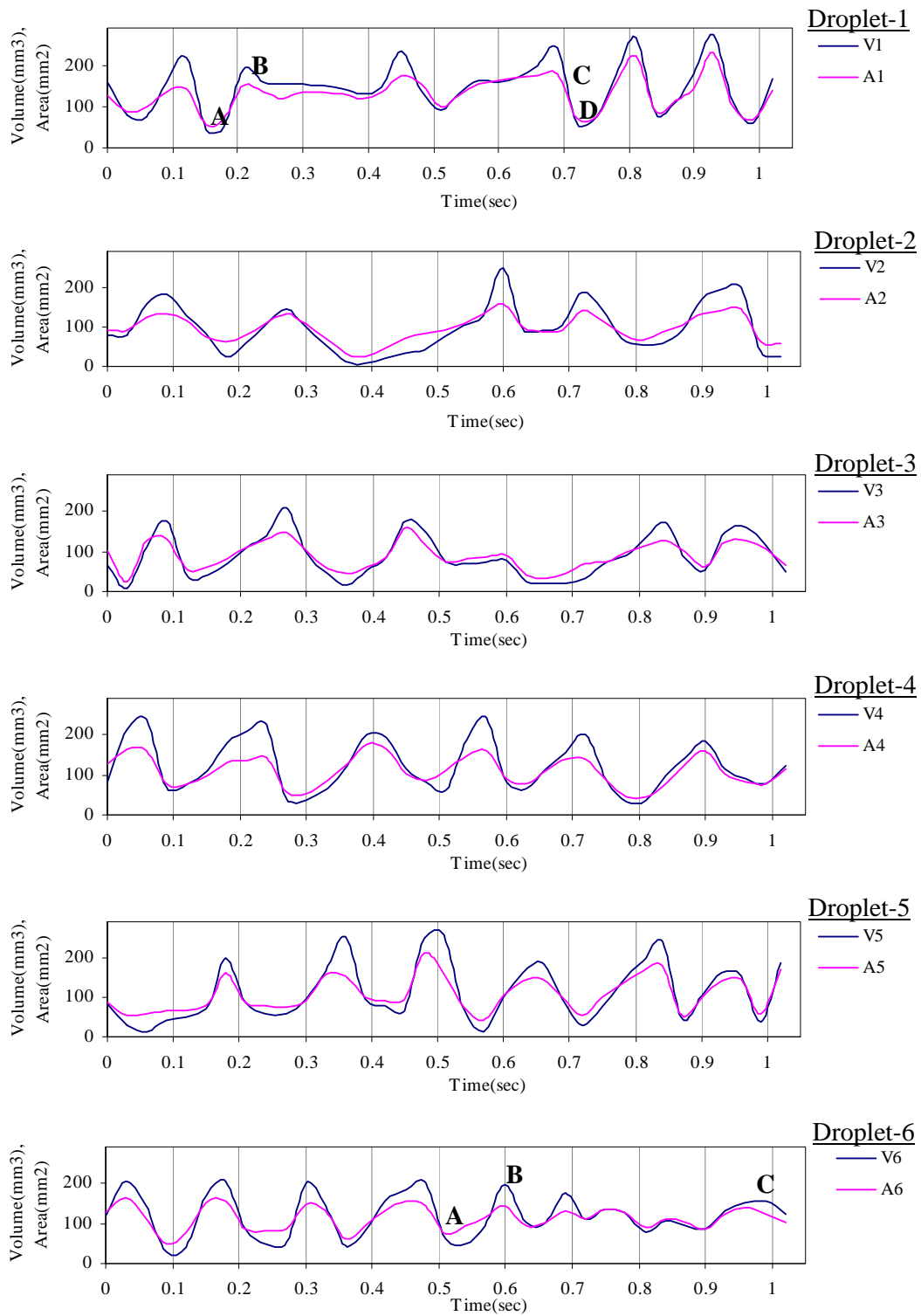


Figure 5.18 Transient volume and surface area at solution flow rate  $0.0163 \text{ kg}\cdot\text{s}^{-1}$  [Re: 34.02]; tube gap 6mm.

#### **5.4 Summary**

The experimental data on inter-tube flow were discussed in this chapter for different tube gap configurations. The inter-tube droplet and jet flow behaviors were explained in detail with the help of the sequential video images and the corresponding transient characteristics profiles. The transient droplet volume and surface area profiles were generated using the image analysis program described in section 4.6. The usefulness of these characteristics profiles will be discussed in the next chapter in which the absorption rate will be calculated for the inter-tube droplet and jet flow modes.



## **CHAPTER 6**

### **RESULTS AND DISCUSSION: INTER-TUBE ABSORPTION**

The prediction of vapour absorption in the inter-tube flow regimes is the main focus of this chapter. The hydrodynamics of inter-tube fluid flow, presented in chapter 5, were obtained from the video image analysis described in chapter 4. The hydrodynamic data are used into the semi-empirical models developed in chapter 3 to simulate the vapour absorption process in the inter-tube flow regime. Upon successful development of the theoretical models for inter-tube droplet and jet flows, the heat and mass transfer coefficients incorporated to the models are determined using a detailed numerical model of falling film regime described in chapter 3. The contribution of the inter-tube absorption to the total absorption is obtained for a range of design and operating conditions of a typical tubular absorber.

#### **6.1 Comparison of the inter-tube absorption models applied to a single drop/jet**

For comparison of present droplet formation model described in section 3.2.2.1 with that of Siyoung and Garimella [88] under the same conditions, the developing drop size was idealized with a hemisphere described in section 3.2.2.2. The results of the present idealized droplet formation model were compared with those of the corresponding model of Siyoung and Garimella [88] in that section too.

The steady jet absorption model described in section 3.2.2.3 can also be solved under the same operating conditions by assuming a hemispherical profile of the steady jet. The absorption rates calculated by the three models for the particular tube gap are presented in the first three rows of Table 6.1. The absorption rates or the change of solution flow rates due to vapour absorption in the tube gap predicted by the three models show a certain amount of variations, but the differences are small.

**Table 6.1 Model comparisons; results of the seventh tube from [88]**

Models used	Absorption rate, $kg.m^{-1}s^{-1}$ [At the end of formation period]
Droplet formation model [idealized, hemispherical droplet]	4.9E-05
Steady jet model [idealized, hemispherical jet]	5.2E-05
Model used by Siyoung and Garimella [hemispherical droplet-formation model]	4.3E-05
Droplet formation model [Present experimental hydrodynamics data]	3.7E-05

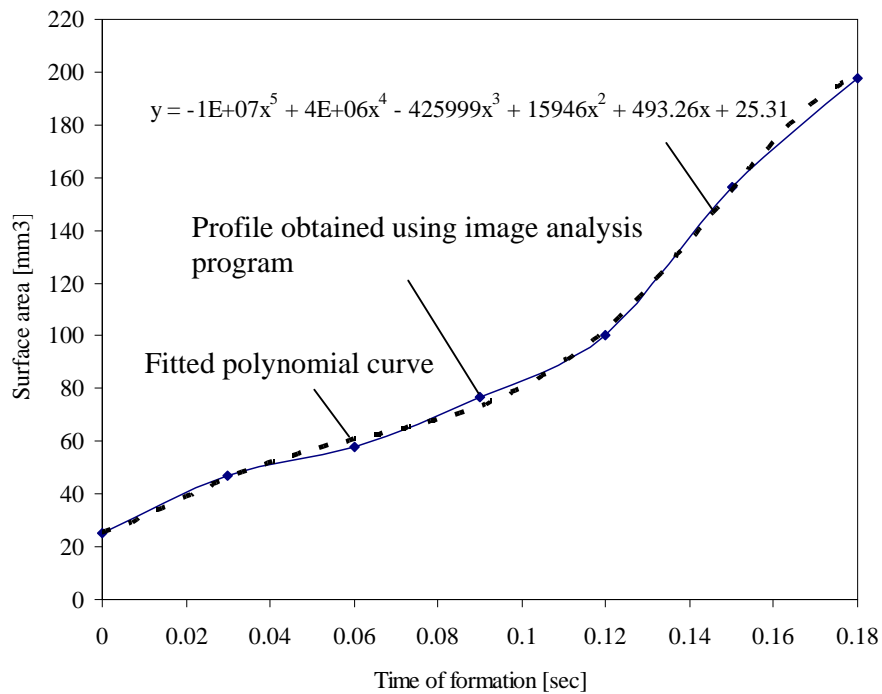


Figure 6.1 Experimental data of a droplet surface area profile with polynomial fit during formation at 6 mm tube gap situation.

Present drop formation model described in section 3.2.2.1 is also solved using the hydrodynamics data from chapter 5. For a typical droplet evolution cycle, the rate of absorption is predicted by the model under similar operating condition of Siyoung and

Garimella [88]. For their case, the tube gap was 6 mm for which present hydrodynamics data are available from section 5.3. The sample droplet surface area profile is presented in Figure 6.1 from which a fitted polynomial is extracted to be used as a direct input to the absorption model of section 3.2.2.1. The droplet volume profile, the time of formation,  $t_f$  and so as the filling rate  $\dot{m}_e = \rho_s V_{\max} / t_f$  are also extracted from the experiment. Except the hydrodynamics data, all other thermo-physical properties and the inlet conditions are kept unchanged with those of [88]. The simulation result for the rate of absorption given by the sample droplet is presented in the last row of Table 6.1 together with the other model results. The rate of absorption varies from the other model results mainly because of the difference in hydrodynamics of present forming droplet.

## 6.2 Simulation results for absorption performance

The inter-tube absorption models described in section 3.2.2.1 and 3.2.2.3 are used to calculate the amount of vapour absorbed in the gap between the second and the third tube of present experimental conditions stated in chapter 4. The hydrodynamic data were presented in section 5.2-5.3. Depending on the flow pattern, relevant models are used for the prediction of vapour absorption rate.

### *Transfer coefficients for inter-tube absorption*

The transfer coefficients in the inter-tube flow regime of a horizontal tubular absorber are difficult to determine especially when the change of flow modes is considered. Based on the modes of inter-tube flow, the heat and mass transfer coefficients could vary. For the droplet or droplet-jet mode inter-tube flow, the correlation used in Siyoung and Garimella [88] could be used in the development stage of the droplet. The correlation is given by Eq. (6.1) below:

$$k_{m,drop} = \frac{24}{7} \left[ \frac{D}{\pi \cdot t_f} \right]^{1/2} \quad (6.1)$$

where  $t_f$  is the time of formation of a droplet. However, for the bridge formation stage of a droplet cycle or the steady jet/sheet flow modes, the above correlation may not be applicable. In the correlation, the mass transfer coefficient is inversely proportional to the time of formation of the droplet. The experimental data presented in chapter 5 revealed that the time of formation of a droplet varies (0.09 s to 0.18 s) even within the droplet cycles originating from the same generating location underneath the tube. For a typical operating condition of the absorber, mass transfer coefficient  $k_m$  could vary from 2.1 E-04 to 1.5 E-04  $m.s^{-1}$  for the time of formation from 0.09 to 0.18 s respectively, if the correlation in Eq. (6.1) is used.

**Table 6.2 Mass transfer coefficient for inter-tube droplet flow**

Time of formation $t_f$ [sec]	$k_m$ [using Eq.(6.1)] [ $m.s^{-1}$ ]	$k_m$ [from detailed numerical model in the falling film regime] [ $m.s^{-1}$ ]
0.09	2.1E-04	0.8E-04
0.12	1.8E-04	
0.15	1.6E-04	
0.18	1.5E-04	

On the other hand, if the mass transfer coefficient is assumed to remain same as that in the falling film regime over the tube, the detailed numerical model gives the value as 0.8E-04  $m.s^{-1}$  for the same operating condition. Thus the falling film regime mass transfer coefficient is much lower than those values calculated using Eq. (6.1) as presented in Table 6.2. A sensitivity analysis presented in Appendix C revealed that if the mass transfer coefficient is lower, the inter-tube mass flux is lower as well. Moreover, for the steady state process like inter-tube jet/sheet flow mode or the bridge formation stage of a droplet cycle, Eq. (6.1) may not be valid. Hence, the falling film regime mass transfer coefficient is used for the inter-tube jet/sheet flow mode. If the

same assumption is not considered for the droplet development stage, the absorption rate during droplet or droplet-jet flow mode will become much higher because of the use of Eq. (6.1). Therefore, as a conservative approach, the values of  $k_m$  obtained numerically from the falling film are used to obtain the results in Table 6.3-6.4 for all inter-tube flow modes. For the heat transfer coefficient  $h_o$ , the heat and mass transfer analogy given in section 3.2.2.4 is used. A detailed sensitivity analysis was carried out to estimate the effect of varying the heat and mass transfer coefficients on the results in Table 6.3-6.4 which are discussed later in this chapter.

#### ***Absorption in the droplet/droplet-jet flow regime***

When the flow pattern shows droplet or droplet-jet flow regime, the droplet formation model stated in section 3.2.2.1 is used to compute rate of vapour absorption in the droplet development and liquid bridge stages until break up. Due to the shorter existence of the pull back stage of a droplet cycle as shown in Figure 5.1, the absorption performance of this stage is ignored. Figures 6.2 and 6.3 show respectively the time variation of the area and the volume of a typical drop for a tube gap of 6 mm and 10 mm respectively. The time interval between measured data points from the video images was 0.03 s as stated in chapter 4. The area and volume at intermediate times were obtained by fitting cubic splines between the measured points using the numerical procedure available in [29]. The cubic splines allow the accurate estimation of the gradient of the drop volume versus time curve which in turn is used to obtain the liquid inflow rate,  $\dot{m}_e$ , to the forming drop as described in section 3.2.2.1. It is seen that the volume and area increase steadily up to the bridging point B when the forming drop makes contact with the tube surface below. After this point the fluid accelerates towards the bottom tube thus decreasing the effective volume and area of the drop. At point C, the liquid bridge between the tube surfaces, snaps and the volume and area are rapidly reduced to zero.

For the application of the present model, the liquid inflow rate during the period AB is obtained by computing the slope of the volume curves in Figure 6.3 at different times which was obtained by differentiating the expressions for the cubic splines.. The slope of the section BC of the curve gives the net outflow of liquid. The liquid inflow during the period BC is assumed to be constant at the value just before the bridge is formed.

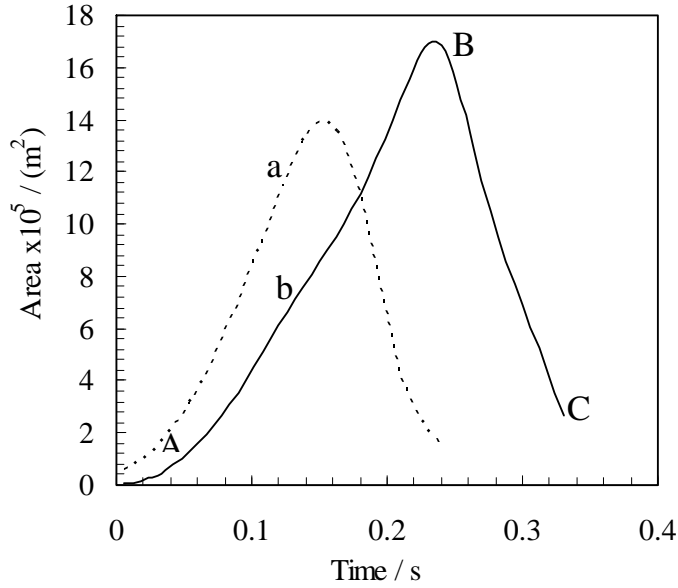


Figure 6.2 Variation of drop area with time. Graphs: (a) tube gap = 6 mm, flow rate  $\Gamma = 0.027 \text{ kg.m}^{-1}\text{s}^{-1}$ , (b) tube gap = 10 mm, flow rate  $\Gamma = 0.02 \text{ kg.m}^{-1}\text{s}^{-1}$ .

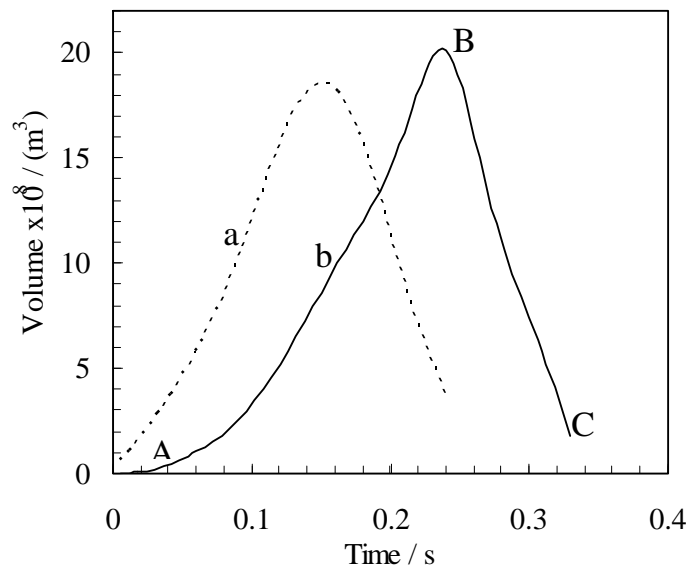


Figure 6.3 Variation of drop volume with time. Graphs: (a) tube gap = 6 mm, flow rate  $\Gamma = 0.027 \text{ kg.m}^{-1}\text{s}^{-1}$ , (b) tube gap = 10 mm, flow rate  $\Gamma = 0.02 \text{ kg.m}^{-1}\text{s}^{-1}$ .

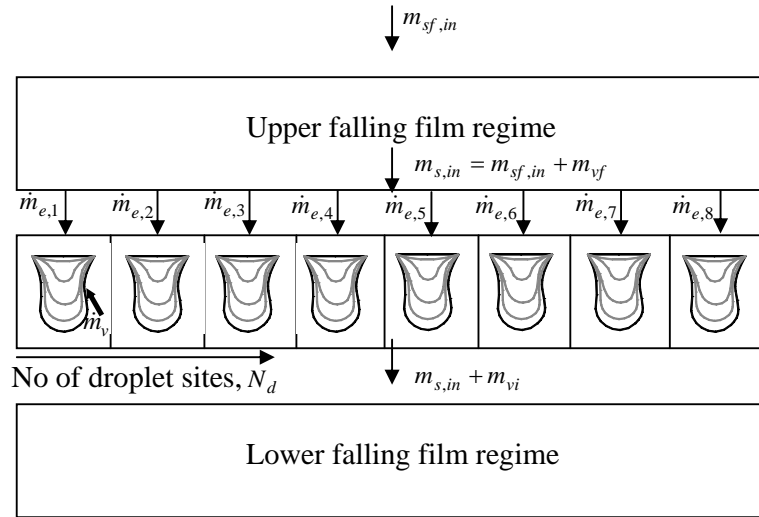


Figure 6.4 Schematic description of inter-tube droplet flow regime; operating conditions are  $w_{s,in} = 0.60$ ,  $T_{s,in} = 39.8^\circ c$ ,  $p = 1.388kpa$ ,  $L = 0.2m$ ,  $r_i = 0.011m$ .

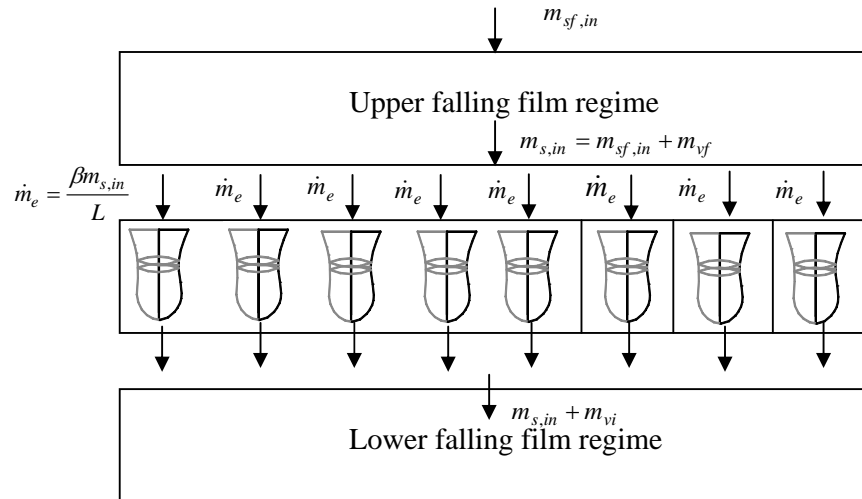


Figure 6.5 Schematic description of inter-tube jet flow regime; operating conditions are  $w_{s,in} = 0.60$ ,  $T_{s,in} = 39.8^\circ c$ ,  $p = 1.388kpa$ ,  $L = 0.2m$ ,  $r_i = 0.011m$ .

A schematic configuration of droplet mode absorption is shown in Figure 6.4. In this inter-tube flow mode, the amount of absorbed vapour by all the droplets generated at several locations underneath a tube is summed up in a total time period of  $\tau$  s. For the droplet formation and bridging period, integration of Eq. (3.2.43) is performed by setting vapour side heat transfer coefficient  $h_v = 0$  for the determination of actual amount of

absorbed vapour of each droplet cycle. The average amount absorbed is therefore calculated dividing the total sum of absorbed vapour by total time period  $\tau$  seconds.

### ***Absorption in the jet flow regime***

When the flow pattern shows jet flow regime, the steady jet model discussed in section 3.2.2.3 is used to simulate the absorption performance. The schematic configuration of jet mode inter-tube flow and absorption is shown in Figure 6.5. At this flow pattern, the shape of jets at the various sites and the position of the sites appeared to remain almost stationary as shown in Figure 5.8 of chapter 5. Hence, a jet profile is selected by fitting polynomial curve to an image similar to those presented in Figure 5.8 and is kept unchanged for an operating condition.

The use of steady jet absorption model helps to calculate the amount absorbed into the specific tube gap. The mass flow rate of each steady jet is found out from the equation given below:

$$\dot{m}_e = \frac{\beta m_{s,in}}{L} \quad (6.2)$$

where  $m_{s,in}$  is the total solution flow rate leaving the upper falling film regime as shown in Figure 6.5. The spacing between the jets  $\beta$  was given in Table 4.7-4.8 for different operating conditions. The rate of absorption during jet mode inter-tube flow is determined by integrating Eq. (3.2.65).

### ***Simulation results***

The absorption rate in the upper falling film regime of Figures 6.4 and 6.5 is computed with the help of the detailed numerical model described in section 3.1.2. The mass transfer coefficient is extracted from the numerical model of falling film regime. The heat transfer coefficient of drop formation and steady jet is obtained from heat and mass transfer analogy stated by Eq. (3.2.77). Though the values of the transfer coefficients



remain constant in present situation, detailed sensitivity analysis is presented in Appendix C for a wide range of transfer coefficients.

**Table 6.3 Absorption rate/Tube gap: 10mm, wetted length: 21cm**

Flow rate $kg.s^{-1}$	Model used	Time duration, $\tau$ s	Total droplet cycles in $\tau$ s	Falling film abs. $m_{vf}$ $kg.m^{-1}s^{-1}$	Inter-tube abs. $m_{vi}$ $kg.m^{-1}s^{-1}$	Inter-tube contribution in total absorption $\frac{m_{vi}}{m_{vf} + m_{vi}} \times 100$ %
0.0227	Jet model	Not applicable	Not applicable	4.30E-04	1.95E-04	31.1
0.0191	Jet model	Not applicable	Not applicable	4.07E-04	2.02E-04	33.2
0.0145	Droplet model	1.08	21	3.72E-04	2.06E-04	35.7
0.0118	Droplet model	1.32	31	3.50E-04	1.97E-04	36.0
0.0079	Droplet model	1.2	22	3.17E-04	1.54E-04	32.7

The absorption rates in both upper falling film regime and inter-tube flow regime shown in Figures 6.4 and 6.5 are compared for which results are presented in Tables 6.3-6.4 for two tube gap situations. The percentage of inter-tube absorption is computed with respect to the total absorption of both upper falling film and inter-tube flow regime. In Table 6.3, the percent contribution of inter-tube absorption to the total absorption is presented at various solution flow rate for the 10 mm tube gap situation. The rate of absorption in both flow regimes is given too. The results indicate that the falling film absorption rate increases with the increase of flow rate whereas inter-tube absorption

rate does not follow similar pattern. The percentage of inter-tube absorption rate varies from 31 to 36 percents of total absorption which is the summation of both upper falling film and inter tube absorption rate.

**Table 6.4 Absorption rate/Tube gap: 6mm, wetted length: 20cm**

Flow rate $kg.s^{-1}$	Model used	Time duration $\tau$ s	Total droplet cycles in $\tau$ s	Falling film abs. $m_{vf}$ $kg.m^{-1}s^{-1}$	Inter-tube absorption $m_{vi}$ $kg.m^{-1}s^{-1}$	Inter-tube contribution in total absorption $\frac{m_{vi}}{m_{vf} + m_{vi}} \times 100$ %
0.0227	Jet model	Not applicable	Not applicable	4.09E-04	1.80E-04	30.6
0.0188	Jet model	Not applicable	Not applicable	3.84E-04	1.87E-04	32.8
0.0147	Droplet model	1.08	21	3.13E-04	1.63E-04	34.3
0.0109	Droplet model	1.32	31	3.29E-04	1.67E-04	33.6
0.0077	Droplet model	1.2	22	3.009E-04	1.35E-04	31.1

The maximum contribution of inter-tube absorption occurs at the solution flow rate 0.0145  $kg.s^{-1}$  which actually provides a droplet-jet flow mode. The minimum contribution on the other hand occurs at flow rate 0.0227  $kg.s^{-1}$  which provides a jet flow mode. Similar results for 6 mm tube gap situation are presented in Table 6.4. The absorption rate in the falling film regime slightly varies due to the slight variation of the operating conditions. The absorption rate in the inter-tube flow regime varies too. In this present tube gap situation, the size of the droplets differs from those of 10 mm tube gap

situation. Also the transient variations of droplet volume and surface area are different which have been discussed in detail in section 5.3. Due to the differences in flow hydrodynamics, absorption performances are slightly different at this tube gap situation. The maximum absorption rate is found in the droplet-jet flow regime at  $0.0147 \text{ kg}\cdot\text{s}^{-1}$  solution flow rate. The percentage of inter-tube absorption rate however varies within narrow range like 30.6 to 34.3 percents.

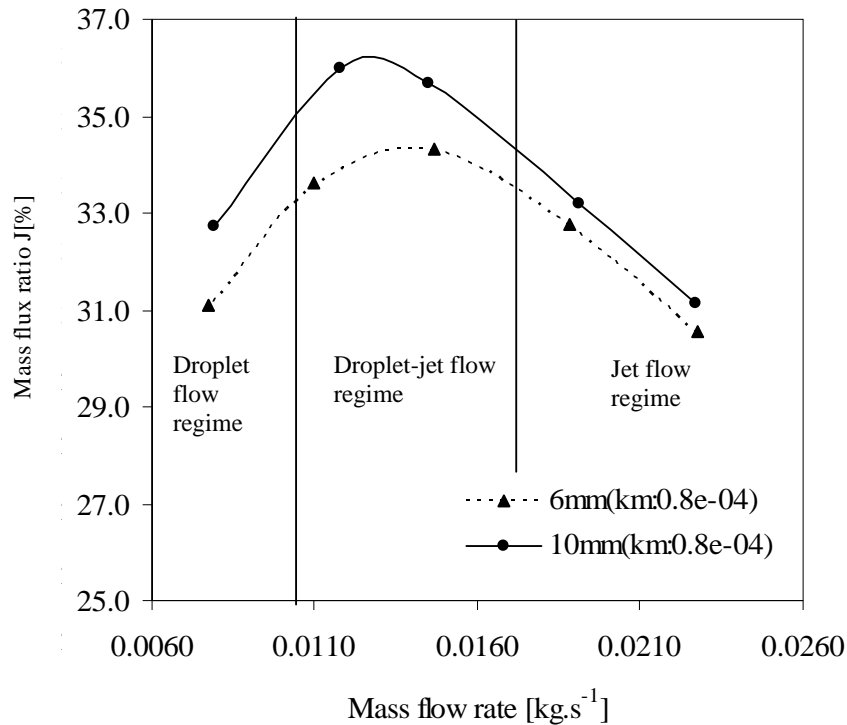


Figure 6.6 Mass flux ratio  $\left[ J = \frac{m_{vi}}{m_{vf} + m_{vi}} 100 \right]$  at varying flow rate and tube gap.

The results presented in Table 6.3 and 6.4 of the mass flux ratio are also plotted graphically in Figure 6.6 for the two tube gap situations. It seems that contribution of vapour absorption is more when 10 mm tube gap situation is considered. However, arriving at general conclusion from these results is hard because of difficulties of inter-tube fluid flow randomness, inter-tube flow hypothesis, uncertainty in data analysis and model predictions. Furthermore, the significance of mass flux ratio could become more useful if a mass flux ratio map is developed with solution mass flow rate similar to the

flow regime map developed by Hu and Jacobi [39]. For such development huge amount of numerical simulation data will become necessary, but the methodology developed in this present study could easily be used for this purpose.

### ***Results from the sensitivity test for the transfer coefficients***

The simulation data presented in Table 6.3 and 6.4 are based upon the known values of transfer coefficients to be used in the inter-tube absorption models. The model prediction could vary if the values of the transfer coefficients vary. As already discussed in section 3.2.2.4, the exact values of transfer coefficients during drop formation or steady jet absorption are unknown. A detailed sensitivity test for the use of varying transfer coefficients in the inter-tube absorption models was therefore undertaken and results are presented in Appendix C. The sensitivity tests reveal that if the values of the heat transfer and the mass transfer coefficient are increased, the inter-tube mass flux for vapour absorption increases with corresponding increase of mass flux ratio

$$\left[ J = \frac{m_{vi}}{m_{vf} + m_{vi}} 100 \right] \text{ and vice versa.}$$

From a scrutiny of the sensitivity data presented in Appendix C, a 40 percent increase of mass transfer coefficient from the base line value ( $k_m = 1.12\text{E-}04 \text{ m.s}^{-1}$ ) produces maximum 25 percent increase of mass flux ratio ( $J = 37 \%$ ) compared to that ( $J = 29.5\%$ ) using the base line mass transfer coefficient ( $k_m = 0.8\text{E-}04 \text{ m.s}^{-1}$ ) among all the operating conditions. Whereas, a 40 percent decrease of mass transfer coefficient from the base line value ( $k_m = 0.48\text{E-}04 \text{ m.s}^{-1}$ ) produces maximum 36 percent decrease of mass flux ratio ( $J = 19 \%$ ) compared to that ( $J = 29.5\%$ ) using the base line mass transfer coefficient ( $k_m = 0.8\text{E-}04 \text{ m.s}^{-1}$ ) among those operating conditions. Similar sensitivity data are obtained for heat transfer coefficient for which model predictions are found less sensitive. For example, a 40 percent increase of heat transfer coefficient from

the base line value produces maximum 9 percent increase of mass flux ratio among all the operating conditions. Whereas, a 40 percent decrease of heat transfer coefficient from the base line value produces maximum 16 percent decrease of mass flux ratio among those operating conditions. More data are presented in Appendix C from the sensitivity analysis.

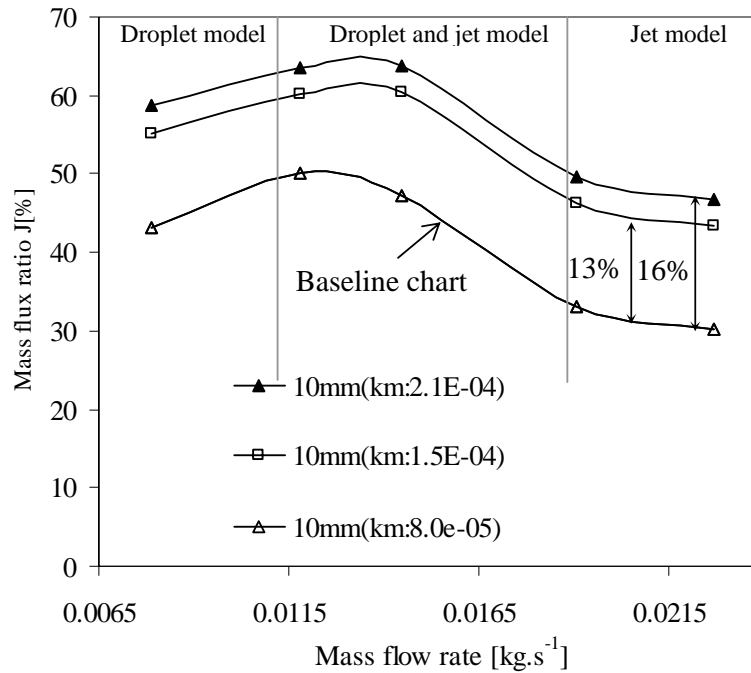


Figure 6.7 Sensitivity of mass flux ratio with higher mass transfer coefficient; Tube gap: 10 mm.

Sensitivity tests were further extended using the mass transfer coefficients given in Table 6.2. The results are plotted in Figure 6.7. The range varies from  $2.1 \text{ E-}04$  to  $1.5 \text{ E-}04 \text{ m.s}^{-1}$  for the mass transfer coefficient,  $k_m$ . The corresponding values of the mass flux ratio at different flow rate are compared to those values obtained using the baseline mass transfer coefficient  $0.8 \text{ E-}04 \text{ m.s}^{-1}$ . Figure 6.7 shows that when the mass transfer coefficient is  $2.1\text{E-}04 \text{ m.s}^{-1}$ , the mass flux ratio is found average 16 % more than the baseline chart. Similarly, when the mass transfer coefficient is  $1.5 \text{ E-}04 \text{ m.s}^{-1}$ , the mass flux ratio is found average 13 % more than the baseline chart.

### 6.3 Summary

The inter-tube flow was studied in an experimental set-up with LiBr as the working fluid as described in chapter 4. Video images obtained were used to determine the time variation of the volume and surface area of the drops formed in the inter-tube region. The volume and surface area of jets formed were obtained in a similar manner. The time dependent volume and surface area profiles were found at several droplet generating sites at different flow rates and at different tube gap situations. The detailed experimental results were presented in chapter 5. The hydrodynamic data obtained from the experiments formed the basis of a simplified model to estimate the vapour absorption rate in the inter-tube region. In this chapter, the simplified models were developed for droplet formation and steady jet flow in order to simulate the absorption performance in the inter-tube region. The predictions of the present models showed satisfactory agreement with those using the semi-empirical model developed by Siyoung and Garimella [88]. The contribution of the inter-tube absorption was calculated at different operating conditions and was found to vary from about 30 to 36 percents of the total absorption with assumed transfer coefficients. A sensitivity analysis showed significant dependence of the simulation results predicted by the models on the varying transfer coefficients.

## **CHAPTER 7**

### **FILM-INVERTING ABSORBERS**

Film-inverting absorber is a potentially viable alternative for the performance improvement of horizontal tubular absorbers. It provides better wetting of the tubes in the absence of various inter-tube flow modes. The alternate surface inversion helps to keep the vapor-liquid interface cool tube after tube. As a result Islam et al. [45] found significant performance improvement using the film-inverting configuration. However, the design of a practical film-inverting absorber needs further development. Islam et al. [45] developed a round-tube film-inverting absorber where guide vanes were used in between the tubes to affect inversion of the film surface. With the use of the guide vanes, the tubes remained in the same vertical plane as for a conventional tube bank. But there was no straightforward procedure for the design of guide vanes. In practice, the design of the guide vanes and their location was somewhat tedious. In this chapter, a new design is proposed for the round tube film-inverting absorber without the use of the guide vanes. The film-inverting hydrodynamics of this novel absorber configuration is tested experimentally to verify the film-inversion process. Later a numerical absorber model is developed to simulate the absorption performance with the film-inverting absorber. Several alternative designs are proposed to make use of the maximum possible surface area of the round tubes in the film-inverting configuration.

#### **7.1 Operating principles of film-inverting absorbers**

In the conventional horizontal tubular absorber, the absorbent solution flows over the cooled absorber surface as a falling film into which the refrigerant vapour is absorbed. The absorption of vapour at the vapour-liquid interface of the film results in the generation of heat of absorption which tends to raise the liquid film temperature. If this heat is not transferred rapidly across the film to the external coolant, the vapour

absorption process could be retarded by the high interface temperature. Much research effort has been devoted to find ways to enhance the vapour absorption process in the conventional tubular absorber [45]. The different types of modifications to improve the performance of the conventional design were discussed in chapter 1. The type of modification based upon the fluid flow characteristics of the falling film and the thermodynamic aspects of the absorption process was stated in section 1.5. One such technique was explored by Islam et al. [45] by implementing the film-inversion process. The purpose of film-inversion is to achieve repeated surface inversion of the falling film. The alternate surface inversion provides the relatively colder surface to come in contact with vapour, tube after tube. As a consequence, a higher vapour absorption rate of the falling film is retained over the tubes similar to the initial part of the absorber.

The principal of operation of the film-inverting round tube absorber is shown schematically in Figure 7.1. The solution flow is introduced at the top-most tube from the distributor on to one half of the first tube. The liquid flows over the tubular surface as a falling film and vapour is absorbed at the exposed surface of the film. Just before the liquid reaches the lowest point in the circular tube, it is guided to flow onto the opposite side of the second tube located directly below the first tube. A flow guiding fin is attached to the second tube to help smooth film-inversion between the tubes. With the help of the guide fin, the surface which was previously in contact with the wall of the first tube is exposed in the second tube. Simultaneously, the exposed film surface over the first tube is the inner surface of the second tube in contact with the wall. The same process continues in the reversed manner over the rest of the tubes. The periodic reversal of the exposed surface over the various tubes results in the enhancement of vapour absorption compared to the vapour absorption rate in the conventional design with same number of tubes.



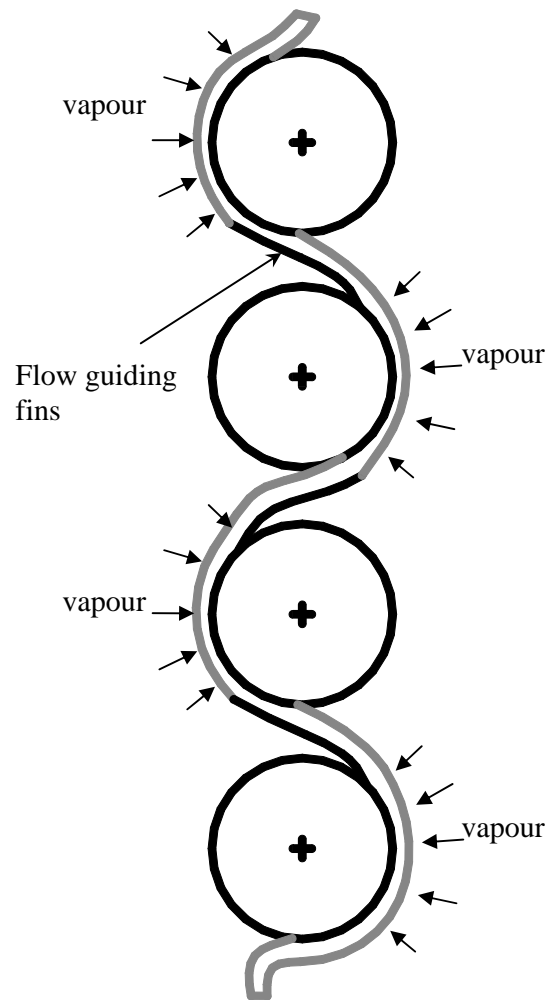


Figure 7.1 Flow over the film-inverting round tube absorber.

The film-inverting round tube absorber proposed by Islam et al. [45] required guide-fins for the purpose of guiding the film flow in the opposite direction as shown in Figure 7.1. The design parameters like the width, angular position of the fins have to be determined for the design of the film-inverting tubular absorbers. Furthermore, the location of the guide fins on the tubular surface decreases a fraction of the participating area of the tubes. In some instances more than 50 percent of the total surface area of the tubular absorber may become unused. In the present study, an alternative design of the film-inverting round tube absorber without the need for guide fins is explored. The basic

concept is to make use of the Coanda Effect for fluid flow over curved surfaces, as described in the following section.

## 7.2 The Coanda Effect

Coanda Effect is the tendency of a moving fluid, liquid or gas, to attach itself to a curved surface and flow along it. It means that when one side of a falling jet is close to a large solid curved surface, a partial vacuum is created between the jet and the surface, as a consequence of which, the jet tends to attach itself to the surface [17]. This is an important consequence of the pressure variation perpendicular to curved streamlines. Though from the definition of a streamline, fluid particles do not have any velocity component perpendicular they nevertheless experience an acceleration perpendicular to the curved streamline. Hence, a pressure variation occurs across the curved streamline because the acceleration requires a net force in the same direction.

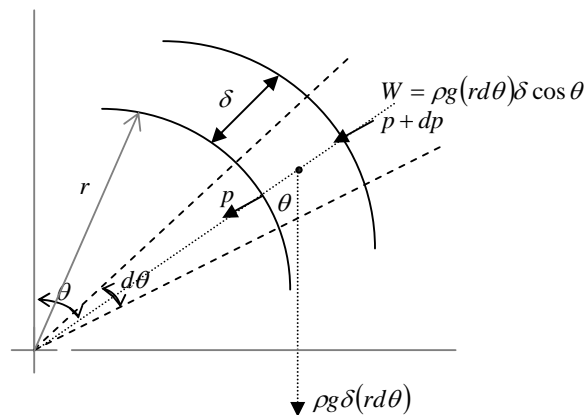


Figure 7.2 Pressure variation perpendicular to streamlines.

Considering two streamlines sufficiently close together and having same center of curvature as shown in Figure 7.2, a force balance of the fluid element of length  $\delta$  normal to streamlines, with cross-sectional area  $(rd\theta)$  and weight  $(\delta\rho g r d\theta)$  per unit length of the streamlines, follows that,

$$(p + dp)(r + \delta)d\theta - p(rd\theta) + (\rho grd\theta)\delta \cos \theta = \rho(rd\theta)\delta a_n \quad (7.1)$$

where  $p$  is the pressure at radius  $r$ ,  $(p + dp)$  is the pressure at radius  $(r + \delta)$  and  $\rho$  is the density of fluid. The centripetal acceleration is  $a_n = v^2 / r$ ; where  $v$  is the velocity along the radius  $r$ . Further simplification gives an expression for the pressure difference in the perpendicular direction of the streamlines as:

$$dP = \rho \delta \frac{v^2}{r} \quad (7.2)$$

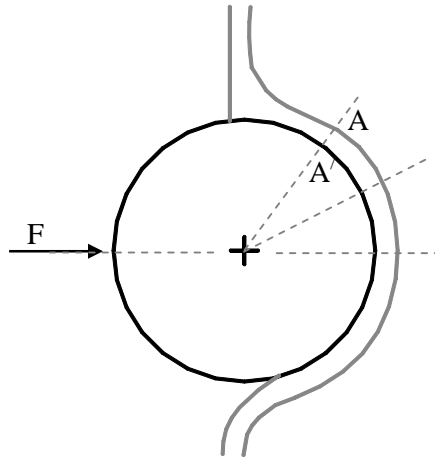


Figure 7.3 Demonstration of Coanda Effect [17].

As a consequence of this pressure variation, a jet of fluid has a tendency to attach itself to a convex solid body. A simple demonstration is the deflection of water jet by using a hollow cylinder as shown in Figure 7.3. When the cylinder is brought closer to the straight falling jet, the streamlines quickly follow the curvature of the cylinder because of a partial vacuum created in the neighborhood of the surface of cylinder. If the outer edge of the stream is at atmospheric pressure, the pressure at the surface of the cylinder is below atmospheric. As a result, the jet does not continue to flow downward at the end of the cylinder; instead it tries to bend towards the bottom of the cylinder and turns over to the opposite side depending on the fluid velocity as indicated in the Figure 7.3.

Coanda Effect has its many applications specially in the development of various fluid-flow devices. In the present study, the Coanda Effect is used to develop a novel film-inverting absorber which is described in the following section

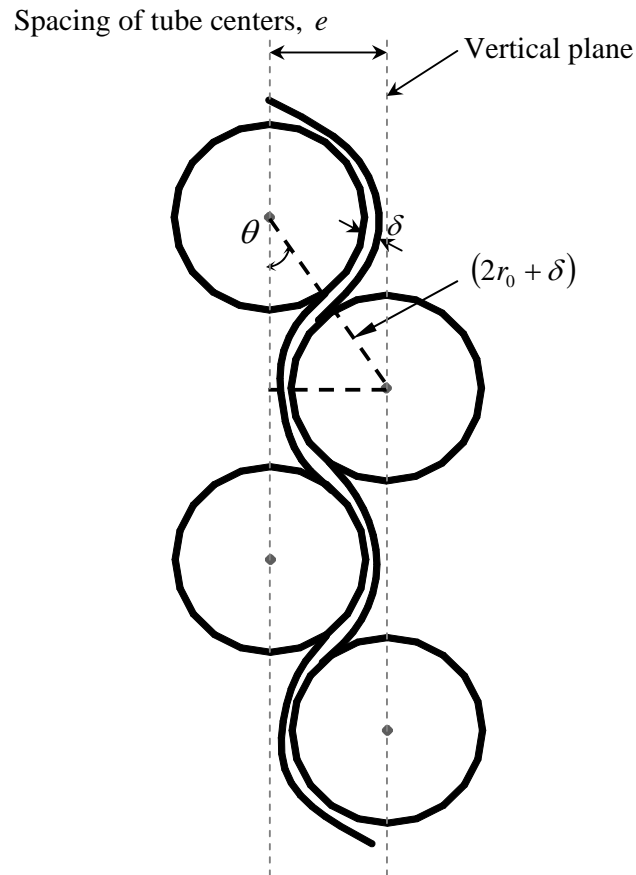


Figure 7.4 Coanda Effect based film inversion; by single film arrangement of the tubes.

### 7.3 Film-inversion based on the Coanda Effect

The basic concept of the proposed film-inversion process is to make use of Coanda Effect of fluid flow over a round tube surface. A thin film of liquid flowing down the side of a tube turns around the opposite side of a second tube when the latter is brought to touch the film. Such behavior of a liquid film can be explained with the help of Coanda Effect described above. The application of this effect actually turns the liquid film between two round tubes arranged vertically as shown schematically in Figure 7.4.

Just after turning on the opposite side of the second tube, the exposed surface of the film flowing over the first tube becomes the inner surface of the film over the second tube and vice versa. Using a number of tubes in an array, repeated film surface reversal, which is the main characteristic of a film-inverting absorber, can be achieved.

***Use of Coanda Effect: array of tubes***

Unlike the conventional design, the arrangement of the tubes for the Coanda-Effect based film-inversion requires the centers of alternate tubes to be in two vertical planes which are slightly separated as seen in Figure 7.4. The horizontal distance between the centers of two consecutive tubes in the array depends on tube gap  $\delta$  and leaving angle  $\theta$ .

Thus the spacing of tube centers  $e$  shown in Figure 7.4 can be expressed as:

$$e = (2r_o + \delta)\sin \theta \quad (7.3)$$

Experimental investigations reveal that the radial gap between two neighboring tubes has to be of the same order as the film thickness. The leaving angle  $\theta$  of the film must be selected to achieve maximum possible surface area of the film. The total participating area is then the sum of the exposed area of the film. Practical value of the leaving angle will be investigated experimentally.

**7.3.1 Experimental investigations of the Coanda-Effect Based Film-Inverting process**

An experimental program was undertaken to investigate the Coanda Effect-Based Film-Inverting (CEBFI) hydrodynamics. The same experimental set-up described in section 4.1 of chapter 4 was used to study the Coanda effect. For the present study, the test section was modified in order to arrange 6 tubes with their centers in two vertical planes. The rest of the set-up remained unchanged. The distributor was placed above the top-most tube in such way that the flow was only distributed to one side of the top most tube. A photograph of the set-up is shown in Figure 4.2.

### 7.3.1.1 Experimental procedure

Before starting the experiments, the test tubes are cleaned thoroughly with sand papers so that surface roughness is increased to provide better surface wetting. The test tubes are assembled in two vertical planes with the desired separation as shown in Figure 7.4. The radial gap between two neighboring tubes, which is nearly equal to the film thickness, is set by trial and error. The test tubes are adjustable from the sides which provide the required flexibility to change the gap. In particular, the horizontal or vertical distances between the axes of the tubes in the assembly could be adjusted even during the running of the experiment to ensure proper solution distribution in alternate directions. The experiment is normally started with a higher solution flow rate to ensure better surface wetting. The flow rate is then gradually decreased and the film flow is observed closely. At the desired flow rate when the film flow alternates from one tube to the next. The screws shown in Figure 7.5 are tightened to ensure the stability of the tube assembly. At different flow conditions, the flow pattern is recorded in video with a digital video camera [CANON MVX 35i], the purpose of which is to obtain the qualitative behaviour of the flow in the CEBFI absorber. The experiments were carried out with water as the working fluid.

### 7.3.1.2 Experimental results: flow observations

The flow characteristics of the film-inverting arrangement are observed from the video images. In Figure 7.5 (a), a left hand sided view of the film flow over the 6 tubes in the presence of illuminating light is shown. At the same operating conditions another view from the right hand side of the tubular arrangement is depicted in Figure 7.5 (b) without the use of the illuminating light. In both the figures, the alternate flow surfaces of the tubular arrangement are clearly noticeable. Studying closely the film flow over the tubes, the following observations are made.

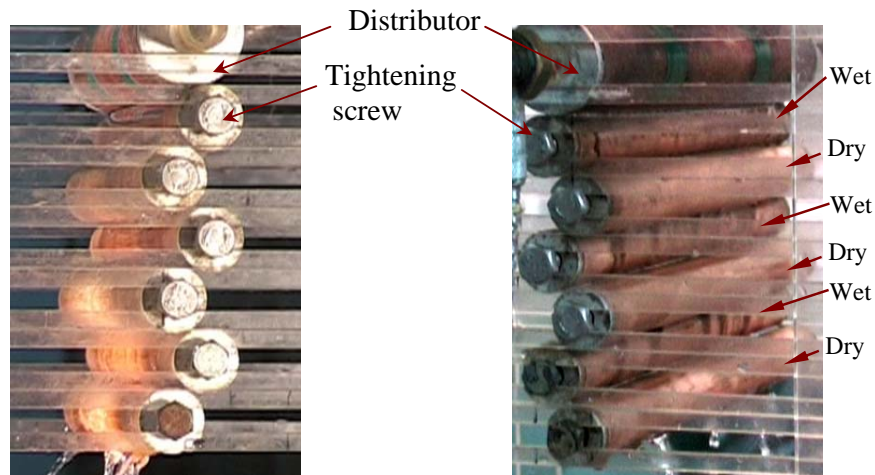


Figure 7.5(a) Left hand side view with light. Figure 7.5(b) Right hand side view without light.

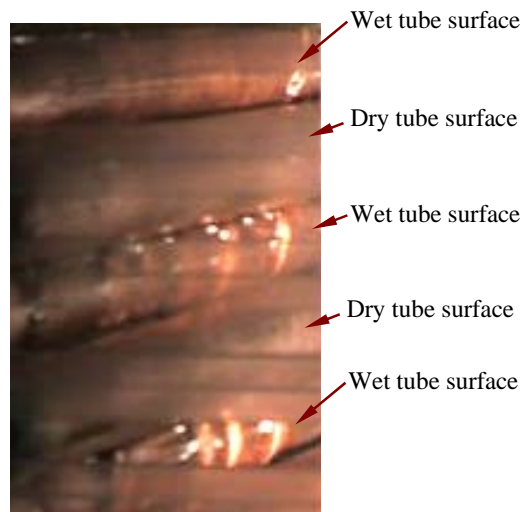


Figure 7.6 A closer view of the alternate flow surfaces.

The flow is introduced at the top-most tube from a distributor which is placed on one side of the top tube. As seen in the bottom-most tube of the arrangement of Figure 7.5(a) and (b), it is interesting to observe that the film flowing down one side of the tube turns around the bottom of the tube and leaves on the opposite side as jets. However in the presence of another tube, positioned slightly off the vertical plane of the first tube and touching the liquid film, the film turns around the second tube. It turns around the nearest curved surface as shown in the case of the upper tubes in the arrangement. This

way the film travels around the alternate sides of the tubes if a bank of staggered tubes is constructed. The radial gap between any two tubes is nearly equal to the film thickness as illustrated in Figure 7.4, which is sufficient for the liquid film to turn and flow without any obstruction.

In Figure 7.6, a closer view of the alternate flow surfaces is presented. The wet surface of the liquid film, falling down the first tube, is seen in the figure. Because the film makes the turn on the opposite side of the second tube, after leaving the first tube, the dry surface of the second tube is observed. In the third tube, where the film turns around the opposite side shows a wet surface in the image. The wet surfaces are identifiable in the figure as reflecting surfaces in the presence of illuminating light. Thus for the bank of six tubes, the alternate film inversion is achieved without the use of guide vanes.

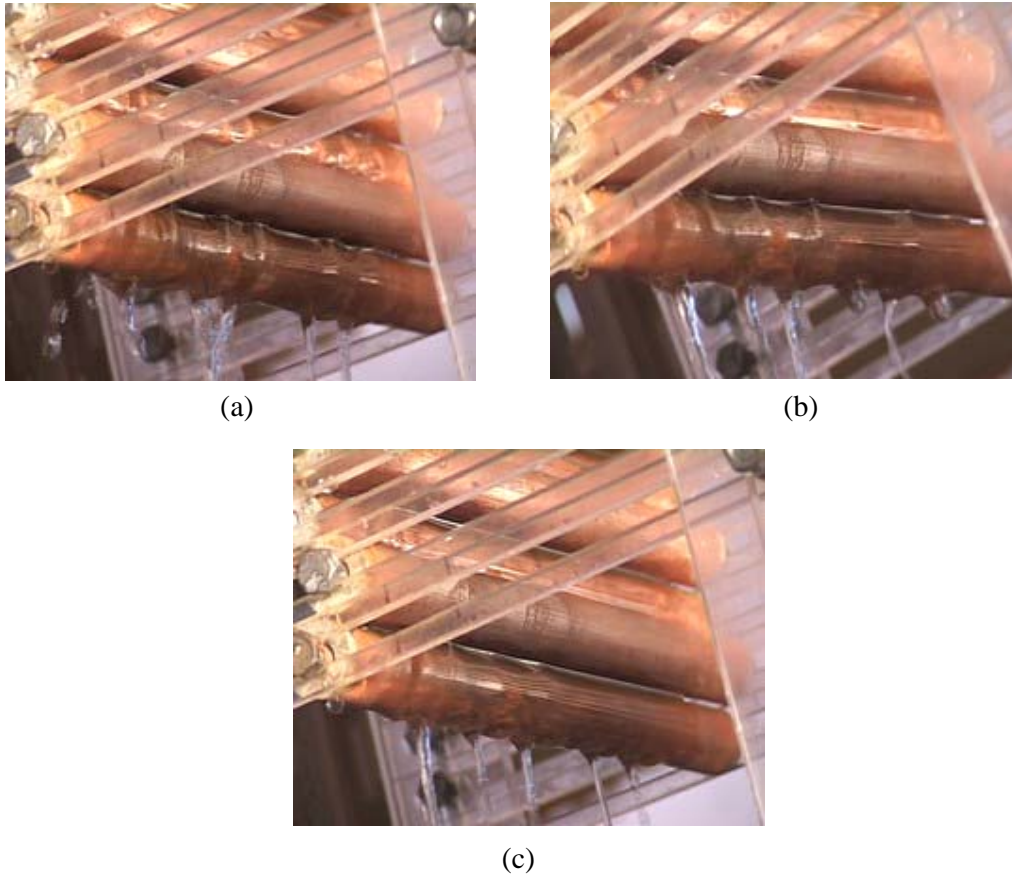


Figure 7.7 Film flow at three different flow rates (a)  $0.022 \text{ kg.s}^{-1}$  (b)  $0.016 \text{ kg.s}^{-1}$  (c)  $0.008 \text{ kg.s}^{-1}$



### 7.3.1.3 Effect of solution flow rate

The effect of varying solution flow rate during film-inversion was investigated. Figures 7.7(a)-(b) show the film flow over the tubes at higher flow rates while Figure 7.7(c) shows the same at lower flow rate. The tube configurations were not changed with the increase of flow rate. At higher flow rate, the flow surface over the tubes is wavier though the waviness diminishes if the flow rate is gradually decreased. Presence of surface waves in the form of rings especially at the higher flow rate may prevent uniform distribution of the flow. It is therefore desirable that the gap between the tubes be such that the film flows with uniform surface wetting and without any flow obstruction. If the tube gap is too large film inversion will not occur because the adjacent tube loses contact with the liquid film. Thus an optimum tube gap has to be provided to ensure film flow without obstruction but sufficiently narrow to cause the Coanda Effect.

### 7.4 Coanda-Effect Based Film-Inverting Absorber (CEBFIA) - numerical model

A detailed numerical model was used to make performance assessment of the Single Film Tube- Coanda- Effect Based Film-Inverting Absorber (SFT-CEBFIA). The model is based on the single round tube model described in section 3.1. It has been discussed previously in section 3.1 that the round tube model requires as an input the incoming and leaving angles of a film to the tube. Since these parameters can be selected arbitrarily, single film tube distributions in a vertical column can easily be incorporated for the CEBFIA model.

The single-tube-model is extended to incorporate the film-inverting process at each inversion point keeping the flow along one side of a tube as illustrated in Figure 7.4. Therefore changes have to be made in the detailed round tube model by defining the film flow path over the tube arrangement. The boundary conditions for the solution film in the physical model are changed as the film flows from one tube to the next so that the inner film surface of the upper tube becomes the exposed surface of the next tube

below. Similarly, the film interface of the upper tube becomes the inner surface of the lower tube. To represent these boundary conditions at each film inversion, the concentrations and temperatures of the solution film at different grid points are changed as follows

$$\begin{aligned} w(\theta_i, i)|_L &= w(\theta_o, N-i)|_{L-1} \\ T(\theta_i, i)|_L &= T(\theta_o, N-i)|_{L-1} \end{aligned} \quad \text{For } 0 \leq i \leq N \quad (7.4)$$

where  $L$  is the current tube,  $\theta_i, \theta_o$  are the entering and leaving angles of the film to the tube.

For all segments of the tube, the direction of the  $y$ -axis is taken as positive from the tube surface to the exposed film surface and  $x$ -axis is positive along the solution flow direction. The velocity field is assumed to be fully-developed following each film inversion and given by the Nusselt velocity distribution [19]. The serpentine coolant flow model is the same as discussed in section 3.1.3 except that the heat flow from the solution film to the coolant occurs only from one side of the tube over which the solution film flows. Solution procedure described in section 3.1.4.3 is followed here with the inclusion of film-inversion tube after tube.

As explained in Figure 3.1, the variation of the film thickness is such that it becomes thicker in the regions nearer to the top and bottom of a tube. Therefore, the solution flow domain has to begin and end sufficiently away from these points of the tube. Since the choices of the film entering and leaving angles to a tube are arbitrary at this stage, a sensitivity analysis was carried out to determine their impact on the predictions of the model. Some results of the sensitivity tests are presented in Table 7.1. For a particular film entering angle to the first tube ( $9^\circ$ ), the film leaving angle to the first tube is varied. The film entering and leaving angles for the rest of the tubes are equal to the film leaving angle to the first tube. For 4 different values of film leaving angle for the first tube ( $9^\circ, 16^\circ, 21^\circ, 26^\circ$ ), the outlet conditions of bulk temperature, concentration, coolant

outlet temperature and mass flux of absorbed vapour are computed. The results presented in the last four columns of Table 7.1 indicate that the outlet conditions of the film-inverting tubular absorber are not strongly dependent on the film entering and leaving angles for the absorber tubes.

**Table 7.1 Sensitivity of the entering and leaving angles**

$\theta_i$ [First tube]	$\theta_o$ [First tube]	$\theta_i$ [Second tube onwards]	$\theta_o$ [Second tube onwards]	$T_{so}$ [ $^{\circ}C$ ]	$w_{so}$ [%LiBr/100]	$T_{wo}$ [ $^{\circ}C$ ]	$m_v$ [ $kg.m^{-2}.s^{-1}$ ]
9	9	9	9	39.82	0.55991	28.77	0.004122
9	16	16	16	40.08	0.55995	28.76	0.004117
9	21	21	21	40.11	0.56020	28.73	0.004092
9	26	26	26	40.09	0.56060	28.69	0.004052

**Table 7.2 Experimental operating conditions of Islam et al. [45]**

Set	$T_{si}$ [ $^{\circ}C$ ]	$w_{si}$ [%LiBr/100]	$T_{wi}$ [ $^{\circ}C$ ]	$m_w$ [ $kg.s^{-1}$ ]	$m_{si}$ [ $kg.m^{-1}.s^{-1}$ ]	$p$ [kPa]
1	39.8	0.604	26.53	0.0887	0.0595	2.15
2	39.8	0.604	26.58	0.0887	0.0446	2.08
3	39.8	0.604	29.43	0.0887	0.0446	2.08
4	39.8	0.604	26.45	0.0887	0.0298	2.21
5	39.8	0.604	29.3	0.0887	0.0298	2.21

#### 7.4.1 Numerical results for Single Film Tube-CEBFIA

The behaviour of SFT-CEBFIA is investigated by performing a detailed numerical simulation study. The operating conditions are selected from the experiments of Islam et al. [45] which are listed in Table 7.2. To obtain a clear understanding of the film inverting mechanism, variation of film temperature, concentration of lithium- bromide and also the concentration of water vapour in the solution are presented in the following

figures 7.8-7.12 at different cross-sections of the flow. The results shown in these figures provide useful information about the development of both the temperature and concentration field after the film inversion at each tube. The lithium-bromide and water vapour concentration variation across the film are shown separately in Figures 7.9 and 7.10 respectively.

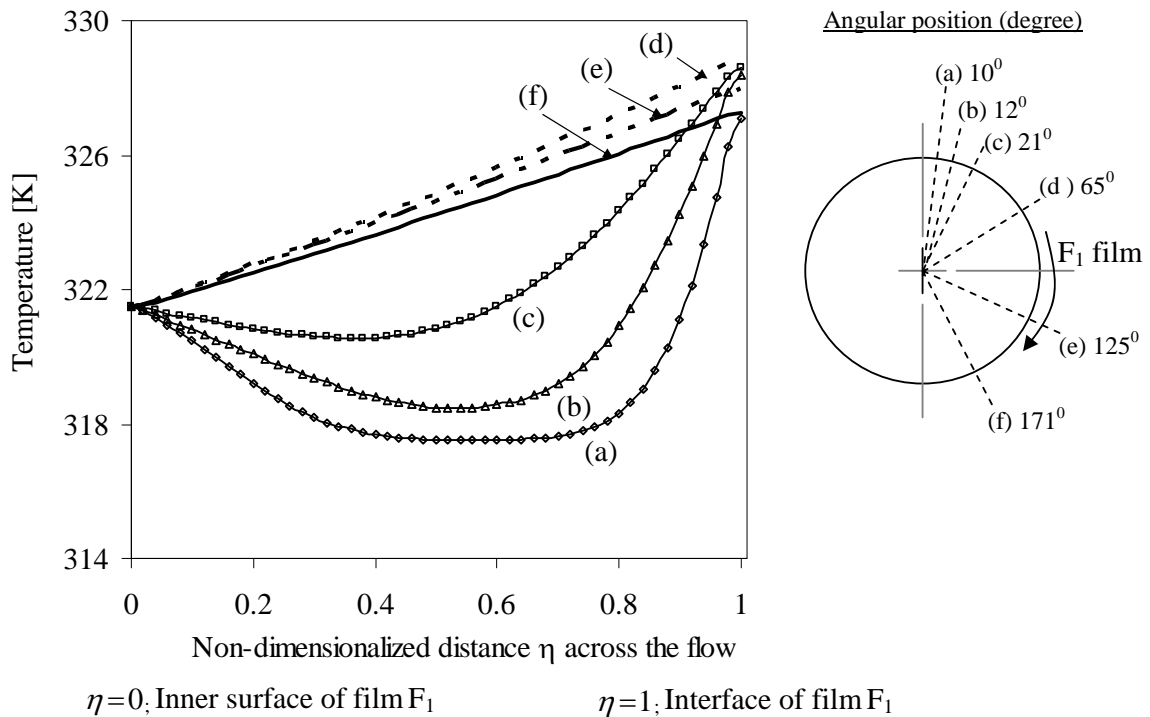


Figure 7.8 Temperature profile across the flow [ $\eta = y/\delta$ ] for the first tube in film-inverting absorber; operating conditions : set-1 in Table 7.2.

In Figure 7.8 temperature profiles at different cross sections of the film along the flow direction of film-inverting absorber are drawn to show the development of temperature field in the very first tube. The solution enters the first tube with a uniform distribution of temperature at the film entering angle  $9^\circ$ . With the increase of angular position, the temperature profile gradually becomes linear as expected. Figure 7.9 shows the development of concentration field where the concentration of LiBr at various cross sections of the film along the flow direction is plotted. Similar to the temperature profile, the film enters to the absorber tube with a uniform concentration profile which

gradually changes to take the shape of fully developed profile. Figure 7.9 suggests that the concentration changes sharply near the interface region and remains nearly constant in the rest of the film. However, as the flow progresses along the tube circumference, the lithium-bromide concentration gradually decreases even near the inner-side of the film, as seen for angles from  $80^{\circ}$  to  $171^{\circ}$ .

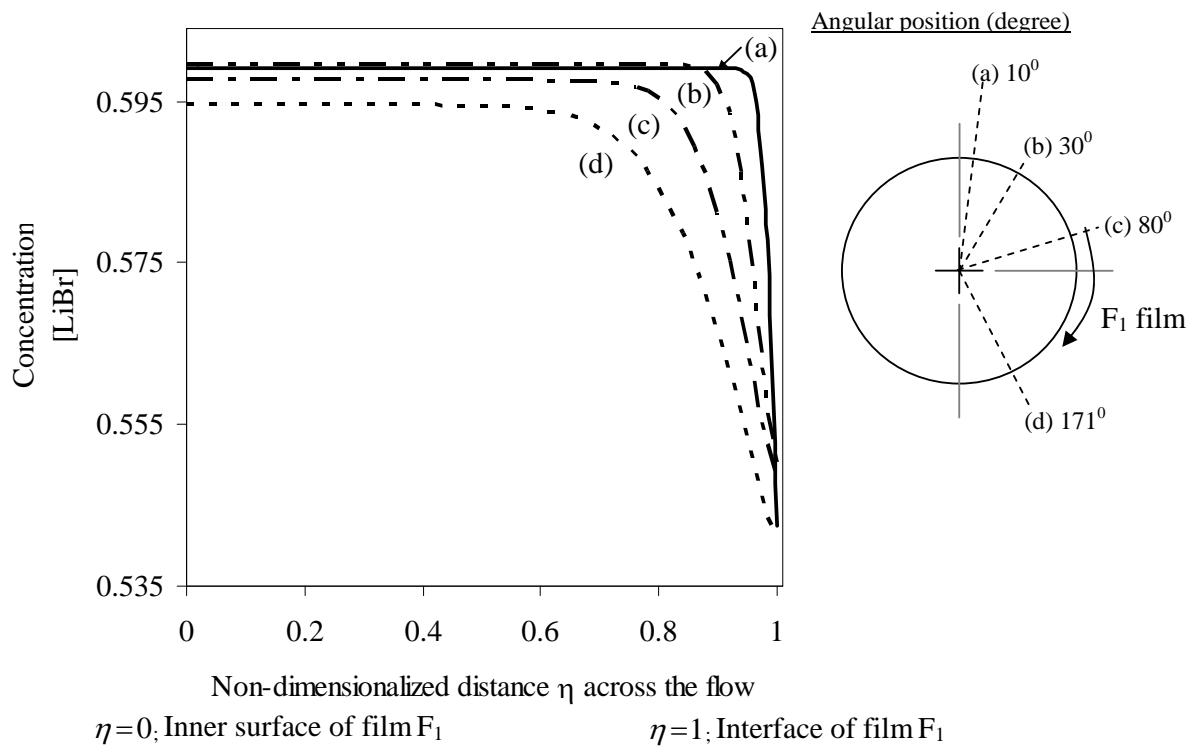


Figure 7.9 Concentration profile across the flow [ $\eta = y/\delta$ ] for the first tube in film-inverting absorber; operating conditions: set-1 in Table 7.2.

After film inversion, the solution film enters the next tube below with an inverted concentration and temperature profiles from the exit of the upper tube for which results are presented in Figures 7.10-7.12. When the surface with higher percentage of LiBr or lower percentage of water becomes the exposed surface of the next tube due to film inversion, rapid absorption occurs at the interface region. As a result LiBr concentration drops significantly at this surface and absorbed vapor diffuses into the stream of solution across the film which is presented in Figure 7.10.

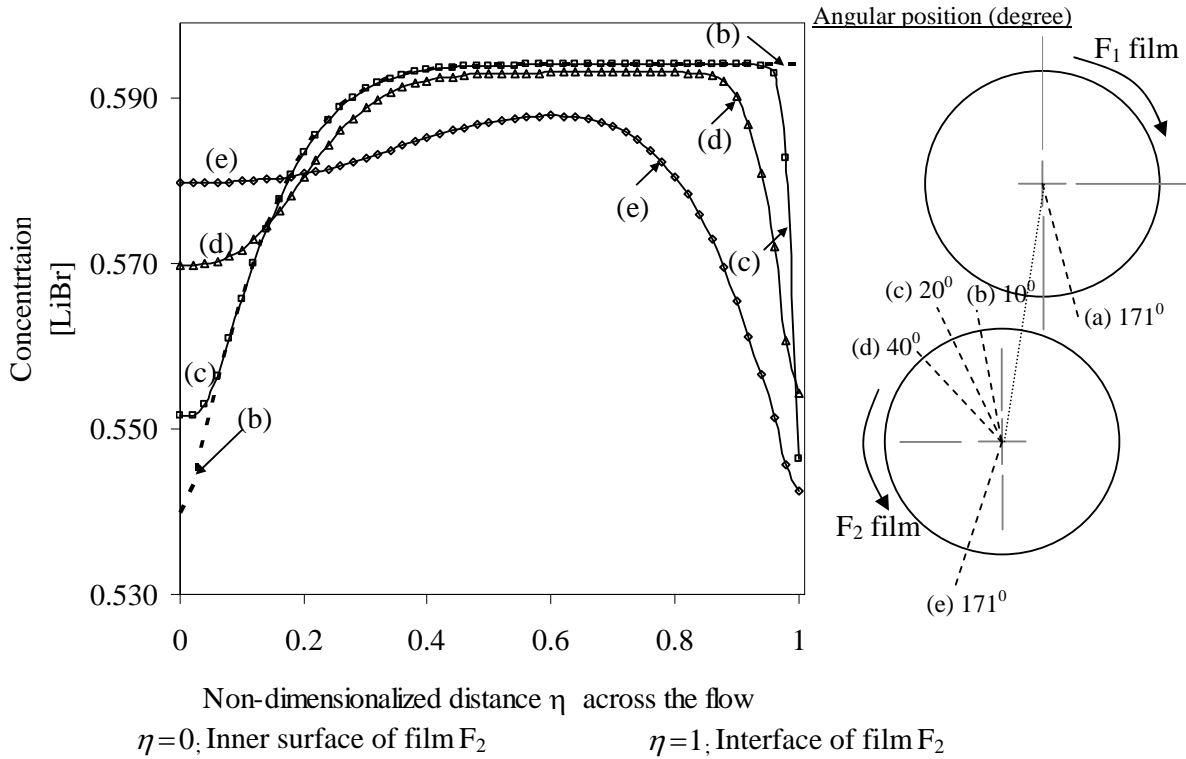


Figure 7.10 Concentration profile (% of LiBr/100) across the flow [ $\eta = y/\delta$ ] for tube 2 in film-inverting absorber ; operating conditions : set-1 in Table 7.2.

However the water vapour does not penetrate deep into the film because the concentration of water vapour is higher at the inner side of the film which previously was the exposed surface of the film. At the inner side of the film nearer to the tube wall, higher percentage of water vapour exists just after the film inversion which is exhibited in Figure 7.11. Consequently higher concentration of water vapour in this region causes the diffusion of water vapour from the inner surface to the bulk of solution. Therefore, a zone showing an almost flat concentration profile is seen at the middle of the film in both Figures 7.10 and 7.11. After traveling further distance down the tube with continuous vapour absorption at the exposed surface, more vapour penetrates the solution film towards the inner side of the film. Moreover, water vapour from the near wall region gradually moves from that side which shows a decrease of water percentage there as shown in Figure 7.11 for angles from  $18^\circ$  to  $171^\circ$ . Hence the near wall LiBr

concentration increases with the increase of angular position shown in Figure 7.10 for the same angles from  $18^\circ$  to  $171^\circ$ .

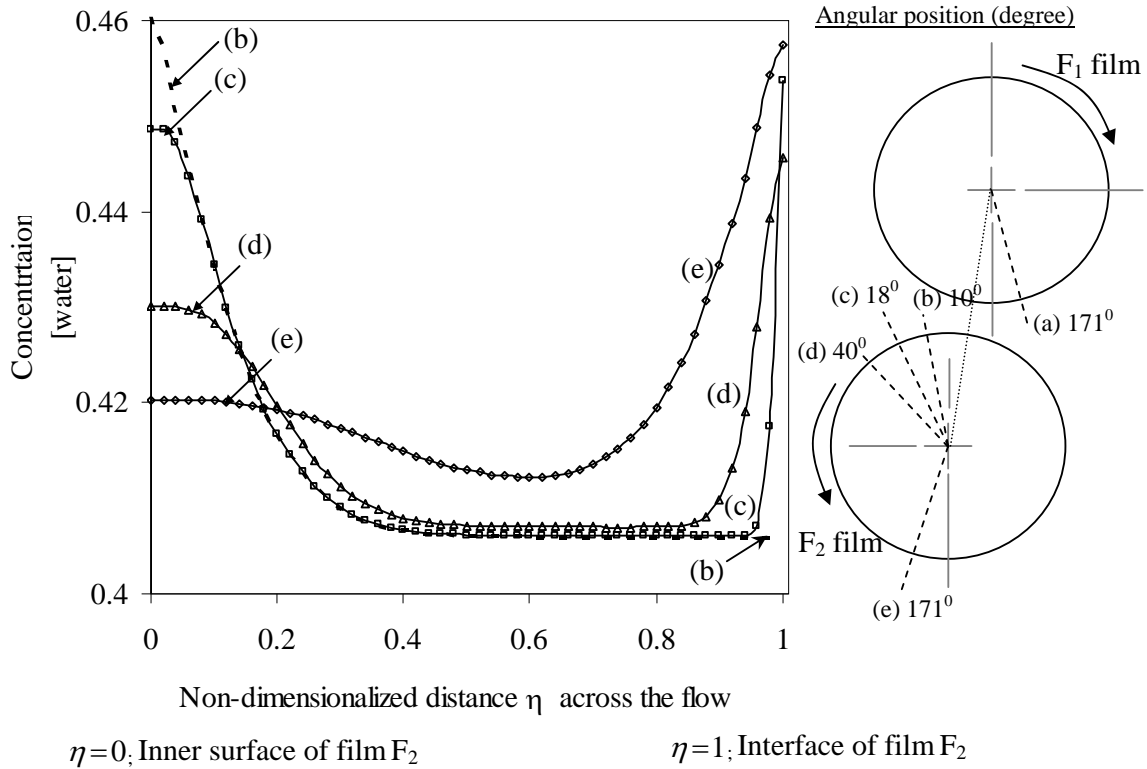


Figure 7.11 Concentration profile (% of water/100) across the flow [ $\eta = y/\delta$ ] for tube 2 in film-inverting absorber; operating conditions: set-1 in Table 7.2.

The development of the temperature field in the second tube is shown in Figure 7.12. After the film inversion the cold surface of the film becomes the exposed surface and hot surface of the film becomes the inner surface. Therefore the new film interface temperature is lower than the equilibrium temperature of the solution which actually causes rapid absorption of vapour right after the film inversion. As a result of this, the interface temperature increases very sharply which gradually decreases towards the bulk region. Since there is hot solution in the near wall region, the temperature starts increasing again after about the middle section of the film. This is the reason for the S-shaped profile of temperature as seen at around 10 to 20 degree from the entrance of the tube. Thereafter, heat flows from the hot film to the coolant causing a decrease of

temperature which tends to produce an almost linear profile indicating that temperature field has become fully developed.

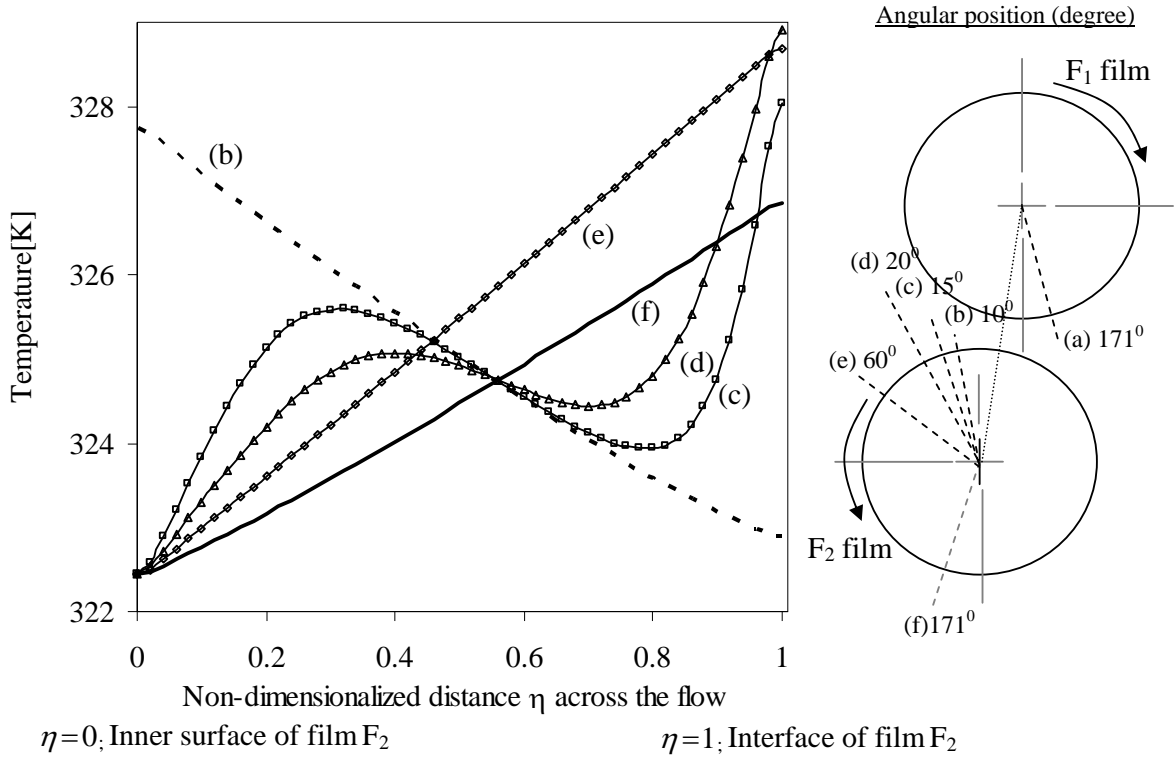


Figure 7.12 Temperature profile across the flow [ $\eta = y/\delta$ ] for tube 2 in film-inverting absorber; operating conditions: set-1 in Table 7.2.

Figures 7.13 (a)-7.13(c) show the mass flux, bulk and interface temperature and concentration variations over the first few tubes for the continuous falling film and inverted falling film predicted by the respective models. It was observed from the experimental study that in the film-inverting arrangement the liquid film moved continuously from one tube to the next because of the smaller gap between the absorber tubes. At each film-inversion, the small gap between the tubes helps to redistribute the film without drop/jet/sheet flow as happens in conventional tubular absorber. Therefore, for the sake of comparison, the inter-tube absorption contribution is not included in the continuous falling film absorber model.



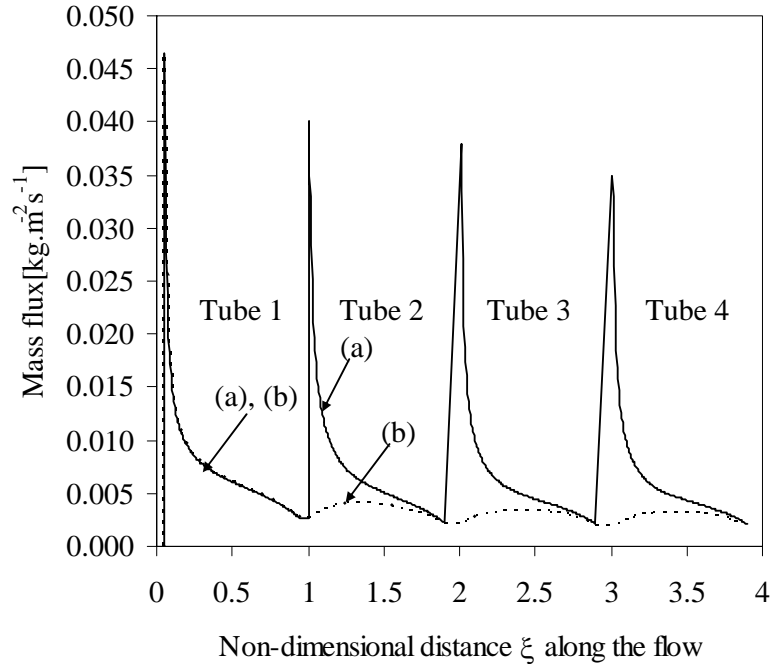


Figure 7.13(a) Variation of mass flux of water vapor along the direction of flow [ $\xi = \theta/\pi$ ]; (a) film-inverting absorber; (b) continuous falling film absorber; operating conditions: set-1 in Table 7.2.

In Figure 7.13(a), the film-inverting arrangement shows much higher absorption rate especially in the tubes after the first tube. The steep rise in absorption rate at the entering region of the falling film just after each film inversion demonstrates the usefulness of film-inverting concept as a means for performance improvement. Following the film inversion, the colder interface quickly attains equilibrium conditions after absorbing a large amount of water vapour. This is the reason for the sudden increase of mass flux seen at the entrance region of tube 2. The high absorption rate at this region also generates a large amount of heat which slowly diffuses into the film. Because of the rapid rise of the temperature at the interface there is a steep decrease of absorption rate shortly after the entrance region. However, with the gradual development of temperature field as exhibited in Figure 7.12, the absorption rate gradually decreases, though with a higher rate than the continuous falling film absorption rate, until film inversion is repeated in the next tube.

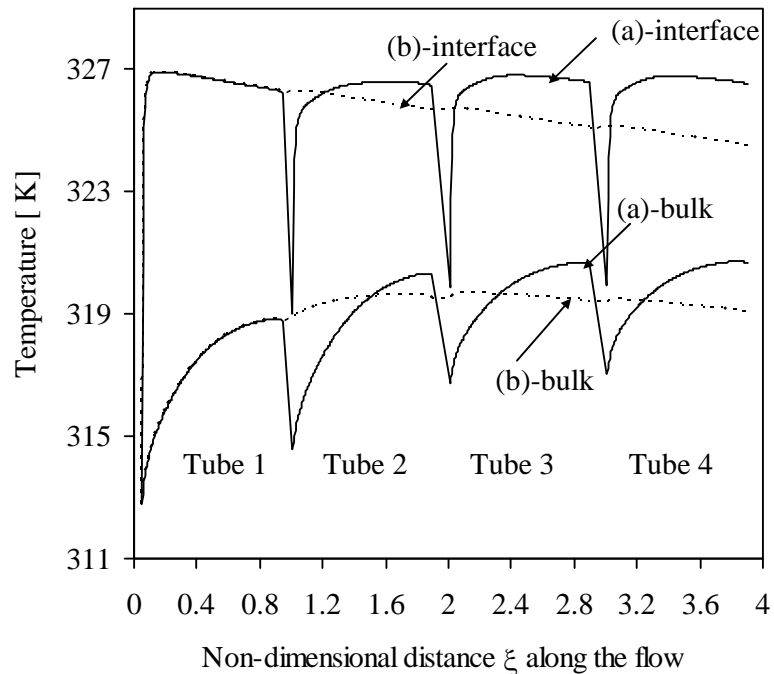


Figure 7.13(b) Variation of bulk and interface temperature along the direction of flow [ $\xi = \theta/\pi$ ]; (a) film-inverting absorber; (b) continuous falling film absorber; operating conditions: set-1 in Table 7.2.

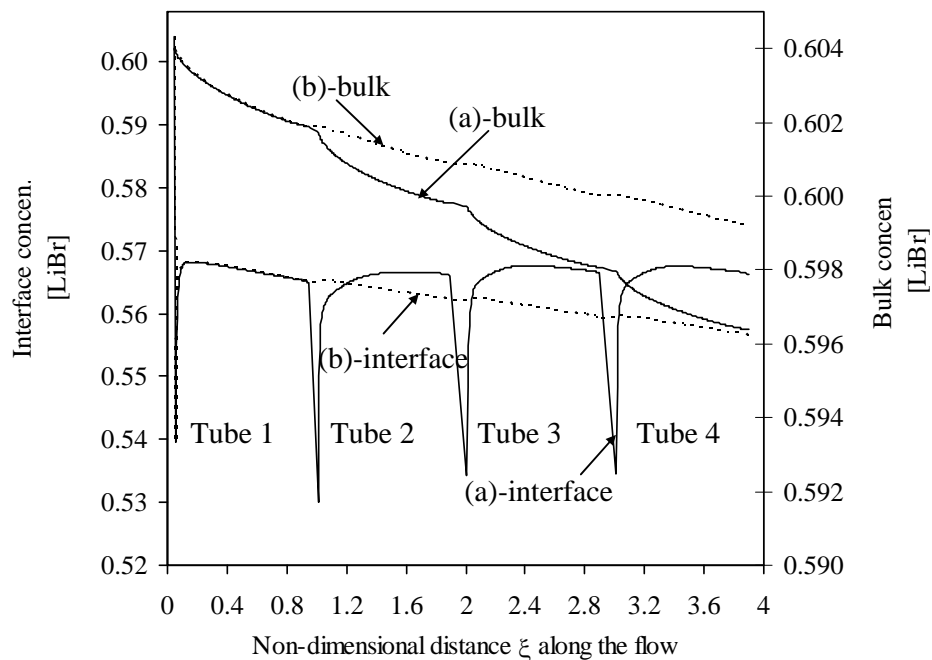


Figure 7.13(c) Variation of bulk and interface concentration along the direction of flow [ $\xi = \theta/\pi$ ]; (a) film-inverting absorber; (b) continuous falling film absorber; operating conditions: set-1 in Table 7.2.

In Figure 7.13(b), the variations of bulk and interface solution temperature are shown over the first few tubes of the absorbers. In the continuous falling film absorber, the bulk temperature shows gradual increase in the first tube which slowly decreases in the rest of the tubes. When film is inverted in the second tube, bulk temperature drastically drops right after the film inversion. As the vapour absorption continues at the interface, bulk temperature gradually increases and attains a maximum at the end of the tube. The whole process is repeated in the other tubes showing an oscillatory pattern of bulk temperature variation in the film inverting absorber. The interface temperature shows gradual decrease along the entire length of the continuous falling film absorber as also seen in Figure 7.13(b). When film inversion occurs in the second tube, the interface temperature drastically drops because of the surface reversal at the entry region of this tube. But unlike the bulk temperature, due to a large amount of vapour absorption the interface temperature sharply increases right after the film inversion and remains nearly steady in the rest part of the tube. The whole process is again repeated in the rest of the tubes with an oscillatory pattern of temperature variation at the interface.

As shown in Figure 7.13(c), the variations of bulk and interface concentration of LiBr are plotted along the first few tubes of both film inverting and continuous falling film absorbers. In both absorbers, bulk concentration gradually decreases along the flow direction. However, the drop in LiBr concentration is more in the film inverting absorber due to the higher absorption rate in this absorber. In the interface region, the gradual drop in LiBr concentration is shown in the figure by the continuous falling film absorber. When film inversion occurs, surface reversal causes drastic drop of concentration in the entrance region of a tube. But concentration sharply rises shortly after the film inversion followed by a gradual increase. In the later part of the tube, concentration shows slight decrease until film inversion is repeated in the next tube. The

oscillatory pattern of interface concentration is visible as the film inversion continues tube-after-tube.

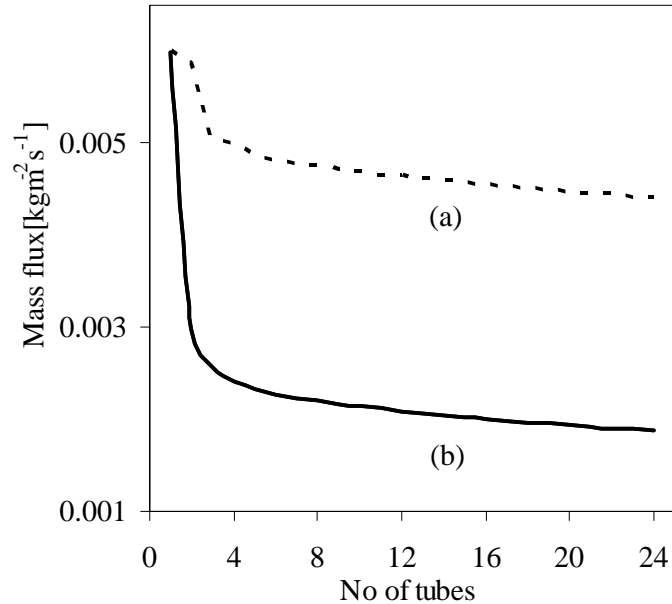


Figure 7.14 Tube-wise variation of mass flux; (a) by the film inverting tubular absorber, (b) by the conventional absorber without film-inversion; experimental condition: set-2 in Table 7.2.

#### 7.4.2 Performance improvement by the film-inverting absorber

Islam et al. [45] tested the performance of a tubular absorber with and without film inversion in the same experimental set-up under similar operating conditions. They developed a numerical model assuming the flow over the tubes to be equivalent to the flow over vertical plate segments. The predictions of the physical model were then compared with experimental data. In the present study, the film-inverting absorber model is developed based on single tube model taking into consideration the curvature effect of each tube. The numerical results obtained from present film-inverting model are compared with the experimental results of Islam et al. [45] in order to verify the predictions. The experimental conditions are given in Table 7.2.

Figure 7.14 shows the tube-wise variation of vapour mass flux by the two tubular absorbers. For the conventional tubular absorbers, the mass flux drops drastically after

the first tube. When the absorption begins at the first tube, the film-interface temperature rises sharply. The interface temperature reduces thereafter as the heat starts to diffuse from bulk solution to the coolant. But continuous absorption process retains higher interface temperature which actually impedes further absorption, especially after the first tube of the conventional tubular absorber.

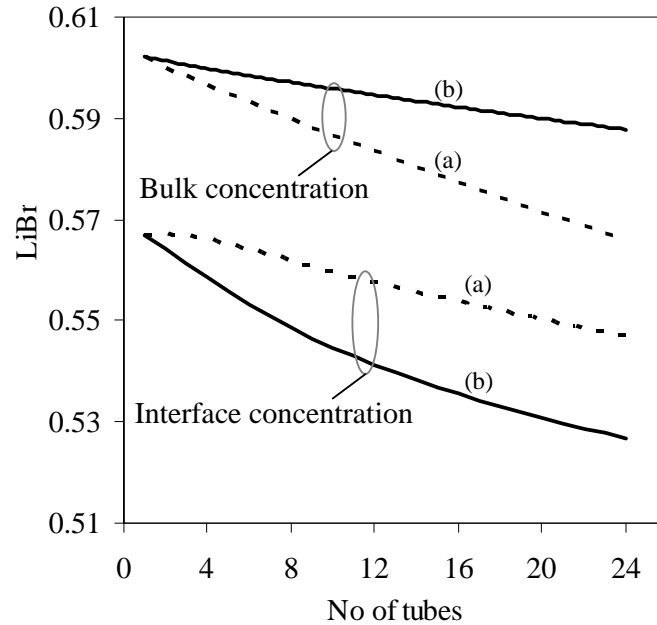


Figure 7.15 Variation of tube-wise averaged interface and bulk concentration (%LiBr/100); by the (a) film inverting tubular absorber, (b) conventional absorber without any film-inversion; experimental condition: set-2 in Table 7.2.

For the film-inverting absorber, the alternate surface inversion helps a colder surface to take part in absorption at the interface such that the average temperature at the interface region is lower. As a consequence, the absorption rate remains higher tube after tube. This way the film-inverting absorber produces a larger absorption of vapour than the conventional tubular absorber. Figure 7.15 illustrates the changes of tube-wise averaged interface and bulk concentration of LiBr solution over the tubes. The bulk concentration drop of the film-inverting absorber is larger because of the higher mass flux of absorbed vapour.

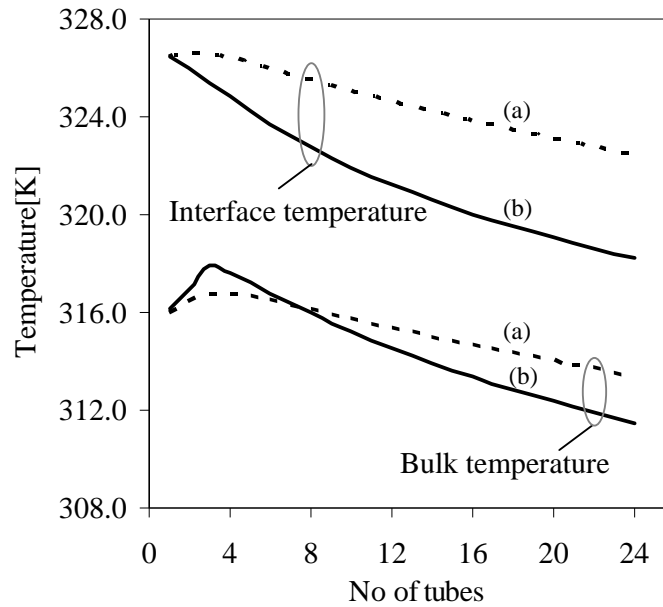


Figure 7.16 Variation of tube-wise averaged interface and bulk temperature; by the (a) film inverting tubular absorber, (b) conventional absorber without any film-inversion; experimental condition: set-2 in Table 7.2.

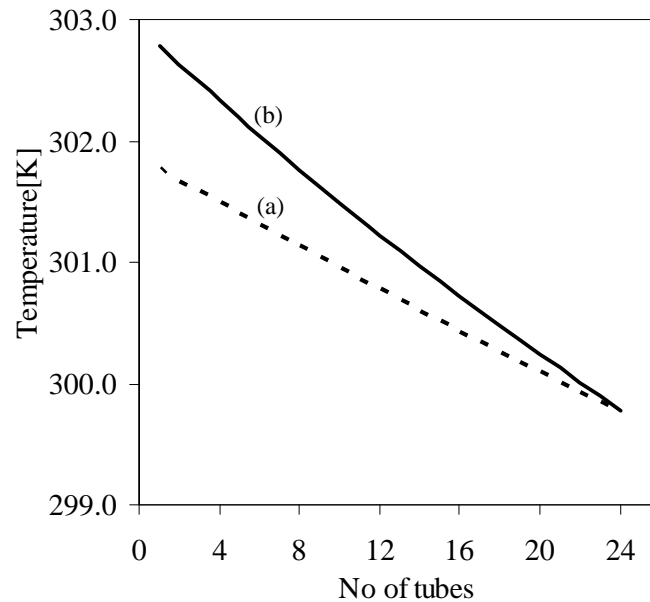


Figure 7.17 Tube-wise variation of coolant average temperature; by the (a) film inverting tubular absorber, (b) conventional absorber without any film-inversion; experimental condition: set-2 in Table 7.2.

In Figure 7.16, the variation of tube-wise averaged interface and bulk temperature of LiBr solution is shown. The solution leaves the film-inverting absorber with higher bulk temperature. The initial sharp rise of temperature in the conventional absorber is reduced in the case of film-inverting absorber. The sharp rise of bulk temperature in the first few

tubes of the conventional absorber occurs mainly because of the difference between the inlet solution temperature and the equilibrium temperature at the inlet concentration. If the inlet solution temperature is much lower than the equilibrium temperature at the inlet, which is the case of the experiments of Islam et al. [45], initially a large amount of vapour is absorbed. As a result, the bulk temperature increases sharply in this region. The details of this process are also discussed in section 3.2.5. In the case of film-inverting absorber, surface reversal helps better transfer of heat in the film causing reduced rise of temperature near the entrance of the absorber.

Figure 7.17 shows the coolant average temperature variation along the absorber. The rise of coolant temperature for the film-inverting absorber is less than the rise of temperature by the conventional absorber because only half of the coolant tubes are participating in the process. As a result, less heat is transferred to the coolant which actually causes the solution film to leave the absorber with higher bulk temperature as shown in Figure 7.16.

**Table 7.3 Absorption performance of tubular film-inverting absorbers**

Set no.	Average mass flux with film inversion [ $kg.m^{-2}.s^{-1}$ ]		Average mass flux without film inversion [ $kg.m^{-2}.s^{-1}$ ]		Percent change with film inversion	
	Present model	Experiments of Islam et al.[45]	Present model	Experiments of Islam et al.[45]	Present model	Experiments of Islam et al.[45]
1	0.004702	0.004060	0.002522	0.002130	86.4	90.6
2	0.004123	0.004140	0.002242	0.002050	83.9	102.0
3	0.004082	0.004170	0.002229	0.002070	83.1	101.4
4	0.004473	0.004070	0.002296	0.002120	94.8	92.0
5	0.004390	0.003930	0.002259	0.002090	94.4	88.0

Table 7.3 presents average mass flux computed for a tubular absorber with and without film inversion at various operating conditions of Islam et al. [45]. The average mass flux was computed based upon the inlet and outlet concentration difference of LiBr solution

after flowing over the bank of horizontal tubes. The operating conditions are summarized in Table 7.2. The numerical model predicts an enhancement of vapour mass flux due to film inversion of about 83-95 percent whereas the vapour mass flux enhancement measured in the actual experiments of Islam et al.[45] were 88-102 percent. The numerical results verify the significant performance improvement due to film inversion as was also observed in the actual experiments of Islam et al. [45]. However the numerical model under predicts the vapour mass flux enhancement. The reason for this lower enhancement predicted by the numerical models is probably due to the limitations of the models, in particular, the exclusion of partial wetting of the tubes. It was observed that film-inverting process causes better film flow distribution over the tubes as shown in Figure 7.5(b). Hence the use of complete wetting of absorber tubes is justified for the film-inverting absorber. On the contrary, for the conventional design without the film-inversion, complete wetting of the tubes is an over-estimation, because the conventional design does involve the partial wetting, as discussed in section 3.3. Therefore, assumption of complete wetting for both the models predicts less performance improvement by the film-inversion process compared to the experimentally measured improvement.

## **7.5 Design considerations for film inverting absorbers**

### ***In-line semi-circular tube design***

The basic film-inverting round-tube absorber tested by Islam et al. [45] is shown in Figure 7.18(a). The tubes are arranged in an 'in-line' configuration and only about one-half of each tube has the liquid film flowing over it. This is a major disadvantage of the design tested by Islam et al. [45]. Several alternative designs are proposed here in order to enable as much surface area as possible to be covered with the liquid film. In Figure 7.18 (b), a design is proposed using semi-circular tubes instead of the full-circular tubes. This design has the advantage of saving some non-participating surface area, but the



vertical flat sides will not carry liquid films. Shown in Figure 7.18 (c) is another design with few columns of semi-circular tubes.

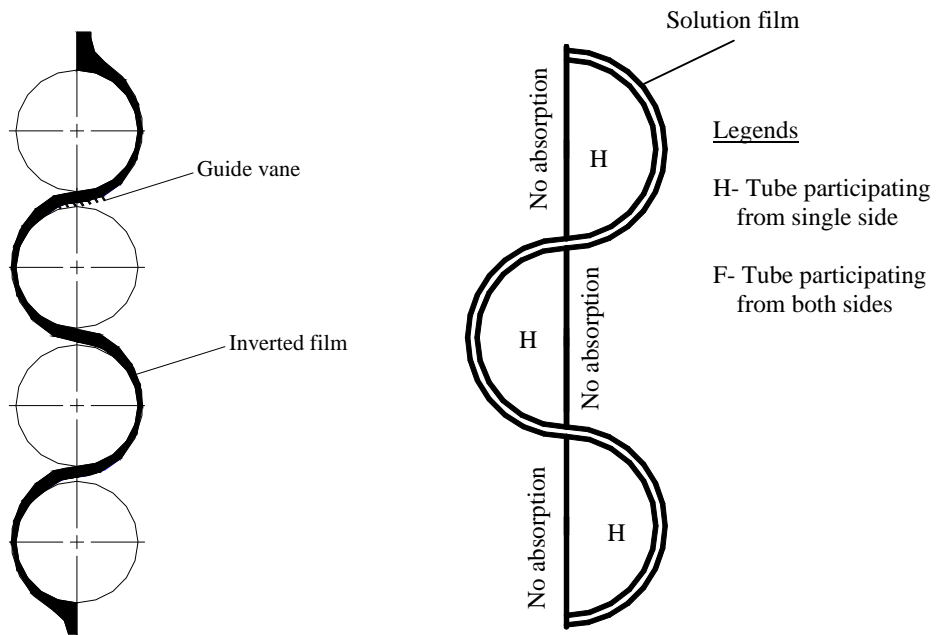


Figure 7.18 (a) Film-inverting design with guide vane [45]

Figure 7.18 (b) Semi-circular film-inverting design [single column]

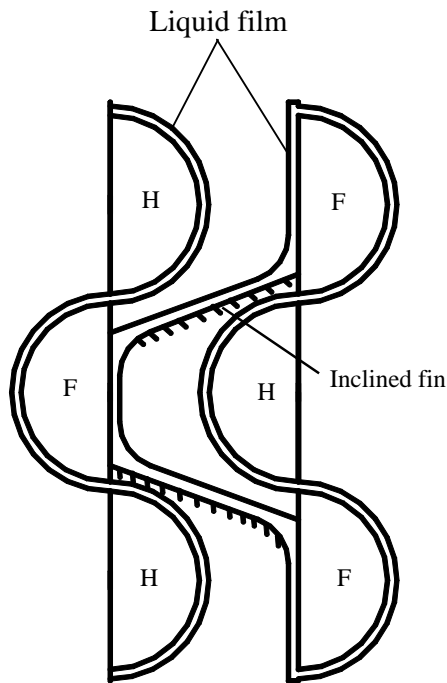


Figure 7.18 (c) Semi-circular film-inverting design [multiple columns].

In this case, most of the straight parts of the semi-circular tubes take part in absorption due to the inclusion of inclined fins. The tubes which are at the two ends of the tube bank will not have the inclined fins. This design could be a better alternative to the design shown in Figure 7.18 (b), but the location of proper inclined fins is difficult to achieve in practice. Moreover, the film flow over the inclined fin is adiabatic, which therefore will increase the temperature of the film. An important consideration for both semi-circular tube designs is the selection of the material for the tubes for operating under vacuum. For the copper tubes, it may be difficult to prevent the flat surface from buckling with the surrounding vacuum pressure and the coolant, flowing inside the tubes at ambient pressure.

#### ***Two-Film-Tube (TFT) film-inverting absorber***

For further design improvement, a Two-Film-Tube (TFT) film inverting absorber is proposed. In this case, multiple columns of Single-Film-Tube (SFT) Coanda Effect-Based Film-Inverting Absorber (SFT-CEBFIA) are used in such way that both surfaces of the round tubes take part in the absorption. Figure 7.19 shows the TFT arrangement for three columns of CEBFIA with 4 tubes in each column. The solution is introduced at the top tube of each column from a common distributor with multiple outlets. The flow rate of different outlets is individually controlled. The objective is to have half of the total solution flow rate along each side of the tube. The solution is collected at the bottom after flowing over the tube array. Except for the tubes at the two outer edges, a significant part of all the inner tubes could participate in the absorption. The vapour is introduced in a cross-flow direction through the gap between the tubes to fully occupy the chamber without any obstruction due to the TFT arrangement. The coolant flows in a serpentine form through the tubes in each column with individual inlet and outlet as indicated in Figure 7.19.

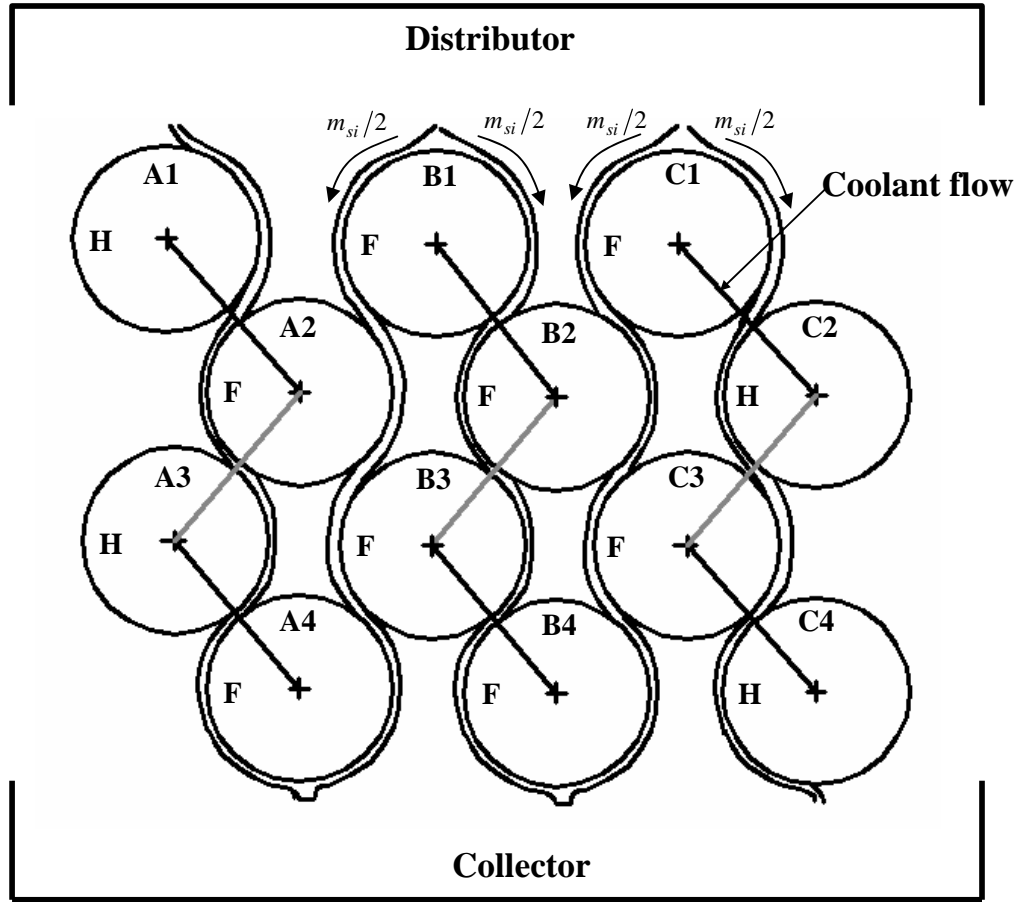
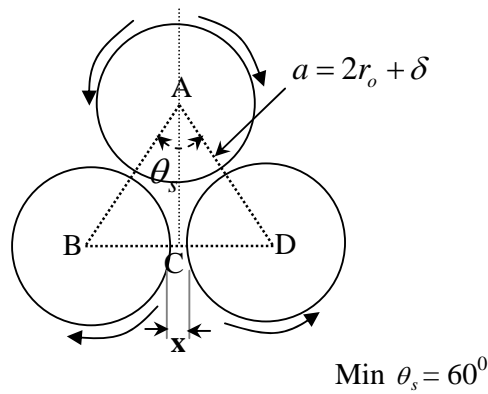
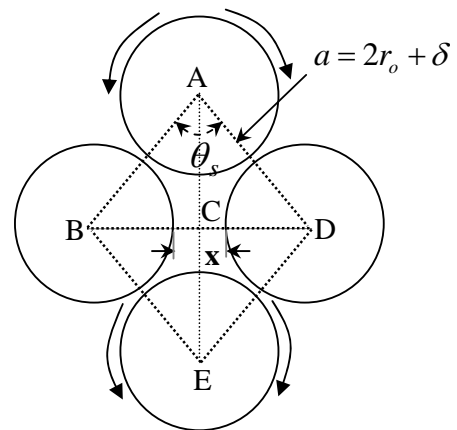


Figure 7.19 Two-film-tube [TFT] assembly of film-inverting absorber.



7.20 (a) Tube arrangement for separation of the flow



7.20 (b) Tube arrangement for flow merging

### 7.5.1 Working principle of Two-Film-Tube CEBFIA

Following description of the CEBFIA-design is based on the configuration shown in Figure 7.19. For convenience, tubes which are participating in absorption with solution flow along both sides are designated by F whereas the tubes which are participating from one side only are designated by H. The middle column of the assembly consists of the tubes which are all designated by F since all are participating from both sides in the absorption. However, the columns on the two sides of the assembly consist of alternate H –tubes and F- tubes. The liquid flowing from both sides of a tube B1 is separated by the two tubes A2 and B2 before reaching the lowermost point of the tube. Tube B3 brings the two separated flow streams to flow over itself from both sides. Tube A4 and B4 separate two streams coming from both sides of B3 and flow along the respective sides of the next two tubes. Adding tubes on the left, right sides of tubes B1, A2, B2 and B3 as shown in Figure 7.19, a TFT assembly is formed which maximizes the participating areas of the film.

#### *Geometry of Two-Film-Tube (TFT) array*

The flow separation angle  $\theta_s$  is determined from the geometry of the tubes as shown in Figure 7.20 (a) and (b). For the equilateral triangle, ABD formed in Figure 7.20 (a), the minimum separation angle is taken as  $60^\circ$ . Since, the gap between two lower tubes ‘x’ should be greater than twice the film thickness  $\delta$ , the separation angle can be determined from the geometry of triangle ABC as :

$$\sin\left(\frac{\theta_s}{2}\right) = \frac{\left[r_o + \frac{x}{2}\right]}{(2r_o + \delta)} \quad (7.5)$$

From Eq. (7.5), the separation angle can be expressed as follows:

$$\theta_s = 2 \sin^{-1} \left[ \frac{(2r_o + x)}{2(2r_o + \delta)} \right] \quad (7.6)$$

where average film thickness  $\delta$  is given by the Nusselts theory [72] as

$$\delta = \frac{1}{\pi} \left[ \frac{3M}{\rho g} \right]^{1/3} \theta = \pi \int_{\theta=0}^{\pi} \sin \theta^{-1/3} d\theta \quad (7.7)$$

Examining Eq. (7.6) and (7.7), the separation angle is found to be a function of tube distance,  $x$  and flow rate,  $\Gamma$ . Since the change in average film thickness with change in solution flow rate is very small ( $<1\text{mm}$ ), separation angle is actually controlled by the tube spacing  $x$ . In section 7.5.3.1, experimental values of the variables  $x, \theta_s$  are obtained under actual operating flow rates.

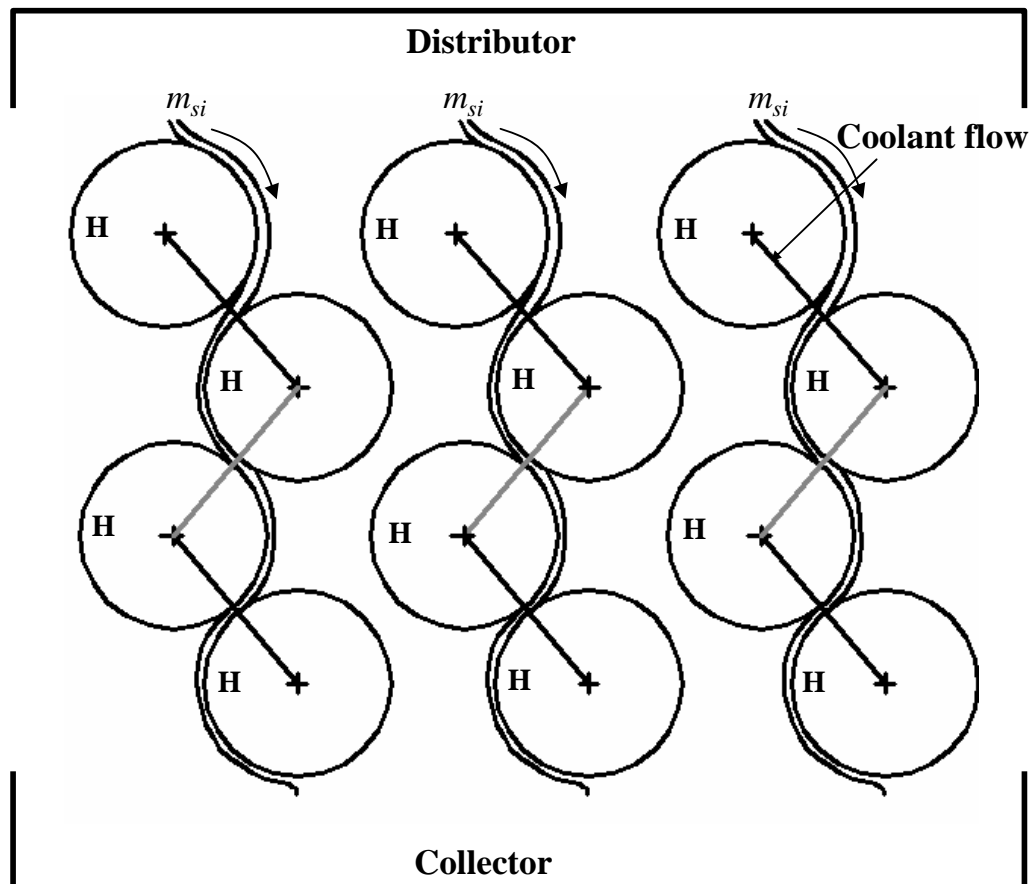
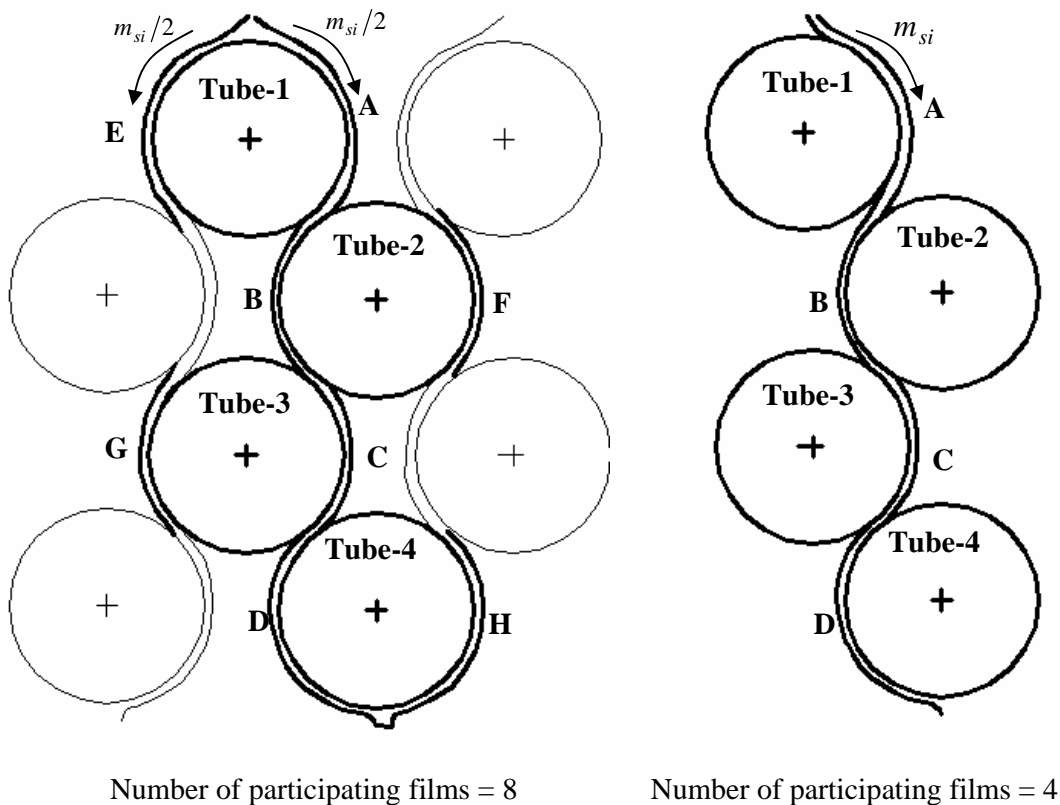


Figure 7.21 Single-Film-Tube [SFT] assembly of film-inverting absorber.

### 7.5.2 Performance evaluation of Two-Film-Tube (TFT) CEBFIA

The performance of the proposed TFT-CEBFIA has been compared with that of a Single Film Tube, SFT-CEBFIA. The SFT assembly with the same number of tubes as the TFT assembly is shown in Figure 7.21. In this arrangement the film flows only on one side of a tube. This is the main difference between the TFT assembly in Figure 7.19 and the SFT assembly in Figure 7.21. In contrast to the TFT assembly, the distributor shown in Figure 7.21 introduces the flow from multiple openings along one side of the first tube of each column. The serpentine coolant flow path is nearly the same for both designs.



7.22 (a) Number of participating films in a TFT column of Figure 7.19

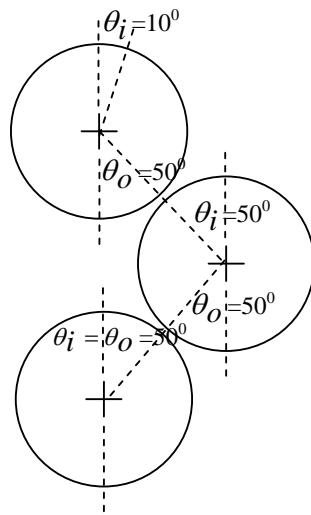
7.22 (b) Number of participating films in a SFT column of Figure 7.21

#### *Comparison of film areas of TFT and SFT assembly*

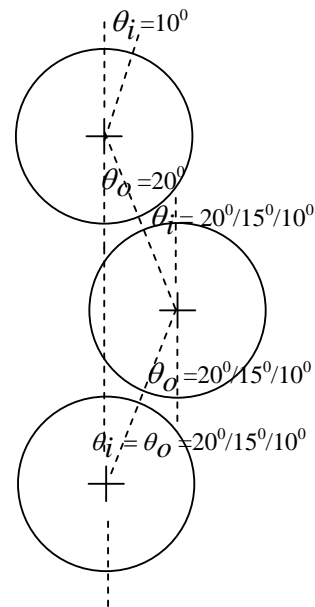
In Figure 7.19, the TFT assembly of CEBFIA shows that the columns which are at the two outer edges consist of alternate single film and two film tubes. However, in practical

design with a large number of columns, the contribution of the two outermost columns would be relatively small. Therefore for the following comparison, the representative two-film-tube column is taken as one of the inner tube-columns indicated in Figure 7.22(a). In contrast to the two-film-tube columns in Figure 7.19, the columns of single-film-tube assembly are all similar to the representative column shown in 7.22(b).

Both designs shown in Figure 7.22 (a) and 7.22(b) consist of 4 tubes in each column. Though the number of tubes is the same, the number of participating liquid films is different. Compared to the films A, B, C, D of the single-film-tube column shown in Figure 7.22(b), a typical two-film-tube column has four more participating films indicated by E, F, G and H in Figure 7.22 (a).



7.22 (c) Film entering and leaving angles for TFT assembly.



7.22 (d) Film entering and leaving angles for SFT assembly.

In Figure 7.22(c), the angular positions at which the liquid film enters and leaves the tubes of TFT column in Figure 7.22(a) are shown. The solution film, coming out from the distributor, enters the top tube at an angle which is different from the film entering angle to the rest of the tubes. The solution film leaves the top tube at an angle which is equal to the half of the separation angle  $\theta_s$  as shown in Figure 7.20(a). The film entering

and leaving angles to the rest of the tubes are therefore equal to the half of the separation angle  $\theta_s$ . The corresponding angular positions for the SFT column in Figure 7.22(b) are shown in Figure 7.22(d). The total participating film area of the two arrangements depends mainly on the angular positions where the film enters and leaves the tubes.

**Table 7.4 TFT assembly of CEBFIA; angular arrangement of Figure 7.22 (c)**

Tube [as shown in Figure 7.22(a)] $n$	Films per tube [as shown in Figure 7.22(a)]	$\theta_i$ [first tube] [deg.]	$\theta_o$ [first tube] or $\theta_i$ [second tube onwards] [deg.]	Participating area for the two-film- tube $A_n =$ $2 \left[ \left( 1 - \frac{\theta_i + \theta_o}{180} \right) \right] \pi r_o$	Total participating area $\sum_{n=1}^{n=4} A_n$
1	A,E	10	50	$1.30 \pi r_o$	$3.97 \pi r_o$
2	B,F	50	50	$0.89 \pi r_o$	
3	C,G	50	50	$0.89 \pi r_o$	
4	D,H	50	50	$0.89 \pi r_o$	

Table 7.4 presents the total participating area of the TFT assembly shown in Figure 7.22(a) when separation angle is  $\theta_s = 100^\circ$ . The solution film enters the top tube at  $\theta_i = 10^\circ$  whereas solution film leaves the tube at  $\theta_o = \theta_s / 2 = 50^\circ$  as shown in Figure 7.22 (c). Both the film entering and leaving angles to the rest of the tubes are  $50^\circ$ s. For this configuration, the participating tube surface area which is covered with the liquid film is calculated for each tube as shown in the 5<sup>th</sup> column of Table 7.4. The total participating area is therefore the sum of the tube-wise participating areas  $A_n$  ( $3.97 \pi r_o$ ), where  $r_o$  is the outer radius of a tube.

Table 7.5 shows similar calculations for the SFT assembly shown in Figure 7.22 (b) for different entering and leaving angles indicated in Figure 7.22 (d). Each tube of the SFT assembly has only one side of it covered with a film. Therefore the number of films is equal to the number of tubes in this design. Based on the different film entering and leaving angle to the tubes, the total participating area is calculated for three



configurations as shown in the last column of Table 7.5. For  $\theta_i = \theta_o = 10^\circ$ , total participating area is found to be  $3.55\pi r_o$  which is about 10 percent less than the total participating area of the TFT assembly shown in Table 7.4.

**Table 7.5 SFT assembly of CEBFIA; angular arrangement of Figure 7.22 (d)**

Films per tube [as shown in Figure 7.22(b)] $n$	$\theta_i$ [first tube] [deg.]	$\theta_o$ [first tube] or $\theta_i$ [second tube onwards] [deg.]	Participating area for the single-film-tube $A_n = \left[ \left( 1 - \frac{\theta_i + \theta_o}{180} \right) \right] \pi r_o$	Total participating area $\sum_{n=1}^{n=4} A_n$
Configuration-1				
A	10	10	$0.89 \pi r_o$	$3.55 \pi r_o$
B	10	10	$0.89 \pi r_o$	
C	10	10	$0.89 \pi r_o$	
D	10	10	$0.89 \pi r_o$	
Configuration-2				
A	10	15	$0.86 \pi r_o$	$3.36 \pi r_o$
B	15	15	$0.83 \pi r_o$	
C	15	15	$0.83 \pi r_o$	
D	15	15	$0.83 \pi r_o$	
Configuration-3				
A	10	20	$0.83 \pi r_o$	$3.16 \pi r_o$
B	20	20	$0.78 \pi r_o$	
C	20	20	$0.78 \pi r_o$	
D	20	20	$0.78 \pi r_o$	

The total participating area of the SFT assembly decreases further if the film leaving angle  $\theta_o$  of the tubes is increased as shown for the configuration 2, 3 of Table 7.5. However, if more tubes are added in a column of TFT arrangement shown in Figure 7.22(a) and SFT arrangement shown in Figure 7.22(b), for the same number of tubes, percent difference of the total participating areas by the two designs decreases even if the angular positions remain same as those shown in Figure 7.22(c) and 7.22(d). It is the top tube of a TFT column whose participating area is more compared to the other tubes

( $1.3\pi r_o$ ). The contribution of the participating area of the top tube of the TFT arrangement in the total summation of tube-wise participating areas decreases if the number of tubes increases in a column.

Furthermore, even though the films A,B,C,D of the SFT assembly shown in Figure 7.22 (b) could be longer than those of TFT assembly because of the different entry and leaving angles, additional films like E, F, G and H of the TFT design shown in Figure 7.22 (a) will provide additional area for vapour absorption. As a result of more participating area of absorption, the absorption performance of the TFT design is more than that of SFT design as described in the following section.

#### 7.5.2.1 Numerical simulation: TFT and SFT CEBFIA designs

The absorption performance of both TFT and SFT assembly of the tube columns shown in Figures 7.22(a) and 7.22(b) are tested under similar operating conditions. The operating conditions are stated in Table 7.2. For the sake of comparison, the total mass flow rate of solution  $m_{si}$  at the top of the two designs remains same. However, in the TFT assembly, the mass flow rate  $m_{si}$  is divided into half flowing along each side of the top tube as shown in Figure 7.22(a). In the SFT assembly, on the other hand, solution flows at the rate of  $m_{si}$  along one side of the top tube as shown in Figure 7.22(b). The numerical solution of the film flow over the four tubes in a single column of both TFT and SFT designs is obtained in a manner similar to the solution of CEBFIA in section 7.4. In the TFT assembly, the total heat transfer from one side of a tube is multiplied by two assuming similar conditions to prevail on both sides of a tube. In order to calculate the vapour absorption rate by the TFT assembly of the absorber tubes, the change in LiBr concentration and the associated change in solution flow rate for film flow over each tube are taken into consideration. The rate of absorption by the four tubes is then compared to similar result obtained from SFT assembly with the same number of tubes.

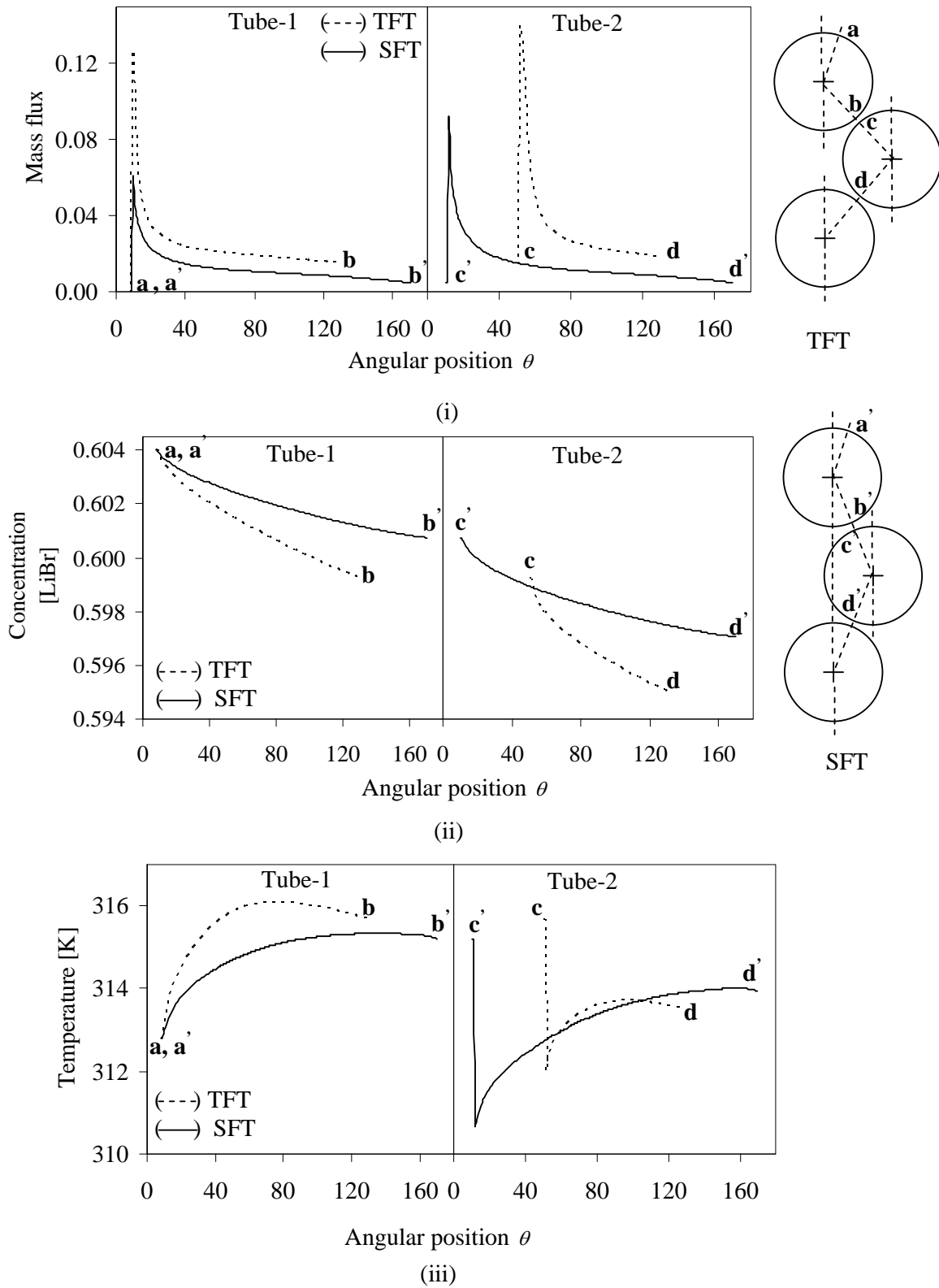


Figure 7.23 Variation of (i) vapour mass flux [ $\text{kg}\cdot\text{m}^{-2}\cdot\text{s}^{-1}$ ] (ii) Bulk concentration [%LiBr/100] (iii) Bulk temperature in the first two tubes of TFT and SFT assembly shown in Figure 7.22(a) and 7.22(b); operating conditions: set 4 in Table 7.2; angular positions are given in Table 7.4 for TFT and configuration 1 in Table 7.5 for SFT.

The variations of mass flux, bulk concentration and temperature along the film flow direction in the first two tubes of the two designs are plotted in Figures 7.23(i)-(iii). It is clearer from the results plotted in the figures that the SFT film length along each side of a tube is longer compared to the TFT film length along each side of a tube. However, the tubes with TFT assembly are participating into absorption from both sides which causes higher rate of vapour absorption in both the tubes as shown in Figure 7.23(i). In both the designs, the absorption rate is much higher at the entrance region of a tube which gradually decreases in the rest of the tube. The drop in bulk concentration of LiBr along the flow direction is plotted in Figure 7.23(ii) for both TFT and SFT configurations. The drop in bulk concentration is much higher in the TFT design especially in the second tube. The larger drop in bulk concentration indicates higher absorption rate which occurs due to the thinner film of the TFT design. Since the mass flow rate along one side of a tube with TFT configuration is half of the mass flow rate along the side of a tube with SFT configuration, the film thickness along each side of a tube with TFT configuration is nearly half as well. As a result, vapour absorption rate and so as the drop in bulk concentration is higher for a film with lower thickness.

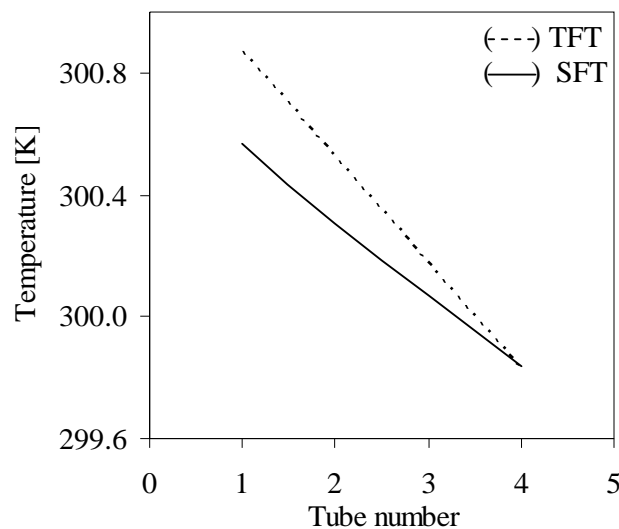


Figure 7.24 Tube-wise variation of coolant temperature of TFT and SFT arrangements shown in Figure 7.22(a) and 7.22(b); operating conditions: set 4 in Table 7.2; angular positions are given in Table 7.4 for TFT and configuration 1 in Table 7.5 for SFT.

The variation of bulk temperature is plotted in Figure 7.23(iii) for both the TFT and SFT designs. The bulk temperature of the film flowing along the side of a tube with TFT configuration is seen higher than that of a tube with SFT configuration especially in the first tube. Because of the larger concentration drop of a thinner film in the TFT design, the rise in temperature is higher in this case.

It also interesting to observe that, for the SFT design, the relatively longer film along a side of a tube is not helping to get better absorption performance. The absorption process mainly dominates the entrance region of a tube as shown in Figure 7.23(i). After the initial sharp rise, the absorption rate falls drastically and displays a steady decrease in the rest of the tube. The longer film can only provide little additional contribution to absorption rate. Similarly for the concentration change shown in Figure 7.23(ii) by the SFT design, the slope of the concentration profile gradually decreases in the later part of the tube. The bulk temperature also achieves a flat profile after the initial sharp rise and shows very little change at the end of the tube with SFT assembly. Hence, the contribution of the thinner and shorter film of the TFT design is found to be more than the contribution of the thicker and longer film of the SFT design in the absorption performance. The tube-wise variations of the average coolant temperature of the two designs are plotted in Figure 7.24. Since the tubes with TFT configuration are participating in absorption from both sides, more heat is transferred to the coolant in this case. As a result, the rise in coolant temperature is more in the TFT than the SFT design. Furthermore, the rate of vapour absorption by the four tubes with both TFT and SFT configurations are separately calculated. The absorption data are summarized in Table 7.6 for three values of the film entering and leaving angles of the SFT assembly given in Table 7.5. These angles remain unchanged for the TFT assembly given in Table 7.4.

**Table 7.6 Comparison absorption performances of TFT and SFT assembly**

No of tubes	$\theta_i, \theta_o$ [TFT]	$\theta_i, \theta_o$ [SFT]	Total area, TFT [ $A_T$ ]	Total area, SFT [ $A_S$ ]	Percent difference of area $\left[ \frac{A_T - A_S}{A_S} \times 100 \right]$	Percent difference of absorption rate $\left[ \frac{m_{v,T} - m_{v,S}}{m_{v,S}} \times 100 \right]$
4	10,50	10,10	$3.97 \pi_o$	$3.55 \pi_o$	11	23
	10,50	10,15	$3.97 \pi_o$	$3.36 \pi_o$	15	26
	10,50	10,20	$3.97 \pi_o$	$3.16 \pi_o$	20	29

The results in the first row of Table 7.6 show that the TFT assembly could increase the absorption rate by about 23 percent compared to the absorption rate by the SFT assembly. The main reason for this performance improvement by the TFT arrangement is the presence of more participating films and consequently more participating area for vapour absorption. As stated before, the number of participating films flowing over the TFT arrangement shown in Figure 7.22(a) is double the number of such films in the SFT arrangement shown in Figure 7.22(b). Moreover, in the TFT arrangement, along each side of a tube, mass flow rate is half compared to the mass flow rate along each side of a tube of the SFT arrangement. As a result, film is much thinner in the case of flow along one side of a tube of the TFT design which also causes more vapour absorption as discussed before. If the angular positions at which the film enters and leaves the tubes of the SFT design increase, the total participating area decreases more which in turn causes a reduction in absorption rate. Hence, the percent difference of the absorption rate between the TFT and the SFT designs increase from 23 to 29 percents as shown in the last column of Table 7.6 if the film entering and leaving angles to the tubes of the TFT design remain unchanged. However, with an increase of tube separation angle in the TFT design, the absorption rate will decrease as in the case of the SFT design. It is seen

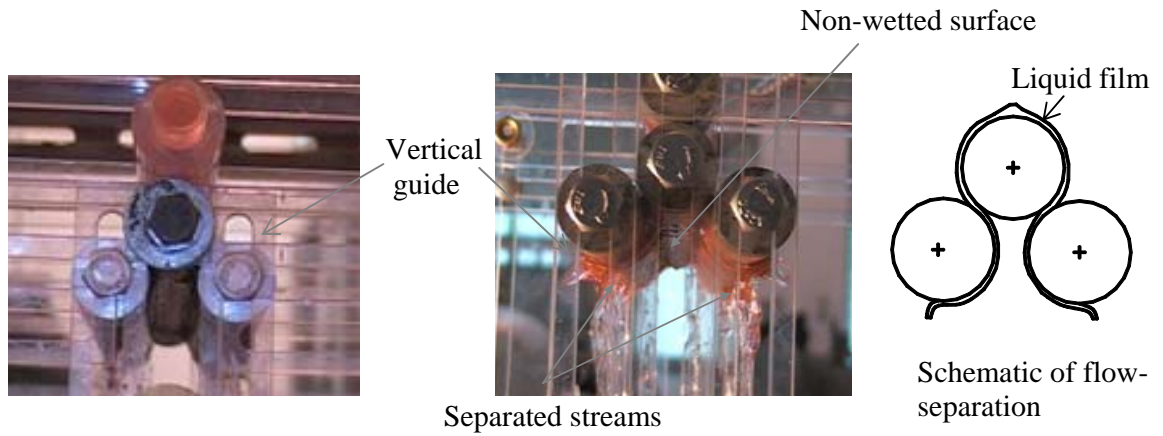
that the tube entering and leaving angles that determine the effective length of the film is an important design parameter for both the SFT and TFT configurations.



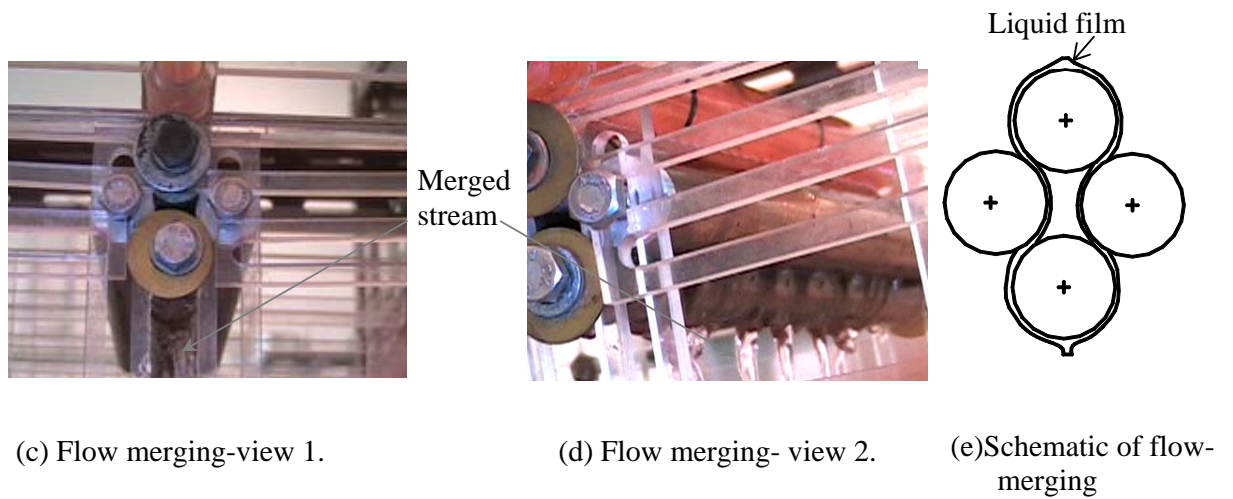
Figure 7.25 Photograph of the test set up with modified test section.

### 7.5.3 Hydrodynamics of the TFT film-inverting absorber

An experimental program was undertaken to establish the feasibility of the TFT arrangement of the film-inverting absorber. The main purpose of this experiment is to observe the film flow hydrodynamics similar to the CEBFI hydrodynamics presented in section 7.3.1.2. The experimental set-up described in section 7.3.1 is used for this purpose with suitable modification of the test section. A photograph of the test set-up is presented in Figure 7.25. Seven tubes of outer diameter 22 mm and length 240 mm are assembled together to obtain the TFT configuration. The design variables like the separation angle  $\theta_s$ , tube gap  $\delta_x$  are determined by trial and error using exploratory experiments.



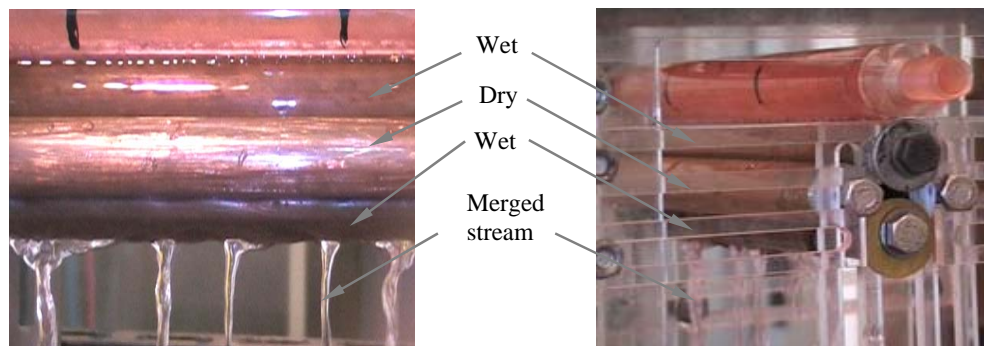
(a) Flow separation at smaller separation angle (b) Flow separation at wider separation angle



(c) Flow merging-view 1.

(d) Flow merging-view 2.

(e) Schematic of flow-merging



(e) Flow merging-view 3.

(f) Flow merging-view 4.

Figure 7.26 Images to explain mechanism of TFT film inversion.



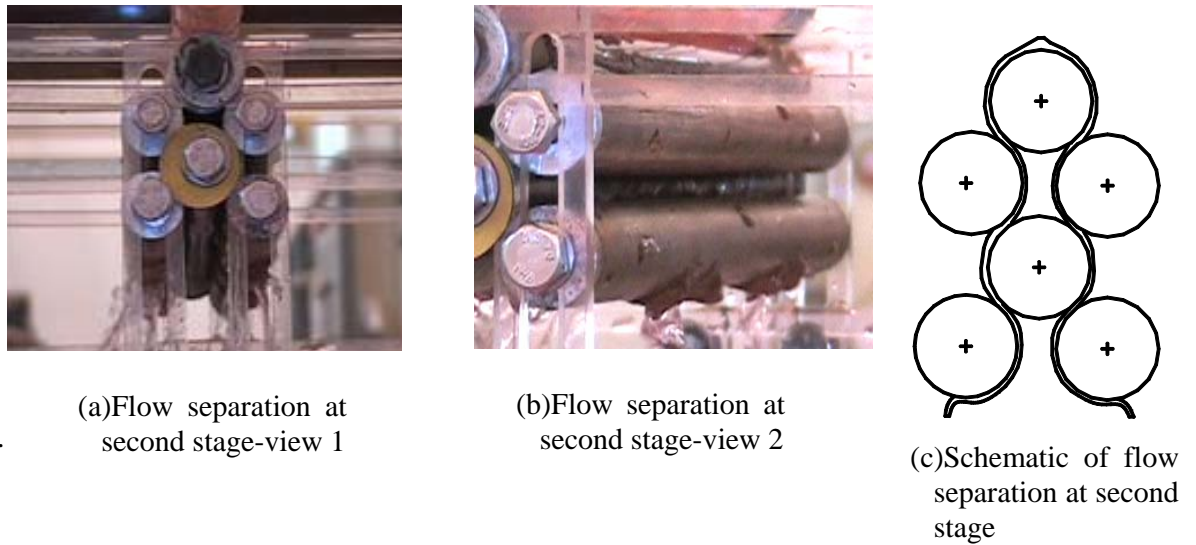


Figure 7.27 Experimental verification of the TFT film-inverting concept

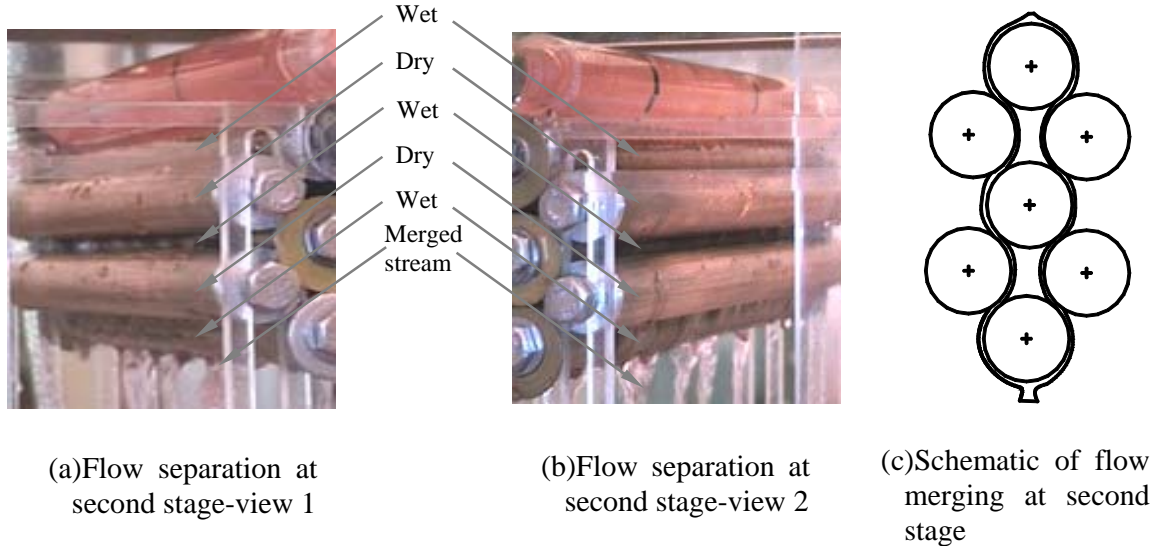


Figure 7.28 Final TFT configurations [flow rate:  $0.0163 \text{ kg}\cdot\text{s}^{-1}$ ].

### 7.5.3.1 Experimental results

The tubes are assembled carefully in the test section in order to perform the flow separation and merging accurately. At each step, the film flow over the tubes is recorded on video. The first step is to position the topmost tube in such way that it is wetted on both sides by the flow from the distributor. The next step is to position the two tubes below the first tube and carefully obtain the liquid stream from both sides of the top tube to flow in opposite directions due to the Coanda Effect. Vertical guide bars are necessary to maintain the proper orientation of the tubes as shown in Figure 7.26 (a) and (b).

Figure 7.26 (a) shows the flow separation due to the two lower tubes. From the picture taken from below, the uniform distribution of film flow after the separation is clearly visible in Figure 7.26 (b). The figure also displays the non-wetted surface at the bottom of the top tube. The flow separation is performed varying the separation angle  $\theta_s$  from 60 degree to less than 180 degree. The tubes cannot be brought too close because that may not separate the flow at all, instead, it may let the liquid stream to flow in one-direction on the tube below. Moreover, care has to be taken to ensure that two tubes are placed at equal distances from the first tube. Figure 7.26(b) shows the flow separation at slightly wider separation angle than the flow separation of Figure 7.26(a). The separation angle cannot be too wide because that may increase the non-participating surface area of the tubes.

In this experiment, separation angle is set at 100 degree. The angle is calculated from the measurements taken for the radial tube gap  $\delta$  and horizontal tube gap  $x$  as shown in Figure 7.20 (a)-(b). The tube gaps are measured with digital calipers to calculate the separation angle using Eq. (7.6). Third step is to place the fourth tube below the two lower tubes so that the two fluid streams are guided to flow along the two sides of this new tube using the Coanda Effect. This operation is termed as merging of the flow streams which is shown in Figure 7.26 (c)-(f) using different viewing positions. In the next step, flow separation is performed again with two more tubes below. Figures 7.27 (a)-(b) show the six tube assembly with flow separation by the two bottommost tubes. Finally, the seventh tube is brought into place between the fifth and sixth tubes to perform the merging of the two separated liquid streams after flowing along the two sides of this tube. The angular views of the seven-tube assembly shown in Figures 7.28 (a)-(b) display the alternate working surfaces with uniform distribution of film over the tubes. When the film flow over the tube assembly is satisfactory in terms of uniform

distribution and surface wetting, the tubes are tightened finally to maintain the stability of the structure.

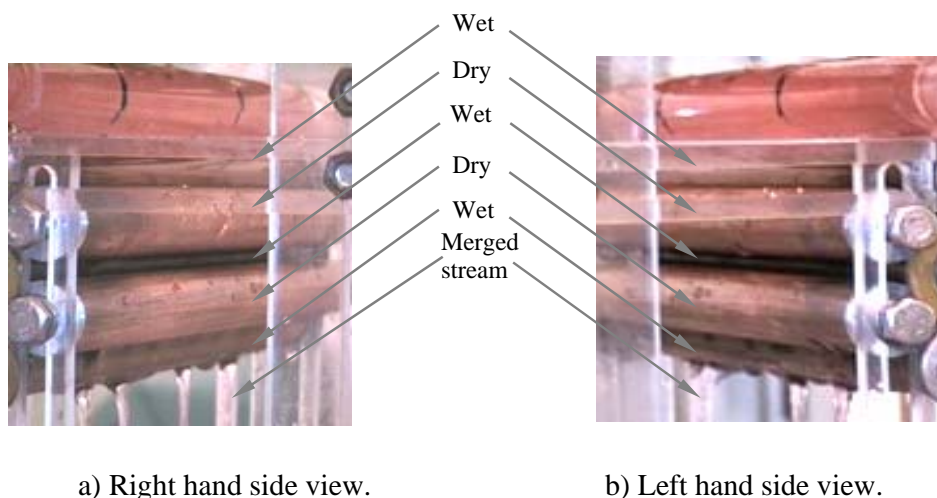


Figure 7.29 Final TFT configuration [flow rate:  $0.008 \text{ kg}\cdot\text{s}^{-1}$ ].

The above experimental procedure is normally undertaken at a moderately high flow rate initially. After achieving the satisfactory flow condition, the flow rate is varied within practical limits. If the tube gap remains unchanged, increase of flow rate may increase the film surface waviness. Furthermore, the flow rate cannot be increased too much because it may cause flow blockage through the small tube gaps. The decrease of flow rate on the other hand minimizes the surface waviness and smoothes out the film. Figures 7.28 (a)-(b) and 7.29 (a)-(b) show the film flow over the TFT assembly at two different flow rates for the same tubular configuration. It was observed that the tube gap did not require adjustment even at very low solution flow rate. But, too low a flow rate could cause poor surface wetting and flow distribution. The workable limit of solution flow rate is therefore found by trial-and-error for this particular tubular configuration. The limit of flow rate is found to be within the actual operating condition of practical falling film absorber.

#### 7.5.4 Practical design aspects of TFT CEBFIA

The above experimental study of TFT CEBFIA flow hydrodynamics demonstrated its feasibility for practical application. The main advantages of this proposed design are (a) the film inversion without the use of any guide vanes/fins and (b) availability of more participating films for a given number of tubes. The TFT design offers more vapour absorption capability mainly because of the availability of more participating films. The advantages of TFT absorber over the conventional tubular absorber are also very significant. Not only does it help to provide a large performance improvement due to film-inversion, but also the problem of absorber drying out is greatly reduced. In the conventional tubular absorber the liquid film becomes narrow as it flows down over the tubes towards the bottom of the absorber, thus creating dry patches. When film-inversion is used, the wetting of the absorber tubes is greatly improved either with the fins used by Islam et al. [45] or with no fins as in the case of present TFT design of CEBFIA. But the additional advantageous feature of the new TFT design is the reduction of the absorber length. The same number of absorber tubes as used in the case of conventional design is re-arranged as multiple columns in the TFT absorber. Numerical simulation results suggest that adding more tubes in new columns create more absorption than adding more tubes in new rows of same column. But TFT absorber requires a careful design of the flow distributor and the collector as in the case of any staggered-tube heat exchanger. Besides this, other design issues that may arise during the operation of the new absorber are described below.

The radial gap between the tubes of the TFT absorber is nearly equal to the average liquid film thickness. Maintaining such a narrow gap between the tubes may present practical problems during fabrication of this proposed design. However, in the present experimental study, the tubes are assembled in such way that the tube gaps are adjustable in both horizontal and vertical directions even during the experiment run. The

tubes are also assembled step by step in order to avoid any flow blockage during the start-up. When satisfactory film flow is achieved at each step, the tubes are tightened in position. Once a satisfactory and stable tube configuration is achieved, the flow rate can vary within a practical range without causing much disturbance to the film flow. The present experimental study has demonstrated the feasibility of the film-inversion process using the Coanda Effect with its many advantages. However, a prototype absorber using the design concept has to be tested over a range of operating conditions before the design can be adopted in practical vapour absorption cooling systems.

### **7.6 Summary**

In this chapter, a new film-inverting tubular absorber was proposed which used the Coanda Effect to achieve film-inversion. The film-inverting mechanism was analyzed in detail with the help of the absorption model of the new film-inverting absorber. The experimental investigation of the film-inverting hydrodynamics was also performed to verify the practical feasibility. In order to increase the vapour absorption rate, a two-film-tube (TFT) film-inverting absorber design was proposed. The performance of the TFT film-inverting absorber was simulated numerically and compared with the single-film-tube (SFT) film-inverting absorber. The TFT film-inverting absorber increased the absorption rate over the SFT design. The practical feasibility of the new design concept was verified by performing experimental investigations of the film-flow hydrodynamics of the TFT absorber. The experimental results demonstrated the feasibility of this novel design.

## **CHAPTER 8**

### **CONCLUSIONS AND**

### **RECOMMENDATIONS**

#### **8.1 Conclusions**

A realistic numerical model of a horizontal-tube-bank absorber that included the detailed geometry and the heat and mass transfer processes was developed. The single round tube model was extended to simulate the bank of horizontal tubes in the practical absorber considering both the film-flow over the tubes as well as the inter-tube flow phenomena between the tubes. The numerical solution for the single round tube was dependent on the film entering and leaving angles to the tube mainly because of the fact that the film is thicker near the entrance and exit regions of a tube. The values of these angles were chosen from a sensitivity analysis. The predictions of the model were compared with the experimental results for a horizontal tube-bundle absorber from published sources. Good agreement was found when inter-tube absorption was incorporated to the model. Partial wetting of the absorber tubes by the solution flow had a significant effect on the predictions. Numerical simulation models were also developed for the equivalent vertical-flat-plate-absorber and the segmented-flat-plate-absorber which have been previously used to simplify the geometry of horizontal tube-bundle absorber. In order to determine the effect of making such geometrical simplifications, the predictions of the models were considered in similar fashion for the simulation of bank of tubes absorber. The use of the equivalent vertical flat plate model resulted in significant deviations in the predictions of the performance of a horizontal tube-bundle absorber. However, the simulation results of the detailed round tube and the segmented flat plate models agreed well. The comparison showed that the present detailed round tube model was capable of providing more realistic information about the changes of different parameters regarding the film flow over the tubes. Hence the detailed numerical model of the round tubes

could be used as the base line to obtain the local and averaged heat and mass transfer coefficients of the horizontal-tube-bank absorber. Moreover, the model could be used to simulate the performance of a film-inverting tubular absorber.

The detailed numerical model discussed above required much computational effort when it was applied for a bank of horizontal tubes of the absorber. Thus, it may not be suitable for routine design application and for the analysis of experimental data. Therefore, a simplified design model was developed for the bank of tubes absorber by taking into consideration the detailed geometry of the tubes and the serpentine flow of coolant. The transfer coefficients required as an input to the simplified design model were determined from the previously developed detailed numerical model. The inter-tube flow and absorption was also incorporated in the model in the form of drop, jet/sheet flow. The simulation results obtained from the detailed numerical model and the simplified round tube model with inter-tube flow were compared with experimental results available in the published literature. There was reasonable trend-wise agreement between the predictions of the two models and the experimental data which had considerable scatter.

The predictions of the simplified round tube model were also compared with those of the detailed numerical model under the known operating conditions. The agreement between the predictions by the two models was good, particularly, when spatially varying heat and mass transfer coefficients were used in the simplified model. When spatially averaged transfer coefficients were used, the predicted exit conditions showed good agreement, but there was some deviation between the predicted spatial distributions of the solution temperature and concentration. Furthermore, the simplified model was used to extract heat and mass transfer coefficients from published experimental data. The numerically computed overall heat transfer coefficients using the detailed numerical model agreed with the extracted values from the simplified design model within about

20 percent while the computed mass transfer coefficients were up to 30 percent higher than the corresponding extracted values. The effect of liquid film thickness variations over the absorber tubes was also examined by taking into account both the linear and non-linear form of the simplified model. The differences in the predicted changes in concentration and temperature at the bottom of the tube by the non-linear and the linear forms of the simplified model are less than 0.1 percent. The approximate expressions for the exponents in the simplified model, which show explicitly the contribution of transfer units for heat and mass transfer, agreed well with exact analysis.

The inter-tube absorption models were developed for the three possible modes of inter-tube flow, viz. droplet, jet and sheet flow modes. The semi-empirical models of inter-tube droplet and steady jet/sheet flow were developed based on the known transfer coefficients for the inter-tube absorption. However, the exact values of the inter-tube transfer coefficients were unknown. Hence, the transfer coefficients in the inter-tube flow regime were assumed to remain the same as those in the falling film regime. In the falling film regime, the transfer coefficients were extracted from the detailed numerical model. In a recent paper, Killion and Garimella [54] have presented the development of an experimental set-up to measure these transfer coefficients. The present inter-tube absorption models would be useful in the analysis of their experiments.

The numerical solution of the inter-tube absorption models required the information on the hydrodynamics of drop development and steady jet flow. Therefore, the detailed experiments on inter-tube flow hydrodynamics were performed for a range of operating conditions including the varying flow rate and the tube spacing. The qualitative descriptions of the inter-tube flow events were made by analyzing the sequential video images. The qualitative behavior formed the basis for the inter-tube flow hypothesis which was used in developing the inter-tube absorption models described above. The



sequential video images were analyzed with the help of an image analysis program to obtain the transient characteristics of inter-tube flow. The experimental data were incorporated in the relevant absorption models to simulate the absorption performances at various operating conditions. The actual contribution of the inter-tube absorption was obtained comparing to the total of falling film and inter-tube absorption rates of a tubular absorber. The percent contribution of inter-tube absorption was found 30 to 36 percents of total absorption with assumed transfer coefficients. A sensitivity analysis showed significant dependence of the simulation results predicted by the models on the varying transfer coefficients. Even though the data presented for the percent contribution of the inter-tube absorption compared to the total absorption was integrated with some limitations of the transfer coefficients, the methodology shown in the present analysis could become a valuable tool for future study.

Film-inverting absorber was considered to be the potentially viable alternative for the performance improvement of horizontal-tube-bank absorber. As an attempt to the improvement of the previous design of Islam et al. [45], a novel film inverting absorber was proposed which did not require the flow guiding fins to cause the film inversion in a horizontal-tube-bank. In the present study, an alternative design was explored which used the Coanda-Effect of fluid flow over curved surfaces to cause the alternate film inversion in a tubular absorber. The experimental investigation of the Coanda-Effect based film-inverting hydrodynamics was performed to verify the practical feasibility of the proposed design. The film-inverting mechanisms were analyzed in details with the help of the developed absorption model of the Coanda-Effect based film-inverting design. The previously developed detailed numerical model was used for this purpose. Though the model predictions depended on the film entering and leaving angles to the tubes, the film-inverting absorber provided significant performance improvement

compared to the conventional design without any film-inversion. The actual reasons of this performance improvement due to film-inversion were explored.

In order to increase the absorption performance more by increasing the participating area of absorption, a Two-Film-Tube film-inverting absorber was proposed by the help of alternate flow separation and flow merging due to Coanda-Effect in multiple columns of tubes. The performance evaluation of the Two-Film-Tube film-inverting absorber was numerically obtained and compared with the Single-Film-Tube film-inverting absorber. It was found that the Two-Film-Tube film-inverting absorber could increase the absorption rate by 23-29 percents more than the Single-Film-Tube design mainly because of the availability of more participating films in the Two-Film-Tube design. However, the vapour absorption performances of both the Two-Film-Tube and the Single-Film-Tube designs were influenced by the film entering and leaving angles to the tubes. The practical feasibility of the new design concept was verified by performing the experimental investigation of the film-flow hydrodynamics of the Two-Film-Tube assembly. The experimental results demonstrated the technical feasibility of the proposed design using the Coanda-Effect with its desirable features such as compactness and increased absorption.

## **8.2 Recommendations**

Following recommendations are made for future extension of the work.

- In the present study, a procedure was shown in order to predict the actual contribution of inter-tube absorption in a tubular absorber which most of the previous researchers thought to be insignificant. However, the model predictions were based on the assumed values of the heat and mass transfer coefficients during the inter-tube absorption in the different flow modes. If the values of the transfer coefficients during drop formation or the steady jet flow are determined

experimentally, the procedure shown here could become more useful in actually predicting the inter-tube absorption. The next phase of the present study could be the development of an experimental program to measure the inter-tube absorption. Such experimental work would be a challenging undertaking suitable for advanced graduate studies.

- The digital video camera used in the present study has the frame speed limit of 30 per second. The accuracy of the transient droplet volume and surface area profiles presented in chapter 5 may improve if a high speed video camera was used. Due to the frame speed limit of the camera, the exact moments for the completion of development stage of a droplet or the break up of a liquid bridge could not be captured on the video in most of the droplet cycles. As a result, an accurate measurement of the droplet evolution cycle was found to be difficult. A high speed video camera with higher pixel resolution may ensure better image quality to improve the image analysis process and so as the accuracy of the capturing of the inter-tube flow events.
- The falling film over a tubular absorber is actually very thin, thickness being hardly a mm. The visualization of such a thin film during the experimental verification of Coanda-Effect Based Film Inverting (CEBFI) process was found to be difficult to show in the digital images. Though the visualization was not a problem in the laboratory for eye-observations of the events. The same problem persisted during pictorially documenting the occurrence of flow separation and merging due to Coanda-Effect in a Two-Film-Tube CEBFI arrangement. The improvement of the flow visualization of the film-inverting process is much required for the proposed design.

---

## REFERENCES

1. Ameer, T.A., H.M. Habib and B.D. Wood. Effects of a Non-absorbable Gas on Interfacial Heat and Mass Transfer for the Entrance Region of a Falling Film Absorber, *Journal of Solar Energy Engineering*, vol. 118, pp.45-49. 1996.
2. Andberg, J.W. and G.C. Vliet. Nonisothermal Absorption of Gases Into Falling Liquid Films. ASME-JSME Thermal Engineering Joint Conference Proceedings (2), pp. 423–431.1983.
3. Andberg, J.W. and G.C. Vliet. Design Guidelines for Water-Lithium Bromide Absorbers, *Ashrae Transaction*, vol. 89(1B), pp.220-232. 1983.
4. Andberg, J.W. and G.C. Vliet. A Simplified Model for Absorption of Vapors into Liquid Films Flowing Over Cooled Horizontal Tubes, *Ashrae Transaction*, vol. 93(2), pp.2454-2466. 1987.
5. Aphornratana, S. and I.W. Eames. Thermodynamic analysis of absorption refrigeration cycles using the second law of thermodynamics method, *Int. J. Refrigeration*, vol. 18(4), pp. 244-252. 1995.
6. Armbruster, R. and J. Mitrovic. Patterns of falling film flow over horizontal smooth tubes. Proceedings of the 10<sup>th</sup> International Heat Transfer Conference, Vol. 3, pp 275-280, 1994.
7. Armbruster, R. and J. Mitrovic. Heat Transfer in Falling Film on a Horizontal Tube, *National Heat Transfer Conference*, vol.314, pp. 13-21.1995.
8. Arora, C.P. *Refrigeration and Air Conditioning*, New Delhi: Tata McGraw-Hill, 2000.
9. ASHRAE Handbook Fundamentals, Equilibrium Chart of Lithium Bromide-Water Solutions, 1791 Tullie Circle, N.E., Atlanta, GA 30329, pp. 17.69. 1989.
10. ASHRAE Handbook Refrigeration, Absorption Cooling, Heating, and Refrigeration Equipment, 1791 Tullie Circle, N.E., Atlanta, GA 30329, pp. 41.1-41.12. 1998.
11. Bejan, A. *Shape and Structure, from Engineering to Nature*, Cambridge university press, Cambridge, UK, 2000.
12. Beutler, A., I. Greiter, A. Wagner, L. Hoffmann, S.Schreier and G. Alefeld. Surfactants and Fluid Properties, *Int. J. Refrigeration*, vol. 19, No. 5, pp.342-346. 1996.
13. Bird, R.B., W.E. Stewart and E.N. Lightfoot. *Transport Phenomena*, Wiley International ed., New York: Wiley & Sons, Inc. 1960.
14. Bleazard, J.G., R.M. DiGuilio and A.S. Teja. Thermal Conductivity of Lithium Bromide – Water Solutions, *AIChE Symposium Series*, vol. 90, No. 298, pp. 23-28. 1994.

15. Brauner, N. Non-Isothermal Vapour Absorption Into Falling Film, *Int. J. Heat Mass Transfer*, vol. 34, No. 3, pp.767-784. 1991.
16. Farhanieh, B. and F. Babadi. Vapor absorption into liquid films flowing over a column of cooled horizontal tubes, *Scientia Iranica*, Vol. 11, No.4, pp 332-338(2004).
17. Massey, B.S. *Mechanics of Fluids*, 8<sup>th</sup> Edition, pp. 108-109, Taylor and Francis, 2006.
18. Chen, Y. and C.Y. Sun. Experimental Study on the Heat and Mass Transfer of a Combined Absorber-Evaporator Exchanger, *Int. J. Heat Mass Transfer*, Vol. 40, No. 4, pp.961-971. 1997.
19. Chowdhury, S.K., D. Hisajima, T. Ohuchi, A. Nishiguchi, T. Fukushima and S. Sakaguchi. Absorption of Vapors into Liquid Films Flowing Over Cooled Horizontal Tubes, *ASHRAE Transaction: Research*, vol. 99(2), pp.81-89. 1993.
20. Conlisk, A.T. The use of boundary layer techniques in absorber design. *ASME Proceedings of the International Absorption Heat Pump Conference*, vol 31, pp. 163–170. 1993.
21. Conlisk, A.T. Analytical Solutions for the Heat and Mass Transfer in a Falling Film Absorber, *Chemical Engineering Science*, vol. 50, No. 4, pp.651-660. 1995.
22. Cosenza, F. and G.C. Vliet. Absorption in Falling Water/LiBr Films on Horizontal Tubes, *ASHRAE Transaction*, vol. 96, 3379, pp.693-701. 1990.
23. Del Rio, O.I. and A. W. Neumann. Axisymmetric Drop Shape Analysis: Computational Methods for the Measurement of Interfacial Properties from the Shape and Dimensions of Pendant and Sessile Drops, *Journal of Colloid and Interface Science*, Vol. 196, pp 136-147, 1997.
24. Deng, S.M. and W.B. Ma. Experimental Studies on the Characteristics of an Absorber Using LiBr/H<sub>2</sub>O Solution as Working Fluid, *International Journal of Refrigeration*, vol. 22, pp. 293-301. 1999.
25. Edwards, D.K., V.E. Denny and A.F. Mills. *Transfer Processes: An Introduction to Diffusion, Convection, and Radiation*. pp. 144 & 166, Hemisphere Pub. Corp., Washington, 1979.
26. Fujita, I. and E. Hihara. Heat and Mass Transfer Coefficients of Falling-film Absorption Process. *International Journal of Heat and Mass Transfer* 2005; 48: 2779-2786.
27. Frances, V.M.S. and J.M.P. Ojer. Validation of a Model for the Absorption Process of H<sub>2</sub>O(vap.) By a LiBr(aq.) in a Horizontal Tube Bundle, Using Multi-factorial Analysis, *International Journal of Heat and Mass Transfer*, vol.46(17), pp.3299-3312. 2003.

28. Ganic, E.N. and M.N. Roppo. An experimental Study of Falling Liquid Film Breakdown on a Horizontal Cylinder During Heat Transfer, *Transactions of ASME*, Vol. 102, pp. 342-346, 1980.
29. Gerald, C.F. and P.O. Wheatley. *Applied numerical analysis*, Addison-Wesley, Menlo Park, California, 1984.
30. Goel, N. and D. Y. Goswami. A Compact Falling Film Absorber, *Journal of Heat Transfer*, Vol. 127, pp. 957-965, 2005.
31. Grigoryeva, N.I. and V.E. Nakoryakov. Exact solution of combined heat and mass transfer problems during film absorption. *Journal of Engineering Physics*, vol. 33 (5) pp. 1349–1353. 1977.
32. Grossman, G. Simultaneous Heat and Mass Transfer in Film Absorption Under Laminar Flow, *International Journal of Heat and Mass Transfer*, vol. 6, No. 3, pp.357-371. 1983.
33. Grossman, G. and K. Gomed. Heat and Mass Transfer in Film Absorption in the Presence of Non-Absorbable Gases, *Int. J. Heat Mass Transfer*, vol. 40, No. 15, pp.3595-3606. 1997.
34. Habib, HM and BD Wood. Simultaneous Heat and Mass Transfer for a Falling Film Absorber - The Two Phase Flow Problem. *Solar Energy Engineering, Proceedings of the 12th Annual International Solar Energy Conference*, ASME, p. 61–67, 1990.
35. Heinonen, E.W. and R.E. Tapscott. Secondary Properties of Aqueous Lithium Bromide Solutions, *Ashrae Transactions*, pp.804-812. 1999.
36. Hihara, E. and T. Saito. Effect of Surfactant on Falling Absorption, *Int. J. Refrig.*, vol. 16, No. 5, pp.339-346. 1993.
37. Hoffmann, L., I. Greiter, A. Wagner, V. Weiss and G. Alefeld. Experimental Investigation of Heat Transfer in a Horizontal Tube Falling Film Absorber with Aqueous Solution of LiBr with and without Surfactants, *Int. J. Refrig.*, vol. 19 No. 5, pp.331-341. 1996.
38. Hozawa, M., M. Inoue, J. Sato and N. Imaishi. Marangoni Convection During Steam Absorption into Aqueous LiBr Solution with Surfactant, *J. Chem. Engrs. Japan*, vol. 242, pp. 209-214. 1991.
39. Hu, X. and A.M. Jacobi. The Intertube Falling Film:Part1-Flow Characteristics, Mode Transitions, and Hysteresis, *Transactions of the ASME*, vol. 118, pp.616-633.1996.
40. Hu, X. and A.M. Jacobi. Departure-site spacing for liquid droplets and jets falling between horizontal tubes, *Experimental Thermal and Fluid Science*, Vol. 16, pp.322-331, 1998.
41. Ibrahim, G.A. and G.A. Vinnicombe. A Hybrid Method to Analyze the Performance of Falling Film Absorbers, *International Journal of Heat and Mass Transfer*, Vol. 36, No. 5, pp. 1383-1390, 1993.

42. Incropera, F.P. and D.P. DeWitt. *Fundamentals of Heat and Mass Transfer*. pp. 322 & 516, John Wiley & Sons, Inc. New York, 1996.
43. Islam, M.R. *Performance Evaluation of Absorbers for Vapor Absorption Cooling Systems*, PhD thesis, National University of Singapore, 2002.
44. Islam, M.R., N.E. Wijesundera and J.C. Ho. Evaluation of Heat and Mass Transfer Coefficients for Falling-Films on Tubular Absorbers, *Int. J. Refrigeration.*, vol. 26, pp. 197-204. 2003.
45. Islam, M.R., N.E. Wijesundera and J.C. Ho. Performance Study of a Falling-Film Absorber With a Film-Inverting Configuration, *Int. J. Refrigeration.*, vol. 26(8), pp. 909-917. 2003.
46. Islam, M.R., N.E. Wijesundera and J.C. Ho. Simplified models for coupled heat and mass transfer in falling-film absorbers, *Int. J. of Heat and Mass Transfer.*, vol. 47(2), pp. 395-406. 2004
47. Morioka, I., M. Kiyota, A. Ousaka and T. Kobayashi. Analysis of Steam Absorption by a Subcooled Droplet of Aqueous Solution of LiBr, *JSME International Journal*, Vol. 35, Series II, No. 3, 1992.
48. Killion, J.D. and S. Garimella. Critical Review of Models of Coupled Heat and Mass Transfer in Falling-film Absorption, *International Journal of Refrigeration*, Vol. 24, pp. 755-797, 2001.
49. Jean-Francois, Roques and John R. Thome. Falling Film Transitions between Droplet, Column, and Sheet Flow Modes on a Vertical Array of Horizontal 19 FPI and 40 FPI Low-Finned Tubes, Vol. 24, pp. 40-45, 2003.
50. Jung, S., C. Sgamboti and H. Perez-Blanco. An Experimental Study of the Effect of Some Additives on Falling Film Absorption, *International Absorption Heat Pump Conference, AES* – vol. 31, pp.49-55. 1993.
51. Kocamustafaogullari, A. and I. Y. Chen. Falling Film Heat Transfer Analysis on a Bank of Horizontal Tube Evaporator, *AiChE Journal*, Vol. 34 (9), 1988.
52. Killion, J.D. and S. Garimella. Gravity-driven Flow of Liquid Films and Droplets in Horizontal Tube Banks, *International Journal of Refrigeration*, vol. 26, pp. 516-526. 2003.
53. Killion, J.D. and S. Garimella. Pendant droplet motion for absorption on horizontal tube banks, *International Journal of Heat and Mass Transfer*, vol. 47, pp. 4403-4414, 2004.
54. Killion, J.D. and S. Garimella. Measurement of Local Absorption Rates in Films and Droplets in Lithium-Bromide/Water Absorbers, *Proceedings of International Sorption Heat Pump Conference*, June 22-24, Denver, Co, USA, 2005.
55. Kim, D. and M. Kim. Heat Transfer Enhancement Characteristics for Falling-Film Evaporation on Horizontal Enhanced Tubes with Aqueous LiBr Solution, *Enhanced Heat Transfer*, vol. 6, pp. 61-69. 1999.

56. Kim, J., H. Lee and S.I. Yu. Absorption of Water Vapour into Lithium Bromide-Based Solutions with Additives Using a Simple Stagnant Pool Absorber, *International Journal of Refrigeration*, vol. 22, pp.188-193. 1999.
57. Kim, K.J., N.S. Berman and B.D. Wood. Experimental Investigation of Enhanced Heat and Mass Transfer Mechanisms Using Additives for Vertical Falling Film Absorber, *International Absorption Heat Pump Conference, AES* – vol. 31, pp.41-47. 1993.
58. Kim, K.J., N.S. Berman, D.S.C.Chau and B.D. Wood. Absorption of Water Vapour into Falling Films of Aqueous Lithium Bromide, *Int. J. Refrig.*, vol. 18, No. 7, pp.486-494. 1995.
59. Kirby, M.J. and H. Perez-Blanco. A design model for horizontal tube water/lithium bromide absorbers, *International Heat Pump and Refrigeration Systems Design, Analysis and Applications*, Vol.32, AES, American Society of Mechanical Engineers, New York, 1994.
60. Kiyota, M., I. Morioka and A. Ousaka. Effect of Surface Geometry in Steam Absorption into a Falling Film of Aqueous Solution of LiBr, *Heat Transfer – Japanese Research*, vol. 24(1), pp.68-79. 1995.
61. Kutateladze, SS, II Gogonin and VI Sosunov. The Influence of Condensate Flow Rate on Heat Transfer in Film Condensation of Stationary Vapour on Horizontal Tube Banks, *International Journal of Heat and Mass Transfer*, Vol. 28, pp 1011-1018, 1985.
62. Matsuda, A., K.H. Choi, K. Hada and T. Kawamura. Effect of Pressure and Concentration on Performance of a Vertical Falling-Film Type of Absorber and Generator Using Lithium Bromide Aqueous Solutions, *Int. J. Refrig.*, vol. 17, No.8 pp.538-542. 1994.
63. McNeely, L.A. Thermodynamic Properties of Aqueous Solutions of Lithium Bromide, *ASHRAE Transactions*, vol. 85, pp.413-434. 1979.
64. Meunier, F., Ed., *Fundamentals of Adsorption 6*, Elsevier, Paris, 1998.
65. Miller, W.A. The experimental analysis of aqueous lithium bromide vertical falling film absorption, PhD thesis, University of Tennessee, Knoxville, 1998.
66. Miller, W.A. and H. Perez-Blanco. Vertical-Tube Aqueous LiBr Falling Film Absorption Using Advanced Surfaces, *International Absorption Heat Pump Conference, AES* – vol. 31, pp.185–202. 1993.
67. Miller, W.A. and M. Keyhani. The Correlation of Simultaneous Heat and Mass Transfer Experimental Data for Aqueous Lithium Bromide Vertical Falling Film Absorption, *Journal of Solar Energy Engineering*, vol. 123, pp.30-42. February 2001.
68. Min, J.K. and D.H. Choi. Analysis of the Absorption Process on a Horizontal Tube Using Navier-Stokes Equations with Surface-Tension Effects, *International Journal of Heat and Mass Transfer*, vol. 42, pp.4567-4578. 1999.



69. Mobius, D. and R. Miller. [Editors], Drops and Bubbles in Interfacial Research, Elsevier Science B. V. All rights reserved, 1998.
70. Moffat, R.J. Describing the Uncertainties in Experimental Results, Experimental Thermal and Fluid Science, Vol. 1, pp 3-17, 1988.
71. Murray, J.G. Purge Needs in Absorption Chillers, ASHRAE Journal, pp. 40-47, October 1993a.
72. Oosthuizen, Patric H. and David Naylor. Edwards, Convective Heat Transfer Analysis, pp. 5756-577, McGraw-Hill International Editions, 1999.
73. Nakoryakov, V.E. and N.I. Grigor'eva. Combined heat and mass transfer during absorption in drops and films. Journal of Engineering Physics, vol. 32 (3), pp. 243–247. 1977.
74. Neima, Brauner. Non-isothermal Vapour Absorption into Falling Film, International Journal of Heat and Mass Transfer, Vol. 34, No. 3, pp 767-784, 1991.
75. Nomura, T., N. Nishimura, S. Wei and S. Yamaguchi. Heat and Mass Transfer Mechanism in the Absorber of Water/LiBr Conventional Absorption Refrigerator: Experimental Examination by Visualized Model, International Absorption Heat Pump Conference, AES–vol. 31, pp.203–208. 1993.
76. Nosoko, T., A. Miyara and T. Nagata. Characteristics of falling film flow on completely wetted horizontal tubes and the associated gas absorption, International Journal of Heat and Mass Transfer, vol. 45, pp 2729-2738, 2002.
77. Pallas, N.R. and Y. Harrison. An automated Drop Shape Apparatus and the Surface Tension of Pure Water, Colloids and Surfaces, Vol. 43, pp 169-194, 1990.
78. Patankar, S.V. Numerical Heat Transfer and Fluid flow, Hemisphere Publishing Corporation, USA. 1980.
79. Patnaik, V. and H. Perez-Blanco. A Counter Flow Heat Exchanger Analysis for the Design of Falling Film Absorbers, International Absorption Heat Pump Conference, AES – vol. 31, pp.209–216. 1993.
80. Patnaik, V. and H. Perez-Blanco. A Study of Absorption Enhancement by Wave Film Flows, Int. J. Heat and Fluid Flow, vol. 17, pp.71-77. 1996.
81. Patnaik, V., H. Perez-Blanco and W.A. Ryan. A Simple Analytical Model for the Design of Vertical Tube Absorbers, ASHRAE Transaction: Research, vol. 99(2), pp.69-80. 1993.
82. Potnis, S.V., T.G. Lenz and E.H. Dunlop. Measurement of Water Diffusivity in Aqueous Lithium Bromide and Lithium Chloride solutions, Chemical Engineering Communications, vol. 139, pp. 41-49. 1995.
83. Rogers, J.T. Laminar Falling Film Flow and Heat Transfer Characteristics on Horizontal Tubes, The Canadian Journal of Chemical Engineering, vol. 59, pp. 213-222. 1981.

84. Rogers, J.T. and S.S. Goindi. Experimental laminar Falling Film Heat Transfer Coefficients on a Large Diameter Horizontal Tube, *The Canadian Journal of Chemical Engineering*, vol. 67, pp. 560-568, 1989.
85. Ryan, W.A. Water Absorption in an Adiabatic Spray of Aqueous Lithium Bromide Solution, *International Absorption Heat Pump Conference, AES* – vol. 31, pp.155–162. 1993.
86. Sabir, H.M., I.W. Eames and K.O. Suen. The Effect of Non-Condensable Gases on the Performance of Film Absorbers in Vapour Absorption Systems, *Applied Thermal Engineering*, vol. 19, pp.531-541. 1999.
87. Schwarzer, B.P., M.S. Rahbar and P. LeGoff. A Spiral Fin Tube: A Novel Type of Falling Film Heat and Mass Exchanger, *International Absorption Heat Pump Conference, AES* – vol. 31, pp.179-183. 1993.
88. Siyoung, J. and S. Garimella. Falling Film and Droplet Mode Heat and Mass Transfer in a Horizontal Tube LiBr/Water Absorber, *International Journal of Heat and Mass Transfer*, vol. 45(7), pp. 1445-1458, 2002.
89. Skelland, A.H.P and S.S. Minhas. Dispersed Phase Mass Transfer during Drop Formation and Coalescence in liquid-liquid extraction, *AIChE Journal*, Vol. 17(6), pp. 1316-1324, 1971.
90. Suryanarayana, N.V. *Engineering Heat Transfer*, Minneapolis/St. Paul: West Publishing Company, pp. 291-428. 1995.
91. Sideman, S., Horn H., Moalem D. Transport Characteristics of Films Flowing over Horizontal Smooth Tubes, *International Journal of Heat and Mass Transfer*, vol. 21(3), pp. 285-294, 1978.
92. Talbi, M.M. and B. Agnew. Exergy Analysis: an Absorption Refrigerator Using Lithium Bromide and Water as the Working Fluids, *Applied Thermal Engineering*, vol. 20, pp.619-630. 2000.
93. Tsai, B. and H. Perez-Blanco. Limits of Mass Transfer Enhancement in Lithium Bromide-Water Absorbers by Active Techniques, *International Journal of Heat and Mass Transfer*, vol. 41, no. 15, pp.2409-2416. 1998.
94. Uddholm, H. and F. Settevall. Model of Dimensioning a Falling Film Absorber in an Absorption Heat Pump, *Int. J. Refrig*, vol. 11, pp.41-45. 1988.
95. Vliet, G.C. and W. Chen. Location of Non-Absorbable Gases in a Simplified Absorber Geometry, *International Absorption Heat Pump Conference, AES* – vol. 31, pp.171–177. 1993.
96. Wassenaar, R.H. Measured and Predicted Effect of Flow Rate and Tube Spacing on Horizontal Tube Absorber Performance, *Int. J. Refrig.*, vol. 19, No. 5, pp.347-355. 1996.

97. Wekken, B.J.C. van der and R.H. Wassenaar. Simultaneous Heat and Mass Transfer Accompanying Absorption Laminar Flow Over a Cooled Wall, *Int. J. Refrig*, vol. 11, pp.70-77. 1988.
98. Whitman, W.C., W.M. Johnson and J. Tomczyk. *Refrigeration and Air Conditioning Technology: Concepts, Procedures, and Troubleshooting Techniques*. 4th edition, pp.1031-1076, Albany, NY USA: Delmar Publishers, Thomson Learning Press. 2000.
99. Wijesundera, N.E., J.C. Ho and M.R. Islam. A Novel Design of Absorbers for Vapor-Absorption Cooling Systems –US Provisional Patent Application, Submitted, 2002.
100. Yang, R. and B.D. Wood. A Numerical Modeling of an Absorption Process on a Liquid Falling Film, *Solar Energy*, vol. 48, No. 3, pp. 195-198. 1992.
101. Yang, R. and T. Jou. Non-Absorbable Gas Effect on the Wavy Film Absorption Process, *International Journal of Heat and Mass Transfer*, vol. 41, pp.3657-3668. 1998.
102. Yigit, A. A Numerical Study of Heat and Mass Transfer in Falling Film Absorber, *Int. Comm. Heat Mass Transfer*, vol. 26, No.2, pp.269-278. 1999.
103. Yoon, J.I, O.K. Kwon and C.G. Moon. Experimental Study of Heat and Mass Transfer on an Absorber with Several Enhancement Tubes, *Heat Transfer – Asian Research*, vol. 28(8), pp.664-673. 1999.
104. Yoshinori, Kawase and Jaromir J. Ulbrecht. Formation of Drops and Bubbles in Flowing Liquids, *Ind. Eng. Chem. Process Des. Dev.* Vol. 20, pp. 636-640, 1981.
105. Yung, D. , J.J. Lorenz and E. N. Ganic. Vapor/Liquid Interaction and Entrainment in Falling Film Evaporators, *Journal of Heat Transfer*, Vol. 102, pp. 20-25, 1980.
106. Ziegler, F. and G. Grossman. Heat-Transfer Enhancement by Additives, *International Journal of Refrigeration*, Vol. 19, No. 5, pp.301-309, 1996.

**APPENDIX A**  
**NUMERICAL MODEL OF TUBULAR ABSORBERS**

**A.1 Numerical solution of the governing equations for the round tube**

The governing equations given in section 3.1.2 are discretized using the finite difference method. The co-ordinate transformation and the discretization process using non-uniform mesh are described in this section. The transformation of co-ordinates is slightly different for the round tube and the flat plate models and hence described separately in the following sections.

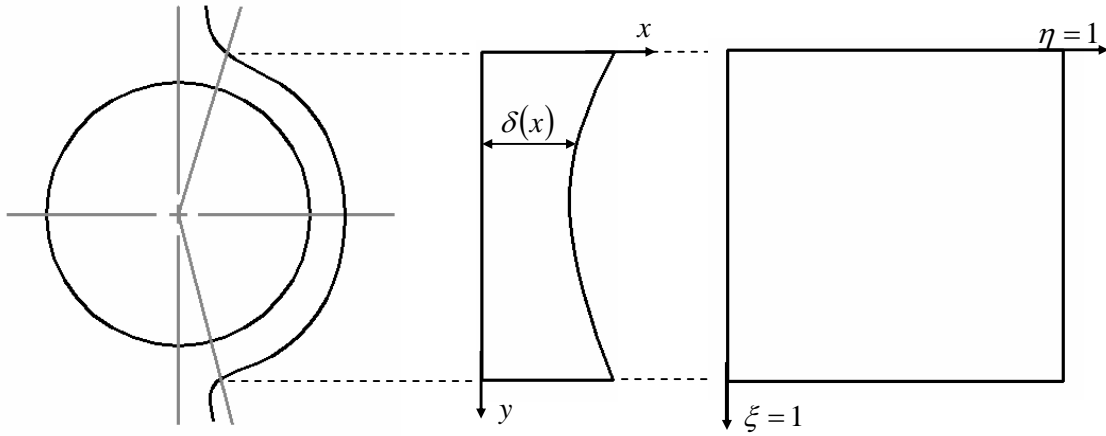


Figure A.1 Transformation of co-ordinates

In order to transform the irregular physical domain into a rectangular domain, following transformation relations are used as also been used by Chowdhury et al. [19].

$$\eta = \frac{y}{\delta} , \xi = \frac{\theta}{\pi} \quad (\text{A.1})$$

Where  $\eta$  is the non-dimensionalized distance along the direction  $y$  and  $\xi$  is the non-dimensionalized distance along the direction  $x$  as shown in Figure A.1.

Corresponding differential relations are:

$$\begin{aligned}
x_\xi &= \frac{\partial x}{\partial \xi} = \pi r_o & y_\xi &= \frac{\partial y}{\partial \xi} = \eta \frac{\partial \delta}{\partial \xi} \\
x_\eta &= \frac{\partial x}{\partial \eta} = 0 & y_\eta &= \frac{\partial y}{\partial \eta} = \delta
\end{aligned} \tag{A.2}$$

Divergence relation is:

$$\nabla \cdot \vec{F} = \frac{\partial F_1}{\partial x} + \frac{\partial F_2}{\partial y} = \frac{1}{(x_\xi y_\eta - x_\eta y_\xi)} \left[ \frac{\partial}{\partial \xi} (y_\eta F_1 - x_\eta F_2) + \frac{\partial}{\partial \eta} (x_\xi F_2 - y_\xi F_1) \right] \tag{A.3}$$

Substituting the above sets of transformation relations Eqs. (A.1)- (A.2), into Eq. (A.3), Eqs. (3.12)- (3.13), (3.1)-(3.3) can be transformed to the following forms respectively:

$$\delta = \left[ \frac{3\nu\Gamma}{\rho g \sin(\pi\xi)} \right]^{\frac{1}{3}} \tag{A.4}$$

Differentiating Eq. (A.4) with respect to  $\xi$ , the rate of change of film thickness is as follows:

$$\frac{d\delta}{d\xi} = \left[ \frac{\nu\Gamma}{9\rho g} \right]^{\frac{1}{3}} \frac{S}{r_o \sin^{\frac{1}{3}}(\pi\xi) \tan(\pi\xi)} \tag{A.5}$$

where the length of flowing film,  $S = \pi r_o$

From Eq. (3.13),

$$u = \frac{g\delta^2 \sin \theta}{\nu} \left[ \eta - \frac{\eta^2}{2} \right] \tag{A.6}$$

Continuity equation becomes;

$$\frac{\partial v}{\partial \eta} = \eta \frac{d\delta}{d\xi} \frac{1}{S} \frac{\partial u}{\partial \eta} - \frac{\delta}{S} \frac{\partial u}{\partial \xi} \tag{A.7}$$

Energy equation becomes;

$$\frac{\partial(uT)}{\partial \xi} - \left( \frac{1}{\delta} \frac{d\delta}{d\xi} \frac{\partial}{\partial \eta} (\eta u T) \right) + \frac{1}{\delta} \frac{d\delta}{d\xi} u T + \left( \frac{S}{\delta} \frac{\partial}{\partial \eta} (vT) \right) - \left( \frac{\alpha S}{\delta^2} \frac{\partial^2 T}{\partial \eta^2} \right) = 0 \tag{A.8}$$

Species concentration equation becomes

$$\frac{\partial(uw)}{\partial\xi} - \left( \frac{1}{\delta} \frac{d\delta}{d\xi} \frac{\partial}{\partial\eta} (\eta uw) \right) + \frac{1}{\delta} \frac{d\delta}{d\xi} uw + \left( \frac{S}{\delta} \frac{\partial}{\partial\eta} (vw) \right) - \left( \frac{DS}{\delta^2} \frac{\partial^2 w}{\partial\eta^2} \right) = 0 \quad (\text{A.9})$$

Differentiating Eq. (A.6) with respect to  $\eta$  and  $\xi$  and substituting in Eq. (A.7) following expression is obtained:

$$\frac{\partial v}{\partial\eta} = \left[ \frac{g \sin\theta}{\nu} \times \frac{d\delta}{d\xi} \times \frac{\delta^2}{S} (\eta - \eta^2) - \frac{\delta}{S} \times \frac{g}{\nu} \left( 2\delta \times \frac{d\delta}{d\xi} \sin\theta + \pi\delta^2 \cos\theta \right) \left( \eta - \frac{\eta^2}{2} \right) \right] \quad (\text{A.10})$$

After the integration of Eq. (A.10) with respect to  $d\eta$ , expression for v-velocity is obtained:

$$v = - \left( \frac{g\delta^2\eta^2}{2\nu \times S} \right) \left[ \frac{d\delta}{d\xi} \times \sin\theta + \pi\delta \left( 1 - \frac{\eta}{3} \right) \cos\theta \right] \quad (\text{A.11})$$

Boundary conditions, Eqs. (3.4)-(3.8) are transformed into the following forms:

$$\text{a) } \left. \begin{array}{l} \xi = \xi_i \\ 0 \leq \eta \leq 1 \end{array} \right\} T = T_{si}, \quad w = w_{si} \quad (\text{A.12})$$

$$\text{b) } \left. \begin{array}{l} \xi_i \leq \xi \leq \xi_o \\ \eta = 0 \end{array} \right\} T = T_{wall}, \quad \frac{\partial w}{\partial\eta} = 0 \quad (\text{A.13})$$

$$\text{c) } \left. \begin{array}{l} \xi_i \leq \xi \leq \xi_o \\ \eta = 1 \end{array} \right\} \dot{m}_v = - \frac{\rho D}{\delta w_{if}} \frac{\partial w}{\partial\eta} \Big|_{\eta=1} \quad (\text{A.14})$$

$$\frac{\partial T}{\partial\eta} \Big|_{\eta=1} = \frac{\delta i_{ab} \dot{m}_v}{k_s} \quad (\text{A.15})$$

$$T_{if} = f(p, w_{if}) \quad (\text{A.16})$$

## A.2 Numerical solution of the governing equations for the flat plate

As stated in Figure 3.2(a), only variable film thickness has to be accommodated into the computational field when a flat plate model is used. Therefore following transformation relations are chosen.

$$\eta = \frac{y}{\delta(x)}, \quad \xi = \frac{x}{P_L} \quad (\text{A.17})$$

where  $P_L$  is circumferential length of the flowing film.

Corresponding differential relations are:

$$\begin{aligned} x_\xi &= P_L & y_\xi &= \eta \frac{\partial \delta}{\partial \xi} \\ x_\eta &= 0 & y_\eta &= \delta \end{aligned} \quad (\text{A.18})$$

Substituting above sets of transformation relations, Eqs. (A.17)- (A.18), into Eq. (A.3), Eqs. (3.12)- (3.13), (3.1)-(3.3) can be transformed in the following forms respectively:

$$\delta = \left[ \frac{3\mathcal{V}\Gamma}{\rho g} \right]^{\frac{1}{3}} \quad (\text{A.19})$$

Differentiating Eq. (A.19) with respect to  $\xi$ , the rate of change of film thickness is as follows:

$$\frac{d\delta}{d\xi} = \dot{m}_v P_L \left[ \frac{\nu}{9\rho g \Gamma^2} \right]^{\frac{1}{3}} \quad (\text{A.20})$$

From Eq. (3.13),

$$u = \frac{g\delta^2}{\nu} \left[ \eta - \frac{\eta^2}{2} \right] \quad (\text{A.21})$$

Continuity equation becomes;

$$\frac{\eta}{\delta L} \frac{d\delta}{d\xi} \frac{\partial u}{\partial \eta} + \frac{1}{\delta} \frac{\partial v}{\partial \eta} = 0 \quad (\text{A.22})$$

Energy equation becomes;

$$\frac{1}{P_L} \frac{\partial(uT)}{\partial \xi} - \left( \frac{\eta}{\delta P_L} \frac{d\delta}{d\xi} \frac{\partial}{\partial \eta} (uT) \right) + \frac{1}{\delta P_L} \frac{d\delta}{d\xi} uT + \left( \frac{1}{\delta} \frac{\partial}{\partial \eta} (vT) \right) - \left( \frac{\alpha}{\delta^2} \frac{\partial^2 T}{\partial \eta^2} \right) = 0 \quad (\text{A.23})$$

Species concentration equation becomes;

$$\frac{1}{P_L} \frac{\partial(uw)}{\partial \xi} - \left( \frac{\eta}{\delta P_L} \frac{d\delta}{d\xi} \frac{\partial}{\partial \eta} (uw) \right) + \frac{1}{\delta P_L} \frac{d\delta}{d\xi} uw + \left( \frac{1}{\delta} \frac{\partial}{\partial \eta} (vw) \right) - \left( \frac{\alpha}{\delta^2} \frac{\partial^2 w}{\partial \eta^2} \right) = 0 \quad (\text{A.24})$$

Boundary conditions are remained same as described in Eqs. (A.12)-(A.16).

### A.3 Discretization of governing equations

The governing equations Eqs. (A.8) – (A.9) or Eqs. (A.23)- (A.24) are discretized using the finite difference method and solved numerically using a 2<sup>nd</sup> order scheme. Due to the presence of strong convection along the flow direction, three-point backward difference scheme is used in this direction. Central difference scheme is used along the cross flow direction.

#### A.3.1 Non-uniform grid generation

Applying non-uniform grid generation techniques in both  $\xi - \eta$  directions, the computational domain was represented by Figure 3.5. Grid size gradually increases in geometric progression manner in both the direction of co-ordinates. For non-uniform mesh size, finite difference scheme is developed by using Taylor series expansion. For second order backward difference and central difference schemes, following relations are developed.

##### A.3.1.1 Backward difference scheme

In Figure A.2, the solid lines represent the grid lines whereas the dotted lines are the cell boundary lines. The first two grid sizes in the figure are expressed as follows if the cell size increases with geometric progression rule.

$$ad\eta = \frac{1}{2}(1 + \beta)d\eta \quad (\text{A.3.1})$$

$$bd\eta = \frac{1}{2}(\beta + \beta^2)d\eta \quad (\text{A.3.2})$$

The functional value at the two neighboring grid points (N-2) and (N-1) are expanded as,



$$f_{N-2} = f_N - (a+b)d\eta \left. \frac{df}{d\eta} \right|_N + \frac{(a+b)^2 d\eta^2}{2} \left. \frac{d^2 f}{d\eta^2} \right|_N + o(d\eta^3) \quad (\text{A.3.3})$$

$$f_{N-1} = f_N - (a)d\eta \left. \frac{df}{d\eta} \right|_N + \frac{(a)^2 d\eta^2}{2} \left. \frac{d^2 f}{d\eta^2} \right|_N + o(d\eta^3) \quad (\text{A.3.4})$$

Above two equations are used to obtain following first order derivative of the function  $f$  with second order accuracy at the grid point  $N$ ,

$$\left. \frac{df}{d\eta} \right|_N = \frac{a^2 f_{N-2} - (a+b)^2 f_{N-1} + b(2a+b)f_N}{ab(a+b)d\eta} \quad (\text{A.3.5})$$

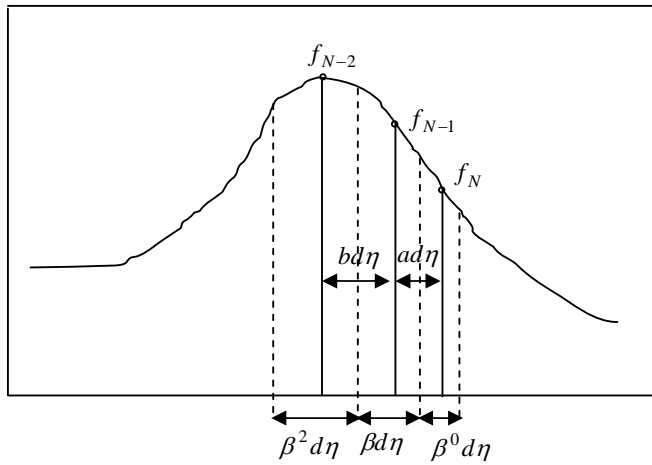


Figure A.2 Taylor series representation for non-uniform grid; backward difference scheme.

For uniform grid, Eq. (A.3.5) is transformed into the following expression by putting

$a = b$ .

$$\left. \frac{df}{d\eta} \right|_N = \frac{f_{N-2} - 4f_{N-1} + 3f_N}{2d\eta} \quad (\text{A.3.6})$$

Eqs. (A.3.3) and (A.3.4) are also used to obtain second order derivative of function  $f$  with second order accuracy at the grid point  $N$  as follows,

$$\left. \frac{d^2 f}{d\eta^2} \right|_N = \frac{2af_{N-2} - 2(a+b)f_{N-1} + 2bf_N}{ab(a+b)d\eta^2} \quad (\text{A.3.7})$$

For uniform grid

$$\left. \frac{d^2 f}{d\eta^2} \right|_N = \frac{f_{N-2} - 2f_{N-1} + f_N}{d\eta^2} \quad (\text{A.3.8})$$

### A.3.1.2 Central difference scheme

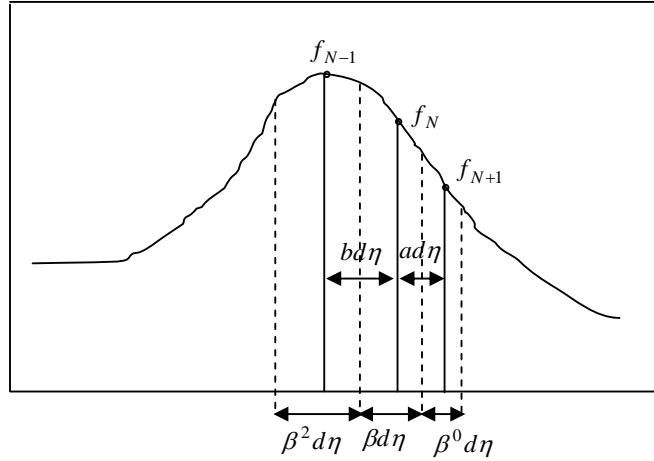


Figure A.3 Taylor series representation for non-uniform grid; central difference scheme.

For the representation shown in Figure A.3, the functional values at grid point (N-1) and (N-2) are

$$f_{N-1} = f_N - (b)d\eta \left. \frac{df}{d\eta} \right|_N + \frac{(b)^2 d\eta^2}{2} \left. \frac{d^2 f}{d\eta^2} \right|_N + o(d\eta^3) \quad (\text{A.3.9})$$

$$f_{N+1} = f_N + (a)d\eta \left. \frac{df}{d\eta} \right|_N + \frac{(a)^2 d\eta^2}{2} \left. \frac{d^2 f}{d\eta^2} \right|_N + o(d\eta^3) \quad (\text{A.3.10})$$

By using above two equations, second order central difference formula for the first order derivative of function f is;

$$\left. \frac{df}{d\eta} \right|_N = \frac{(a^2 - b^2)f_N - a^2 f_{N-1} + b^2 f_{N+1}}{ab(a+b)d\eta} \quad (\text{A.3.11})$$

For uniform grid, above expression becomes,

$$\left. \frac{df}{d\eta} \right|_N = \frac{f_{N+1} - f_{N-1}}{2d\eta} \quad (\text{A.3.12})$$

Expanding Eqs. (A.3.9) and (A.3.10) until 4<sup>th</sup> order error terms and rearranging resulting equations, second order central difference formula for the second order derivative of function  $f$  is,

$$\left. \frac{d^2 f}{d\eta^2} \right|_N = \frac{(2a)f_{N-1} - 2(a+b)f_N + 2bf_{N+1}}{ab(a+b)d\eta^2} \quad (\text{A.3.13})$$

For uniform grid, the expression becomes,

$$\left. \frac{d^2 f}{d\eta^2} \right|_N = \frac{f_{N-1} - 2f_N + f_{N+1}}{d\eta^2} \quad (\text{A.3.14})$$

Eqs. (A.3.5), (A.3.7), (A.3.11), (A.3.13) are used at any nodal point within the flow field in both the co-ordinate directions. But Eqs. (A.3.11) and (A.3.13) are not applicable to the boundary nodes. On the boundary nodes, backward difference scheme is applied.

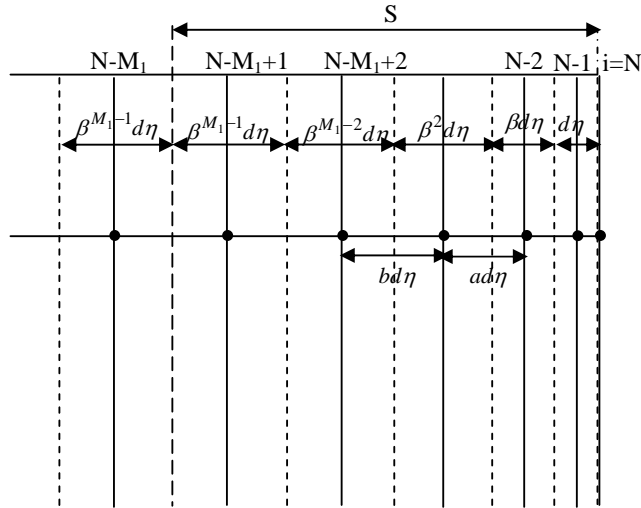


Figure A.4 Non-uniform grid along  $\eta$  direction.

**Grid size variations along the co-ordinate directions**

In Figure A.4, following definitions are used;

$N$  = total number of cells

$M_1$  = number of non-uniform cells

$i$  = current grid point at the cell centre

S= length of non-uniform grid zone

(1-S)= length of uniform grid zone

Since non-uniform grid increases with geometric progression rule, the length of non-uniform grid zone, S is

$$S = d\eta \left[ \frac{\beta^{M_1} - 1}{\beta - 1} \right] \quad (\text{A.3.15})$$

For known values of  $M_1$  and S,  $d\eta$  is calculable from Eq. (A.3.15). Total number of cells or grid points N is calculated from following expression.

$$N = \text{Int} \left( \frac{1-S}{d\eta} \right) + M_1 \quad (\text{A.3.16})$$

Where  $\text{Int}(\ )$  indicates integer value of the bracketed term.

Two corresponding grid sizes in Figure A.4 are therefore expressed as follows,

In the non-uniform grid zone,

$$\left. \begin{aligned} ad\eta &= \frac{1}{2} [\beta^{N-i-1} + \beta^{N-i}] d\eta \\ bd\eta &= \frac{1}{2} [\beta^{N-i} + \beta^{N-i+1}] d\eta \end{aligned} \right\} \text{where } i = N \rightarrow (N - M_1 + 2) \quad \text{A.3.17}$$

At the interface of non-uniform and uniform grid zone,

$$\left. \begin{aligned} ad\eta &= \frac{1}{2} [\beta^{M_1-2} + \beta^{M_1-1}] \\ bd\eta &= \beta^{M_1-1} d\eta \end{aligned} \right\} \text{where } i = (N - M_1 + 1) \quad (\text{A.3.18})$$

In the uniform grid zone,

$$\left. \begin{aligned} ad\eta &= \beta^{M_1-1} d\eta \\ bd\eta &= \beta^{M_1-1} d\eta \end{aligned} \right\} \text{where } i = (N - M_1) \rightarrow 1 \quad (\text{A.1.19})$$

Above formulas can be used in any direction of co-ordinate. The values of  $\beta, N, M_1, S$  are arbitrarily selected, until grid independent results are obtained.

### A.3.2 Discretization of energy equation

Applying central difference scheme along the  $\eta$ -direction and three-point backward difference scheme along the  $\xi$ -direction, discretized form of Eq. (A.8) at node point (j,i) shown in Figure A.5 becomes,

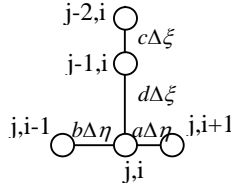


Figure A.5 Nodal distribution

$$\begin{aligned}
 & \frac{c^2 u(j-2,i)T(j-2,i) - (c+d)^2 u(j-1,i)T(j-1,i) + c(c+2d)u(j,i)T(j,i)}{(c+d)cd\Delta\xi} \\
 & - \left( \frac{1}{\delta(j)} \frac{d\delta}{d\xi} \right) \frac{\eta_i (a^2 - b^2) u(j,i)T(j,i) - (a^2) \eta_{i-1} u(j,i-1)T(j,i-1) + b^2 \eta_{i+1} u(j,i+1)T(j,i+1)}{ab(a+b)\Delta\eta} \\
 & + \frac{1}{\delta(j)} \frac{d\delta}{d\xi} u(j,i)T(j,i) + \frac{S}{\delta(j)} \frac{(a^2 - b^2)v(j,i)T(j,i) - a^2 v(j,i-1)T(j,i-1) + b^2 v(j,i+1)T(j,i+1)}{ab(a+b)\Delta\eta} \\
 & - \frac{\alpha S}{ab(a+b)\{\delta(j)\Delta\eta\}^2} [2aT(j,i-1) - 2(a+b)T(j,i) + 2bT(j,i+1)] = 0
 \end{aligned} \tag{A.3.20}$$

Where  $\Delta\xi = d\xi$  and  $\Delta\eta = d\eta$

The values of  $\eta$  in Eq. (A.3.20) are determined from following expressions in the regions shown in Figure A.4.

$$\left. \begin{aligned}
 \eta_i &= \eta_{i-1} + \frac{1}{2} \Delta\eta [\beta^{N-i} + \beta^{N-i-1}] \quad \left\{ i = (N-1) \rightarrow (N-M_1+1) \right. \\
 \eta_i &= \eta_{i-1} + \frac{1}{2} \Delta\eta [\beta^{N-M_1}] \quad \left\{ i = (N-M_1+1) \rightarrow 1 \right. \\
 \eta_N &= 1 - \frac{1}{2} \Delta\eta \quad ; \quad i = N \\
 \eta_0 &= \frac{1}{2} \beta^{M_1-1} \Delta\eta \quad ; \quad i = 0
 \end{aligned} \right\} \tag{A.3.21}$$

Summing up the coefficients of  $T(j,i)$  from Eq. (A.3.20):

$$A(i) = \left[ \begin{aligned}
 & \frac{c(c+2d)u(j,i)}{cd(c+d)\Delta\xi} - \frac{1}{\delta(j)} \frac{d\delta}{d\xi} \frac{(a^2 - b^2)\eta_i u(j,i)}{ab(a+b)\Delta\eta} + \frac{1}{\delta(j)} \frac{d\delta}{d\xi} u(j,i) \\
 & + \frac{S}{\delta(j)} \frac{(a^2 - b^2)v(j,i)}{ab(a+b)\Delta\eta} + \frac{DS}{\delta(j)^2} \frac{2(a+b)}{ab(a+b)\Delta\eta^2}
 \end{aligned} \right] \tag{A.3.22}$$

Coefficients of  $T(j, i-1)$ :

$$B(i) = \left[ \frac{\eta_{i-1}}{\delta(j)} \frac{d\delta}{d\xi} \frac{u(j, i-1)}{ab(a+b)\Delta\eta} - \frac{S}{\delta(j)} \frac{a^2}{ab(a+b)\Delta\eta} v(j, i-1) - \frac{\alpha S}{\{\delta(j)\Delta\eta\}^2} \frac{2a}{ab(a+b)} \right] \quad (\text{A.3.23})$$

Coefficients of  $T(j, i+1)$ :

$$C(i) = \left[ -\frac{\eta_{i+1}}{\delta(j)} \frac{d\delta}{d\xi} \frac{b^2 u(j, i+1)}{ab(a+b)\Delta\eta} + \frac{S}{\delta(j)} \frac{b^2 v(j, i+1)}{ab(a+b)\Delta\eta} - \frac{\alpha S}{\{\delta(j)\Delta\eta\}^2} \frac{2b}{ab(a+b)} \right] \quad (\text{A.3.24})$$

The constants are:

$$F(i) = \frac{(c+d)^2 u(j-1, i) T(j-1, i)}{cd(c+d)\Delta\xi} - \frac{c^2 u(j-2, i) T(j-2, i)}{cd(c+d)\Delta\xi} \quad (\text{A.3.25})$$

Using the above expressions, discretized form of Eq. (A.3.20) around the node  $(j, i)$

becomes,

$$B(i)T(j, i-1) + A(i)T(j, i) + C(i)T(j, i+1) = F(i) \quad (\text{A.3.26})$$

Eqs. (A.3.22)-(A.3.25) are used only in the non-uniform grid zone i.e. when  $N < i \leq N - M_1 + 1$  along  $\eta$  direction.

The temperature coefficients of Eq. (A.3.26) are expressed within the uniform grid zone simply stating  $a = b$  or  $c = d$  wherever applicable.

In the uniform grid zone along the direction of  $\eta$  i.e. when  $i = 1 \rightarrow (N - M_1)$ , the coefficients of Eq. (A.3.26) become,

$$A(i) = \left[ \frac{c(c+2d)u(j, i)}{cd(c+d)\Delta\xi} + \frac{1}{\delta(j)} \frac{d\delta}{d\xi} u(j, i) + \frac{DS}{\delta(j)^2} \frac{2}{\Delta\eta^2} \right] \quad (\text{A.3.27})$$

$$B(i) = \left[ \frac{\eta_{i-1}}{\delta(j)} \frac{d\delta}{d\xi} \frac{u(j, i-1)}{2\Delta\eta} - \frac{S}{\delta(j)} \frac{1}{2\Delta\eta} v(j, i-1) - \frac{\alpha S}{\{\delta(j)\Delta\eta\}^2} \right] \quad (\text{A.3.28})$$

$$C(i) = \left[ -\frac{\eta_{i+1}}{\delta(j)} \frac{d\delta}{d\xi} \frac{u(j, i+1)}{2\Delta\eta} + \frac{S}{\delta(j)} \frac{v(j, i+1)}{2\Delta\eta} - \frac{\alpha S}{\{\delta(j)\Delta\eta\}^2} \right] \quad (\text{A.3.29})$$

$$F(i) = \frac{(c+d)^2 u(j-1, i) T(j-1, i)}{(c+d)\Delta\xi} - \frac{c^2 u(j-2, i) T(j-2, i)}{cd(c+d)\Delta\xi} \quad (\text{A.3.30})$$

### A.3.2.1 Near wall treatment at $i = 1$

Figure A.6 shows that the region of  $i = 1$  is within the uniform grid zone. Putting a grid point on the last cell boundary at  $i = 0$ , following expressions are developed,

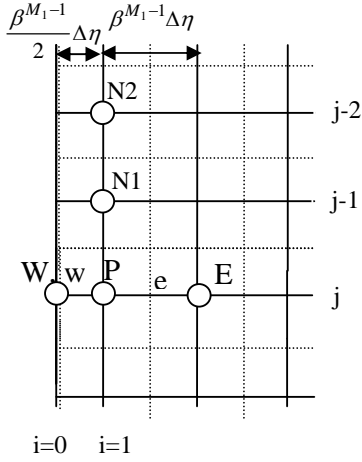


Figure A.6 Control volume near the wall

For constant wall,

$$T(j,0) = T_{WALL}$$

Discretization of Eq. (A.8) at  $i = 1$  and using of above relation provides,

$$A(1) = \left[ \frac{c(c+2d)u(j,1)}{cd(c+d)\Delta\xi} + \frac{1}{\delta(j)} \frac{d\delta}{d\xi} u(j,1) + \frac{DS}{\delta(j)^2} \frac{2}{\Delta\eta^2} \right] \quad (\text{A.3.31})$$

$$B(1) = 0 \quad (\text{A.3.32})$$

$$C(1) = \left[ -\frac{\eta_2}{\delta(j)} \frac{d\delta}{d\xi} \frac{u(j,2)}{2\Delta\eta} + \frac{S}{\delta(j)} \frac{v(j,2)}{2\Delta\eta} - \frac{\alpha S}{\{\delta(j)\Delta\eta\}^2} \right] \quad (\text{A.3.33})$$

$$F(1) = \frac{(c+d)^2 u(j-1,i)T(j-1,i)}{(c+d)\Delta\xi} - \frac{c^2 u(j-2,i)T(j-2,i)}{cd(c+d)\Delta\xi} + T(j,0) \left( \frac{\alpha S}{\{\delta(j)\Delta\eta\}^2} \right) \quad (\text{A.3.34})$$

### A.3.2.2 Near interface treatment

Interface region is within the non-uniform grid zone. Therefore, following developments are based on the grid representation shown in Figure A.4.

The discretization of Eq. (A.8) at the node  $i=(N-1)$  shown in Figure A.4 and application of boundary condition Eq. (A.16) produces the following results:

$$A(N-1) = \left[ \begin{array}{l} \frac{c(c+2d)u(j, N-1)}{cd(c+d)\Delta\xi} - \frac{1}{\delta(j)} \frac{d\delta}{d\xi} \frac{(a^2-b^2)\eta_{N-1}u(j, N-1)}{ab(a+b)\Delta\eta} + \frac{1}{\delta(j)} \frac{d\delta}{d\xi} u(j, N-1) \\ + \frac{S}{\delta(j)} \frac{(a^2-b^2)v(j, N-1)}{ab(a+b)\Delta\eta} + \frac{DS}{\delta(j)^2} \frac{2(a+b)}{ab(a+b)\Delta\eta^2} \end{array} \right] \quad (A.3.35)$$

$$B(N-1) = \left[ \frac{\eta_{N-2}}{\delta(j)} \frac{d\delta}{d\xi} \frac{u(j, N-2)}{ab(a+b)\Delta\eta} - \frac{S}{\delta(j)} \frac{a^2}{ab(a+b)\Delta\eta} v(j, N-2) - \frac{\alpha S}{\{\delta(j)\Delta\eta\}^2} \frac{2a}{ab(a+b)} \right] \quad (A.3.36)$$

$$C(N-1) = 0 \quad (A.3.37)$$

$$F(N-1) = \left[ \begin{array}{l} \frac{(c+d)^2 u(j-1, N-1) T(j-1, N-1)}{(c+d)\Delta\xi} - \frac{c^2 u(j-2, N-1) T(j-2, N-1)}{cd(c+d)\Delta\xi} \\ + T(j, N) \left( -\frac{\eta_N}{\delta(j)} \frac{d\delta}{d\xi} \frac{b^2 u(j, N)}{ab(a+b)\Delta\eta} + \frac{S}{\delta(j)} \frac{b^2 v(j, N)}{ab(a+b)\Delta\eta} - \frac{\alpha S}{\{\delta(j)\Delta\eta\}^2} \frac{2b}{ab(a+b)} \right) \end{array} \right] \quad (A.3.38)$$

Combining all the expressions above, following Tri-Diagonal matrix is formed:

$$\begin{array}{cccccccc|ccc} A(1) & C(1) & 0 & 0 & . & . & . & . & 0 & T(j,1) & F(1) \\ B(2) & A(2) & C(2) & 0 & & & & & 0 & T(j,2) & F(2) \\ 0 & B(3) & A(3) & C(3) & & & & & 0 & T(j,3) & F(3) \\ . & 0 & B(4) & A(4) & C(4) & & & & 0 & T(j,4) & F(4) \\ . & . & . & & & & & & . & . & . \\ . & . & . & & & & & & . & . & . \\ . & . & . & & & & & & . & . & . \\ . & . & . & & & 0 & B(N-3) & A(N-3) & C(N-3) & 0 & T(j, N-3) & F(N-3) \\ . & . & . & & & 0 & B(N-2) & A(N-2) & C(N-2) & T(j, N-2) & F(N-2) \\ 0 & . & . & . & . & . & 0 & 0 & B(N-1) & A(N-1) & T(j, N-1) & F(N-1) \end{array} = \quad (A.3.39)$$

Above equations are developed at any  $j$ -th position along  $\xi$  co-ordinate. As shown in Figure A.5, the two corresponding back rows along the direction  $j$ , are non-uniformly spaced. The values of  $c$  and  $d$  are calculated similar to the procedure of  $a$  and  $b$  calculation stated by Eqs. (A.3.17)-(A.3.19). In the uniform grid zone, same formulae are used along the  $\xi$  co-ordinate by putting  $c = d$  in the respective equations.



### A.3.3 Discretization of species concentration equation

In the non-uniform grid zone, i.e. when  $N < i \leq N - M_1 + 1$  as shown in Figure A.4, applying similar discretization techniques described in section A.3.2 for Eq. (A.9), following expression is obtained,

$$\begin{aligned} & \frac{c^2 u(j-2, i) T(j-2, i) - (c+d)^2 u(j-1, i) w(j-1, i) + c(c+2d) u(j, i) w(j, i)}{(c+d)cd\Delta\xi} \\ & - \left( \frac{1}{\delta(j)} \frac{d\delta}{d\xi} \right) \frac{\eta_i (a^2 - b^2) u(j, i) w(j, i) - (a^2) \eta_{i-1} u(j, i-1) w(j, i-1) + b^2 \eta_{i+1} u(j, i+1) w(j, i+1)}{ab(a+b)\Delta\eta} \\ & + \frac{1}{\delta(j)} \frac{d\delta}{d\xi} \frac{u(j, i) w(j, i) + \frac{S}{\delta(j)} \frac{(a^2 - b^2) v(j, i) w(j, i) - a^2 v(j, i-1) w(j, i-1) + b^2 v(j, i+1) w(j, i+1)}{ab(a+b)\Delta\eta}}{ab(a+b)\Delta\eta} \\ & - \frac{DS}{ab(a+b)\{\delta(j)\Delta\eta\}^2} [2aw(j, i-1) - 2(a+b)w(j, i) + 2bw(j, i+1)] = 0 \end{aligned}$$

Summing up the coefficients, following relations are obtained,

$$A(i) = \left[ \frac{c(c+2d)u(j, i)}{cd(c+d)\Delta\xi} - \frac{1}{\delta(j)} \frac{d\delta}{d\xi} \frac{(a^2 - b^2)\eta_i u(j, i)}{ab(a+b)\Delta\eta} + \frac{1}{\delta(j)} \frac{d\delta}{d\xi} u(j, i) + \frac{S}{\delta(j)} \frac{(a^2 - b^2)v(j, i)}{ab(a+b)\Delta\eta} \right] + \frac{DS}{\delta(j)^2} \frac{2(a+b)}{ab(a+b)\Delta\eta^2}$$

$$B(i) = \left[ \frac{\eta_{i-1}}{\delta(j)} \frac{d\delta}{d\xi} \frac{u(j, i-1)}{ab(a+b)\Delta\eta} - \frac{S}{\delta(j)} \frac{a^2}{ab(a+b)\Delta\eta} v(j, i-1) - \frac{DS}{\{\delta(j)\Delta\eta\}^2} \frac{2a}{ab(a+b)} \right]$$

$$C(i) = \left[ -\frac{\eta_{i+1}}{\delta(j)} \frac{d\delta}{d\xi} \frac{b^2 u(j, i+1)}{ab(a+b)\Delta\eta} + \frac{S}{\delta(j)} \frac{b^2 v(j, i+1)}{ab(a+b)\Delta\eta} - \frac{DS}{\{\delta(j)\Delta\eta\}^2} \frac{2b}{ab(a+b)} \right]$$

$$F(i) = \frac{(c+d)^2 u(j-1, i) w(j-1, i)}{cd(c+d)\Delta\xi} - \frac{c^2 u(j-2, i) w(j-2, i)}{cd(c+d)\Delta\xi}$$

Therefore discretized form of Eq. (A.9) becomes

$$B(i)w(j, i-1) + A(i)w(j, i) + C(i)w(j, i+1) = F(i) \quad (\text{A.3.40})$$

In the uniform grid zone i.e. when  $i = 1 \rightarrow (N - M_1)$

$$A(i) = \left[ \frac{c(c+2d)u(j, i)}{cd(c+d)\Delta\xi} + \frac{1}{\delta(j)} \frac{d\delta}{d\xi} u(j, i) + \frac{DS}{\delta(j)^2} \frac{2}{\Delta\eta^2} \right] \quad (\text{A.3.41})$$

$$B(i) = \left[ \frac{\eta_{i-1}}{\delta(j)} \frac{d\delta}{d\xi} \frac{u(j, i-1)}{2\Delta\eta} - \frac{S}{\delta(j)} \frac{1}{2\Delta\eta} v(j, i-1) - \frac{DS}{\{\delta(j)\Delta\eta\}^2} \right] \quad (\text{A.3.42})$$

$$C(i) = \left[ -\frac{\eta_{i+1}}{\delta(j)} \frac{d\delta}{d\xi} \frac{u(j, i+1)}{2\Delta\eta} + \frac{S}{\delta(j)} \frac{v(j, i+1)}{2\Delta\eta} - \frac{DS}{\{\delta(j)\Delta\eta\}^2} \right] \quad (\text{A.3.43})$$

$$F(i) = \frac{(c+d)^2 u(j-1, i)w(j-1, i)}{(c+d)\Delta\xi} - \frac{c^2 u(j-2, i)w(j-2, i)}{cd(c+d)\Delta\xi} \quad (\text{A.3.44})$$

### A.3.3.1 Near wall Treatment

Applying boundary condition Eq. (A.13) at  $i = 1$  shown in Figure A.6, following relation is obtained

$$w(j, 0) = w(j, 1)$$

Discretization of Eq. (A.9) at the 2<sup>nd</sup> node  $i = 1$  shown in Figure A.6 and using of above relation provides

$$A(1) = \left[ \frac{c(c+2d)u(j, 1)}{cd(c+d)\Delta\xi} + \frac{1}{\delta(j)} \frac{d\delta}{d\xi} u(j, 1) + \frac{DS}{\delta(j)^2} \frac{1}{\Delta\eta^2} \right] \quad (\text{A.3.45})$$

$$B(1) = 0 \quad (\text{A.3.46})$$

$$C(1) = \left[ -\frac{\eta_2}{\delta(j)} \frac{d\delta}{d\xi} \frac{u(j, 2)}{2\Delta\eta} + \frac{S}{\delta(j)} \frac{v(j, 2)}{2\Delta\eta} - \frac{DS}{\{\delta(j)\Delta\eta\}^2} \right] \quad (\text{A.3.47})$$

$$F(1) = \frac{(c+d)^2 u(j-1, 1)w(j-1, 1)}{(c+d)\Delta\xi} - \frac{c^2 u(j-2, 1)w(j-2, 1)}{cd(c+d)\Delta\xi} \quad (\text{A.3.48})$$

### A.3.3.2 Near interface region

Applying boundary condition Eq. (A.15) at  $i = (N-1)$  shown in Figure A.4, following expression is achieved

$$w(j, N) = \left( \frac{\rho D}{\rho D + m_v(j)\delta(j)\Delta\eta} \right) w(j, N-1) \quad (\text{A.3.49})$$

Therefore, by using above relation, the coefficients of discretized form of Eq. (A.9) at  $i = (N-1)$  are

$$A(N-1) = \left[ \begin{array}{l} \frac{c(c+2d)u(j, N-1)}{cd(c+d)\Delta\xi} - \frac{1}{\delta(j)} \frac{d\delta}{d\xi} \frac{(a^2-b^2)\eta_{N-1}u(j, N-1)}{ab(a+b)\Delta\eta} + \frac{1}{\delta(j)} \frac{d\delta}{d\xi} u(j, N-1) \\ + \frac{S}{\delta(j)} \frac{(a^2-b^2)v(j, N-1)}{ab(a+b)\Delta\eta} + \frac{DS}{\delta(j)^2} \frac{2(a+b)}{ab(a+b)\Delta\eta^2} \\ + \frac{\rho D}{\rho D + \dot{m}_v(j)\delta(j)\Delta\eta} \left( \begin{array}{l} -\frac{\eta_N}{\delta(j)} \frac{d\delta}{d\xi} \frac{b^2u(j, N)}{ab(a+b)\Delta\eta} + \frac{S}{\delta(j)} \frac{b^2v(j, N)}{ab(a+b)\Delta\eta} \\ -\frac{DS}{\{\delta(j)\Delta\eta\}^2} \frac{2b}{ab(a+b)} \end{array} \right) \end{array} \right] \quad (\text{A.3.50})$$

$$B(N-1) = \left[ \begin{array}{l} \frac{\eta_{N-2}}{\delta(j)} \frac{d\delta}{d\xi} \frac{u(j, N-2)}{ab(a+b)\Delta\eta} - \frac{S}{\delta(j)} \frac{a^2}{ab(a+b)\Delta\eta} v(j, N-2) \\ -\frac{DS}{\{\delta(j)\Delta\eta\}^2} \frac{2a}{ab(a+b)} \end{array} \right] \quad (\text{A.3.51})$$

$$C(N-1) = \left[ \begin{array}{l} -\frac{\eta_N}{\delta(j)} \frac{d\delta}{d\xi} \frac{b^2u(j, N)}{ab(a+b)\Delta\eta} + \frac{S}{\delta(j)} \frac{b^2v(j, N)}{ab(a+b)\Delta\eta} \\ -\frac{DS}{\{\delta(j)\Delta\eta\}^2} \frac{2b}{ab(a+b)} \end{array} \right] \quad (\text{A.3.52})$$

$$F(N-1) = \left[ \begin{array}{l} \frac{(c+d)^2 u(j-1, N-1)w(j-1, N-1)}{(c+d)\Delta\xi} \\ -\frac{c^2 u(j-2, N-1)w(j-2, N-1)}{cd(c+d)\Delta\xi} \end{array} \right] \quad (\text{A.3.53})$$

Therefore the following Tri-Diagonal matrix is formed:

$$\begin{array}{cccccccccccc} A(1) & C(1) & 0 & 0 & . & . & . & . & . & . & 0 & \left| \begin{array}{l} w(j,1) \\ w(j,2) \\ w(j,3) \\ w(j,4) \\ . \\ . \\ . \\ w(j, N-3) \\ w(j, N-2) \\ w(j, N-1) \end{array} \right| & \left| \begin{array}{l} F(1) \\ F(2) \\ F(3) \\ F(4) \\ . \\ . \\ . \\ F(N-3) \\ F(N-2) \\ F(N-1) \end{array} \right| \\ B(2) & A(2) & C(2) & 0 & & & & & & & 0 & & \\ 0 & B(3) & A(3) & C(3) & & & & & & & 0 & & \\ . & 0 & B(4) & A(4) & C(4) & & & & & & 0 & & \\ . & . & . & & & & & & & & . & & \\ . & . & . & & & & & & & & . & & \\ . & . & . & & & & & & & & . & & \\ . & . & . & & & & 0 & B(N-3) & A(N-3) & C(N-3) & 0 & & \\ . & . & . & & & & 0 & B(N-2) & A(N-2) & C(N-2) & & & \\ 0 & . & . & . & . & . & 0 & 0 & B(N-1) & A(N-1) & & & \end{array} = \quad (\text{A.3.54})$$

#### A.4 Sensitivity analysis of entering and leaving angle to a tube

From the discussions made in section 3.1.4.3, the computational domain for the film flow over a single tube has to start with sufficient distance away from the top and bottom dead centre of a tube. As demonstrated in Figure 3.6, the values of the film entering and leaving angle to a tube are chosen based on a sensitivity analysis. The procedure of this sensitivity analysis is as follows. At first, a baseline value for the film entering and leaving angle to a tube are chosen based on a sensitivity analysis. The procedure of this sensitivity analysis is as follows. At first, a baseline value for the film entering and leaving angle to the tube  $\theta_i, \theta_o$  are taken arbitrarily. For simplicity, the values are kept equal for these two angles,  $\theta_i, \theta_o$ . Afterwards, a total of  $\pm 70\%$  variations are allowed with respect to the base values of  $\theta_i, \theta_o$ . The model predictions for the tube-wise variations of mass flux, bulk temperature and concentration are obtained for each of the selected angular values within the prescribed range. The results are plotted graphically in Figures A.7-A.9. The percent difference between the mass flux, temperature and concentration predictions obtained using the base line value and those obtained using the new value of the angles  $\theta_i, \theta_o$  are observed. The percent differences of the results indicate the degree of sensitivity.

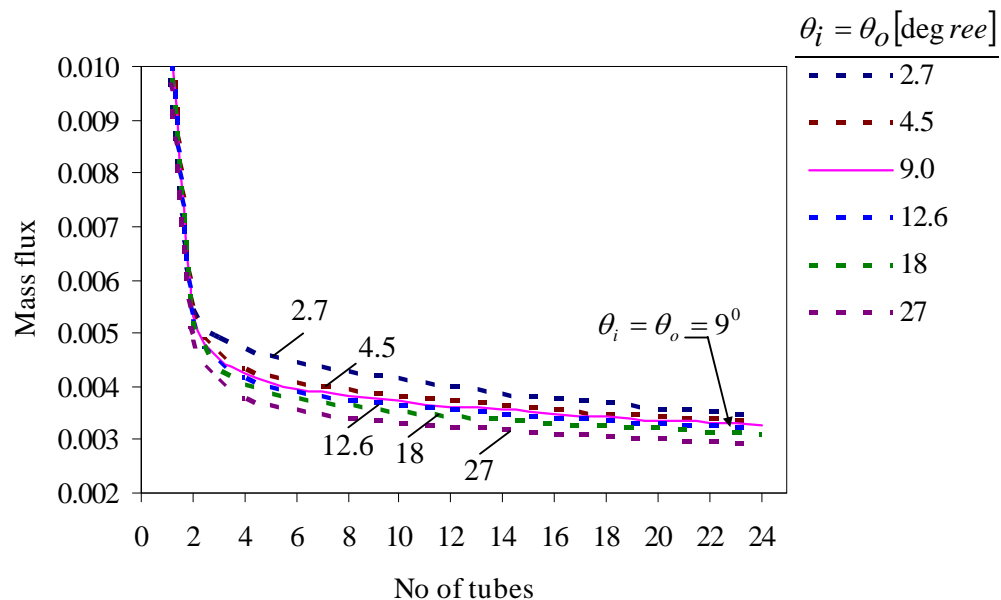


Figure A.7 Sensitivity of mass flux [ $\text{kg.m}^{-2}\text{s}^{-1}$ ] at different angular values: operating conditions of Islam [43].

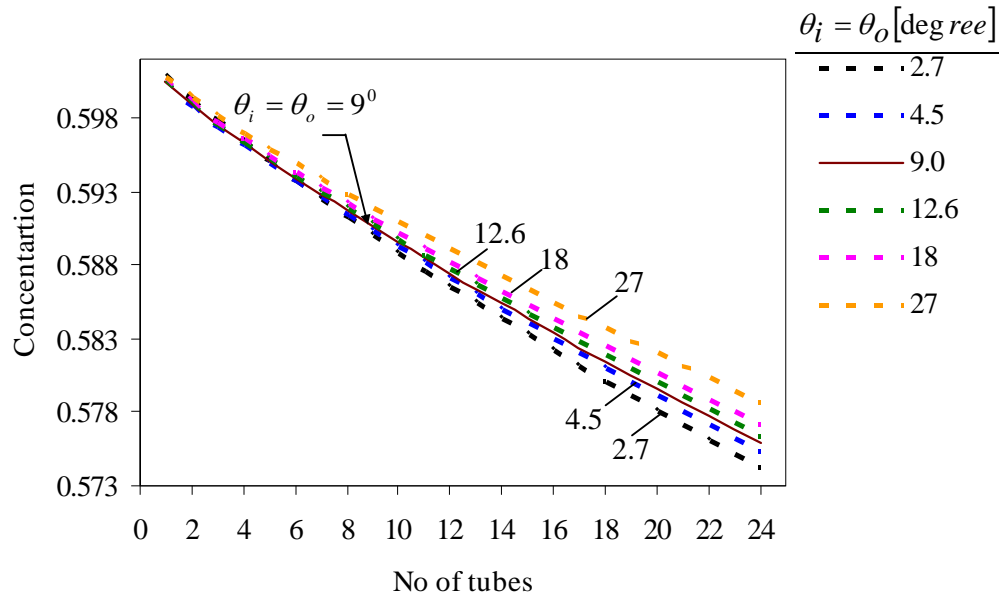


Figure A.8 Sensitivity of bulk concentration [%LiBr/100] at different angular values: operating conditions of Islam [43].

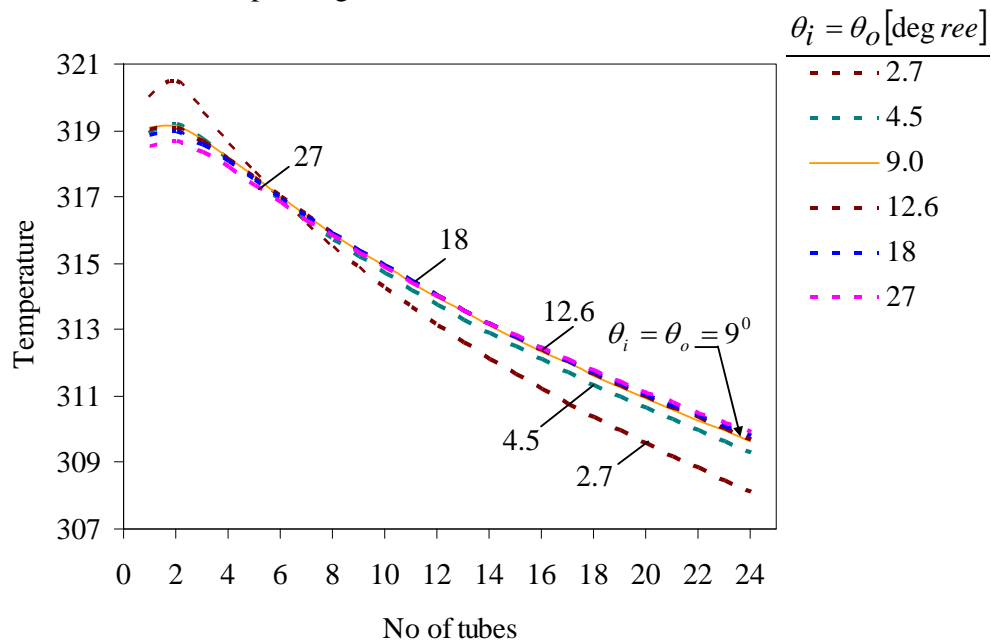


Figure A.9 Sensitivity of bulk temperature [K] at different angular values: operating conditions of Islam [43].

As shown in Figure A.7, the tube-wise variation of mass flux decreases as the values of the angles increase. The possible reason for this behaviour is the decrease of participating surface area of the film flow over the tube with larger values of the angles of the film entering and leaving a tube which causes corresponding decrease of mass

flux. Similar results for the tube-wise variation of bulk concentration and temperature of LiBr solution are plotted for several values of the film entering and leaving angles to the tubes as shown in Figure A.8 and A.9 respectively. All these results indicate that among the three parameters i.e. the mass flux, concentration and temperature, mass flux are most sensitive to the angular values of  $\theta_i, \theta_o$ . A scrutiny of the sensitivity data reveals that for 70% increase of  $\theta_i, \theta_o$  ( $15.3^\circ$ ) from the base line value ( $9^\circ$ ), the mass flux calculated at the absorber outlet is 4% lower than the calculated mass flux using the base line angular value. Whereas for 70% decrease of  $\theta_i, \theta_o$  ( $2.7^\circ$ ) from the base line value ( $9^\circ$ ), the mass flux calculated at the absorber outlet is 4.7% higher than the calculated mass flux using the base line angular value. The difference between the temperature and concentration results for the angular values of  $15.3^\circ$  and  $2.7^\circ$  compared to the results obtained using baseline value of  $9^\circ$  is 0.08% and 0.49 % respectively for temperature and 0.48 % and 0.29 % respectively for concentration. After getting the sensitivity results, the base line value  $9^\circ$  is taken as the value of film entering and leaving angle to the tubes to obtain the simulation results presented in chapter 3.

## **APPENDIX B**

### **UNCERTAINTY OF IMAGE ANALYSIS**

The image analysis program that has been undertaken to analyze the frame by frame video images is based on the edge detection process. The purpose of the edge detection process is to regenerate the droplet profiles. As discussed previously in section 4.6, the droplet profiles are generated selecting co-ordinate points along the edge of the droplets in the images. Hence the procedure is known as manual edge detection process. The edge detection may improve if higher quality images are achieved or an automated edge detection process can be found. The effects of automated edge detection instead of the manual edge detection process are discussed in this section. In addition, application of the manual edge detection to an improved quality image is also described.

#### **B.1 Manual edge detection process**

In section 4.6, the methodology of image analysis program had been discussed. The first step was to read the droplet or jet profiles from the sequential video images within a fixed time period. The profiles of the droplet or jet were generated by the help of the manual edge detection process. Image analysis software Matrox Inspector was used for this purpose which had the option to choose as many points as possible along the boundary of a droplet. A sample image is shown in Figure B.1 with the 'cross' signs along the droplet boundary. The profile of the droplet was thus generated accumulating the co-ordinate points. Droplet volume and surface area were computed afterwards by applying solid revolution theorem to the axi-symmetric droplet/jet.

The manual edge detection process may not be very accurate because it involves numerous mouse clicks along the boundary of the droplet. Even if the higher image quality is achieved, all it needs to maneuver along the droplet profile onto the computer screen. Also this process becomes tedious when time dependent profiles are in concern. The transient droplet volume and surface area profiles which had been illustrated in

section 5.1-5.3 required huge effort in the application of the manual edge detection for each and every droplet. Less effort is required if an automated edge detection process can be deployed which may increase the accuracy of measurement as well.

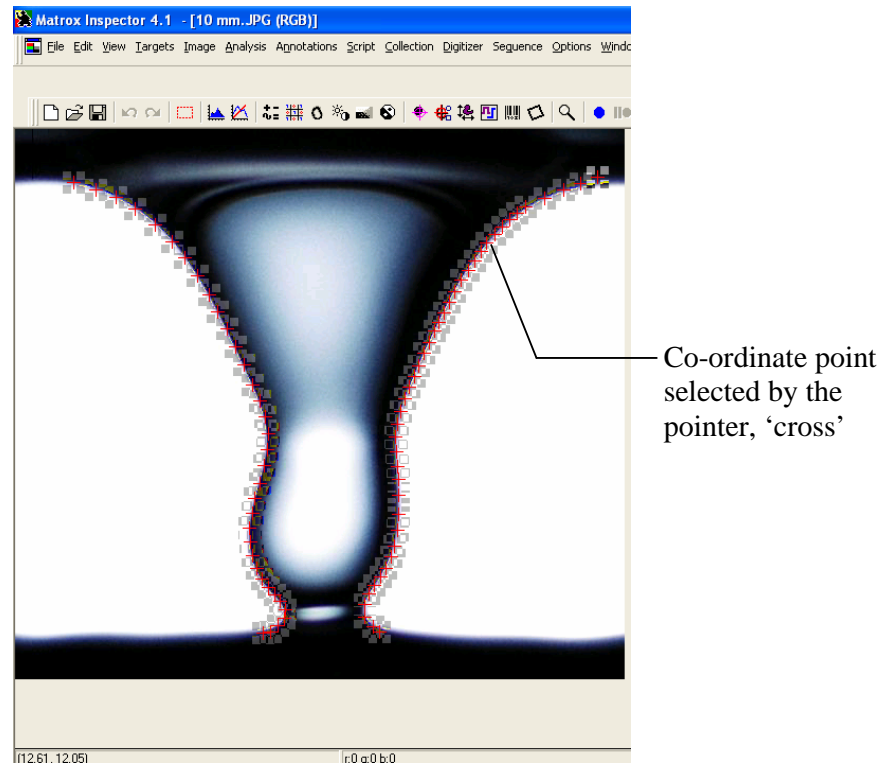


Figure B.1 Manual edge detection process using Matrox Inspector

## B.2 Semi automated edge detection process

In order to compare the accuracy of manual edge detection process deployed for current research, a semi-automated edge detection process is analyzed too. In this case, commercial software MATLAB is used to auto generate the droplet profile based on the known colour intensity value along the droplet boundary. The process is named by semi-automated edge detection because the intensity value along the droplet boundary is to manually examine writing a computer code in MATLAB. From the MATLAB graphics window, the colour intensity is read for any point on the image where the mouse pointer is placed.



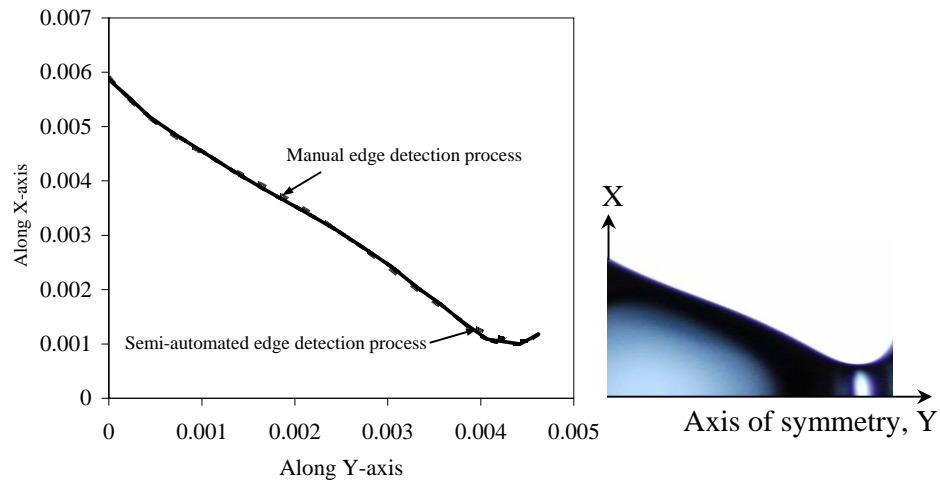


Figure B.2 Comparison of the two edge detection processes for a sample jet at 6 mm tube gap situation.

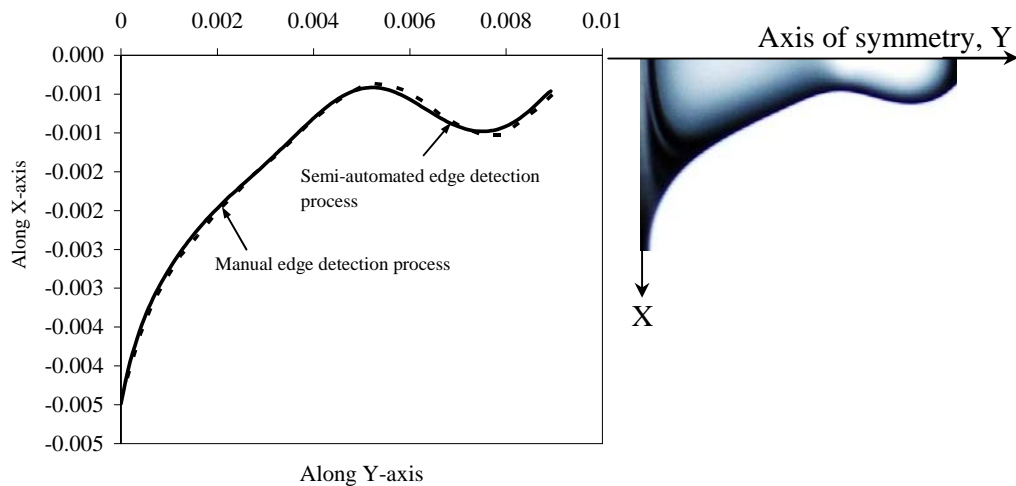


Figure B.3 Comparison of the two edge detection processes for a sample jet at 10 mm tube gap situation.

The procedure is to examine the droplet boundary intensity value first which however remains constant along the entire boundary profile. Next, a separate computer code written in MATLAB is used to read and store the X-Y co-ordinates of the grid points whose intensity match with the known intensity value which indicate the grid points are along the droplet boundary profile. Traversing along the given distances along the X and Y co-ordinates, all the boundary co-ordinate points thus can be stored with expense

of few seconds. Those co-ordinate points are then used to plot the regenerated droplet profile.

The main advantage of the semi-automated edge detection process is that it can save a lot of effort involved in manual edge detection process. But the accuracy of this process depends highly on the resolution of the image. The images are required to be very sharp and free from noises. The images taken with the video camera used for this current research were found ineffective to deploy the semi-automated edge detection process mainly because of the lower resolution. For our interest, a digital still camera [NIKON D100] was used to take some pictures of the inter-tube jet-flow mode because of the time-independent nature. The jet profiles were regenerated using the semi-automated edge detection process described above. The results are discussed in the following section.

### **B.3 Comparison of the two edge detection processes**

The accuracy of both manual and semi-automated edge detection processes is examined by selecting a few high quality images taken by digital camera [NIKON D100]. In Figure B.2, the jet profiles generated by the two processes are shown for the jet image at 6 mm tube gap situation. Along one side of the axis of symmetry, the generated profiles by the two processes agree very well. Similar profiles for a jet formed at 10 mm tube gap situation are plotted in Figure B.3. This figure also indicates well agreement between the profiles generated by the two processes. Therefore, the accuracy of the manual edge detection process may not be too different from the accuracy of the semi automated process when a high quality image is concerned. However, to deal with a lower resolution image, both the edge detection processes may encounter some inaccuracies.

**Table B.1 Error analysis of the edge detection processes.**

Method	Tube gap situation	Volume of each jet $V, m^3$	Area of each jet $A, m^2$	Absorption in the gap by single jet $kg.m^{-1}s^{-1}$	% Difference in the absorption rate by the two methods
Semi-auto	5 mm	2.62E-07	1.79E-04	3.25E-04	5.33
Manual		2.70E-07	1.83E-04	3.42E-04	
Semi-auto	9 mm	2.46E-07	1.71E-04	2.84E-04	3.26
Manual		2.55E-07	1.79E-04	2.93E-04	

The effect of the use of different edge detection processes is also examined for the prediction of absorption rate by the inter-tube absorption model. Both the manual and semi-automated edge detection processes are used separately to obtain the jet profile from the image shown in Figure B.1 taken with digital still camera [NIKON D100]. The axi-symmetric jet volume and surface area are computed applying the solid revolution theorem to the jet profile generated by the two processes. The inter-tube jet mode absorption model described in section 3.2.2.3 is then used to compute the rate of absorption by the jets from the two processes. The results are tabulated in Table B.1 for the two tube gap situations. The computed volume, surface area and rate of absorption by the jets differ within reasonable limit. The percent differences between the results are

given too. The rate of absorption computed using the manual process differs by 3.2-5.3 percents from the rate of absorption computed using the semi-automated process.



Figure B.4 Sample images taken by video camera (400x300 pixels).

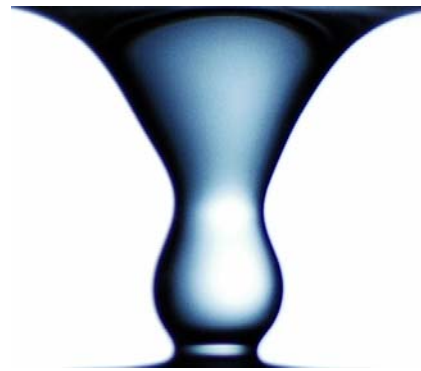


Figure B.5 Sample images taken by still camera (3008x2000 pixels).

#### **B.4 Image quality and the manual edge detection process**

The video camera [CANON MVX35i] used in the present experimental program provides images with 0.12 Mega pixels. Manual edge detection would become much more accurate if a better resolution of the images is found. As described previously in section B.2, a digital still camera with 6.0 Mega pixels was used to take a few still images of the inter-tube events under similar experimental conditions. The same edge detection process was undertaken to read the droplet profile from the images and was found more accurate. Figure B.4 shows a sample image when the images were taken with the video camera. Figure B.5 shows a sample image when the images were taken with the still camera. The cameras were operated at the same time during the recording of the inter-tube flow events at a particular operating condition. It is clear from the figures that the image taken by the digital still camera is much better than that of digital video camera. The interest is now to obtain the jet profile from the two images using the manual edge detection process. After that both the generated profiles are used to compute the volume and surface area of the respective jets. Finally, the information is

used to predict the absorption rate by the two jets using jet-mode absorption model discussed in section 3.2.2.3.

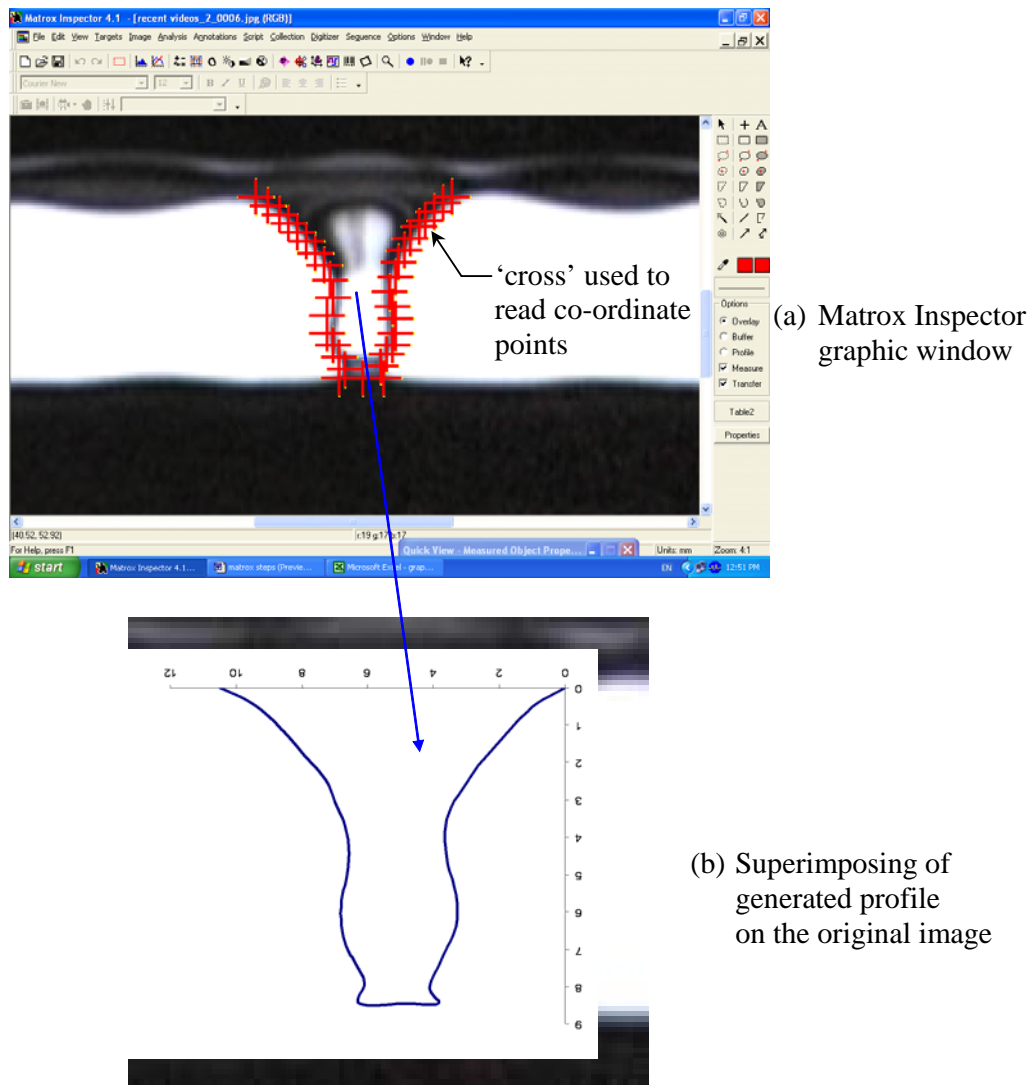


Figure B.6 Application of manual edge detection on image taken by video camera [CANON MVX 35i].

Figure B.6 illustrates the manual edge detection onto the image of Figure B.4 using Matrox Inspector. Because of the lower resolution of the image, the relative size of the ‘cross’, indicated in the Figure B.6(a) becomes larger which slightly impedes the edges to be seen clearly. The regenerated jet profile is superimposed to the original image

which is shown in Figure B.6 (b). The accuracy of the edge detection increases if same process is undertaken onto the image of Figure B.5. The illustration was shown in Figure B.1. For such higher resolution image, not only the edges are seen much more clearly but also the relative size of the ‘cross’ is much smaller. Due to these advantages, the accuracy of the manual edge detection greatly improves. However, the actual impact of this measuring inaccuracy on the prediction of absorption rate is determined. The results of the absorption rate predicted by the two images of Figure B.4 and B.5 are presented below.

**Table B.2 Error analysis of different images.**

Image	Tube gap situation	Volume of each jet $V, m^3$	Area of each jet $A, m^2$	Flow rate $kg.s^{-1}$	Absorption in the gap by using jet image $kg.m^{-1}s^{-1}$	% Difference in the results by the two images
Present expt.	6 mm	3.09E-07	1.72E-04	0.0227	3.16E-04	3.47
Still image		3.05E-07	1.95E-04		3.27E-04	
Present expt.	10 mm	2.24E-07	1.75E-04	0.018	3.17E-04	4.6
Still image		2.47E-07	1.92E-04		3.31E-04	

The aim of this current research was to obtain time dependent profiles of the inter-tube flow modes for which the still camera might not work. However for the jet mode inter-tube flow, the images can be taken with still camera because of the time independent

nature of the jets. Performing this, the percent difference of the jet mode absorption rate by the jet profiles obtained from two different images is calculated. Table B.2 shows the rate of absorption by the single jets for two different flow rate and tube spacing cases. If the rate of absorption predicted by the jet image with higher resolution, similar to the image shown in Figure B.5, is considered the base value for each case, the percent of error in the absorption rate predicted by the image with lower resolution or the present experimental case is presented in the table. The error in the results varies within 3.4-4.6 percents.

---

**APPENDIX C**

**SENSITIVITY ANALYSIS**

**C.1 Sensitivity analysis with varying transfer coefficients**

The contribution of inter-tube absorption to the total absorption was expressed by mass flux ratio in chapter 6 which was defined as follows

$$J = \frac{m_{vi}}{m_{vi} + m_{vf}} \quad (C.1)$$

where  $m_{vi}$  is the mass flux in the inter-tube flow regime and  $m_{vf}$  is the mass flux in the falling-film regime.

The simulation data for the mass flux ratio presented in Table 6.3 and 6.4 were based upon the extracted average values of falling film heat and mass transfer coefficients from the detailed numerical model described in section 3.1.1. In this section, the main purpose is to check the sensitivity of the developed absorption models described in section 3.2.2.1 and 3.2.2.3 using varying transfer coefficients because the exact values of these transfer coefficients in the inter-tube flow regimes are unknown. A detailed sensitivity testing program is undertaken to show the sensitivity of the developed inter-tube absorption models in terms of calculated mass flux ratio with varying mass transfer and heat transfer coefficients. The sensitivity test procedure is as follows. First, the base line values of these transfer coefficients are selected from the detailed numerical model applied to the falling film regime. Next each of the two transfer coefficients is allowed to vary within  $\pm 40\%$  of the base value. Within the range, selected values for the transfer coefficients are taken to be used into the inter-tube absorption models. For each input of the transfer coefficients, the other input variables like the inlet solution temperature and concentration, coolant flow rate and coolant inlet temperature are kept constant. The hydrodynamic data for the inter-tube flow modes are kept constant throughout the test procedure. Moreover, the spatial distributions of the inter-tube droplets and jets along



the absorber tube are neglected. The solution flow rate is then varied within the experimental range covered in chapter 4. At different flow rate, the relevant inter-tube absorption models from section 3.2.2.1, 3.2.2.3 and the single round tube model discussed in section 3.1.1 are used to calculate the value of mass flux ratio,  $J$ . It is important to know that at a time one transfer coefficient is varied. For example, when mass transfer coefficient is varied, heat transfer coefficient is kept constant with the base line value and vice versa. The data are presented in graphical form in Figures C.1-C.4 for the two different tube gap situations.

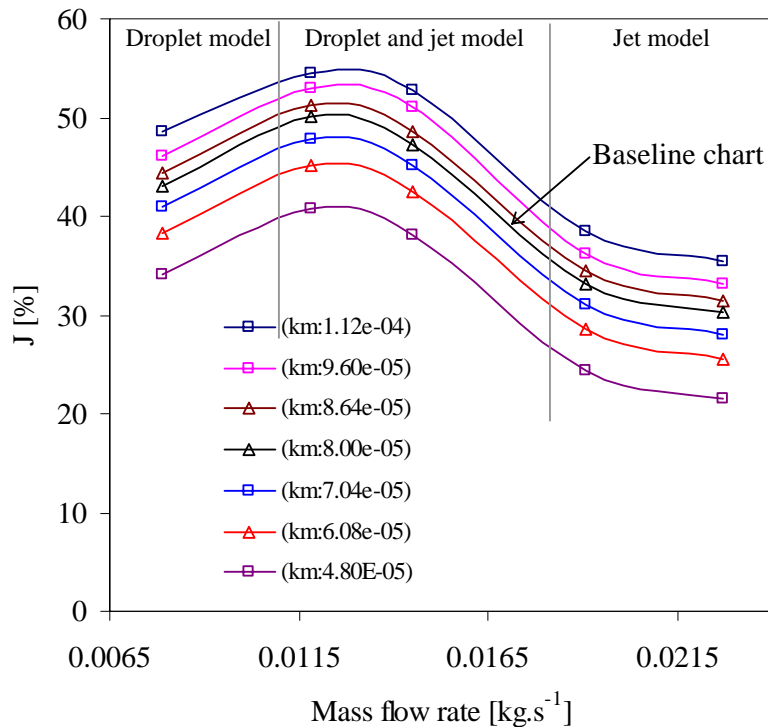


Figure C.1 Sensitivity of mass flux ratio with varying mass transfer coeff.  $k_m$  [tube gap: 10 mm].

In Figure C.1, the sensitivity of varying mass transfer coefficient applied to the inter-tube absorption models are presented for 10 mm tube gap situation. The range of flow rate is kept within the operating experimental range given in chapter 4. The base line mass transfer coefficient is chosen to be  $8.0E-05 \text{ m.s}^{-1}$  for which the mass flux ratio varies with the solution flow rate. The heat transfer coefficient is remained constant at

the baseline value of  $4730 \text{ W.m}^{-2}\text{K}^{-1}$ . For other input values of the mass transfer coefficient, the mass flux ratio also varies with the solution flow rate in similar fashion. The sensitivity charts thus created are observed to follow similar trend lines. When the mass transfer coefficient is higher than the baseline value, the mass flux ratio increases at all flow rates. Similarly, lower mass transfer coefficient than the baseline mass transfer coefficient decreases the mass flux ratio significantly. The interesting point to notice here is that the mass flux ratio is more sensitive to the lower values of mass transfer coefficient as the data points are more sparsely distributed in the lower side of the baseline chart. Similar sensitivity charts are generated for 6 mm tube gap situation as plotted in Figure C.2. Keeping the same baseline mass transfer coefficient, the variations of mass flux ratio are depicted at various solution flow rate. The mass flux ratio charts are also following similar trend lines at different input of the mass transfer coefficient and are found more sensitive to the lower mass transfer coefficients.

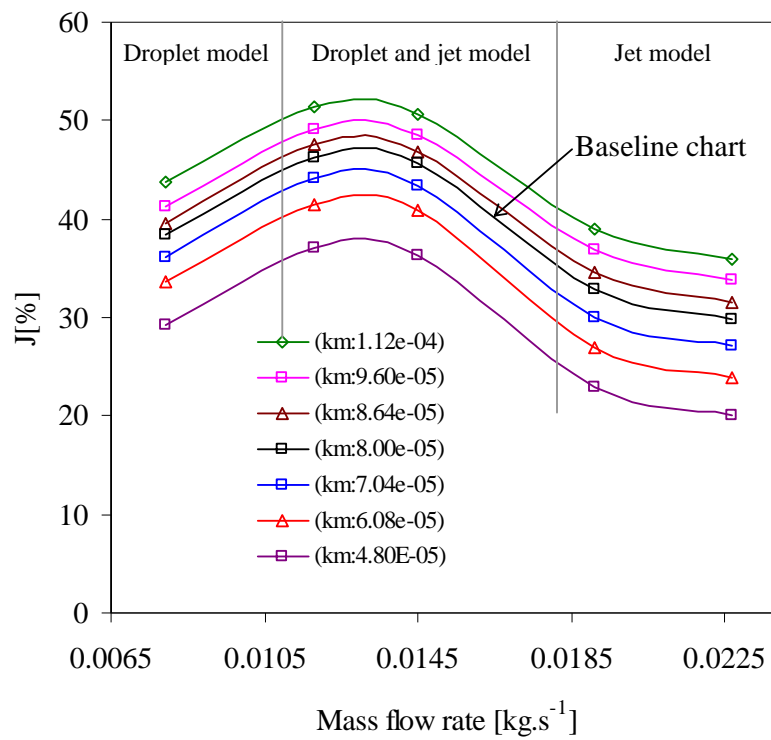


Figure C.2 Sensitivity of mass flux ratio with varying mass transfer coeff.  $k_m$  [tube gap: 6 mm]

In Figure C.3 and C.4, the sensitivity data of the heat transfer coefficient are presented for 10 mm and 6 mm tube gap situation respectively. In this case, the mass transfer coefficient is kept constant with the baseline value of  $8.0E-05 \text{ m.s}^{-1}$  whereas the heat transfer coefficient is varied within a wide range deviating  $\pm 40\%$  from the baseline value of  $4730 \text{ W.m}^{-2}\text{K}^{-1}$ . The sensitivity charts for the variation of mass flux ratio with the solution flow rate at different input of the heat transfer coefficient exhibit similar trend lines. When the heat transfer coefficient is higher than the baseline heat transfer coefficient, mass flux ratio is higher as well at all data points compared to the corresponding points on the baseline chart.

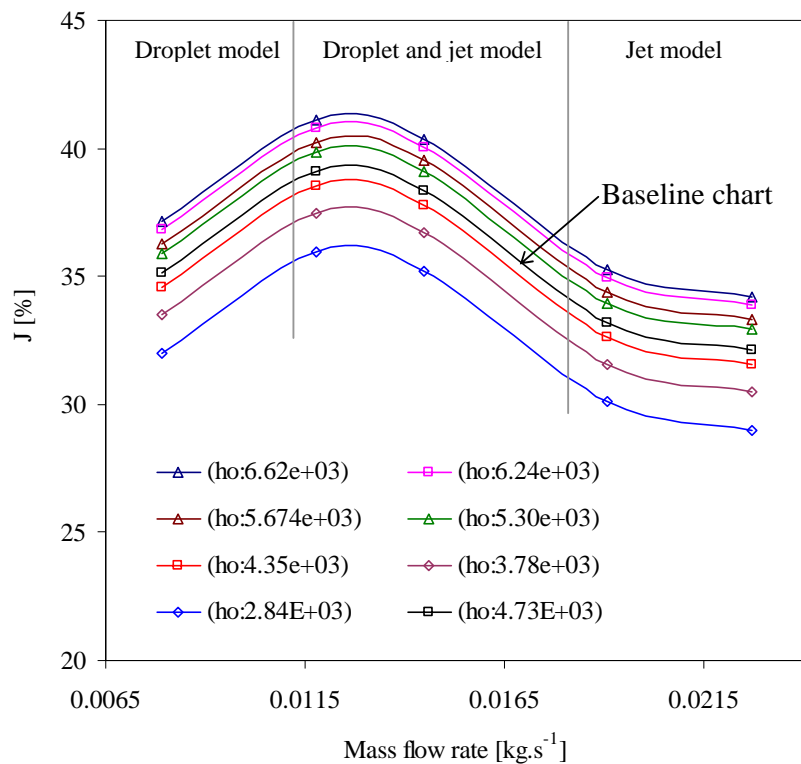


Figure C.3 Sensitivity of mass flux ratio with varying heat transfer coeff.  $h_o$  [tube gap;10 mm]

In contrast when the heat transfer coefficient is lower than the baseline heat transfer coefficient, mass flux ratio is also lower at all data points. Moreover, similar to the mass

transfer coefficient sensitivity charts, the models are more sensitive to the lower values of heat transfer coefficient compared to the higher values of heat transfer coefficient.

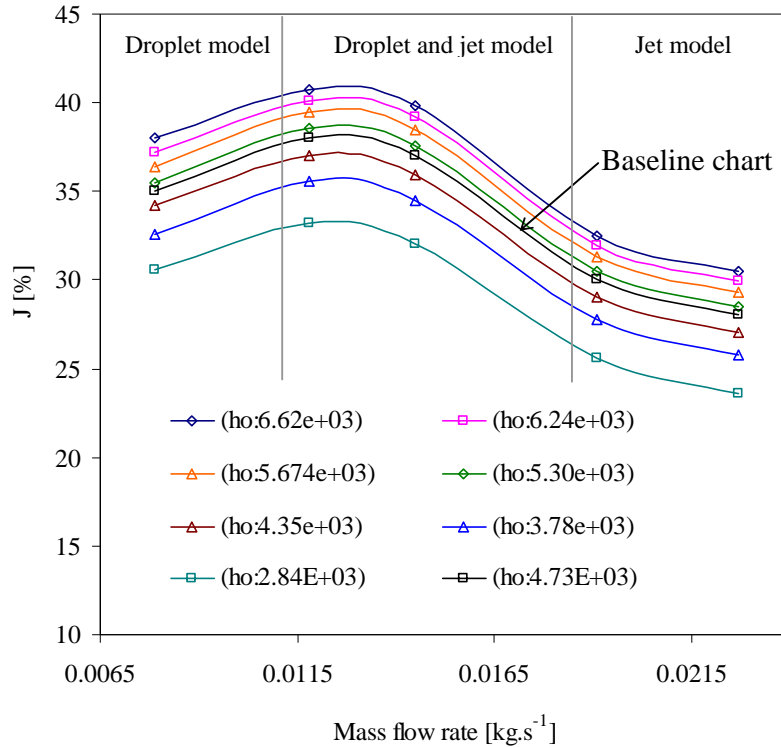


Figure C.4 Sensitivity of mass flux ratio with varying heat transfer coeff.  $h_o$  [tube gap: 6 mm]

## C.2 Sensitivity analysis with varying inlet temperature and concentration

The sensitivity of the inter-tube absorption models with varying inlet solution temperature and concentration are presented in this section. The purpose is to examine the use of hydrodynamics data at such inlet solution temperature and concentration that differs from the actual absorber inlet conditions described in section 6.2. The actual experiments on inter-tube hydrodynamics were performed at the operating conditions described in Table 4.1. The extracted hydrodynamic data presented in section 5.1-5.3 were assumed unchanged to be used under a different set of absorber operating conditions stated in section 6.2. The simulation data were presented in Table 6.3-6.4. In

this section, both the inlet temperature and concentration are varied at a time deviating -40% to +20% from the base value temperature while -10% to +10% from the base value concentration. The base values of both temperature and concentration are the absorber operating condition [  $w_{s,in} = 0.6, T_{s,in} = 39.8^{\circ}c$  ] described in section 6.2.

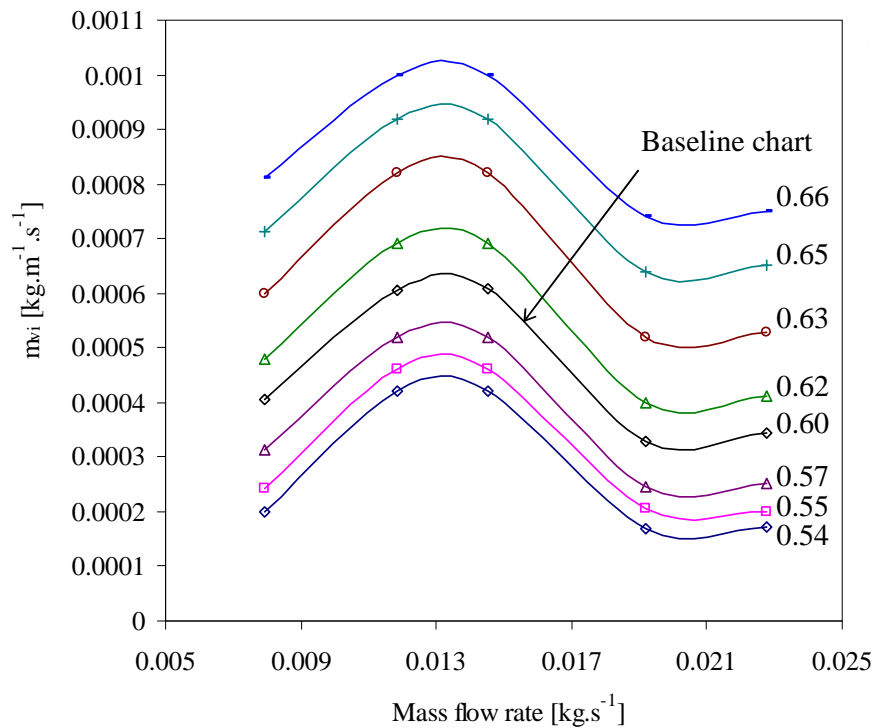


Figure C.5 Sensitivity of inter-tube mass flux with varying inlet concentration of LiBr solution [%LiBr/100] for a tube gap of 10 mm.

The sensitivity data for varying inlet concentration is presented in Figure C.5 in terms of inter-tube mass flux with change in solution flow rate. The procedure to operate different inter-tube absorption models based on the solution flow rate is similar to that described in section C.1. Sensitivity results reveal that if the inlet solution concentration increases keeping the base value inlet temperature unchanged, the absorber inlet condition becomes more favorable to vapour absorption indicating much increase of vapour mass flux  $m_{vi}$ . A 10% increase of inlet concentration from the base value (0.66) causes maximum 99 % increase of mass flux compared to the base line chart among the

different operating flow rate situations. On the other hand if the inlet solution concentration decreases the absorber inlet condition becomes less favorable to vapour absorption so the inter tube vapour mass flux decreases significantly. A -10% decrease of inlet concentration from the base value (0.54) causes maximum 51 % decrease of mass flux compared to the base line chart among the different operating flow rate situations.

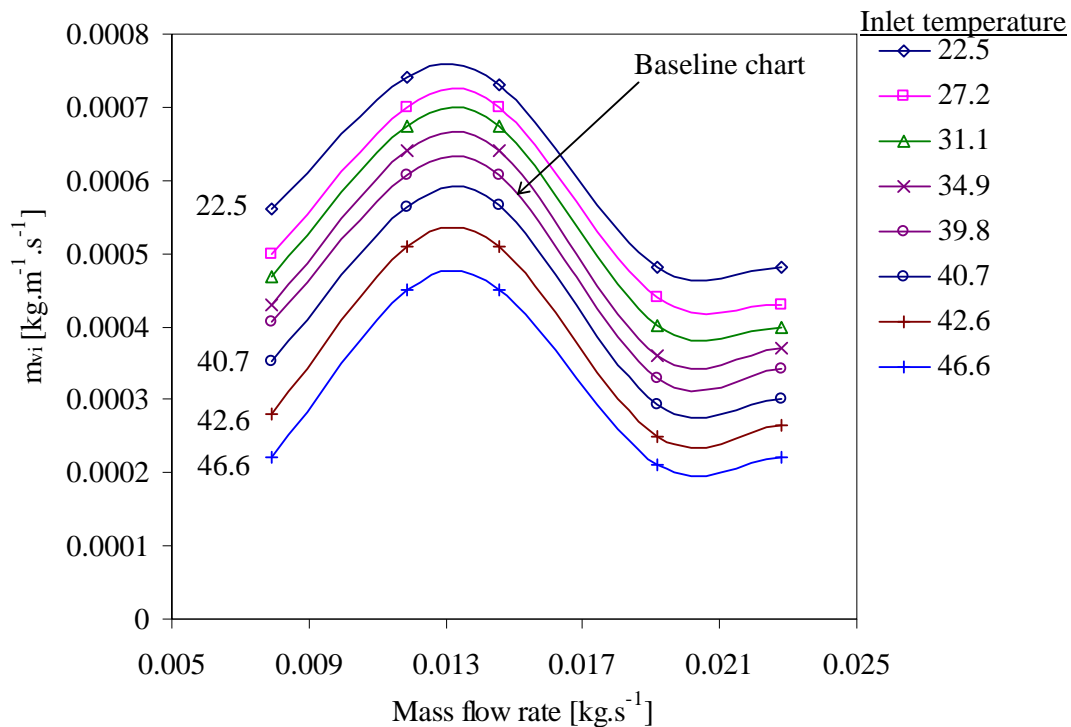


Figure C.6 Sensitivity of inter-tube mass flux with varying inlet temperature LiBr solution [<sup>0</sup>C] for a tube gap of 10 mm.

The sensitivity data for varying inlet temperature is presented in Figure C.6 in terms of inter-tube mass flux with change in solution flow rate. Sensitivity results reveal that if the inlet solution temperature decreases keeping the base value of inlet concentration unchanged, the absorber inlet condition becomes more favorable to vapour absorption indicating much increase of vapour mass flux  $m_{vi}$ . A -40% decrease of inlet temperature from the base value (22.5<sup>0</sup> C) causes maximum 45 % increase of mass flux compared to the base line chart among the different operating flow rate situations. On the other hand

if the inlet solution temperature increases the absorber inlet condition becomes less favorable to vapour absorption so the inter tube vapour mass flux decreases significantly. A +20% increase of inlet temperature from the base value (46.6<sup>0</sup> C) causes maximum 46 % decrease of mass flux compared to the base line chart among the different operating flow rate situations.

It is to be remembered that absorption process is driven by the water-vapour pressure at the solution vapour interface which is a function of both solution temperature and concentration. The same vapour pressure can be developed by many combinations of temperature and concentration of solution as explained by the temperature-pressure-concentration diagram for LiBr-water solutions. Therefore, not a single variable like the temperature or concentration is allowed to vary in such way that the equilibrium condition is overruled. The ranges selected for present sensitivity analysis are within the equilibrium conditions at each particular temperature-concentration and pressure.

**APPENDIX D**  
**CALIBRATION OF FLOW METER**  
**AND FABRICATION DETAILS**

**D.1 Flow meter calibration**

The flow meter is calibrated using 54% wt. concentration of LiBr solution. The volume flow meter reading is converted to the mass flow rate of solution for sets of operating flow rates. The mass flow rate of solution is measured by collecting the amount of liquid in a measuring flask within a specific time period using a stop watch. For each flow rate, several measurements are recorded for which the average mass flow rate is calculated. The mass flow rate thus obtained is then plotted against the flow meter reading at each condition. The calibration chart is exhibited in Figure D.1.

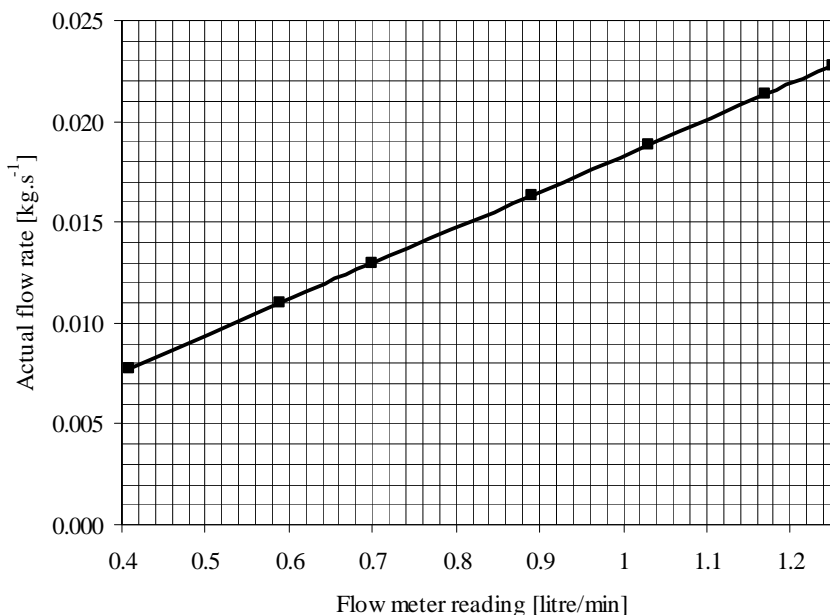
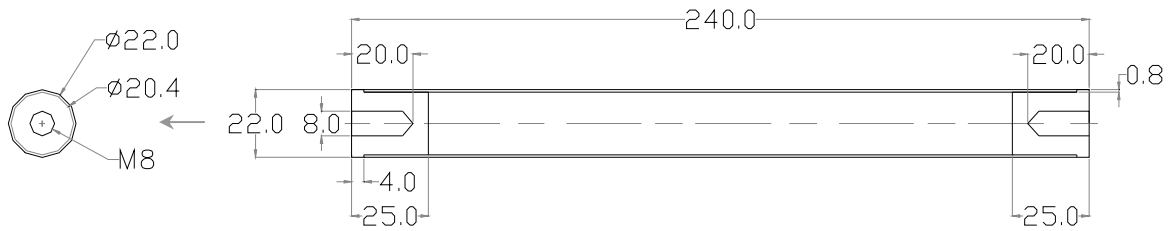


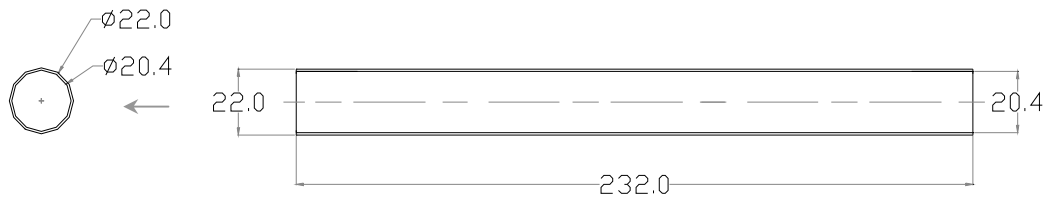
Figure D.1 Flow meter calibration chart for 54% wt. concentration of LiBr.



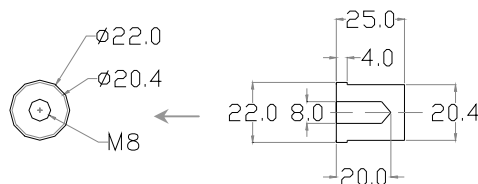
## D.2 Detailed drawing of test tubes



(a) Assembly of test tube with press fitted solid aluminum pieces.



(b) Test tube

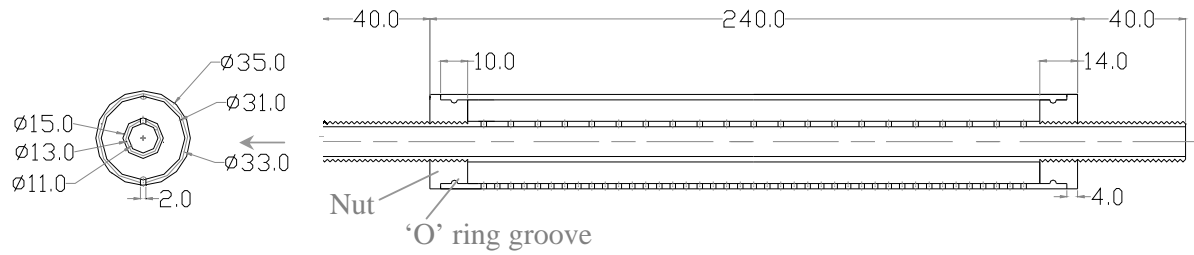


(c) Solid aluminum with threaded centre hole

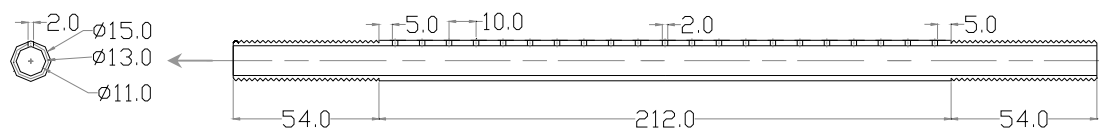
Figure D.2 Detailed drawings of the test tube [dimension unit: mm].

The test tubes are made of copper. In order to support the test tubes from both sides into the test section guide bars as shown in Figure 4.3 of chapter 4, solid aluminum pieces with threaded centre hole in each are press fitted inside the hollow copper tube from both sides. The dimensions of the test tube and specially designed solid aluminum piece are provided in Figure D.2.

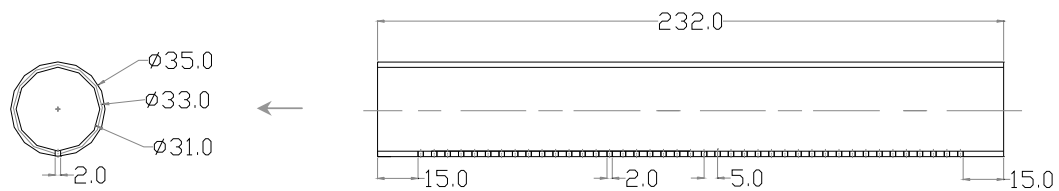
### D.3 Detailed drawing of distributor



(a) Assembly drawing of the distributor.



(b) Inner tube of the distributor



(c) Outer tube of the distributor

Figure D.3 Detailed drawings of the distributor [dimension unit: mm].

The flow distributor, the design of which is similar to that used by Killion and Garimella [52], consists of two concentric tubes. The solution enters the inner tube and flows into the annular space through holes in the inner tube wall. Evenly spaced holes at the bottom of the outer tube wall discharge the solution as a series of jets onto the first tube of the absorber. The detailed design of different parts of the distributor is provided in Figure

D.3. The two concentric tubes are held by the help of two specially designed nuts from both sides as shown in Figure D.3 (a). The inner threads of the nut match with the outer threads of the inner tube to seal off the liquid flow. The nuts holding the inner tube from both sides are gently pushed inside the outer tube by the help of 'O' rings fitted to the grooves around the nuts as indicated in Figure D.3 (a). Thus, the liquid flow to the annular space is completely sealed off except flowing through the holes underneath the outer tube wall. For convenience the inner tube is made of Perspex with threaded external parts as shown in Figure D.3 (b) so that two other external nuts can be used to fix the inner tube with the test section guide bars for better stability. The outer tube is made of copper. The nuts which are pressed inside the tubes shown in Figure D.3 (a) are made of brass. The external nuts are made of Perspex.

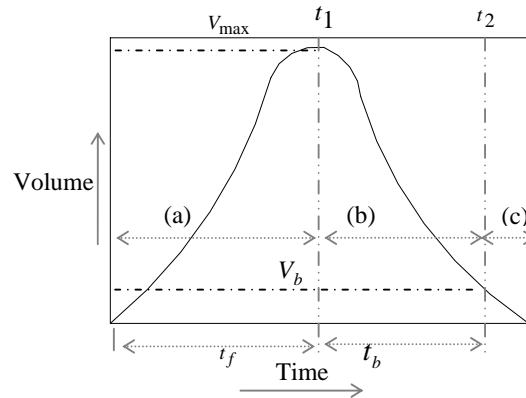
**APPENDIX E****INTER-TUBE FLOW HYPOTHESIS****E.1 Mass continuity of the flow between the tubes**

Figure E.1 Typical droplet cycle; (a) development stage, (b) bridge form stage, (c) pull back stage.

The summation of the quantities in Eqs. (5.2) and (5.3) described in section 5.2.2 is the actual amount flows between two tubes for each droplet cycle. If total summation is taken for each droplet cycle at each location within  $\tau$  sec of time, newly calculated flow rate is as follows;

$$m_{s,cal} = \frac{1}{\tau} \sum_1^{N_d} \left[ \frac{V_{max}}{t_f} \times \rho(t_2 - t_1) + (V_{max} - V_b) \rho \right] \quad (E.1)$$

The newly calculated mass flow rate from Eq. (E.1) is compared with the actual mass flow rate of solution. The percentage of error is shown at the end of Tables E.1-E.3 for three different flow rate situations. For each droplet cycle at each generating location within the period of  $\tau$  sec, the quantities in the RHS of Eq. (E.1) are calculated and presented in the Tables E.1-E.3. The newly calculated mass flow rate named as adjusted flow rate is shown in a separate row at the end of each table. The actual flow rate per unit length of tube is multiplied with the tube length in each image to show the measured flow rate is also presented at the end of each table. In Table E.1, The actual or measured

flow rate is 33 percent higher than the adjusted or calculated flow rate for present operating condition. For two other flow rate cases, calculated flow rate is 27 and 37 percent higher than actual flow rates. It is comprehensible that the percent errors not only occur due to the uncertainty of the image analysis program, measurement difficulties of  $V_{\max}$ ,  $V_b$  from the video images, but also due to the assumed hypothesis of inter-tube flow which had been discussed in section 5.2.2. The inter-tube droplet flow hypothesis presented in section 5.2.2 was developed for the purpose of interconnecting the droplet formation model and steady jet model for each droplet cycle. Present error estimations indicate that the developed hypothesis could only be suggested as an approximation of actual event. These error values may be presented as an error estimation of implementing the inter-tube droplet flow hypothesis under the assumption that the mass flow rate during bridge formation stage remains equal to the average filling rate of the developing stage.

Table E.1 Error estimation at flow rate 0.0079 kg.s<sup>-1</sup>; tube gap 10 mm.

Time period		1.2 sec									
Droplet station		1									
Cycle	t <sub>f</sub>	t <sub>1</sub>	t <sub>2</sub>	t <sub>b=t<sub>2</sub>-t<sub>1</sub></sub>	V <sub>max</sub> [mm <sup>3</sup> ]	V <sub>b</sub> [mm <sup>3</sup> ]	(V <sub>max</sub> -V <sub>b</sub> )	V <sub>max</sub> /t <sub>f</sub>	(V <sub>max</sub> -V <sub>b</sub> )ρ	ρ(V <sub>max</sub> /t <sub>f</sub> )t <sub>b</sub>	m <sub>c</sub> [kg.s <sup>-1</sup> ]
1	0.15	0.15	0.21	0.06	1.74E+02	3.65E+01	1.37E-07	1.16E-06	2.19E-04	1.11E-04	1.85E-03
2	0.24	0.48	0.57	0.09	1.88E+02	4.64E+01	1.42E-07	7.84E-07	2.27E-04	1.13E-04	1.25E-03
3	0.12	0.72	0.78	0.06	1.78E+02	5.48E+01	1.23E-07	1.48E-06	1.97E-04	1.43E-04	2.38E-03
4	0.18	0.99	1.08	0.09	1.62E+02	2.67E+01	1.35E-07	9.00E-07	2.17E-04	1.30E-04	1.44E-03
Droplet station		2									
Cycle	t <sub>f</sub>	t <sub>1</sub>	t <sub>2</sub>	t <sub>b=t<sub>2</sub>-t<sub>1</sub></sub>	V <sub>max</sub> [mm <sup>3</sup> ]	V <sub>b</sub> [mm <sup>3</sup> ]	(V <sub>max</sub> -V <sub>b</sub> )	V <sub>max</sub> /t <sub>f</sub>	(V <sub>max</sub> -V <sub>b</sub> )ρ	ρ(V <sub>max</sub> /t <sub>f</sub> )t <sub>b</sub>	m <sub>c</sub> [kg.s <sup>-1</sup> ]
1	0.24	0.3	0.42	0.12	1.62E+02	3.84E+01	1.24E-07	6.75E-07	1.98E-04	1.30E-04	1.08E-03
2	0.15	0.6	0.66	0.06	2.01E+02	2.36E+01	1.78E-07	1.34E-06	2.84E-04	1.29E-04	2.15E-03
3	0.21	0.93	0.99	0.06	2.12E+02	3.35E+01	1.78E-07	1.01E-06	2.85E-04	9.67E-05	1.61E-03
Droplet station		3									
Cycle	t <sub>f</sub>	t <sub>1</sub>	t <sub>2</sub>	t <sub>b=t<sub>2</sub>-t<sub>1</sub></sub>	V <sub>max</sub> [mm <sup>3</sup> ]	V <sub>b</sub> [mm <sup>3</sup> ]	(V <sub>max</sub> -V <sub>b</sub> )	V <sub>max</sub> /t <sub>f</sub>	(V <sub>max</sub> -V <sub>b</sub> )ρ	ρ(V <sub>max</sub> /t <sub>f</sub> )t <sub>b</sub>	m <sub>c</sub> [kg.s <sup>-1</sup> ]
1	0.18	0.18	0.27	0.09	2.19E+02	3.59E+01	1.83E-07	1.22E-06	2.94E-04	1.75E-04	1.95E-03
2	0.15	0.45	0.54	0.09	2.04E+02	3.69E+01	1.67E-07	1.36E-06	2.67E-04	1.95E-04	2.17E-03
3	0.24	0.81	0.9	0.09	2.05E+02	2.18E+01	1.84E-07	8.55E-07	2.94E-04	1.23E-04	1.37E-03
Droplet station		4									
Cycle	t <sub>f</sub>	t <sub>1</sub>	t <sub>2</sub>	t <sub>b=t<sub>2</sub>-t<sub>1</sub></sub>	V <sub>max</sub> [mm <sup>3</sup> ]	V <sub>b</sub> [mm <sup>3</sup> ]	(V <sub>max</sub> -V <sub>b</sub> )	V <sub>max</sub> /t <sub>f</sub>	(V <sub>max</sub> -V <sub>b</sub> )ρ	ρ(V <sub>max</sub> /t <sub>f</sub> )t <sub>b</sub>	m <sub>c</sub> [kg.s <sup>-1</sup> ]
1	0.12	0.12	0.21	0.09	1.87E+02	3.65E+01	1.50E-07	1.55E-06	2.40E-04	2.24E-04	2.49E-03
2	0.09	0.33	0.42	0.09	2.08E+02	3.90E+01	1.69E-07	2.31E-06	2.71E-04	3.33E-04	3.70E-03
3	0.18	0.63	0.72	0.09	1.94E+02	1.70E+01	1.77E-07	1.08E-06	2.84E-04	1.55E-04	1.73E-03
4	0.21	0.96	1.02	0.06	1.90E+02	5.26E+01	1.38E-07	9.05E-07	2.20E-04	8.69E-05	1.45E-03
Droplet station		5									
Cycle	t <sub>f</sub>	t <sub>1</sub>	t <sub>2</sub>	t <sub>b=t<sub>2</sub>-t<sub>1</sub></sub>	V <sub>max</sub> [mm <sup>3</sup> ]	V <sub>b</sub> [mm <sup>3</sup> ]	(V <sub>max</sub> -V <sub>b</sub> )	V <sub>max</sub> /t <sub>f</sub>	(V <sub>max</sub> -V <sub>b</sub> )ρ	ρ(V <sub>max</sub> /t <sub>f</sub> )t <sub>b</sub>	m <sub>c</sub> [kg.s <sup>-1</sup> ]
1	0.18	0.18	0.27	0.09	2.17E+02	2.66E+01	1.90E-07	1.20E-06	3.04E-04	1.73E-04	1.93E-03
2	0.09	0.39	0.48	0.09	2.10E+02	2.17E+01	1.89E-07	2.34E-06	3.02E-04	3.36E-04	3.74E-03
3	0.09	0.6	0.69	0.09	1.67E+02	2.59E+01	1.41E-07	1.86E-06	2.26E-04	2.67E-04	2.97E-03
4	0.12	0.84	0.9	0.06	1.93E+02	3.36E+01	1.59E-07	1.61E-06	2.54E-04	1.54E-04	2.57E-03
5	0.21	1.14	1.17	0.03	2.17E+02	9.81E+01	1.19E-07	1.03E-06	1.90E-04	4.96E-05	1.65E-03
Droplet station		6									
Cycle	t <sub>f</sub>	t <sub>1</sub>	t <sub>2</sub>	t <sub>b=t<sub>2</sub>-t<sub>1</sub></sub>	V <sub>max</sub> [mm <sup>3</sup> ]	V <sub>b</sub> [mm <sup>3</sup> ]	(V <sub>max</sub> -V <sub>b</sub> )	V <sub>max</sub> /t <sub>f</sub>	(V <sub>max</sub> -V <sub>b</sub> )ρ	ρ(V <sub>max</sub> /t <sub>f</sub> )t <sub>b</sub>	m <sub>c</sub> [kg.s <sup>-1</sup> ]
1	0.15	0.27	0.36	0.09	2.01E+02	2.49E+01	1.76E-07	1.34E-06	2.82E-04	1.93E-04	2.15E-03
2	0.15	0.54	0.63	0.09	1.90E+02	3.51E+01	1.54E-07	1.26E-06	2.47E-04	1.82E-04	2.02E-03
3	0.12	0.78	0.87	0.09	2.04E+02	3.45E+01	1.70E-07	1.70E-06	2.71E-04	2.45E-04	2.72E-03

Actual flow rate, 2Γ [kg.m <sup>-1</sup> .s <sup>-1</sup> ]	Tube length in each image [m]	Adjusted flow rate [kg.s <sup>-1</sup> ]	Measured flow rate [kg.s <sup>-1</sup> ]	%diff
0.039	0.14	0.0056	0.00749	33.62

Table E.2 Error estimation at flow rate  $0.0118 \text{ kg.s}^{-1}$ : tube gap 10 mm.

Time period	1.32 sec											
<b>Droplet station 1</b>												
<b>Cycle</b>	$t_f$	$t_1$	$t_2$	$t_2-t_1$	$V_{\max}[\text{mm}^3]$	$V_b[\text{mm}^3]$	$(V_{\max}-V_b)$	$V_{\max}/t_f$	$(V_{\max}-V_b)\rho$	$\rho(V_{\max}/t_f)*(t_2-t_1)$	$m_{s,\text{new}} [\text{kg.s}^{-1}]$	
1	0.09	0.24	0.33	0.09	182.154323	28.372377	1.53782E-07	2.0239E-06	0.000246051	0.000291447	0.003238299	
2	0.12	0.48	0.57	0.09	153.603526	35.687613	1.17916E-07	1.28E-06	0.000188665	0.000184324	0.002048047	
3	0.09	0.69	0.78	0.09	210.086521	47.231114	1.62855E-07	2.3343E-06	0.000260569	0.000336138	0.003734871	
4	0.15	0.99	1.08	0.09	157.055461	26.698102	1.30357E-07	1.047E-06	0.000208572	0.000150773	0.001675258	
<b>Droplet station 2</b>												
<b>Cycle</b>	$t_f$	$t_1$	$t_2$	$t_2-t_1$	$V_{\max}[\text{mm}^3]$	$V_b[\text{mm}^3]$	$(V_{\max}-V_b)$	$V_{\max}/t_f$	$(V_{\max}-V_b)\rho$	$\rho(V_{\max}/t_f)*(t_2-t_1)$	$m_{s,\text{new}} [\text{kg.s}^{-1}]$	
1	0.18	0.18	0.24	0.06	212.96127	63.806504	1.49155E-07	1.1831E-06	0.000238648	0.000113579	0.001892989	
2	0.12	0.39	0.48	0.09	174.10491	56.470859	1.17634E-07	1.4509E-06	0.000188214	0.000208926	0.002321399	
3	0.12	0.63	0.75	0.12	183.353525	48.859802	1.34494E-07	1.5279E-06	0.00021519	0.000293366	0.002444714	
4	0.15	0.93	0.99	0.06	216.532255	37.318572	1.79214E-07	1.4435E-06	0.000286742	0.000138581	0.002309677	
5	0.15	1.17	1.26	0.09	196.015239	41.480342	1.54535E-07	1.3068E-06	0.000247256	0.000188175	0.002090829	
<b>Droplet station 3</b>												
<b>Cycle</b>	$t_f$	$t_1$	$t_2$	$t_2-t_1$	$V_{\max}[\text{mm}^3]$	$V_b[\text{mm}^3]$	$(V_{\max}-V_b)$	$V_{\max}/t_f$	$(V_{\max}-V_b)\rho$	$\rho(V_{\max}/t_f)*(t_2-t_1)$	$m_{s,\text{new}} [\text{kg.s}^{-1}]$	
1	0.15	0.15	0.24	0.09	196.184304	38.477965	1.57706E-07	1.3079E-06	0.00025233	0.000188337	0.002092633	
2	0.15	0.42	0.48	0.06	166.060477	38.083269	1.27977E-07	1.1071E-06	0.000204764	0.000106279	0.001771312	
3	0.15	0.66	0.72	0.06	209.314016	52.906831	1.56407E-07	1.3954E-06	0.000250251	0.000133961	0.002232683	
4	0.12	0.84	0.93	0.09	172.793982	11.663973	1.6113E-07	1.4399E-06	0.000257808	0.000207353	0.00230392	
5	0.15	1.11	1.2	0.09	153.064724	28.136539	1.24928E-07	1.0204E-06	0.000199885	0.000146942	0.00163269	
<b>Droplet station 4</b>												
<b>Cycle</b>	$t_f$	$t_1$	$t_2$	$t_2-t_1$	$V_{\max}[\text{mm}^3]$	$V_b[\text{mm}^3]$	$(V_{\max}-V_b)$	$V_{\max}/t_f$	$(V_{\max}-V_b)\rho$	$\rho(V_{\max}/t_f)*(t_2-t_1)$	$m_{s,\text{new}} [\text{kg.s}^{-1}]$	
1	0.15	0.27	0.36	0.09	206.874075	22.792721	1.84081E-07	1.3792E-06	0.00029453	0.000198599	0.002206657	
2	0.15	0.54	0.6	0.06	183.31248	20.921459	1.62391E-07	1.2221E-06	0.000259826	0.00011732	0.001955333	
3	0.15	0.78	0.9	0.12	173.24889	50.111037	1.23138E-07	1.155E-06	0.000197021	0.000221759	0.001847988	
4	0.12	1.05	1.14	0.09	183.641155	35.785908	1.47855E-07	1.5303E-06	0.000236568	0.000220369	0.002448549	
<b>Droplet station 5</b>												
<b>Cycle</b>	$t_f$	$t_1$	$t_2$	$t_2-t_1$	$V_{\max}[\text{mm}^3]$	$V_b[\text{mm}^3]$	$(V_{\max}-V_b)$	$V_{\max}/t_f$	$(V_{\max}-V_b)\rho$	$\rho(V_{\max}/t_f)*(t_2-t_1)$	$m_{s,\text{new}} [\text{kg.s}^{-1}]$	
1	0.12	0.21	0.3	0.09	188.861255	20.921459	1.6794E-07	1.5738E-06	0.000268704	0.000226634	0.00251815	
2	0.09	0.42	0.51	0.09	202.128256	53.457754	1.48671E-07	2.2459E-06	0.000237873	0.000323405	0.003593391	
3	0.09	0.63	0.72	0.09	208.285669	45.004324	1.63281E-07	2.3143E-06	0.00026125	0.000333257	0.003702856	
4	0.06	0.81	0.96	0.15	202.477218	39.462286	1.63015E-07	3.3746E-06	0.000260824	0.000809909	0.005399392	
5	0.12	1.11	1.2	0.09	160.401249	42.800747	1.17601E-07	1.3367E-06	0.000188161	0.000192481	0.002138683	
<b>Droplet station 6</b>												
<b>Cycle</b>	$t_f$	$t_1$	$t_2$	$t_2-t_1$	$V_{\max}[\text{mm}^3]$	$V_b[\text{mm}^3]$	$(V_{\max}-V_b)$	$V_{\max}/t_f$	$(V_{\max}-V_b)\rho$	$\rho(V_{\max}/t_f)*(t_2-t_1)$	$m_{s,\text{new}} [\text{kg.s}^{-1}]$	
1	0.12	0.24	0.27	0.03	133.56092	78.966053	5.45949E-08	1.113E-06	8.73518E-05	5.34244E-05	0.001780812	
2	0.12	0.42	0.51	0.09	197.241559	62.03923	1.35202E-07	1.6437E-06	0.000216324	0.00023669	0.002629887	
3	0.12	0.66	0.84	0.18	184.360283	47.939456	1.36421E-07	1.5363E-06	0.000218273	0.000442465	0.002458137	
4	0.06	0.93	1.02	0.09	197.241559	30.582938	1.66659E-07	3.2874E-06	0.000266654	0.00047338	0.005259775	
<b>Droplet station 7</b>												
<b>Cycle</b>	$t_f$	$t_1$	$t_2$	$t_2-t_1$	$V_{\max}[\text{mm}^3]$	$V_b[\text{mm}^3]$	$(V_{\max}-V_b)$	$V_{\max}/t_f$	$(V_{\max}-V_b)\rho$	$\rho(V_{\max}/t_f)*(t_2-t_1)$	$m_{s,\text{new}} [\text{kg.s}^{-1}]$	
1	0.09	0.3	0.45	0.15	170.102603	36.008622	1.34094E-07	1.89E-06	0.00021455	0.000453607	0.003024046	
2	0.18	0.66	0.72	0.06	171.417067	50.870192	1.20547E-07	9.5232E-07	0.000192875	9.14224E-05	0.001523707	
3	0.18	0.93	1.02	0.09	168.935176	61.857084	1.07078E-07	9.3853E-07	0.000171325	0.000135148	0.001501646	
4	0.12	1.17	1.29	0.12	202.530348	34.896045	1.67634E-07	1.6878E-06	0.000268215	0.000324049	0.002700405	
<b>Actual flow rate, <math>2\Gamma [\text{kg.m}^{-1}\text{s}^{-1}]</math></b>	0.059				<b>Tube length in each image [m]</b>			0.00871		<b>Measured flow rate [kg.s<sup>-1</sup>]</b>		<b>%diff</b>
					0.147					0.01108		27.164741

Table E.3 Error estimation at flow rate at  $0.0145 \text{ kg.s}^{-1}$ : tube gap 10 mm.

Time period	1.08 sec															
<b>Droplet station 1</b>																
<b>Cycle</b>	$t_r$	$t_1$	$t_2$	$t_2-t_1$	$V_{max}[mm^3]$	$V_b[mm^3]$	$(V_{max}-V_b)[m^3]$	$V_{max}/t_r$	$(V_{max}-V_b)\rho$	$p(V_{max}/t_r)(t_2-t_1)$	$m_{s,new} [kg.s^{-1}]$					
1	0.06	0.27	0.36	0.09	218.831691	36.898116	1.81934E-07	3.64719E-06	0.00029109	0.000525196	0.005835512					
2	0.06	0.45	0.57	0.12	134.954493	54.523436	8.04311E-08	2.24924E-06	0.00012869	0.000431854	0.003598786					
3	0.03	0.6	0.72	0.12	129.587764	42.148175	8.74396E-08	4.31959E-06	0.0001399	0.000829362	0.006911347					
4	0.06	0.99	1.08	0.09	218.831691	36.898116	1.81934E-07	3.64719E-06	0.00029109	0.000525196	0.005835512					
<b>Droplet station 2</b>																
<b>Cycle</b>	$t_r$	$t_1$	$t_2$	$t_2-t_1$	$V_{max}[mm^3]$	$V_b[mm^3]$	$(V_{max}-V_b)[m^3]$	$V_{max}/t_r$	$(V_{max}-V_b)\rho$	$p(V_{max}/t_r)(t_2-t_1)$	$m_{s,new} [kg.s^{-1}]$					
1	0.09	0.15	0.3	0.15	150.422711	42.518234	1.07904E-07	1.67136E-06	0.00017265	0.000401127	0.002674182					
2	0.09	0.42	0.54	0.12	192.289423	38.076259	1.54213E-07	2.13655E-06	0.00024674	0.000410217	0.003418479					
3	0.09	0.66	0.78	0.12	168.30028	27.289674	1.41011E-07	1.87E-06	0.00022562	0.000359041	0.002992005					
4	0.09	0.9	1.05	0.15	150.422711	42.518234	1.07904E-07	1.67136E-06	0.00017265	0.000401127	0.002674182					
<b>Droplet station 3</b>																
<b>Cycle</b>	$t_r$	$t_1$	$t_2$	$t_2-t_1$	$V_{max}[mm^3]$	$V_b[mm^3]$	$(V_{max}-V_b)[m^3]$	$V_{max}/t_r$	$(V_{max}-V_b)\rho$	$p(V_{max}/t_r)(t_2-t_1)$	$m_{s,new} [kg.s^{-1}]$					
1	0.06	0.06	0.15	0.09	144.05321	21.113822	1.22939E-07	2.40089E-06	0.0001967	0.000345728	0.003841419					
2	0.09	0.3	0.45	0.15	164.656034	17.877958	1.46778E-07	1.82951E-06	0.00023484	0.000439083	0.002927218					
3	0.21	0.69	0.78	0.09	212.407407	82.871104	1.29536E-07	1.01146E-06	0.00020726	0.000145651	0.001618342					
4	0.03	0.81	0.87	0.06	165.847209	21.113822	1.44733E-07	5.52824E-06	0.00023157	0.000530711	0.008845184					
<b>Droplet station 4</b>																
<b>Cycle</b>	$t_r$	$t_1$	$t_2$	$t_2-t_1$	$V_{max}[mm^3]$	$V_b[mm^3]$	$(V_{max}-V_b)[m^3]$	$V_{max}/t_r$	$(V_{max}-V_b)\rho$	$p(V_{max}/t_r)(t_2-t_1)$	$m_{s,new} [kg.s^{-1}]$					
1	0.12	0.24	0.3	0.06	149.049795	47.368567	1.01681E-07	1.24208E-06	0.00016269	0.00011924	0.001987331					
2	0.12	0.45	0.51	0.06	209.344451	4.7360748	2.04608E-07	1.74454E-06	0.00032737	0.000167476	0.002791259					
3	0.15	0.66	0.78	0.12	179.499646	44.53954	1.3496E-07	1.19666E-06	0.00021594	0.00022976	0.001914663					
4	0.12	0.96	1.02	0.06	147.707964	47.368567	1.00339E-07	1.2309E-06	0.00016054	0.000118166	0.00196944					
<b>Droplet station 5</b>																
<b>Cycle</b>	$t_r$	$t_1$	$t_2$	$t_2-t_1$	$V_{max}[mm^3]$	$V_b[mm^3]$	$(V_{max}-V_b)[m^3]$	$V_{max}/t_r$	$(V_{max}-V_b)\rho$	$p(V_{max}/t_r)(t_2-t_1)$	$m_{s,new} [kg.s^{-1}]$					
1	0.09	0.42	0.57	0.15	179.711003	14.624043	1.65087E-07	1.99679E-06	0.00026414	0.000479229	0.003194862					
2	0.18	0.78	1.02	0.24	204.01537	47.661127	1.56354E-07	1.13342E-06	0.00025017	0.000435233	0.00181347					
<b>Droplet station 6</b>																
<b>Cycle</b>	$t_r$	$t_1$	$t_2$	$t_2-t_1$	$V_{max}[mm^3]$	$V_b[mm^3]$	$(V_{max}-V_b)[m^3]$	$V_{max}/t_r$	$(V_{max}-V_b)\rho$	$p(V_{max}/t_r)(t_2-t_1)$	$m_{s,new} [kg.s^{-1}]$					
1	0.09	0.18	0.39	0.21	145.445915	27.948474	1.17497E-07	1.61607E-06	0.000188	0.000542998	0.002585705					
2	0.15	0.57	0.78	0.21	203.753894	14.447845	1.89306E-07	1.35836E-06	0.00030289	0.000456409	0.002173375					
3	0.09	0.9	1.08	0.18	166.297075	87.244724	7.90524E-08	1.84775E-06	0.00012648	0.000532151	0.002956392					
<b>Actual flow rate, <math>2\Gamma [kg.m^{-1}.s^{-1}]</math></b>	0.0726				<b>Tube length in each image [m]</b>			0.12		<b>Adjusted flow rate <math>[kg.s^{-1}]</math></b>		0.0087	<b>Measured flow rate <math>[kg.s^{-1}]</math></b>	0.012	<b>%diff</b>	37.43